Towards Hybrid Trapping of Cold Molecules and Cold Molecular Ions

Inauguraldissertation

zur

Erlangung der Würde eines Doktors der Philosophie

vorgelegt der

Philosophisch-Naturwissenschaftlichen Fakultät

der Universität Basel

von

Dominik Haas

aus

Waldenburg (BL)

Basel, 2019

Genehmigt von der Philosophisch-Naturwissenschaftlichen Fakultät
auf Antrag von

Prof. Dr. Stefan Willitsch und Prof. Dr. Sebastiaan Y. T. van de Meerakker

Basel, den 21.05.2019

Prof. Dr. Martin Spiess
Dekan

Abstract

A pinhole discharge unit as well as a dielectric barrier discharge (DBD) head were developed for the Nijmegen pulsed valve (NPV) and the molecular beam properties accessible from each source were characterised and compared. The discharge conditions were optimised for maximum hydroxyl radical density. It was found that the DBD source yields colder OH radicals, whereas the pinhole discharge source provides a threefold larger radical density compared to the DBD discharge head.

Translationally cold packages of hydroxyl radicals ($T_{\mathrm{trans}} > 1mK$) were produced by means of Stark deceleration and a 124-stage Stark decelerator was set up in the laboratory. The decelerator was conditioned, characterised and optimised for operation at low final velocities ($v < 40$ m/s). The performance of the decelerator was assessed by determining the density of OH radicals available after the deceleration process.

In a final step, a translationally cold OH package was loaded into a cryogenic magnetic trap. The trap design, the coupling of the magnetic trap to the Stark decelerator and the loading efficiency were numerically optimised employing a direct search algorithm on Monte-Carlo trajectory simulations. The cryogenic environment efficiently prevents blackbody radiation from pumping OH radicals out of trappable states and the background pressure improved significantly. Under cryogenic conditions the 1/e trap lifetime improved by a factor of 30 compared to room temperature. The magnetic trap forms part of a hybrid trapping scheme for neutral molecules and ionic species. This novel type of trap represents a versatile environment for investigating ion-neutral molecule reactions in the cold regime, while offering full control over the contributing quantum states.

Acknowledgements

First and foremost I wish to thank Stefan Willitsch for offering me the unique opportunity to be part of such an exciting research project. His encouragement, guidance and invaluable advice were of great significance for the success of this project.

I would like to express my gratitude to Dongdong Zhang, who supervised this project and was always available for discussions and advice. His willingness to share his time and knowledge so generously and his active support in the project are very much appreciated. Dong, it was a great pleasure to work with you.

Special thanks go to the Nijmegen research group of Bas van de Meerakker for the rewarding collaboration and for giving Dong and me such a warm welcome to their facility. In particular, I would like to extend my sincere thanks to Sebastiaan (Bas) van de Meerakker for agreeing to co-examine this project, for sharing his extensive professional knowledge with me and advising me on the development of the gas nozzle and trap in several Skype sessions. I would like to acknowledge Andre van Roij, who advised me on how to assemble a Stark decelerator. I am thankful to Niek Janssen for developing the electronics of the DBD discharge unit.

I am grateful to all members of the research group for creating a pleasant work environment and engaging in stimulating discussions. The fun hours and exciting excursions we had together never failed to lighten up my mood and lift my spirits. In particular, I would like to thank Claudio von Planta and Christian Mangeng for their constructive and enriching contributions to the project. Many thanks to Thomas Kierspel for bringing fresh impetus and ideas to the group and the project and for his constructive suggestions for improvement. A big thank you also goes to Pascal Eberle for supplementing this thesis with high-quality pictures of the experimental setup in Fig. 4.8 a) and b) and Fig. 4.15 b).

I would like to thank the master and project students Sebastian Scherb and Dominik Ostermayer for contributing to this project and to Ludger Ploenes for his valuable support in characterising the valve.

I am particularly grateful for the assistance provided by the members of our in-house mechanical workshop: The reliable technical support and precise manufacturing of the mechanical components by Philipp Knöpfel, Grischa Martin and Dieter Wild were the key to success in the construction of the experimental setup and their valuable inputs and suggestions contributed significantly to the entire project.

I would like to acknowledge Anatoly Johnson for his help with adjusting the lasers. I am also indebted to Georg Holderied from the electronic workshop for his constant support and advice.

We thank Prof. Jun Ye for kindly making available to us construction drawings of his pinhole discharge unit, upon which the discharge head of the Nijmegen pulsed valve is based.

Thanks are also due to the Swiss National Foundation for the financial support that made this work possible.

Finally, my deep appreciation goes to my family for their unwavering support and continuous encouragement throughout my years of study.

Contents

Chapter 1

Introduction to cold molecules

In recent years, cold molecules have become the subject of intensive study [1–5]. The interest in cold molecules was fostered by the achievements in cold ($T < 1$ K) and ultracold ($T < 1$ mK) atomic physics, where laser and evaporative cooling have paved the way for investigating chemical reactions in the cold and ultracold regime [3, 6, 7]. By laser cooling atoms and atomic ions [8, 9], temperatures as low as a few micro-Kelvin can be achieved, which is significantly colder than the lowest naturally occurring temperatures of approx. 10 K within interstellar clouds [10]. Consequently, the coldest known spots in the universe are to be found in laser cooling laboratories around the globe. Laser cooling relies on the repeated absorption and isotropic scattering of photons from a laser beam detuned below an atomic transition frequency [9]. The exchange of momentum between the laser beam and the absorbing atom leads to the withdrawal of kinetic energy, thereby slowing the atom's motion. Like cold and ultracold atoms have revolutionised the field of atomic physics, cold molecules are no less likely to have a similarly profound impact. Cold molecules are at the forefront of many recent investigations as they offer appealing prospects such as spectroscopic precision measurements for the search of physics beyond the Standard Model [5, 11, 12] and the investigation of collisions at very low temperatures [13–15]. Moreover, cold molecules represent promising systems for quantum computation [16, 17]. Additionally, molecules possess a complex internal energy structure, which renders them interesting targets for spectroscopic investigations [5]. There is a strong link between the structure of molecules and their chemical reactivity [18, 19]. Additionally, molecules can possess electric and magnetic moments, which are handles allowing for exquisite control over the orientation of molecular species in space [20, 21].

Generally, cold denotes temperatures below 1 K and ultracold refers to temperatures below 1 mK [3]. In the field of cold atomic and molecular physics, "temperatures" are often used to denote kinetic or potential energies by dividing through Boltzmann's constant k_B [2]. At low temperatures, the de Broglie wavelength $\Lambda = \frac{h}{p}$ of atoms and molecules increases

significantly.

$$\Lambda = \frac{h}{p} = \frac{h}{m \cdot v} = \frac{h}{\sqrt{2\pi m k_{\mathrm{B}} T}}\,, \tag{1.1}$$

where h denotes Planck's constant, k_{B} represents Boltzmann's constant, m is the mass of the molecule and T denotes the temperature [2, 3]. Under room temperature conditions, an OH molecule displays a de Broglie wavelength of 0.25 Å and the matter wave extends over 33 Å for OH molecules at 16 mK (4 m/s), which is a typical translational temperature encountered in the magnetic trap described in chapter 6 of this thesis. The de Broglie wavelength of the trapped molecules is significantly larger then the OH bond length of 0.97 Å [22]. As the molecule's matter wave reaches beyond the typical interaction distance of intermolecular forces, wave-like properties start dominating the course of chemical reactions in the cold regime [2, 3]. An important quantity for characterising an ensemble of cold molecules is the phase-space density ρ_{D}, which is defined as the product between the number density n and the cubed de Broglie wavelength Λ^3, i.e. $\rho_{\mathrm{D}} = n \cdot \Lambda^3$ [2]. Provided a sufficiently dense and cold sample can spatially be confined, quantum degeneracy is reached below $n\Lambda^3 = 2.6$ [3]. It is insightful to consult Fig. 2 in the review article by M. T. Bell and T. P. Softley [3] in order to assess the phase-space density regime accessible by the various methods for producing cold molecules.

Unlike atomic species, molecules possess a complex internal energy structure due to additional vibrational and rotational degrees of freedom and are usually not amenable to laser cooling. Non-favourable Franck-Condon factors can lead to rapid branching of excited states, which imposes a problem for maintaining a closed cooling cycle [23]. In spite of all the difficulties associated with laser cooling molecules, successful laser cooling and magneto-optical trapping of molecules have been demonstrated [16, 23–25].

Due to the complexity and the currently restricted chemical scope of laser cooling schemes, most cold molecular species are produced by following different strategies [1]. It is common practice to distinguish between direct and indirect methods [2, 3]. Here, indirect refers to cooling schemes not starting with molecular species. Instead, ultracold atomics are combined to form cold molecules through Feshbach resonance tuning [26] or photoassociation [27]. While these indirect methods give access to extraordinarily high phase-space densities at temperatures below 1 µK, they are usually limited to alkali dimers [2, 3].

On the other hand, direct cooling schemes rely on molecular sources and the different methods available can be classified as phase-space density enhancing or as methods which at best preserve the phase-space density [2, 3]. In order to achieve phase-space compression during the cooling process, dissipative forces are required for the irreversible removal

of energy, which is also referred to as "genuine cooling" [3]. Cooling methods pertaining to the phase-space density enhancing type include microwave-induced evaporative cooling [28], Sisyphus cooling [29, 30], buffer gas cooling [31, 32] and laser cooling [16, 23–25]. Phase-space density enhancing cooling is particularly appealing in combination with a trap environment [3]. Evaporative cooling relies on removing particles with a high thermal energy of motion from a trap. This can be achieved by lowering the trap depth temporarily or with the help of an RF knife [28]. The remaining molecules are colder and occupy less space within the trap which results in an increased phase-space density ρ_{D}. Of all the cooling methods mentioned in this section, buffer gas cooling is the most universal, as the cooling is collision mediated and the method is applicable to most small molecules. Hot molecules are entrained in a cryogenic buffer gas and thermalisation with the cold bath is achieved eventually. Temperatures of a few Kelvin can be reached with such a cooling scheme [32, 33].

As Stark [34, 35], optical Stark [36, 37] and Zeeman [38–40] decelerators rely on conservative forces for slowing a selected portion of a molecular beam, they belong to the class of direct methods which do not increase the phase-space density. In accordance with Liouville's theorem (see sec. 3.2.1), the maximum achievable phase-space density is identical to the one provided by the molecular beam upon incoupling into the decelerator [3]. It is therefore imperative to start with a dense molecular beam source. The Stark deceleration technique exploits the Stark effect experienced by polar molecules in switched inhomogeneous electric fields, thereby producing a molecular package at translational temperatures of $T_{\mathrm{trans}} > 1$ mK. The working principle of a Zeeman decelerator is similar to Stark deceleration, except that the Zeeman effect of species with a magnetic moment is exploited, which offers complementarity of the species that are amenable to deceleration [35]. Instead of slowing molecules with switched fields, nozzles rotating at high speeds have successfully been employed to slow and accelerate molecular beams [41–43]. Other mechanical sources of slow molecules have been realised in the form of a rotating centrifuge decelerator [44, 45] and a rotating paddle [46]. Alternatively, centrifugal forces can be exploited in a stationary quadrupolar guide, which acts as velocity filter for slow molecules [47]. In combination with effusive gas sources, such a setup provides a continuous source of cold molecules. It is common to combine non-phase-space-compressing methods with techniques capable of increasing the phase-space density [28–30, 48, 49].

In this thesis, a pulsed molecular beam valve is employed for the production of a cold and dense molecular beam of hydroxyl radicals via electric dissociation of water vapour. For that purpose, a pinhole discharge head as well as a dielectric barrier discharge unit were designed to fit the Nijmegen pulsed valve [50] and the characterisation of the two

discharge sources is described in chapter 4. While the OH radicals within the molecular beam are internally cold and display a narrow velocity spread, the forward motion of the molecular beam is fast (usually 425-470 m/s for krypton as a carrier gas) and a 124-stage Stark decelerator was set up to decelerate packages of OH radicals below 30 m/s. As Stark deceleration does not allow for compression of phase space, the radical source as well as the operation of the decelerator were optimised for maximum signal intensity at low final velocities. The construction and the optimisation of the deceleration conditions are described in chapter 5. In a final step, the hydroxyl radicals were loaded into a cryogenic magnetic trap, which is the topic of chapter 6. The trap loading process was modelled and optimised by means of Monte Carlo trajectory simulations. Compared to room temperature trapping, the cryogenic environment allows for prolonged trapping lifetimes due to the lower background pressure and the reduction in BBR intensity reaching the trap centre. The work presented in this thesis represents the prelude towards the long-standing goal of investigating elastic, inelastic and reactive collisions between neutral molecules and molecular ions inside a hybrid trap [51]. A central theme present in all three experimental chapters, i.e. chapters 4, 5 and 6, is the determination of densities in the source chamber and after the decelerator exit.

Chapter 2 provides background information on the hydroxyl radical, which is in many ways the protagonist of the experiments described here. Due to their low mass to Stark shift ratio, OH radicals are ideally suited for Stark deceleration and the magnetic moment allows for magnetic trapping. An introduction to the working principles of Stark deceleration and the concept of phase stability is given in chapter 3.

Chapter 2

The OH radical

Compared to atoms, which are the subject of investigation in atomic physics, molecules display a much more diverse energetic structure. A complete description of a molecule requires accounting for the motion of the nuclei, whereas in atoms, it is sufficient to consider the motion of electrons around the nucleus. Within the Born-Oppenheimer approximation, the motion of a molecule's nuclei can be separated from the motion of the electrons [52, 53] and the energetic structure of a molecule can be divided into electronic, vibrational and rotational contributions. While this rich internal energy structure leads to an increased complexity of molecules and their spectra, it also offers more flexibility and versatility in the types of experiments that can be performed with molecular species [5]. Another key difference setting molecules apart from atomic species is their diverse geometric structure. By employing molecules, it is possible to study spatially relevant aspects of chemistry. Many molecules possess electric or magnetic dipole moments, which allows for their spatial manipulation in electric and magnetic fields [35]. In fact, it has been demonstrated that the spatial motion of molecules can be controlled on such an exquisite level that it is possible to slow [35], guide [47], confine [54, 55] and spatially align [21] molecules.

The purpose of this chapter is to provide an introduction to the hydroxyl radical's energetic structure, which is probed during the LIF spectroscopy performed at various points in the thesis. Furthermore, the hydroxyl radical is a diatomic molecule with a low mass featuring an electric as well as a magnetic dipole moment. The interaction of the dipole moments with electric or magnetic fields leads to the splitting of rotational energy levels, which is referred to as Stark or Zeeman effect. In the context of this thesis, the Stark effect is used for slowing OH molecules and the Zeeman interaction is exploited for confining translationally cold hydroxyl radicals inside a magnetic trap. Finally, expressions allowing for the calculation of the Stark and Zeeman energy level splittings are derived.

2.1 Energy level structure of OH

In molecular spectroscopy, the Born-Oppenheimer approximation is of great importance as it allows for the decoupling of the electron motion from the motion of the nuclei [53, 56]. The molecular Hamiltonian is given by the following expression [53]:

$$\begin{aligned}\hat{H} =& -\frac{\hbar^2}{2}\sum_{\alpha}\frac{\nabla_{\alpha}^2}{M_{\alpha}} - \frac{\hbar^2}{2m_{\mathrm{e}}}\sum_{i}\nabla_{\mathrm{i}}^2 + \sum_{\alpha}\sum_{\beta>\alpha}\frac{Z_{\alpha}Z_{\beta}e^2}{4\pi\varepsilon_0 r_{\alpha\beta}} \\ & - \sum_{\alpha}\sum_{i}\frac{Z_{\alpha}e^2}{4\pi\varepsilon_0 r_{i\alpha}} + \sum_{i}\sum_{j>i}\frac{e^2}{4\pi\varepsilon_0 r_{ij}} \\ =& \hat{T}_{\mathrm{N}} + \hat{T}_{\mathrm{e}} + \hat{V}_{\mathrm{NN}} + \hat{V}_{\mathrm{eN}} + \hat{V}_{\mathrm{ee}}\,, \end{aligned} \tag{2.1}$$

where the terms denote the kinetic energy of the nuclei $\hat{T}_{\mathrm{N}}$, the kinetic energy of the electrons $\hat{T}_{\mathrm{e}}$, the potential energy due to inter-nuclear repulsion $\hat{V}_{\mathrm{NN}}$, the potential energy associated with the electron-nuclei interaction $\hat{V}_{\mathrm{eN}}$ and the potential energy resulting from the repulsion between the electrons $\hat{V}_{\mathrm{ee}}$. Furthermore, M_{α} denotes the mass of the α-th nucleus, m_{e} is the mass of an electron, Z denotes multiples of the elementary charge e and ε_0 is the permittivity of free space. Inter-particle separations are denoted by r. Unfortunately, it is very complicated to solve Schrödinger's equation $\hat{H}\Psi = E\Psi$ for the Hamiltonian given in Eqn. 2.1.

While the electrostatic interaction involving the positively charged nuclei and the negatively charged electrons are similar in magnitude, the mass of an electron is approximately 1836 times lower than that of a proton. Therefore, the electrons are moving much faster than the nuclei and it is a valid assumption to consider constant positions of the nuclei on timescales relevant to the motion of the electrons. The wave function can then be approximated by [53]:

$$\Psi^{(n)} \approx \Psi_{\mathrm{el}}^{(n)}(\vec{r}_{\mathrm{e}}, \vec{r}_{\mathrm{N}}) \cdot \theta_N^{(n)}(\vec{r}_{\mathrm{N}})\,, \tag{2.2}$$

where $\Psi_{\mathrm{el}}^{(n)}(\vec{r}_{\mathrm{e}}, \vec{r}_{\mathrm{N}})$ denotes the electronic wave function in the n-th electronic state and depends on the electronic $\vec{r}_{\mathrm{e}}$ and nuclear $\vec{r}_{\mathrm{N}}$ coordinates. $\theta_N(\vec{r}_{\mathrm{N}})$ represents the nuclear wave function, which solely depends on the nuclear coordinates. Setting the kinetic energy Hamiltonian of the nuclear motion $\hat{T}_{\mathrm{N}}$ to zero and inserting the product Ansatz from Eqn. 2.2 into the Schrödinger equation allows to retrieve a purely electronic form of the Schrödinger equation [53].

$$\begin{aligned}\left(\hat{T}_{\mathrm{e}} + \hat{V}_{\mathrm{NN}} + \hat{V}_{\mathrm{eN}} + \hat{V}_{\mathrm{ee}}\right)\Psi_{\mathrm{el}}^{(n)}(\vec{r}_{\mathrm{e}}, \vec{r}_{\mathrm{N}}) &= \left(\hat{H}_{\mathrm{el}} + \hat{V}_{\mathrm{NN}}\right)\Psi_{\mathrm{el}}^{(n)}(\vec{r}_{\mathrm{e}}, \vec{r}_{\mathrm{N}}) \\ &= U^{(n)}(\vec{r}_{\mathrm{N}})\Psi_{\mathrm{el}}^{(n)}(\vec{r}_{\mathrm{e}}, \vec{r}_{\mathrm{N}})\,, \end{aligned} \tag{2.3}$$

where $U^{(n)}(\vec{r}_{\mathrm{N}})$ represents the combined electronic energy E_{el} and constant potential energy V_{NN} at fixed $\vec{r}_{\mathrm{N}}$. The superscript (n) refers to the electronic state $|n\rangle$. Changing the molecule's nuclear configuration results in different values of $U^{(n)}(\vec{r}_{\mathrm{N}})$, which is also referred to as the Born-Oppenheimer potential energy surface. Usually, $U^{(n)}(\vec{r}_{\mathrm{N}})$ is a multi-dimensional hypersurface, but for diatomic molecules $U^{(n)}(\vec{r}_{\mathrm{N}})$ only depends on the position of two nuclei and the potential energy needs to be determined for different internuclear separations only. $U^{(n)}(\vec{r}_{\mathrm{N}})$ can be regarded as the potential which governs the motion of the nuclei. This leads to the Schrödinger equation for the nuclear motion, which is given by the following expression [53]:

$$\left(\hat{T}_{\mathrm{N}} + U^{(n)}(\vec{r}_{\mathrm{N}})\right) \theta_{\mathrm{N}}(\vec{r}_{\mathrm{N}}) = E_{\mathrm{N}}^{(n)}\, \theta_N(\vec{r}_{\mathrm{N}})\,, \tag{2.4}$$

where $E_{\mathrm{N}}^{(n)}$ denotes the energy associated with the nuclear motion, given the electronic state is $|n\rangle$. As the different types of molecular motion such as translation, rotation and vibration take place on different time scales, the nuclear wave function $\theta_{\mathrm{N}}^{(n)}(\vec{r}_{\mathrm{N}})$ may be separated into individual parts [53, 57].

$$\theta_{\mathrm{N}}^{(n)} \approx \phi_{\mathrm{tr}} \cdot \phi_{\mathrm{rot}} \cdot \phi_{\mathrm{vib}} \tag{2.5}$$

and it is convenient to express the molecular Hamiltonian in the following form:

$$\hat{H} = \hat{H}_{\mathrm{el}} + \hat{H}_{\mathrm{vib}} + \hat{H}_{\mathrm{rot}}\,. \tag{2.6}$$

In the following sections, the electronic and vibrational energy structure of diatomic molecules will be discussed briefly. The discussion of the rotational energy structure is relegated to sections 2.2 and 2.3, as it is more involved.

2.1.1 Electronic energy level structure

For a diatomic molecule consisting of two nuclei A and B, the electronic Hamiltonian $\vec{H}_{\mathrm{el}}$ given in Eqn. 2.3 can be cast into the following form [53]:

$$\begin{aligned}\hat{H}_{\mathrm{el}} &= -\frac{\hbar^2}{2m_{\mathrm{e}}} \sum_i \nabla_{\mathrm{i}}^2 + \frac{Z_{\mathrm{A}} Z_{\mathrm{B}} e^2}{4\pi\varepsilon_0 r_{\mathrm{AB}}} - \sum_i \frac{Z_{\mathrm{A}} e^2}{4\pi\varepsilon_0 r_{\mathrm{A\,i}}} - \sum_i \frac{Z_{\mathrm{B}} e^2}{4\pi\varepsilon_0 r_{\mathrm{B\,i}}} + \sum_i \sum_{j>i} \frac{e^2}{4\pi\varepsilon_0 r_{ij}} \\ &= \hat{T}_{\mathrm{e}} + \hat{V}_{\mathrm{AB}} + \hat{V}_{\mathrm{eA}} + \hat{V}_{\mathrm{eB}} + \hat{V}_{\mathrm{ee}}\,,\end{aligned} \tag{2.7}$$

which is in line with the Born-Oppenheimer approximation. The electronic wave function ψ_{el} is composed of molecular orbitals (MO), which in turn are obtained from a linear combination of atomic orbitals (LCAO). As outlined in ref. [53], the electronic wave

function ψ_{el} needs to be written in the form of a Slater determinant. The energy level diagram, which arises from the linear combination of atomic orbitals is depicted in Fig. 2.1. In this thesis only two electronic states of OH are relevant, the $X^2\Pi$ ground state and the first electronic excited state $\mathrm{A}^2\Sigma^+$. The electronic configuration of the ground state is given by

$$\mathrm{X}^2\Pi : (1\mathrm{s})^2\ (2\mathrm{s}\sigma)^2\ (2\mathrm{p}\sigma)^2\ (2\mathrm{p}\pi)^3 \tag{2.8}$$

and the electronic configuration of the first electronically excited state is obtained by promoting an electron from the $2\mathrm{p}\sigma$ MO into the $2\mathrm{p}\pi$ MO.

$$\mathrm{A}^2\Sigma^+ : (1\mathrm{s})^2\ (2\mathrm{s}\sigma)^2\ (2\mathrm{p}\sigma)^1(2\mathrm{p}\pi)^4\,. \tag{2.9}$$

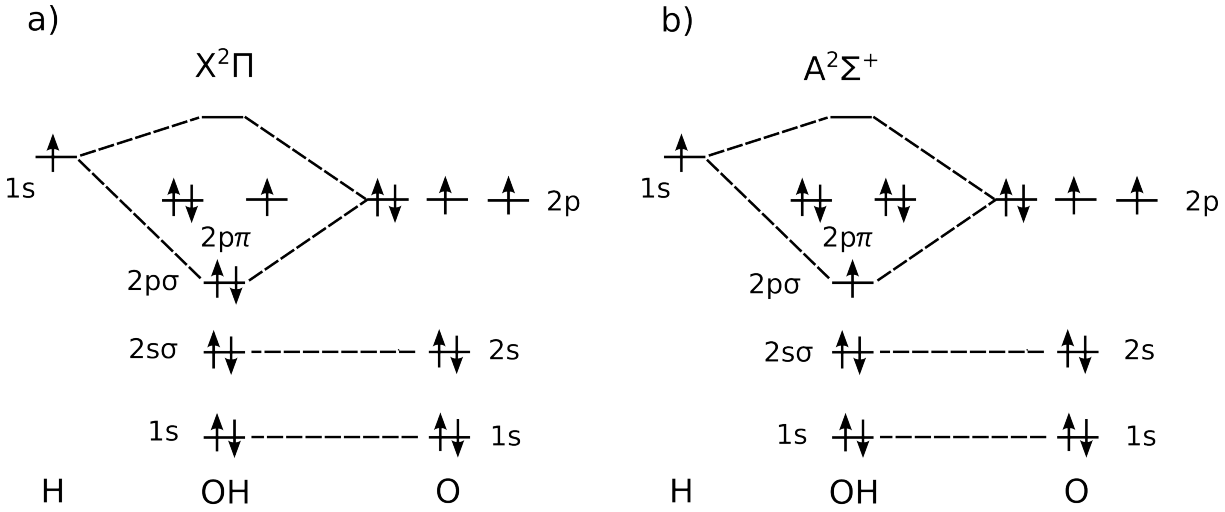

Figure 2.1: Molecular orbital (MO) diagram of OH in the **a)** $\mathrm{X}^2\Pi$ electronic ground state and **b)** in the first electronic excited state $\mathrm{A}^2\Sigma^+$. In the $\mathrm{A} \leftarrow \mathrm{X}$ transition, an electron is excited from the $2\mathrm{p}\sigma$ to the $2\mathrm{p}\pi$ MO. The arrows represent electrons with spin quantum numbers $m_{\mathrm{s}} = 1/2$ and $m_{\mathrm{s}} = -1/2$.

2.1.2 Vibrational energy level structure

The Hamiltonian for a harmonic oscillator consisting of two nuclei is given by the following expression [53]:

$$\frac{-\hbar^2}{2\mu}\frac{\mathrm{d}\,\phi_{\mathrm{vib}}(y)}{\mathrm{d}\,y^2} + \frac{1}{2}ky^2\phi_{\mathrm{vib}}(y) = E_{\mathrm{vib}}\,\phi_{\mathrm{vib}}(y)\,, \tag{2.10}$$

where y denotes the internuclear separation, k is the spring constant and μ represents the reduced mass. The vibrational wave functions ϕ_{vib} are Hermite functions [53] and the

energies E_{vib} of the harmonic oscillator are given by

$$E_{\mathrm{vib}} = hc\tilde{\nu}\,(v + \frac{1}{2})\,, \tag{2.11}$$

where $\tilde{\nu}$ is the vibrational wave number and v denotes the vibrational quantum number. The vibrational frequency ω_{vib} is related to the spring constant k via:

$$\omega_{\mathrm{vib}} = \sqrt{\frac{k}{\mu}}\,. \tag{2.12}$$

As the assumption of a harmonic potential $U(y) = 1/2\,k\,y^2$ is only valid in proximity to the equilibrium position of the Born-Oppenheimer potential, the Morse potential [53, 56] is frequently used instead and an energy correction of $hc\tilde{\nu}\,(v+1/2)^2\,x_{\mathrm{e}}$ needs to be added to Eqn. 2.11 when using this enhanced model. x_{e} is the anharmonicity constant, which is related to the dissociation energy D_{e} via the following expression:

$$x_{\mathrm{e}} = \frac{\tilde{\nu}}{4D_{\mathrm{e}}}\,. \tag{2.13}$$

When using Morse potentials, the energy spacings between two subsequent vibrational energy levels are no longer constant, but are reduced with increasing v. The selection rules for the anharmonic oscillator are $\Delta v = \pm 1, \pm 2 + \pm 3 \cdots$, where the fundamental transition $\Delta v = \pm 1$ is usually strongest. Furthermore, the dipole moment has to change along the axis of vibration [53]. For OH in the $X^2\Pi$ electronic ground state, the equilibrium position on the Born-Oppenheimer potential lies at an internuclear separation of $R_{\mathrm{eq}} = 0.97$ Å [58] and the vibrational wave number $\tilde{\nu}$ is 3737.76 cm^{-1} [58]. The unitless anharmonicity constant amounts to $x_{\mathrm{e}} = 0.0227$ [58]. Molecular parameters for OH in the $X^2\Pi$ and the $A^2\Sigma$ states are listed in Tab. 2.2.

2.2 Hund's coupling cases

In a diatomic molecule, contributions to the total angular momentum $\vec{J}$ can originate from the net electronic orbital angular momentum $\vec{L}$, the total electron spin $\vec{S}$, the nuclear spin $\vec{I}$ and the rotation of the molecular frame $\vec{R}$ [56, 59]. The coupling between these momenta can be of significantly different strength. Depending on the coupling hierarchy, different energetic structures evolve which affect the spectroscopy of diatomic molecules. Following a classification scheme proposed by F. Hund, five different coupling cases (a)-(e) can be distinguished, of which only the (a) and (b) cases are relevant in the context of this thesis. Many more coupling cases arise if the hyperfine structure (HFS) is included.

The angular momentum vectors required in the subsequent discussion are listed here for convenience [56, 60]:

vector	quantum number	description
$\vec{L}$	L	electronic orbital angular momentum
$\vec{\Lambda}$	Λ	projection of $\vec{L}$ onto the internuclear axis
$\vec{S}$	S	total electron spin angular momentum
$\vec{\Sigma}$	Σ	projection of $\vec{S}$ onto the internuclear axis
$\vec{J}$	J	total angular momentum ($\vec{J} = \vec{L} + \vec{S} + \vec{R}$)
$\vec{\Omega}$	Ω	projection of $\vec{J}$ onto the internuclear axis ($\vec{\Omega} = \vec{\Sigma} + \vec{\Lambda}$)
$\vec{N}$	N	total angular momentum without spin ($\vec{N} = \vec{J} - \vec{S}$)
$\vec{R}$	R	nuclear angular momentum of rotation ($\vec{R} = \vec{N} - \vec{L}$)
$\vec{I}$	I	nuclear spin angular momentum

Table 2.1: Summary of different angular momentum vectors and angular momentum quantum numbers required for the description of momentum coupling in Hund's case (a) and (b) molecules, adapted from [56, 60].

2.2.1 Hund's case (a)

The coupling scheme pertaining to Hund's case (a) is depicted in Fig. 2.2 a). In this coupling scheme, the electronic orbital angular momentum $\vec{L}$ is tightly coupled to the internuclear axis by electrostatic interactions with the nuclear framework of the molecule [59]. Furthermore, large spin-orbit interactions couple the total electron spin angular momentum $\vec{S}$ to $\vec{L}$, such that both momenta are coupled to the internuclear axis. The strength of the spin-orbit interaction is parametrised by the constant A_{SO} and the Hamiltonian for the interaction is $\hat{H}_{\mathrm{SO}} = A_{\mathrm{SO}}\vec{L} \cdot \vec{S}$ [56, 60].

The projections of $\vec{L}$ and $\vec{S}$ onto the internuclear axis are well defined and the corresponding quantum numbers are Λ and Σ. For OH in the electronic ground state $X^2\Pi$, $\Lambda = \pm 1$ and $\Sigma = \pm 1/2$. Since Λ and Σ are positively and negatively valued quantum numbers, they can be perceived as vectors pointing to the right or the left on the molecular axis. Upon their addition, the resulting vector is formed by $\vec{\Omega} = \vec{\Lambda} + \vec{\Sigma}$. For OH, Ω evaluates to $\Omega = \pm 1/2$ and $\Omega = \pm 3/2$. It is common to include the value of $|\Omega|$ in the term symbol ${}^{2|\Sigma|+1}|\Lambda|_{|\Omega|}$. The spin-orbit interaction splits the energy structure of OH into two spin-orbit manifolds, which is denoted by $X^2\Pi_{3/2}$ and $X^2\Pi_{1/2}$. As the spin-orbit coupling constant A_{SO} is negative for OH, the $X^2\Pi_{3/2}$ manifold is lower in energy [56].

$\vec{R}$ denotes the nuclear rotational angular momentum and lies normal to the molecular axis. Vector addition of $\vec{\Omega}$ and $\vec{R}$ results in the total angular momentum $\vec{J}$, i.e. $\vec{J} = \vec{\Omega} + \vec{R}$. The good quantum numbers are $J, \Omega, \Lambda, \Sigma$, which allows case (a) wave functions to be written as $|J, \Omega, \Lambda, \Sigma\rangle$. In pure Hund's case (a) molecules, the spin-orbit coupling constant needs to be significantly larger than the rotational constant B ($A_{\mathrm{SO}} \gg B$) in order to assure that $\vec{L}$ and $\vec{S}$ remain coupled, which ensures that Σ and Ω are good quantum numbers. Comparing the $X^2\Pi$ spin-orbit interaction constant A_{SO} of OH to the rotational constant B results in $A/B \approx -7.5$ (see Tab. 2.2). The magnitude of this ratio is too low for OH $X^2\Pi$ to be a pure Hund's case (a) molecule and mixing between different Ω states has to be accounted for. OH in the electronic ground state contains a certain amount of Hund's case (b) character, which becomes more pronounced at larger values of J [53, 56].

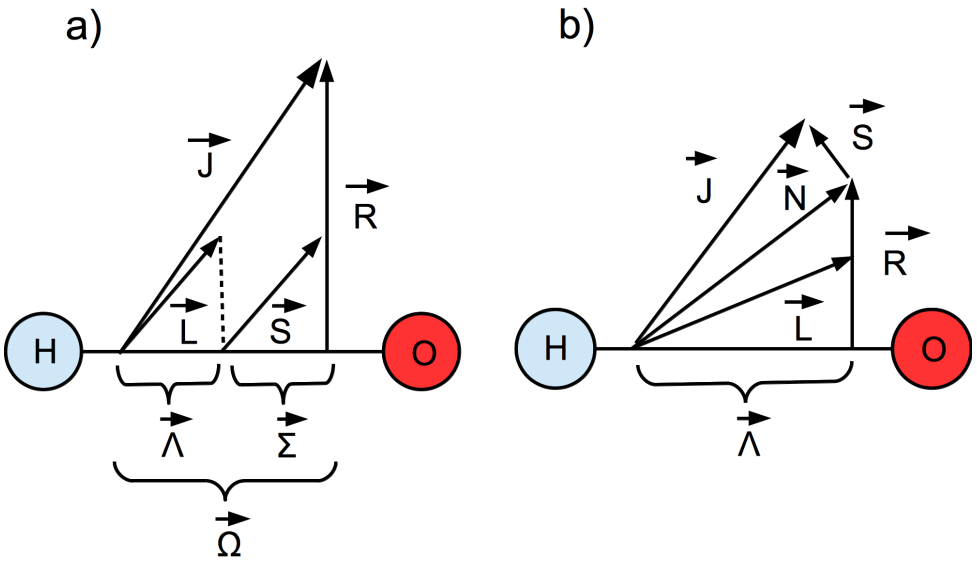

Figure 2.2: Hund's coupling cases. **a)** Hund's case (a) coupling scheme. The electronic orbital angular momentum $\vec{L}$ is bound to the internuclear axis by electrostatic interactions and the total electron spin angular momentum $\vec{S}$ couples onto $\vec{L}$. The resulting total angular momentum is denoted by $\vec{J}$ and rotations of the nuclear framework are described by $\hat{\vec{R}} = \hat{\vec{J}} - \hat{\vec{L}} - \hat{\vec{S}}$. Good quantum numbers for Hund's case (a) are: $J, \Omega, \Lambda, \Sigma$. **b)** Hund's case (b) coupling scheme. The electronic orbital angular momentum $\vec{L}$ is bound to the internuclear axis, but the total electron spin angular momentum $\vec{S}$ couples to $\vec{N}$. Good quantum numbers are: J, N, S, Λ.

2.2.2 Hund's case (b)

As depicted in Fig. 2.2 b), the total electron spin angular momentum $\vec{S}$ is no longer coupled to the internuclear axis in Hund's case (b), while $\vec{L}$ remains coupled to the molecular axis electrostatically. Usually, this type of coupling arises in Σ electronic states

and also applies to the $A^2\Sigma^+$ first electronic excited state of OH. $\vec{S}$ couples to $\vec{N}$, the total angular momentum without spin, and this type of coupling is referred to as spin-rotation interaction, the coupling constant of which is usually denoted by γ. The Hamilton operator for the coupling is expressed by $\hat{H}_{\mathrm{SR}} = \gamma\vec{N}\cdot\vec{S}$. While Λ remains a good quantum number, Ω no longer fulfils this criterion and for Hund's case (b) the good quantum numbers are: J, N, S, Λ. $\vec{N}$ is obtained by the vectorial addition of $\vec{\Lambda}$ and $\vec{R}$, i.e. $\vec{N} = \vec{\Lambda}+\vec{R}$. Likewise, $\vec{J}$ is obtained by $\vec{J} = \vec{N} + \vec{S}$ [56, 60].

2.3 OH LIF spectroscopy

2.3.1 Energy level structure for Hund's case (a) molecules

It is convenient to use the Hund's case (a) formalism for describing the effective rotational Hamiltonian $\hat{H}_{\mathrm{eff}}^{\mathrm{rot}}$ of OH in the $X^2\Pi$ ground state and taking into account spin-orbit interaction results in the following expression [53, 60]:

$$\hat{H}_{\mathrm{eff}}^{\mathrm{rot}} = \hat{H}_{\mathrm{rot}} + \hat{H}_{\mathrm{SO}} = B_v\vec{R}^2 + A_{\mathrm{SO}}\vec{L}\cdot\vec{S} = B_v(\vec{J}-\vec{L}-\vec{S})^2 + A_{\mathrm{SO}}\vec{L}\cdot\vec{S}\,, \tag{2.14}$$

where B_v is the rotational constant, which depends on the vibrational quantum number v [60]. The effective Hamiltonian in Eqn. 2.14 can be evaluated on the following wave function, which is expressed in terms of Hund's case (a) quantum numbers [60]:

$$\Psi_{\mathrm{eff}} = |\mathrm{el}\rangle\,|\mathrm{vib}\rangle\,|\mathrm{rot}\rangle = |n\Lambda\rangle\,|S\Sigma\rangle\,|v\rangle\,|JM_J\Omega\rangle\,, \tag{2.15}$$

where n is the electronic state label, v denotes the vibrational quantum number and $|JM_J\Omega\rangle$ is a rigid rotor wave function. As described in refs. [56, 60], the rigid rotor wave function may be written in the following form:

$$|J,\Omega,M_J\rangle = \sqrt{\frac{2J+1}{8\pi^2}}D^{J^*}_{M_J\Omega}(\phi,\theta,\chi)\,, \tag{2.16}$$

where M_J is the projection of $\vec{J}$ onto the lab-fixed quantisation axis, which is given by an electric or a magnetic field. M_J adopts values in the range $-J, -J+1, \cdots, J$ and in the absence of preferred spatial orientation the M_J levels are degenerate. $D^{J^*}_{M_J\Omega}(\omega)$ denotes the Wigner D-function and $\omega = (\phi,\theta,\chi)$ are Euler angles, which describe the rotation of the molecule relative to the space fixed axis $(X, Y, Z;\ \omega = (0,0,0))$ and the angle convention in refs. [56, 60] is followed. χ denotes the orientation of the molecule with respect to the internuclear axis and is dispensable in a diatomic molecule as there are only two rotational degrees of freedom [53, 60].

In Hund's case (a) $X^2\Pi$ states, the projections of $\vec{L}$ and $\vec{S}$ onto the internuclear axis can adopt values of $\Lambda = \pm 1$ and $\Sigma = \pm 1$, which results in $\Omega = \pm 3/2, 1/2$. Therefore, it is convenient to work with a parity adapted basis set. What the parity adapted basis should look like is best determined by considering the behaviour of the overall wave function upon application of the inversion operator $\hat{I}$ in the lab-fixed frame. This operator translates the space-fixed coordinates (X, Y, Z) into $(-X, -Y, -Z)$ and the effect on the wave function is inferred by looking at $\hat{I}\,\Psi_{\text{eff}} = \hat{I}\left(|\text{el}\rangle\,|\text{vib}\rangle\,|\text{rot}\rangle\right) = \pm\Psi_{\text{eff}}$. It can be shown [53, 60] that the wave function given in Eqn. 2.15 transforms as follows under application of the space-fixed inversion operator $\hat{I}$:

$$\hat{I}\,|n\Lambda\rangle\,|S\Sigma\rangle\,|v\rangle\,|J\Omega M_J\rangle = (-1)^{(J-S+s)}|n,-\Lambda\rangle\,|S,-\Sigma\rangle\,|v\rangle\,|J,-\Omega,M_J\rangle\,, \tag{2.17}$$

where the parameter s is one for Σ^- states and zero for all other states. Under inversion, the sign of Λ, Σ and Ω changes. As the vibration only depends on the internuclear separation, $|v\rangle$ is not affected by the transformation. From Eqn. 2.17 it can be perceived that the transformed wave function picks up a pre-factor, which is either -1 or 1 and is referred to as parity.

For OH in Hund's case (a) states, the parity adapted basis can be written in the following short-hand notation [35, 61]:

$$|J,\Omega,M_J,\varepsilon\rangle = \frac{1}{\sqrt{2}}\big(|J,\Omega,M_J\rangle + \varepsilon|J,-\Omega,M_J\rangle\big)\,, \tag{2.18}$$

$\varepsilon = \pm 1$ denotes the symmetry of the wave function and relates to the total parity in the following way [62, 63]:

$$p = \varepsilon\,(-1)^{(J-S)}\,. \tag{2.19}$$

For OH in the $^2\Pi_{3/2}$ and $^2\Pi_{1/2}$ states, $S = 1/2$ and wave functions with $+(-1)^{J-1/2}$ parity are designated with a label e, whereas wave functions with $-(-1)^{J-1/2}$ are assigned a parity label f for half-integer values of J [53]. A clear and concise introduction to the concept of parity can be found in refs. [53, 60].

In the parity adapted basis, the Hamiltonian in Eqn. 2.14 can be represented by the following matrix, which applies to the e and the f parity block [53, 60].

$$H_{\text{eff}}^{e/f} = \begin{pmatrix} B_v\big[J(J+1) - 7/4\big] + A_{\text{SO}}/2 & -B_v\sqrt{J(J+1) - 3/4} \\ -B_v\sqrt{J(J+1) - 3/4} & B_v\big[J(J+1) + 1/4\big] - A_{\text{SO}}/2 \end{pmatrix} \tag{2.20}$$

Diagonalisation of the above matrix (Eqn. 2.20) leads to expressions for the rotational energy levels of the $\Omega = 3/2$ and $\Omega = 1/2$ manifolds. As the Hamiltonian does not couple states with opposite parity, the energies obtained display a two-fold degeneracy.

$$E(|^2\Pi_{3/2}, JM_J\, e/f\rangle, F_1) = B_v\left[(J-1/2)(J+3/2) - 1/2X\right] \tag{2.21}$$

$$E(|^2\Pi_{1/2}, JM_J\, e/f\rangle, F_2) = B_v\left[(J-1/2)(J+3/2) + 1/2X\right], \tag{2.22}$$

where $X = \sqrt{4(J-1/2)(J+3/2) + (Y-2)^2}$ and $Y = A_{SO}/B_v$ [53, 60].

The eigenfunctions of Eqn. 2.20 for the different spin-orbit manifolds are given by [64]:

$$|^2\Pi_{3/2}, JM_J\epsilon\rangle = a_J|J, \Omega = 1/2, M_J\epsilon\rangle + b_J|J, \Omega = 3/2, M_J\epsilon\rangle \tag{2.23}$$

$$|^2\Pi_{1/2}, JM_J\epsilon\rangle = -b_J|J, \Omega = 1/2, M_J\epsilon\rangle + a_J|J, \Omega = 3/2, M_J\epsilon\rangle, \tag{2.24}$$

The coefficients a_J and b_J determine how strong the mixing between the $\Omega = 1/2$ and $\Omega = 3/2$ manifolds are for a given rotational level J. The expansion coefficients a_J and b_J are given by [64]:

$$a_J = \sqrt{\frac{X + (Y-2)}{2X}}, \tag{2.25}$$

$$b_J = \sqrt{\frac{X - (Y-2)}{2X}}. \tag{2.26}$$

The mixing between the $\Omega = 3/2$ and the $\Omega = 1/2$ spin-orbit manifolds represents a deviation from Hund's case (a) as Ω becomes increasingly ill-defined with increasing mixing. For large J values, the mixing increases and the situation pertains to an intermediate case between Hund's case (a) and (b). Even though OH belongs to such an intermediate case, it is convenient to adhere to Hund's case (a) labels. However, the $\Omega = 3/2$ manifold is sometimes also labelled with F_1 and the $\Omega = 1/2$ manifold with F_2, which is Hund's case (b) notation [56, 60]. The mixing coefficients will become important for the calculation of the Stark and Zeeman shifts later on. For OH in the $X^2\Pi_{3/2}$ $J = 3/2$ state, the mixing coefficients from ref. [64] are $a_J = 0.174$ and $b_J = 0.98$.

So far, the energy levels for $\varepsilon = \pm 1$ have been degenerate. However, the degeneracy is lifted if one includes mixing between the $X^2\Pi$ ground state and the first electronic excited state $A^2\Sigma^+$. The mixing is caused by second order effects arising from the interaction of the electron orbital angular momentum $\vec{L}$ and the rotation of the molecular framework $\vec{R}$. The energy splitting is referred to as Λ-doubling and the energy of the splitting is

$h\nu_\Lambda = 0.056$ cm^{-1} for OH in the $X^2\Pi_{3/2}, J = 3/2$ state [65]. The effective rotational Hamiltonian including $\hat{H}_\Lambda$ can be found in ref. [56].

2.3.2 Energy level structure for Hund's case (b) molecules

The first electronic excited state OH $A^2\Sigma^+$ is best described within the framework of Hund's case (b) coupling scheme. In this case, $\vec{\Lambda} = 0$ and $\vec{N} = \vec{R}$. Moreover, exploiting that $\vec{R} = \vec{J} - \vec{S}$ allows to write the effective Hamiltonian in the following form [53, 60]:

$$\hat{H}_{\text{eff}} = \hat{H}_{\text{rot}} + \hat{H}_{\text{SR}} = B_v \vec{N}^2 + \gamma_v \vec{N} \cdot \vec{S} = B_v \vec{N}^2 + \frac{\gamma_v}{2} (\vec{J}^2 - \vec{S}^2 - \vec{N}^2) , \tag{2.27}$$

where the spin-rotation interaction has been accounted for by $\gamma_v \vec{N} \cdot \vec{S}$. γ_v depends on the vibrational level v and determines the strength of the interaction. The last part of Eqn. 2.27 makes use of operator substitutions outlined in ref. [66]. This leads to the convenient result that all matrix elements are diagonal in the $|n\Lambda\rangle|JNSM_J\rangle$ basis and the eigenvalues are given by [56, 67]:

$$E = B_v N (N+1) + \frac{\gamma_v}{2} \big(J(J+1) - S(S+1) - N(N+1)\big) \tag{2.28}$$

For OH in the $A^2\Sigma^+$ state, $J = N \pm 1/2$ and $S = 1/2$, which allows for the distinction of two cases [53, 67]:

$$F_1(N) = B_v N (N+1) + \frac{\gamma_v}{2} N \tag{2.29}$$

and

$$F_2(N) = B_v N (N+1) - \frac{\gamma_v}{2} (N+1) . \tag{2.30}$$

It can be perceived that the spin-rotation interaction splits the rotational energy into two branches, which is referred to as ρ-doubling [68]. The $F_1(N)$ energy pertains to the case $N = J - 1/2$ and $F_2(N)$ corresponds to $N = J + 1/2$ [53]. As J ranges from $|N - S|, |N - S + 1|, \cdots |N + S|$, the parity is now given by [56, 60]:

$$p = (-1)^N \tag{2.31}$$

The most important molecular constants for of OH in the $A^2\Sigma^+$ state are summarised in table Tab. 2.2.

2.3.3 LIF spectroscopy on the A $\leftrightarrow$ X transition

Throughout this thesis, OH radicals are detected via laser induced fluorescence (LIF). Laser radiation at 282 nm is used to excite OH radicals from their $X^2\Pi(v = 0)$ ground state to the first electronically excited state $A^2\Sigma^+(v = 1)$, where v denotes the vi-

constants	$X^2\Pi(v=0)$	$A^2\Sigma^+(v=0)$	$A^2\Sigma^+(v=1)$
B (cm^{-1})	18.535	16.961 [69]	16.129 [69]
A (cm^{-1})	-139.051		
γ (cm^{-1})	-0.119	0.226 [68]	0.216 [68]
μ (D)	1.655		
T_e (cm^{-1})	–	32684.1 [58]	
ω_e (cm^{-1})	3737.76 [58]	3178.8 [58]	
$\omega_e x_e$ (cm^{-1})	84.881 [58]	92.91 [58]	
r_e (Å)	0.97 [58]	1.01 [58]	

Table 2.2: Selected molecular constants for OH. If not stated otherwise, the values were taken from ref. [56].

brational quantum number. Off-resonant fluorescence at 313 nm is collected from the $A^2\Sigma^+(v=1)$–$X^2\Pi(v=1)$ transition. The difference between the excitation wavelength and the wavelength at which fluorescence photons are collected allows for good discrimination against stray light using optical bandpass filters. The theory developed in the two previous chapters can be used to calculate the relative location of rotational energy levels involved in the excitation process. Additionally, energy terms for the electronic and vibrational states have to be added. For electric dipole allowed transitions, the selection rules in Hund's case (b) notation can be summarised as follows [69]:

$$\Delta J = 0, \pm 1 \quad \Delta M_J = 0, \pm 1 \tag{2.32}$$

and

$$\Delta N = 0, \pm 1, \pm 2\,, \tag{2.33}$$

where ΔJ denotes the change in total angular momentum and ΔN is the change of the total angular momentum excluding spin. Moreover, the symmetry selection rule demands that the parity changes $+ \leftrightarrow -$ [53, 69]. Following Dieke and Crosswhite [69], the transitions are labelled by the following scheme:

$$\Delta N_{F'F''}(N'')\,, \tag{2.34}$$

where ΔN adopts values from $\Delta N = -2, -1, 0, 1, 2$, which correspond to the labels O, P, Q, R and S. N'' denotes the N quantum number of the $X^2\Pi$ ground state, F' refers to the ρ-doublet component in the excited state $A^2\Sigma^+$ and F'' represents the spin-orbit manifold of the ground state $X^2\Pi_\Omega$. In case $F' = F''$, only one label is used [69]. Selected electric dipole allowed transitions are depicted in Fig. 2.3.

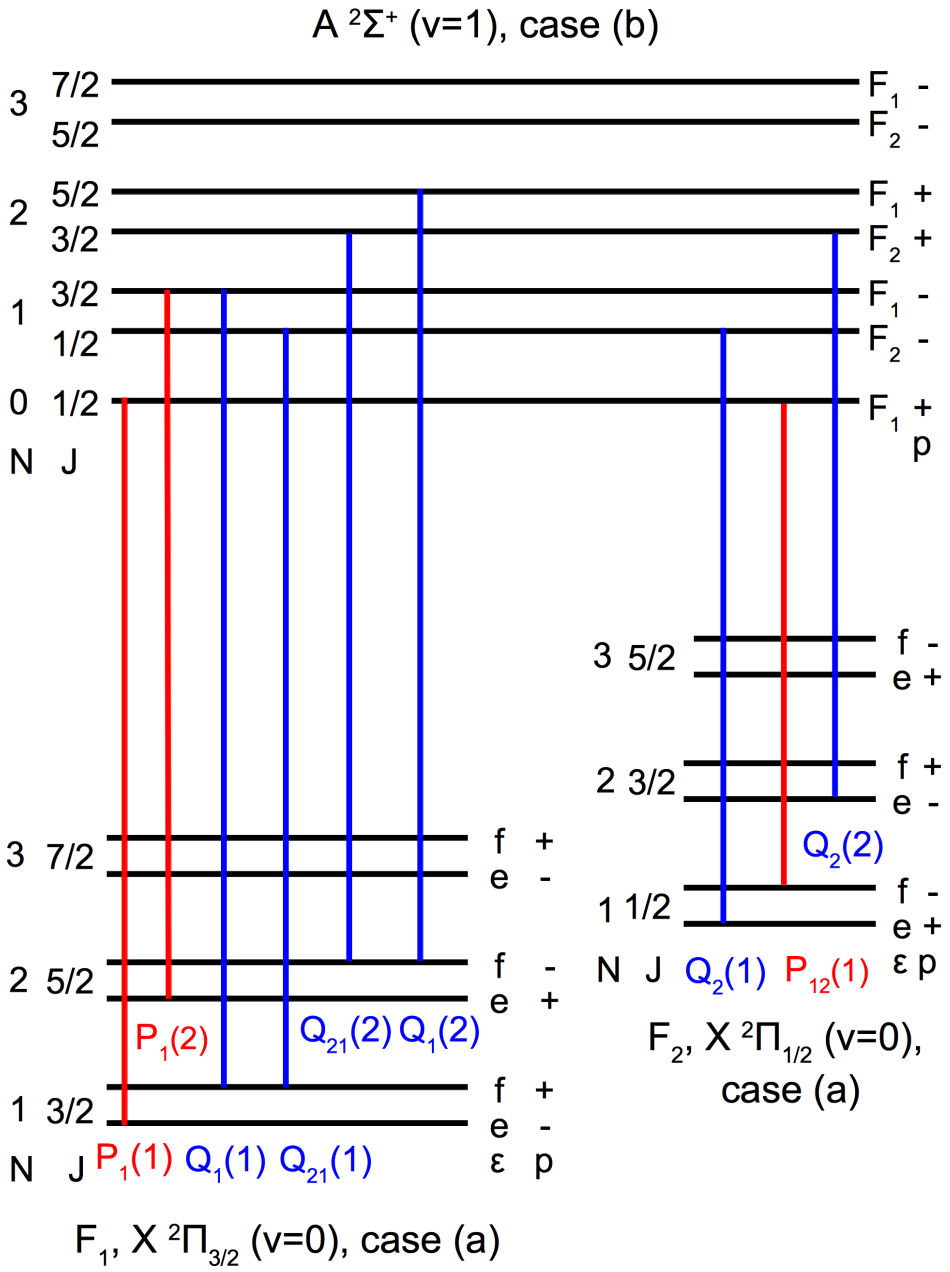

Figure 2.3: Schematic energy level diagram for OH in the electronic ground state $X^2\Pi(v = 0)$ and the first electronically excited state $A^2\Sigma^+(v = 1)$. The electronic ground state is split into two spin-orbit manifolds, of which $\Omega = 3/2$ is lower in energy. Selected transitions are indicated and labelled according to the scheme in Eqn. 2.34.

2.4 OH in external electric and magnetic fields

The hydroxyl radical is a very appealing molecule, as it offers a permanent electric dipole moment $\vec{\mu}_e$ as well as a magnetic moment $\vec{\mu}_m$. The rotational energy level splittings caused by interactions with electric (Stark effect) or magnetic (Zeeman effect) fields are sufficiently strong such that OH can conveniently be manipulated. In this thesis, switched

inhomogeneous electric fields are employed for slowing OH molecules in a Stark decelerator and magnetic fields are used for confining a translationally cold OH cloud between bar magnets. By symmetry, the electric dipole moment vector $\vec{\mu}_\mathrm{e}$ points along the internuclear axis [60]. Moreover, OH is an open-shell radical species and features a magnetic moment $\vec{\mu}_\mathrm{m}$. Usually, the orientation of the molecular electric and magnetic moments is described in the molecule-fixed coordinate system. As electric and magnetic fields are defined in the laboratory frame, it becomes necessary to relate the orientation of the molecule-fixed coordinate system (x, y, z) to the coordinate system of the laboratory (X, Y, Z) by making use of Euler angles (ϕ, θ, χ) [52, 63]. The situation is depicted in Fig. 2.4 and it is assumed that the $\vec{E}$ and $\vec{B}$ fields are applied along the Z-axis. Classically, the energy associated with the orientation of the dipole $\vec{\mu}$ in the presence of a field $\vec{F}$ is given by [70]:

$$E_\mathrm{interact} = -\vec{F} \cdot \vec{\mu} = -|\vec{F}| \cdot |\vec{\mu}| \cos(\theta)\,. \tag{2.35}$$

In the following two sections, this classical picture will be expanded to a quantum mechanical analogon, where the angle θ is quantised, and the quantum state dependent orientation of the dipole moment relative to the field along the space fixed Z-axis has to be described by a probability function [71]. Molecules drawn towards regions of higher field strength are referred to as high-field seekers, whereas molecules being repelled from regions of high field strength are termed low-field seekers [70].

Before starting with the derivation of the Stark and Zeeman matrix elements, it is worth noticing how the Stark $\hat{H}_\mathrm{S}$ and Zeeman $\hat{H}_\mathrm{Z}$ Hamiltonians integrate into the field-free molecular Hamiltonian $\hat{H}_\mathrm{eff}$ [52, 63].

$$\hat{H}_\mathrm{eff} = \hat{H}_0 + \hat{H}_\mathrm{S} + \hat{H}_\mathrm{Z}\,. \tag{2.36}$$

As discussed in sections 2.3.1 and 2.3.2, the field free Hamiltonian $\hat{H}_0$ takes into account rotation, spin-orbit coupling, spin-rotation coupling and Λ-doubling (see refs. [56, 60]) [63].

$$\hat{H}_0 = \hat{H}_{rot} + \hat{H}_\mathrm{SO} + \hat{H}_\mathrm{SR} + \hat{H}_\Lambda\,. \tag{2.37}$$

2.4.1 Stark effect

In this section, the first order matrix elements for the Stark effect are derived following the approach outlined in references [60, 71, 72]. Adhering to the geometry depicted in Fig. 2.4, where the electric field points along the Z-axis and the electric dipole lies along

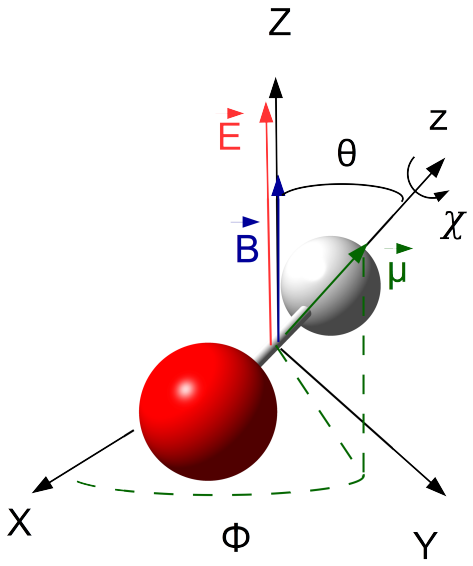

Figure 2.4: Orientation of the molecule-fixed coordinate system (x, y, z) relative to the space-fixed coordinate system in the laboratory (X, Y, Z). The relative orientation of the two coordinate systems is described by Euler angles (ϕ, θ, χ). χ denotes the orientation of the molecule with respect to the internuclear axis z and is dispensable as diatomic molecules only have two rotational degrees of freedom [53, 60]. The electric field $\vec{E}$ and the magnetic field $\vec{B}$ are applied along the Z axis. The electric and magnetic dipole moments denoted by $\vec{\mu}$ point along the internuclear axis z [63].

the z-axis, simplifies the projection from the molecule-fixed frame to the space-fixed frame. The Stark Hamiltonian may then be written in the following way:

$$\hat{H}_{\mathrm{S}} = -\vec{\mu}_{\mathrm{e}} \cdot \vec{E} = -\mu_{\mathrm{e},z} E_Z \cos(\theta)\,, \tag{2.38}$$

where the direction cosine converts between the molecule-fixed and the space-fixed axis. Subsequently, the rigid rotor wave functions from Eqn. 2.16 are employed for obtaining the following matrix elements [60, 71, 72]:

$$\begin{aligned}
&\langle J\Omega M_J| -\mu_{\mathrm{e},z} E_Z \cos(\theta)|J'\Omega' M_J'\rangle = -\mu_{\mathrm{e},z} E_Z \langle J\Omega M_J|\cos(\theta)|J'\Omega' M_J'\rangle = -\mu_{\mathrm{e},z} E_Z \langle\cos(\theta)\rangle \\
&= -\mu_{\mathrm{e},z} E_Z \frac{\sqrt{(2J+1)(2J'+1)}}{8\pi^2} \int d\Omega\, D^J_{M_J\Omega}(\omega) D^1_{00}(\omega) (-1)^{M_J'-\Omega'} D^{J'}_{-M_J'-\Omega'}(\omega) \\
&= -\mu_{\mathrm{e},z} E_Z \sqrt{(2J+1)(2J'+1)} (-1)^{M_J'-\Omega'} \begin{pmatrix} J & J' & 1 \\ M_J & -M_J' & 0 \end{pmatrix} \begin{pmatrix} J & J' & 1 \\ \Omega & -\Omega' & 0 \end{pmatrix}.
\end{aligned} \tag{2.39}$$

In the above derivation, $|J, \Omega, M_J\rangle$ has been replaced by the corresponding rigid rotor wave functions given in Eqn. 2.16 and the analytic expression for the evaluation of the integral can be found in refs. [56, 60]. Furthermore, the derivation makes use of the

relation $\cos(\theta) = D^1_{00}(\omega)$, where $\omega = (\phi, \theta, \chi)$ [60]. The $3j$-symbols lead to the following selection rules for the Stark effect:

$$J = J', \quad J = J' \pm 1, \quad M_J = M'_J, \quad \Omega = \Omega' . \tag{2.40}$$

From a geometric point of view, the expectation value $\mu_{e,z}\langle\cos(\theta)\rangle$ determines the contribution of the vector component $\mu_{e,z}$ along the Z-axis. In the following discussion, it is assumed that the $J = J' \pm 1$ selection rule can be neglected as the rotational energy level spacing in OH is relatively large [35]. This leads to $J = J'$, $M_J = M'_J$, $\Omega = \Omega'$ and replacing the $3j$-symbols with analytic expressions from references [56, 60] yields the following expression for $\langle\cos(\theta)\rangle$:

$$\begin{aligned}
\langle\cos(\theta)\rangle &= (-1)^{M_J-\Omega}(2J+1)\begin{pmatrix} J & J & 1 \\ M_J & -M_J & 0 \end{pmatrix}\begin{pmatrix} J & J & 1 \\ \Omega & -\Omega & 0 \end{pmatrix} \\
&= (-1)^{M_J-\Omega}(2J+1)(-1)^{J-M_J}\frac{2M_J}{[(2J+2)(2J+1)(2J)]^{1/2}}(-1)^{J-\Omega}\frac{2\Omega}{[(2J+2)(2J+1)(2J)]^{1/2}} \\
&= \frac{M_J\Omega}{J(J+1)}.
\end{aligned} \tag{2.41}$$

Multiplying the result for the direction cosine from Eqn. 2.41 by $-\mu_{e,z}E_Z$ results in the first-order Stark energy:

$$E^{(1)}_{\text{Stark}} = \langle J\Omega M_J|-\mu_{e,z}E_Z\cos(\theta)|J\Omega M_J\rangle = -\mu_{e,z}E_Z\langle\cos(\theta)\rangle = -\mu_{e,z}E_Z\frac{M_J\Omega}{J(J+1)}. \tag{2.42}$$

The Stark Hamiltonian $\hat{H}_S$ only couples states of opposite parity and by taking into account the parity adapted basis introduced in Eqn. 2.18, the following matrix can be constructed [35]:

$\hat{H}_{\text{Stark}}$	$\lvert J, \Omega, M_J, e\rangle$	$\lvert J, \Omega, M_J, f\rangle$
$\langle J, \Omega, M_J, e\rvert$	0	Q
$\langle J, \Omega, M_J, f\rvert$	Q	E_Λ

Λ-doubling is taken into account by adding the Λ-splitting energy to the lower right matrix element and for OH in the $^2\Pi_{3/2}$ $J = 3/2$ state, $E_\Lambda = 0.056$ cm^{-1} [65]. Upon diagonalisation of the matrix, the following expression for the Stark energy is obtained [35]:

$$E_{\text{Stark}} = \frac{E_\Lambda}{2} \pm \sqrt{\left(\frac{E_\Lambda}{2}\right)^2 + Q^2}, \tag{2.43}$$

where the off-diagonal element Q is given by:

$$\begin{aligned} Q &= \langle J, \Omega, M_J, e|\hat{H}_S|J, \Omega, M_J, f\rangle \\ &= \langle J, \Omega, M_J, f|\hat{H}_S|J, \Omega, M_J, e\rangle = -\mu_{e,z} E_Z \frac{M_J \Omega_{\text{eff}}}{J(J+1)}. \end{aligned} \tag{2.44}$$

As discussed in section 2.3.1, OH is not a pure Hund's case (a) molecule and $\Omega_{\text{eff}} = 1.46$ is used due to mixing between the $X^2\Pi_{3/2}$ and $X^2\Pi_{1/2}$ spin-orbit manifolds for $J = 3/2$.

$$\Omega_{\text{eff}} = (1/2\, {a_J}^2 + 3/2\, {b_J}^2) = 1.46\,. \tag{2.45}$$

Evaluating Eqn. 2.43 with $\Omega_{\text{eff}} = \pm 1.46$ leads to the Stark shifts depicted in Fig. 2.5.

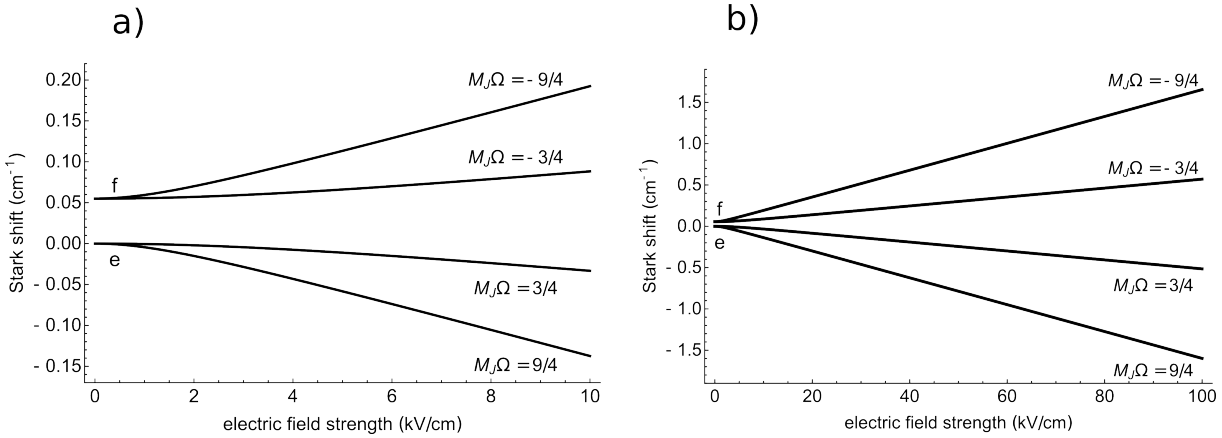

Figure 2.5: Stark shift of OH in the $X^2\Pi_{3/2}$, $J = 3/2$ state for **a)** low electric field strengths and at high electric field strengths **b)**. The graphs were obtained by evaluating Eqn. 2.43. The energy splitting is quadratic at low electric field strengths.

2.4.2 Zeeman effect

Assuming that the $\vec{B}$-field is applied along the Z-axis, as depicted in Fig. 2.4, the Zeeman Hamiltonian may be expressed as follows [35]:

$$\hat{H}_{\text{Zeeman}} = -\vec{\mu}_{\text{m}} \cdot \vec{B} = \frac{\mu_B}{\hbar} \cdot (\vec{L} + g_{\text{s}}\vec{S})\vec{B} = \frac{\mu_B}{\hbar} B \cdot (\hat{L}_z + g_{\text{s}}\hat{S}_z)\cos(\theta)\,. \tag{2.46}$$

The sign between the second and the third term changes due to the negative polarity of the electron charge. Furthermore, it is assumed that the magnetic moment lies along the internuclear axis, i.e. $\vec{\mu}_{\text{m}} \approx (0, 0, -\frac{\mu_B}{\hbar}(\hat{L}_z + g_{\text{s}}\hat{S}_z))$ [62]. g_{s} is the free electron g-factor ($g_{\text{s}} \approx 2.00232$) and μ_{B} denotes Bohr's magneton, which is given by the following expression:

$$\mu_{\text{B}} = \frac{e\hbar}{2m_{\text{e}}} \approx 9.274 \cdot 10^{-24}\,\text{J/T}\,. \tag{2.47}$$

Unlike the Stark Hamiltonian, the Zeeman Hamiltonian couples states of equal parity only. Evaluating the Zeeman Hamiltonian given in Eqn. 2.46 on the parity adapted basis introduced in Eqn. 2.18 and setting $J' = J$ results in the following first order Zeeman matrix elements, which are diagonal in Λ and Σ.

$$\begin{aligned}
&\langle \Lambda\Sigma J\Omega M_J\varepsilon|H_z|\Lambda\Sigma J'\Omega' M'_J\varepsilon'\rangle \\
&= (2J+1)(-1)^{M'_J-\Omega'}\begin{pmatrix} J' & 1 & J \\ -\Omega' & 0 & \Omega \end{pmatrix}\begin{pmatrix} J' & 1 & J \\ -M'_J & 0 & M_J \end{pmatrix}\mu_B B(\Lambda + g_s\Sigma)\,\delta_{\varepsilon,\varepsilon'} \\
&\overset{J'=J}{=} (2J+1)(-1)^{M_J-\Omega}\begin{pmatrix} J & J & 1 \\ \Omega & -\Omega & 0 \end{pmatrix}\begin{pmatrix} J & J & 1 \\ M_J & -M_J & 0 \end{pmatrix}\mu_B B(\Lambda + g_s\Sigma)\,\delta_{\varepsilon,\varepsilon'} \\
&= (2J+1)(-1)^{M_J-\Omega}(-1)^{J-\Omega}(-1)^{J-M_J}\frac{4M_J\Omega}{(2J+2)(2J+1)(2J)}\mu_B B(\Lambda + g_s\Sigma)\,\delta_{\varepsilon,\varepsilon'} \\
&= \frac{\mu_B B\Omega M_J(\Lambda + g_s\Sigma)}{(J+1)J}\,\delta_{\varepsilon,\varepsilon'}\,. \qquad (2.48)
\end{aligned}$$

Again, the $3j$-symbols have been replaced with analytic expressions from refs. [56, 60]. The selection rules are $M_J = M'_J$, $\Omega = \Omega'$ and $J' = J$. $J' = J \pm 1$ is also allowed, but leads to higher-order terms. Plotting Eqn. 2.48 for OH $X^2\Pi_{3/2}$, $J = 3/2$ with $\Omega_{\text{eff}} = 1.46$ from Eqn. 2.45 results in the energy splitting pattern depicted in Fig. 2.6. As the Zeeman Hamiltonian does not couple states of different parity, the Λ-doublet splitting is clearly visible. The different energy level splitting of the Zeeman shift has important consequences when loading a magnetic trap with OH molecules exiting a Stark decelerator. For the trap loading experiments described in chapter 6, translationally cold packages of OH radicals in the $X^2\Pi_{3/2}$, $J = 3/2, M_J = \pm 3/2$ state leave the decelerator. As only the $M_J = +3/2$ component is magnetically low-field seeking, half of the population will be lost upon entering the B-field of the magnetic trap.

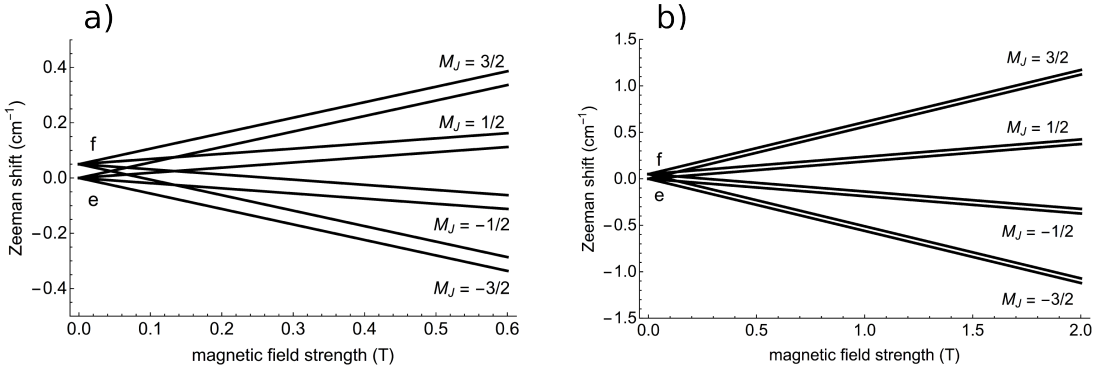

Figure 2.6: Zeeman shift of OH in the $^2\Pi_{3/2}$, $J = 3/2$ state for magnetic field strengths up to **a)** 0.6 T and for magnetic field strengths up to **b)** 2.0 T. As the Zeeman Hamiltonian only couples states of equal parity, the Λ-doublet splitting is clearly visible. The f-levels are separated by 0.056 cm^{-1} relative to the e-levels.

Chapter 3

Stark deceleration and trajectory simulations

3.1 Introduction

As discussed in chapter 1, cold molecules hold promising prospects and have become the subject of intense study. Prior to conducting experiments with cold molecules, a reliable source for their production and cooling is required. In this thesis, a Stark decelerator is employed for the production of translationally cold packages of OH radicals. Typically, a Stark deceleration experiment is preceded by the formation of a molecular beam and the hydroxyl radicals were produced by means of electric dissociation of water vapour seeded in a noble carrier gas. As discussed in chapter 4, molecular beams offer efficient cooling of the internal degrees of freedom and a large portion of the hydroxyl radicals are in their rotational and vibrational ground state. While the velocity spread within the molecular beam is narrow, the energy removed during cooling of the internal degrees of freedom has been converted into a supersonic flow in the laboratory frame of reference. Subsequently, the molecular beam is coupled into a Stark decelerator, which serves the purpose of removing kinetic energy from the fast molecular beam.

Stark deceleration is applicable to a wide range of molecules with a sufficiently large dipole moment and a suitable Stark shift to mass ratio such as OH, SH, CH and NH_3, to name just a few [35, 70]. In this thesis, the hydroxyl radical is the molecule of choice as it has a low mass and possesses an effective dipole moment μ_{eff} of 1.67 D [35]. Furthermore, OH in the $J = 3/2, M_J\Omega = -9/4$ state experiences a large first order Stark shift of approx. 1.6 cm^{-1} at electric field strengths of 100 kV/cm. Stark deceleration exploits the Stark energy experienced in switched inhomogeneous electric fields to repeatedly remove kinetic energy from the molecular package along the forward direction of motion. After a

sufficient number of slowing cycles, velocities below 30 m/s can be reached at the exit of the decelerator. In an electric field, the force acting on the OH molecule's dipole is given by [35, 70]:

$$\vec{F}(\vec{r}) = \mu_{\text{eff}}(|\vec{E}|)\,\nabla|\vec{E}(\vec{r})| = \overline{\mu\cos(\theta)}\,\nabla|\vec{E}| = -\nabla W_{\text{Stark}}\,. \tag{3.1}$$

where $\vec{E}(\vec{r})$ denotes the electric field at a position $\vec{r}$ and θ is the angle between the electric field and the dipole. μ_{eff} represents the effective dipole moment, which depends on the quantum state of the molecule. In a quantum mechanical treatment of the interaction between a molecule's dipole moment and an electric field, the angle of alignment θ is quantised, which is referred to as space quantisation [70]. Molecules with a positive value of μ_{eff} are drawn towards regions of high field strength and are referred to as "high-field seekers". Likewise, molecules with a negative value of μ_{eff} are deflected towards regions with a low electric field strength and are termed "low-field seekers" [70]. It is molecules in low-field seeking quantum states, which are amenable to stark deceleration. Furthermore, "low-field seekers" can be trapped with a suitable static electric field configuration [73, 74].

The Stark deceleration technique was developed in the research group of G. Meijer and the first successful Stark deceleration experiments on molecules were conducted by R. Bethlem and co-workers in 1999 [34]. Since then, the technique has been refined [75–77] and optimised [78–82] significantly. An analogy between the longitudinal equation of motion in a Stark decelerator and a biased pendulum has been drawn by B. Friedrich and K. Gubbels [83, 84]. S.Y.T. van de Meerakker and co-workers [77] investigated the transverse stability of the decelerator. Furthermore, detailed accounts on the extension of the phase stability model to higher-order resonances and their characterisation are given in refs. [76, 85]. As Stark deceleration is a versatile source of cold polar molecules and offers good state purity, it has found widespread use in many experiments. Stark deceleration has been reviewed in references [35, 70, 86, 87]. Stark decelerators have been employed for precision spectroscopy [5], loading of magnetic [49, 54, 88] and electrostatic traps [73, 74] as well as for surface scattering experiments [89]. Molecular fountains have been realised by mounting Stark decelerators upwards [90], such that the direction of deceleration opposes the gravitational force. Due to the exquisite control over the velocity of the molecular package exiting the decelerator and the narrow velocity spread within the package, Stark decelerators have successfully been employed in scattering experiments [14, 15, 91–93]. Besides the diverse applications for Stark deceleration, different types of decelerators have been developed such as a wire decelerator [94], a chip-based deceleration scheme [95, 96], alternating gradient (AG) decelerators for molecules in low-field seeking states [97] and travelling-wave ring decelerators offering improved transversal focussing properties [98–101].

A part of this thesis consisted of setting up and characterising a 124-stage Stark decelerator. The decelerator was optimised for operation at low final velocities ($v_{\text{final}} < 30$ m/s) [102] and was subsequently employed for loading a magnetic trap. In this chapter, the operation principles of a Stark decelerator are introduced and expressions for the description of the longitudinal equation of motion are derived following references [35, 61, 70, 76, 103]. Additionally, transverse focussing within the decelerator is discussed. In a final section, Monte Carlo trajectory simulations for modelling the phase-space evolution of a molecular package inside the decelerator are described.

3.2 Operation principle of Stark decelerators

3.2.1 Liouville's Theorem

According to the classification scheme for sources of cold molecules prevalent in the literature [2, 3] and introduced in chapter 1, Stark deceleration pertains to the class of direct methods, which indicates that a molecular source is employed for loading the decelerator. Furthermore, Stark deceleration makes use of conservative forces and consequently, the phase-space density cannot be increased during the deceleration process [35]. At best, the phase-space density of a packet leaving the decelerator is identical to the phase-space density of the molecular beam's portion coupled into the decelerator. As the package within the decelerator is composed of a multitude of OH particles, the situation of a many-body system arises. Such systems can be conveniently described within the framework of Hamiltonian mechanics and by adopting a phase-space notation [104].

The phase-space coordinates of an N-particle system within the decelerator can be described by $\vec{q} = (q_1, q_2, \cdots, q_{3N})$ and $\vec{p} = (p_1, p_2, \cdots, p_{3N})$, where $\vec{q}$ denotes the configuration space and $\vec{p}$ represents the momentum space [104]. Knowledge of the Hamiltonian determines the phase-space trajectories at all subsequent times, given an initial starting point. Consequently, phase-space trajectories do not cross, as this would lead to ambiguity with respect to the origin of motion [35, 104]. In parametric notation, a trajectory in phase space can be written as $(\vec{q}(t), \vec{p}(t))$. If the particle trajectories take place under the influence of conservative forces, the Hamiltonian of the system is equal to the sum of kinetic and potential energy and may be written as [104]:

$$H(\vec{p}, \vec{q}, t) = T + W = \sum_{i=1}^{3N} \frac{{p_i}^2}{2m} + W(q_i)\,, \tag{3.2}$$

where $W(\vec{q})$ denotes the position-dependent potential energy and m is the mass. As the forces in a Stark decelerator can always be derived from the Stark potential energy (see Eqn. 3.1), the deceleration relies entirely on conservative forces.

The phase-space density of an N-particle system can be formulated as

$$\rho_{6N}(\vec{p},\vec{q},t) = \frac{\mathrm{d}\,N}{\mathrm{d}\,q^{3N}\mathrm{d}\,p^{3N}} = \frac{\mathrm{d}\,N}{\mathrm{d}\,V_{6N}} \Rightarrow \int_{V_{6N}} \rho(\vec{p},\vec{q},t)\,\mathrm{d}\,q^{3N}\mathrm{d}\,p^{3N} = N\,, \tag{3.3}$$

where $\vec{p}$ is the momentum space, $\vec{q}$ represents the configuration space and t is the time [105–107]. The density at a given point in phase space is then equal to the infinitesimal change of the particle number inside a box with a volume $\mathrm{d}\,V_{6N} = \mathrm{d}\,q^{3N}\mathrm{d}\,p^{3N}$ placed around the coordinates under consideration. The density is a convenient quantity as it allows to propagate the N-body system in time by looking at the evolution of the density distribution instead of treating the system on a per-particle basis [106]. By considering the rate of change of the number of particles in a test volume V_t, the following expression is obtained [105]:

$$\frac{\mathrm{d}N_\mathrm{t}}{\mathrm{d}t} = \frac{\partial}{\partial t}\int_{V_\mathrm{t}} \rho_{6N}(\vec{p},\vec{q},t)\,\mathrm{d}\,q^{3N}\mathrm{d}\,p^{3N} = -\oint_{S_\mathrm{t}} \rho_{6N}(\vec{p},\vec{q},t)\,\vec{v}_\mathrm{ph}\,\mathrm{d}\,\vec{S}\,, \tag{3.4}$$

where the last term describes the particle flux through the closed surfaces S_t bounding the test volume and $\vec{v}_\mathrm{ph} = (\dot{q}_1, \dot{q}_2, \cdots, \dot{q}_{3N}, \dot{p}_1, \dot{p}_2, \cdots, \dot{p}_{3N})$ denotes the phase-space velocity. Making use of Gauss's theorem results in [105]:

$$\int_{V_\mathrm{t}} \frac{\partial}{\partial t}\,\rho_{6N}(\vec{p},\vec{q},t) + \nabla_\mathrm{ph}(\rho_{6N}(\vec{p},\vec{q},t)\,\vec{v}_\mathrm{ph})\,\mathrm{d}\,q^{3N}\mathrm{d}\,p^{3N} = 0\,, \tag{3.5}$$

where $\vec{\nabla}_\mathrm{ph} = (\partial/\partial\vec{q},\, \partial/\partial\vec{p})$ and it can be shown (see [105]) that $\vec{\nabla}_\mathrm{ph}\cdot\vec{v}_\mathrm{ph} = 0$, which yields Liouville's theorem [104–107]:

$$\frac{\partial}{\partial t}\,\rho_{6N}(\vec{p},\vec{q},t) + \vec{v}_\mathrm{ph}(\vec{\nabla}_\mathrm{ph}\,\rho_{6N}(\vec{p},\vec{q},t)) = \tag{3.6}$$

$$\frac{\partial}{\partial t}\,\rho_{6N}(\vec{p},\vec{q},t) + \sum_{i=1}^{3N}\left(\frac{\partial\,\rho_{6N}}{\partial q_i}\dot{p}_i + \frac{\partial\,\rho_{6N}}{\partial p_i}\dot{q}_i\right) \equiv \frac{\mathrm{d}}{\mathrm{d}t}\,\rho_{6N}(\vec{p},\vec{q},t) = 0\,. \tag{3.7}$$

Liouville's theorem states that the total derivative of the phase-space density ρ_{6N} with respect to time is zero. By keeping the positions $\vec{q}$ and momenta $\vec{p}$ constant, the sum in Eqn. 3.7 evaluates to zero and $\frac{\partial}{\partial t}\,\rho_{6N}(\vec{p},\vec{q},t) = 0$. This indicates that the system is in equilibrium and the density does not change over time [106]. Furthermore, Liouville's theorem demands that the overall phase-space density is constant at all times, provided the system evolves under the influence of conservative forces, i.e. position-dependent forces

that can be derived from a potential [105–107]. Eqn. 3.7 is a continuity equation, which implies that phase-space density is neither generated nor destroyed and that particles in phase space behave like a streaming fluid [107]. Liouville's theorem is also valid for particles in time-varying fields, which was shown by Ketterle and Pritchard [108]. However, the theorem breaks down for laser-cooling, where velocity dependent forces are exploited for increasing the phase-space density [105].

In accordance with Eqn. 3.7, the phase-space density at any point on a trajectory is identical to the value the system displayed at the starting point. While the phase-space density has to remain constant, it is possible to redistribute the density among the many body system's $6N$ degrees of freedom [106]. Fig. 3.1 a) displays the evolution of a grey phase-space region from a time $t = 0$ to a point in time $t = 1$ in the absence of a potential (and therefore fore), which corresponds to free flight of the particles. The initial distribution displays a momentum spread Δp as well as a position spread Δq. A time $\Delta t = 1$ later, the momentum spread is still identical, but the position spread has increased according to the momentum spread of the particles. While the phase space is tilted at $t = 1$, it is important to notice, that the area of the grey shaded region is identical to the original distribution. Hence, the phase-space density at $t = 1$ is identical to the one at $t = 0$ [104, 106]. Eqn. 3.7 is of the same form as the continuity equation of incompressible flows [104, 105, 109]. Therefore, it can be insightful to draw an analogy between a particle system's motion through phase space and the incompressible flow of a fluid. The fluid's shape may change over time, but the volume always stays constant [35, 106], which also applies to the phase-space volume bounded by the grey region in Fig. 3.1. In principle, it is sufficient to consider only the black outer boundary region at a time $t = 0$ and to determine into which shape it evolves at $t = 1$ [35]. As the black line always bounds the particle package in phase space, determining the evolution of the boundary represents an efficient way of tracking a many-body system's motion [35].

Within a confining potential, bound phase-space trajectories adopt the form of closed lines. The potential of a trap and the corresponding isoenergetic trajectories in phase space are depicted in Fig. 3.1 b). For the remainder of this section, the terminology introduced in ref. [35] is employed. The thick blue line represents the trajectory of a particle for which the sum of kinetic and potential energy is identical to the depth of the confining potential. This limiting trajectory is referred to as "separatrix" and represents the boundary of stable trapping. The loading of magnetic or electrostatic traps requires good phase-space overlap between the emittance of the beam and the acceptance of the trap, where the emittance denotes the shape or area of a molecular package in phase space [35]. In the context of Fig. 3.1 b), the acceptance refers to the shape of the equipotential

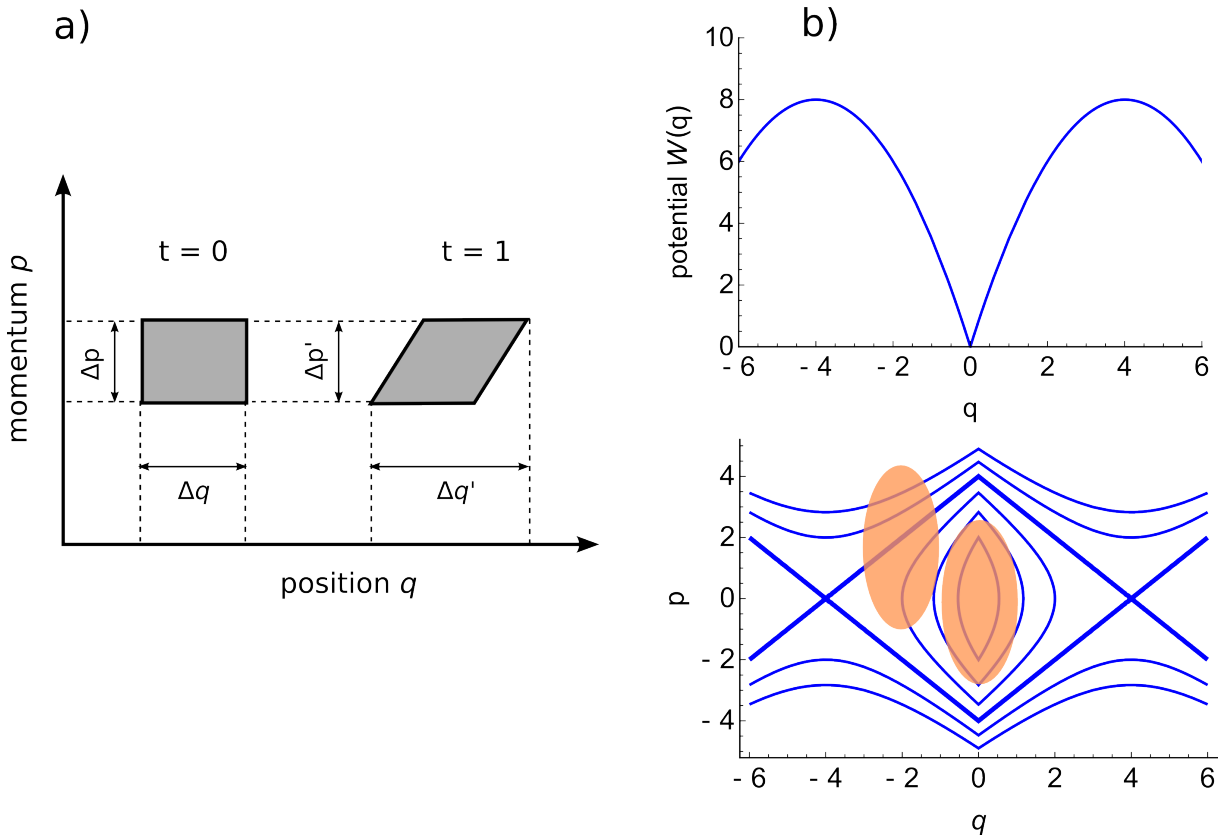

Figure 3.1: **a)** Illustration of phase-space evolution in the absence of a force. Due to the momentum spread at $t = 0$, the phase space is rotated at $t = 1$. As the grey shaded areas are equal in size at all times, the phase-space density is conserved [35, 104, 106]. **b)** Illustration of phase-space dynamics inside a confining potential $W(q)$. The upper graph displays the confining potential and isoenergetic particle trajectories in q, p-space are depicted in the lower panel. In phase space, the trajectories of confined particles correspond to closed lines, which are being traversed in clockwise direction. The thick blue line indicates the separatrix and the orange ellipsoids represent the emittance of a particle source coupled into the trap. The incoupling of the upper left ellipsoid is poor, whereas the centred ellipsoid is coupled in well. In both cases, the phase space is not perfectly matched to the shape of the contour lines [35, 103].

lines [35]. The phase-space overlap after loading of the trap is depicted in Fig. 3.1 b) for two different cases. The upper left orange emittance is misaligned with respect to the trap centre and a part of the distribution reaches beyond the separatrix. After loading, the particles lying outside of the separatrix are lost. While the loss of particles lying outside of the separatrix is not necessarily detrimental to the phase-space density inside the trap, the deviation of the emittance from the trap centre leads to an oscillatory motion of the trapped package [35]. While Liouville's theorem still applies and the total number of particles within the trap stays constant, the phase-space density after a certain temporal evolution is distributed between $\vec{q}$ and $\vec{p}$ in an unfavourable way, such that it becomes difficult to address the entire phase space experimentally, e.g. with a laser beam.

Ideally, the emittance is centred around the deepest point of the trap, as depicted for the second orange emittance in Fig. 3.1. Furthermore, the shape of the emittance should be identical to the trap's acceptance in order to prevent a "breathing" type of motion [35, 75]. Monte Carlo trajectory simulations are an invaluable tool for keeping track of the six dimensional phase-space evolution of a molecular package inside the decelerator and the trap. Chapters 5 and 6 rely on this technique for extracting information on the phase-space distribution at various points within the experimental setup.

3.2.2 Operation principle and phase-space stability

A Stark decelerator employs switched inhomogeneous electric fields produced by a periodic array of dipolar electrodes to slow down pulsed packages of polar molecules to translational temperatures $T_{\mathrm{trans}} > 1$ K [35]. A Stark decelerator consists of alternating horizontal and vertical electrode pairs, which are separated by a longitudinal distance L, as indicated in Fig. 3.2. The electrodes are connected to a fast high voltage switch and strong inhomogeneous electric fields result from applying a positive potential to the upper electrode rods and a negative potential of equal magnitude to the lower electrodes, while keeping adjacent electrode pairs grounded. As depicted in Fig. 5.2 and Fig. 5.4, the electrode pairs are mounted to an equipotential rail system, such that electrodes separated by a distance $2L$ are switched simultaneously. The orientation between subsequent electrode pairs changes from horizontal to vertical or vice versa in order to ensure transverse confinement of the package [77].

The electrodes are switched to high potentials upon the approach of a molecular package and the switching scheme is depicted in Fig. 3.2. While flying towards the HV-electrode, the molecules in low-field-seeking Stark states experience a force opposing the direction of travel and the forward kinetic energy is transferred into potential energy. Before reaching the maximum of the potential hill, the fields are switched and the molecular package starts flying towards the subsequent pair of electrodes, which results in a further reduction of the longitudinal velocity. In Fig. 3.2, switching the high voltage to the subsequent pair of electrodes corresponds to shifting the potential $W(\phi)$ by π radians. This is equivalent to switching between the upper and lower potential energy curves $W(\phi)$ when tracing out the particle's longitudinal trajectory through the decelerator. The switching takes place between alternatingly horizontal and vertical electrode pairs. Here, ϕ denotes the reduced longitudinal position of a particle and is defined as follows [35, 70]:

$$\phi = \pi \cdot \frac{x}{L}\,, \tag{3.8}$$

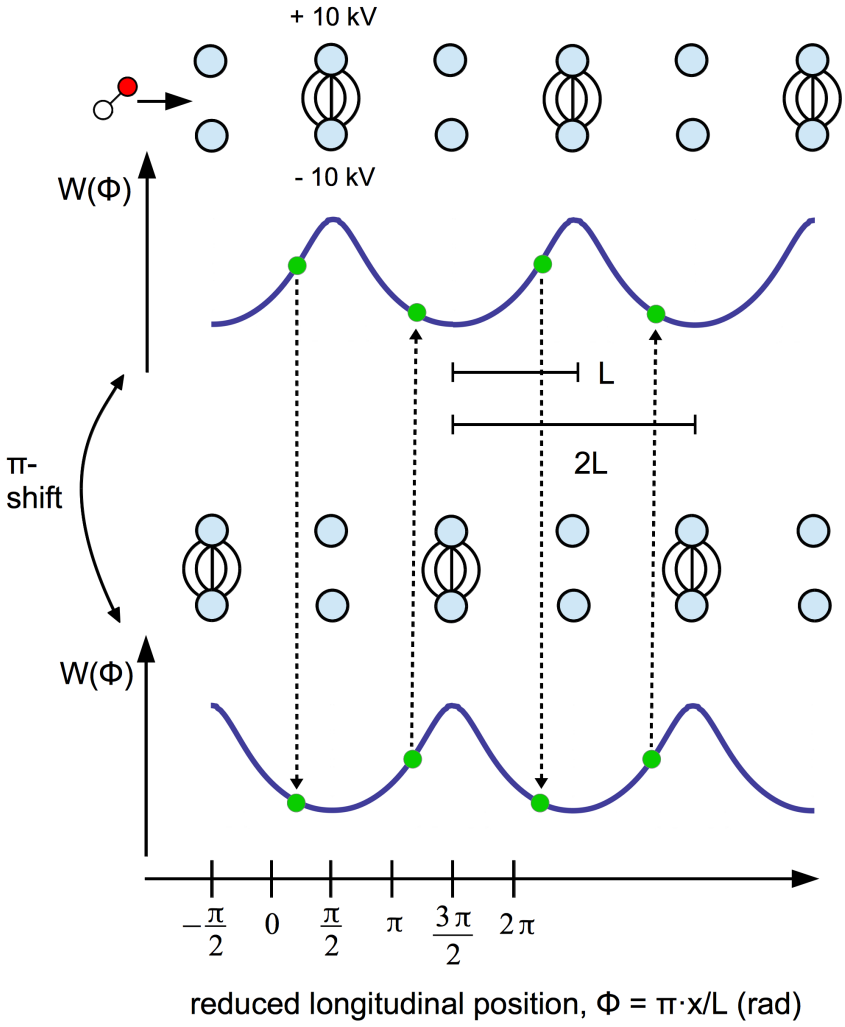

Figure 3.2: Illustration of the switching scheme employed in Stark deceleration. The longitudinal separation between the electrodes amounts to $L = 5.5$ mm. The second electrode pair is switched on as soon as a package of molecules has surpassed the centre of the first pair. The Stark shift experienced by low-field seeking molecules leads to a force which opposes the direction of travel. As the molecules climb up the Stark energy slope $W(\phi)$, kinetic energy is transferred into potential energy, which leads to slowing of the molecular package in the longitudinal direction. By switching the potential to subsequent electrode pairs, the slowing process can be repeated many times. The synchronous particle is depicted by the green circle. The electrode pairs bearing high voltage are drawn with surrounding field lines and after switching the HV potential to the next electrode pair, the particle's trajectory continues on the potential energy curve displaying a shift of π radians, as indicated by arrows. The phase angle definition from refs. [35, 70] applies.

where x denotes the longitudinal position of the particle relative to the midpoint between two neighbouring electrode pairs and L stands for the electrode separation in the longitudinal direction ($L = 5.5$ mm for our decelerator). As the Stark potential $W(\phi)$ displays a period of $2L$, the reduced longitudinal position represents a convenient quantity for expressing a particle's position on the potential curve. ϕ is also referred to as phase angle and this thesis follows the phase angle definition given in refs. [35, 70]. In Fig. 3.2, $\phi = 0$ is located at the center position between two sets of HV-electrodes and $\phi = \pi/2$ corresponds to the maximum of the potential energy curve $W(\pi/2)$ just before switching [61].

The final velocity of the packet is controlled by the phase angle of a "synchronous molecule"

$$\phi_0 = \pi \cdot \frac{x_{\text{synchr.}}}{L}\,, \tag{3.9}$$

which is a measure for the proximity of the synchronous molecule to the next high voltage electrode. In Fig. 3.2, the position of the synchronous molecule is denoted by a green point. The synchronous molecule is an ideal particle traversing the decelerator on the centre line and flying to a fixed position before the potential is switched. Consequently, the synchronous particle looses a constant amount of energy per stage in accordance with a given phase angle ϕ_0. At a phase angle $\phi_0 = 0$, there is no net deceleration and the decelerator rather acts as a velocity filter. Phase angles satisfying $0 < \phi_0 \leq \pi/2$ lead to deceleration, whereas phase angles in the range $-\pi/2 \leq \phi_0 < 0$ result in acceleration of a molecular package inside the decelerator [35].

While the synchronous particle represents an ideal particle with a velocity v_0, the decelerator is loaded from a molecular beam, which displays a spatial and velocity spread. Consequently, not all particles reach the ϕ_0 position simultaneously with the synchronous molecule. Assuming that a particle lags behind the synchronous molecule and reaches a position with $\phi < \phi_0$ upon switching the fields, less energy was removed and the particle will experience a longer section of the falling Stark slope after switching. Therefore, the phase angle of the non-synchronous particle increases until eventually overtaking the synchronous molecule and the process is reversed. Under the influence of the deceleration potential, the automatic readjustment of the particle position relative to the synchronous molecule is an important concept called phase stability [70, 76]. Phase stability is also of great importance in charged particle accelerators [110]. Molecules within a phase-stable region of the decelerator oscillate around the synchronous molecule. A better understanding of phase stability can be gained from the longitudinal equation of motion discussed in the next section.

3.2.3 Longitudinal equation of motion

The treatment of the longitudinal equation of motion given here follows the approach outlined in references [35, 61, 70, 76, 103]. As the Stark energy $W(\phi_0)$ along the decelerator's centre line $W(\phi_0)$ is a $2L$-periodic function (see Fig. 3.2), it can be expressed in the form of a Fourier series. Moreover, the Stark potential $W(\phi_0)$ is symmetric around an electrode pair. The lower potential in Fig. 3.2 may be expanded into the following Fourier series:

$$\begin{aligned} W_{\text{low}}(\phi_0) &= \frac{a_0}{2} + \sum_{n=1}^{\infty} a_n \cos\left(n\left(\phi_0 + \frac{\pi}{2}\right)\right) \\ &= \frac{a_0}{2} - a_1\sin(\phi_0) - a_2\cos(2\phi_0) + a_3\sin(3\phi_0) + a_4\cos(4\phi_0) - \cdots . \end{aligned} \tag{3.10}$$

ϕ_0 denotes the phase angle of the synchronous particle and the expansion coefficients are given by a_n (in units of energy), where $n \in \mathbb{N}_0$. It should be noticed that the maximum value of the Fourier series in Eqn. 3.10 occurs at $\phi_0 = -\frac{\pi}{2}$ or more generally $\phi_0 = k\cdot 2\pi - \frac{\pi}{2}$, where $k \in \mathbb{Z}$. Therefore, the expansion series pertains to the lower potential curve depicted in Fig. 3.2, which is expressed by the "low" subindex. As switching the potential is equivalent to introducing a phase shift of π, the Fourier series of the upper curve is given by:

$$W_{\text{up}}(\phi_0) = W_{\text{low}}(\phi_0 + \pi) = \frac{a_0}{2} + \sum_{n=1}^{\infty} a_n \cos\left(n\left(\phi_0 + \frac{3\pi}{2}\right)\right) . \tag{3.11}$$

The kinetic energy loss of a synchronous molecule between two successive switching events is then given by:

$$\begin{aligned} \Delta W(\phi_0) &= W_{up}(\phi_0) - W_{\text{low}}(\phi_0) = W_{\text{low}}(\phi_0 + \pi) - W_{\text{low}}(\phi_0) \\ &= \left(\frac{a_0}{2} + \sum_{n=1}^{\infty} a_n \cos\left(n\left(\phi_0 + \frac{3\pi}{2}\right)\right)\right) - \left(\frac{a_0}{2} + \sum_{n=1}^{\infty} a_n \cos\left(n\left(\phi_0 + \frac{\pi}{2}\right)\right)\right) \\ &\overset{n=1}{\approx} a_1\left(\cos\left(\phi_0 + \frac{3\pi}{2}\right) - \cos\left(\phi_0 + \frac{\pi}{2}\right)\right) = 2a_1\sin(\phi_0) . \end{aligned} \tag{3.12}$$

Omitting terms higher in order than $n = 1$ leads to an energy loss of $2a_1\sin(\phi_0)$ for the synchronous molecule in between two subsequent switching events. $\Delta W(\phi_0)$ is defined for a synchronous molecule only, as it has to be assured that the particle travels a full distance L before the fields are switched. As the switching times are defined by the synchronous particle reaching ϕ_0, the position of non-synchronous particles and their energy loss during a switching cycle cannot generally be inferred from Eqn. 3.12.

The derivation of the longitudinal equation of motion requires an expression for the continuous and position-dependent force acting during a stage. Integrating the force over the length of interaction, i.e. a single stage, is required to yield $\Delta W(\phi_0)$. Assuming that the synchronous molecule's change in velocity Δv_0 is small compared to the velocity v_0 at which it traverses a single stage, a continuous average force can be defined in the following way:

$$\bar{F}(\phi_0) = \frac{-\Delta W(\phi_0)}{L} = -\frac{2a_1 \sin(\phi_0)}{L}\,. \tag{3.13}$$

The equation of motion can be extended to non-synchronous molecules provided that they travel at the same velocity v_0 as the synchronous molecule. The average force at a non-synchronous position $\phi = \phi_0 + \Delta\phi$ is then given by:

$$\bar{F}(\phi_0 + \Delta\phi) = \frac{-\Delta W(\phi_0 + \Delta\phi)}{L} = -\frac{2a_1 \sin(\phi_0 + \Delta\phi)}{L}\,. \tag{3.14}$$

Consequently, the restoring force of a non-synchronous particle towards the synchronous particle is given by:

$$\bar{F}_{\text{rel.}}(\phi_0, \Delta\phi) = \bar{F}(\phi_0 + \Delta\phi) - \bar{F}(\phi_0) = -\frac{2a_1}{L}(\sin(\phi_0 + \Delta\phi) - \sin(\phi_0))\,. \tag{3.15}$$

By making use of $\Delta x = \frac{L}{\pi} \cdot \Delta\phi$, the equation of motion can be cast into the following form, which is amenable to numerical integration.

$$\begin{aligned} m\frac{\mathrm{d}^2\Delta x}{\mathrm{d}t^2} = \frac{mL}{\pi}\frac{\mathrm{d}^2\Delta\phi}{\mathrm{d}t^2} = \bar{F}(\phi_0 + \Delta\phi) - \bar{F}(\phi_0) = -\frac{2a_1}{L}(\sin(\phi_0 + \Delta\phi) - \sin(\phi_0)) \Rightarrow \\ \frac{mL}{\pi}\frac{\mathrm{d}^2\Delta\phi}{\mathrm{d}t^2} + \frac{2a_1}{L}(\sin(\phi_0 + \Delta\phi) - \sin(\phi_0)) = 0\,. \end{aligned} \tag{3.16}$$

m denotes the mass of the molecule and a_1 is the first order ($n = 1$) energy term, which can be approximated by $a_1 \approx (W(\frac{3\pi}{2}) - W(\frac{\pi}{2}))/2$ when considering the lower diagram in Fig. 3.2. Only taking into account positions in the vicinity of the synchronous molecule, i.e. $\Delta\phi$ is small, $\sin(\phi_0 + \Delta\phi)$ can be approximated in the following way:

$$\sin(\phi_0 + \Delta\phi) = \sin(\phi_0)\cos(\Delta\phi) + \cos(\phi_0)\sin(\Delta\phi) \approx \sin(\phi_0) + \cos(\phi_0)\Delta\phi\,. \tag{3.17}$$

Substituting $\sin(\phi_0 + \Delta\phi)$ in Eqn. 3.16 with the expression obtained in Eqn. 3.17 for small phase angle deviations, the equation of motion can be solved analytically and the oscillation frequency ω around the synchronous particle is determined by the spring constant k.

$$\frac{mL}{\pi}\frac{\mathrm{d}^2\Delta\phi}{\mathrm{d}t^2} + \frac{2a_1}{L}\cos(\phi_0)\Delta\phi = 0 \Rightarrow \tag{3.18}$$

$$\frac{\mathrm{d}^2\Delta\phi}{\mathrm{d}t^2} = -\frac{2\pi a_1}{mL^2}\cos(\phi_0)\Delta\phi = -\frac{k}{m}\Delta\phi = -\omega^2\Delta\phi \Rightarrow \Delta\phi = e^{i\cdot\omega\Delta\phi} \Rightarrow \tag{3.19}$$

$$\omega = \sqrt{\frac{k}{m}} = \sqrt{\frac{2\pi a_1}{mL^2}\cos(\phi_0)}\,. \tag{3.20}$$

During a deceleration cycle, the non-synchronous particle is pushed towards the synchronous molecule by the Stark decelerator's potential energy surface. $\bar{F}_{\mathrm{rel.}}$ described in Eqn. 3.15 can be considered as a restoring force arising from a potential well travelling along with the synchronous molecule at a velocity v_0. Within the well, non-synchronous molecules located at an off-centre position $\Delta\phi$ are pushed back towards the synchronous molecule. The effective potential energy associated with the position of the non-synchronous particle within the potential well can be expressed by making use of the integral relation between force and potential energy stated in Eqn. 3.21. The expression takes into account the relative force between the two particles $\bar{F}_{\mathrm{rel.}}(\phi_0, \Delta\phi)$, which acts along the infinitesimal change of separation $\mathrm{d}\Delta\phi$ along the deceleration axis. The potential W_{eff} is obtained by integrating $\bar{F}_{\mathrm{rel.}}$ from zero to the desired deflection $\Delta\phi$, which is reminiscent of stretching a mechanical spring over a certain distance from the equilibrium position.

$$\begin{aligned} W_{\mathrm{eff}}(\phi_0, \Delta\phi) &= -\int_0^{\Delta x} \bar{F}_{\mathrm{rel.}}(\phi_0, \Delta\phi)\,\mathrm{d}\Delta x = -\frac{L}{\pi}\int_0^{\Delta\phi} \bar{F}_{\mathrm{rel.}}(\phi_0, \Delta\phi)\,\mathrm{d}\Delta\phi \\ &= \frac{-2a_1}{\pi}\Big[\cos(\phi_0 + \Delta\phi) + \sin(\phi_0)\Delta\phi\Big]_0^{\Delta\phi} \\ &= \frac{-2a_1}{\pi}(\cos(\phi_0 + \Delta\phi) + \sin(\phi_0)\Delta\phi - \cos(\phi_0))\,. \end{aligned} \tag{3.21}$$

Eqn. 3.21 allows for the determination of the potential depth $W_{\mathrm{eff}}(\phi_0, \Delta\phi)$ a molecule with a phase difference of $\Delta\phi$ experiences. The above expression was used for plotting the upper panels of Fig. 3.3. As the point of switching the fields moves further up the Stark slope with increasing phase angle ϕ_0, the potential well needs to be shifted accordingly. In order to account for this spatial shift, $\Delta\phi$ is substituted with $\Delta\phi = \phi - \phi_0$ in Eqn. 3.21, which results in the expression used for plotting Fig. 3.4 a).

$$W_{\mathrm{eff}}(\phi_0, \phi - \phi_0) = \frac{-2a_1}{\pi}(\cos(\phi) + \sin(\phi_0)(\phi - \phi_0) - \cos(\phi_0))\,. \tag{3.22}$$

The rapid shrinking of the potential well with increasing phase angles ϕ_0 is depicted in Fig. 3.4 a). The position of a non-synchronous particle is given by $\phi = \phi_0 + \Delta\phi$.

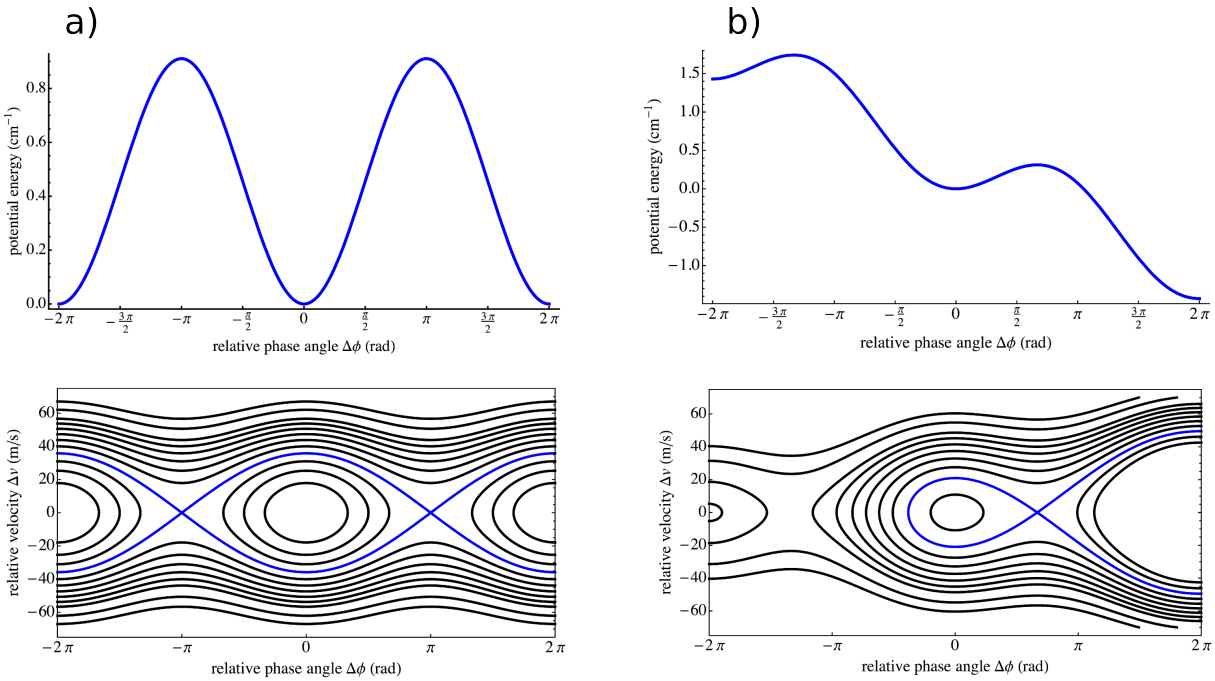

Figure 3.3: **a)** Effective potential $W_{\text{eff}}(\phi_0, \Delta\phi) = W_{\text{eff}}(0, \Delta\phi)$ for OH in the $J = 3/2, M_J\Omega = -9/4$ state (upper panel). The decelerator is operated at a phase angle $\phi_0 = 0$ (guiding mode). The corresponding phase stability diagram is depicted in the lower panel and the separatrix is accentuated in blue. **b)** Effective potential $W_{\text{eff}}(\phi_0, \Delta\phi)$ for a decelerator operated at $\phi_0 = 30°$ (upper panel). Compared to guiding, the phase-stable region is reduced and molecules with a kinetic energy surmounting the well depth are lost from the package. The phase-space stability diagram depicted in the lower panel displays a reduction of the area bounded by the separatrix compared to guiding. [103]

In a next step, the maximum and minimum of the effective potential is determined by differentiating Eqn. 3.21 with respect to $\Delta\phi$ and by requesting that the resulting expression equates to zero.

$$\frac{\partial}{\partial\Delta\phi} W_{\text{eff}}(\phi_0, \Delta\phi) = \frac{2a_1}{\pi}(\sin(\phi_0 + \Delta\phi) - \sin(\phi_0)) = 0\,. \tag{3.23}$$

Equation 3.23 is satisfied for $\Delta\phi = 0$, which pertains to the minimum, and for $\Delta\phi = \pi - 2\phi_0$, which denotes the position of the maximum.

In a frame of reference moving with the synchronous particle, the kinetic energy of a non-synchronous particle is given by $1/2m\Delta v^2$. The total energy of a non-synchronous particle in this co-moving frame is therefore given by the sum of the kinetic energy $1/2\,m\,\Delta v^2$ resulting from the motion towards or away from the synchronous molecule and the potential energy expressed in terms of the synchronous particle's phase ϕ_0 and the deviation of the

non-synchronous particle $\Delta\phi$ from ϕ_0.

$$\begin{aligned} E_{\text{tot}} &= 1/2\, m\, \Delta v^2 + W_{\text{eff}}(\phi_0, \Delta\phi) \\ &= 1/2\, m\Delta\, v^2 - \frac{2a_1}{\pi}(\cos(\phi_0 + \Delta\phi) + \sin(\phi_0)\Delta\phi - \cos(\phi_0))\,. \end{aligned} \tag{3.24}$$

Finally, an expression for the closed blue contour lines in the lower panels of Fig. 3.3 is derived. These lines are also referred to as separatrices and denote the phase space within which a stable operation is possible. All molecules bounded by the separatrix traverse the decelerator in a phase-stable manner, which indicates that they remain within the "bucket" into which they were loaded. For this purpose, $\Delta\phi = \pi - 2\phi_0$ is substituted into Eqn. 3.21 and the maximum potential energy $W_{\text{eff}}^{\max}(\phi_0, \pi - 2\phi_0)$ is given by:

$$\begin{aligned} W_{\text{eff}}^{\max}(\phi_0, \pi - 2\phi_0) &= \frac{-2a_1}{\pi}(\cos(\pi - \phi_0) + \sin(\phi_0)(\pi - 2\phi_0) - \cos(\phi_0)) \\ &= \frac{-2a_1}{\pi}(-2 \cdot \cos(\phi_0) + \sin(\phi_0)(\pi - 2\phi_0))\,. \end{aligned} \tag{3.25}$$

$W_{\text{eff}}^{\max}(\phi_0, \pi - 2\phi_0)$ denotes the maximum potential energy a particle can have relative to the synchronous molecule, such that the trajectory is still phase stable. Replacing E_{tot} in Eqn. 3.24 with $W_{\text{eff}}^{\max}(\phi_0, \pi - 2\phi_0)$ from Eqn. 3.25 allows for the derivation of an expression giving the maximum Δv values which are still trapped by the effective potential W_{eff}.

$$\begin{aligned} 1/2\, m\, \Delta v^2 - \frac{2a_1}{\pi}(\cos(\phi_0 + \Delta\phi) + \sin(\phi_0)\Delta\phi - \cos(\phi_0)) = \\ \frac{-2a_1}{\pi}(-2 \cdot \cos(\phi_0) + \sin(\phi_0)(\pi - 2\phi_0)) \Rightarrow \\ 1/2\, m\, \Delta v^2 - \frac{2a_1}{\pi}\left(\cos(\phi_0 + \Delta\phi) + \cos(\phi_0) + \sin(\phi_0)(\Delta\phi - \pi + 2\phi_0)\right) = 0 \Rightarrow \\ \Delta v = \pm\left[\frac{4a_1}{\pi m}\left(\cos(\phi_0 + \Delta\phi) + \cos(\phi_0) + \sin(\phi_0)(\Delta\phi - \pi + 2\phi_0)\right)\right]^{1/2}\,. \end{aligned} \tag{3.26}$$

The above equation assumes a positive value of a_1. Again, the separatrix needs to be shifted to the switching position ϕ_0 by applying the substitution $\Delta\phi \rightarrow \phi - \phi_0$ to Eqn. 3.26. The resulting expression was used for plotting the phase stable region of the decelerator for various phase angles ϕ_0, as depicted in Fig. 3.4 b).

$$\Delta v = \pm\left[\frac{4a_1}{\pi m}\left(\cos(\phi) + \cos(\phi_0) + \sin(\phi_0)(\phi - \pi + \phi_0)\right)\right]^{1/2}\,. \tag{3.27}$$

It is interesting to notice, that Eqn. 3.27 is identical to the expression derived by B. Friedrich in ref. [83] (Eqn. 87) for the case of a biased mechanical pendulum. The

analogy between the equations of motion for a Stark decelerator and the biased pendulum is discussed in references [83, 84].

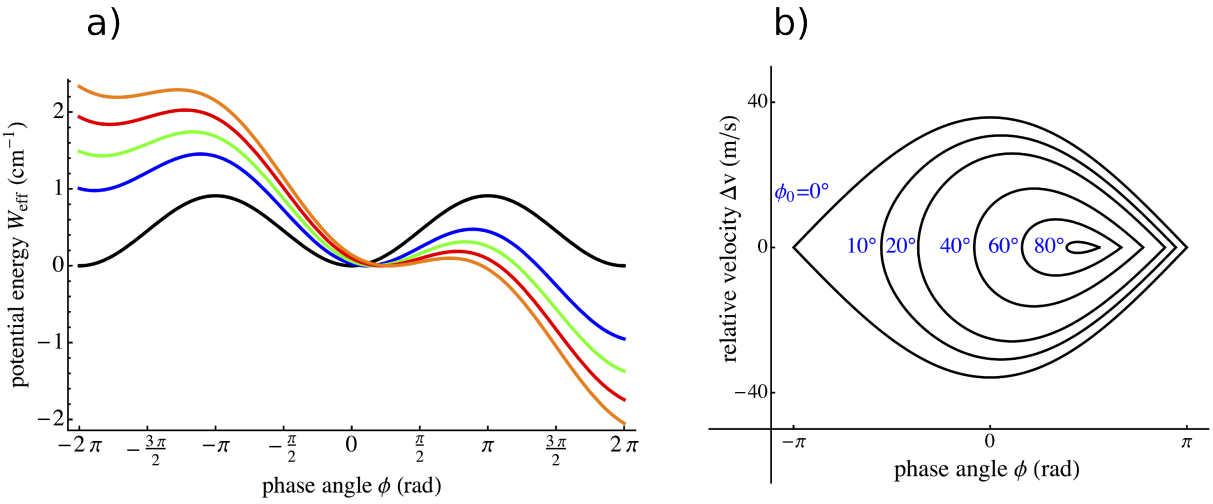

Figure 3.4: **a)** Potential energies $W_{\text{eff}}(\phi_0, \phi)$ for various different phase angles ϕ_0: black 0°, blue 20°, green 30°, red 40°, orange 50°. The minimum of the potential W_{eff} is centred around the phase of the synchronous molecule ϕ_0. With increasing phase angle, the minimum of the phase stable "bucket" moves to the right and the well depth is reduced significantly. The depicted potentials are identical to those encountered in the analytic treatment of a biased pendulum [83, 84]. **b)** Longitudinal phase-stable region (acceptance) of the decelerator for various operation phase angles ϕ_0. The area bounded by the black separatrices corresponds to the particle flux though the decelerator. At higher phase angles more kinetic energy is lost per stage, but at the same time, the phase stable volume decreases and fewer molecules exit the decelerator.

3.2.4 Final velocity and timing sequence

As the synchronous molecule looses an equal amount of energy per stage, the remaining kinetic energy and with that the final velocity after the decelerator can be estimated. The change in kinetic energy of the synchronous molecule per deceleration stage is given by $\Delta K(\phi_0)$ and depends on the phase angle ϕ_0. The change in kinetic energy is equal, but opposite to the change in potential energy $\Delta W(\phi_0)$, which is expressed by [35, 70]:

$$\Delta K(\phi_0) = -\Delta W(\phi_0) = W(\phi_0) - W(\phi_0 + \pi) = -2a_1 \sin(\phi_0)\,, \tag{3.28}$$

where $\Delta W(\phi_0)$ from Eqn. 3.12 applies. $\Delta K(\phi_0)$ is negative, as the molecule looses kinetic energy. After the i-th switching cycle, the remaining kinetic energy is given by $E_i(\phi_0)$ and the corresponding velocity is $v_i(\phi_0)$.

$$E_i(\phi_0) = \frac{1}{2} m v_{\text{initial}}^2 + i\Delta K(\phi_0) = \frac{1}{2} m v_i(\phi_0)^2\,. \tag{3.29}$$

Rearranging Eqn. 3.29 for the final velocity $v_{\text{final}}(\phi_0)$ results in [70, 103]

$$v_{\text{final}}(\phi_0) = v_{i=n}(\phi_0) = \sqrt{v_{\text{initial}}^2 + \frac{2n\Delta K(\phi_0)}{m}}\,, \tag{3.30}$$

where n denotes to total number of switching events. The decelerator described in this thesis is composed of 124 stages, which allows for a total of 123 switching cycles. The final velocities achievable after the decelerator depend on the initial velocity of the molecular beam and on the deceleration phase angle. Fig. 3.5 depicts the velocity space addressable on our decelerator.

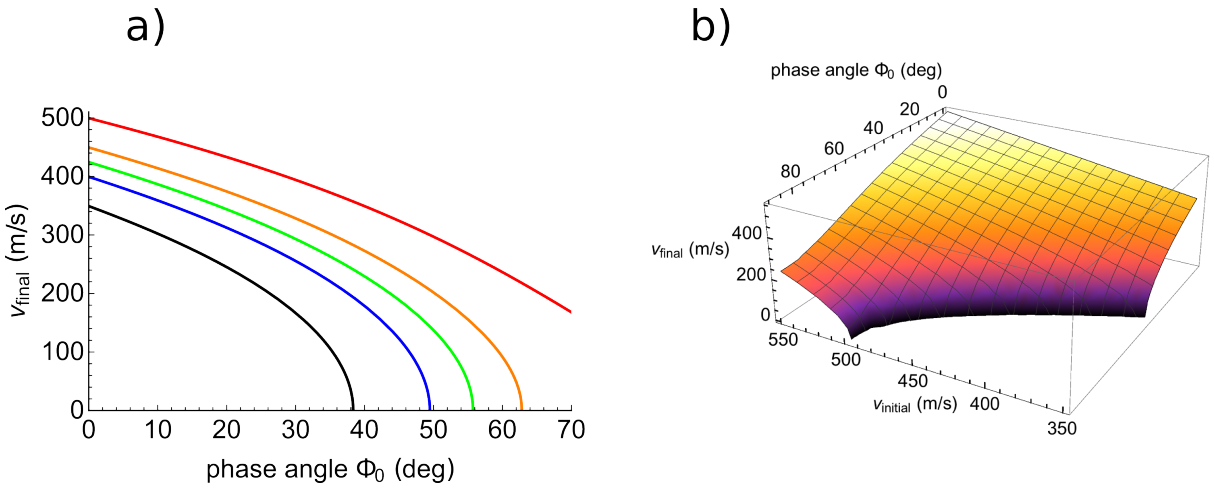

Figure 3.5: **a)** Final velocities as a function of the phase angle ϕ_0, given initial velocities of 350 m/s (black), 400 m/s (blue), 425 m/s (green), 450 m/s (orange) and 500 m/s (red). For an initial beam velocity of 500 m/s, the deceleration power is insufficient to reach velocities below 180 m/s when operating at 70°. A maximum kinetic energy of 1.43 cm^{-1} can be removed per stage when operating at 90° and the total number of switching cycles amounts to $n = 123$. **b)** Three dimensional representation of the velocity space addressable on our 124-stage Stark decelerator for initial velocities in the range of 350-550 m/s and phase angles between $0 - 90°$.

With every traversed stage, the synchronous molecule travels more slowly. While the time between two subsequent switching events is short initially, the high voltage pulses become longer towards the end of the decelerator as it takes more time for the slowed synchronous molecule to reach the switching point ϕ_0. The previous statement only applies if the decelerator is not operated in guiding mode ($0 < \phi_0$). The time at which the molecule reaches the i-th stage can be found by rearranging Eqn. 3.29 for $v_i(\phi_0)$ and replacing ΔK with $-\Delta W(\phi_0)$ from Eqn. 3.12. Here, it is convenient to replace i with

x/L, where x denotes the longitudinal position inside the decelerator [70].

$$v_i(x) = \sqrt{v_{\text{initial}}^2 - \frac{x}{L}\frac{2}{m}2a_1 \sin(\phi_0)}\,. \tag{3.31}$$

The time at which the molecule has reached the i-th stage is obtained by integrating $\mathrm{d}\,t = \frac{\mathrm{d}\,x}{v(x)}$ with respect to $\mathrm{d}x$ [70].

$$t(i) - t(0) = \int_{t(0)}^{t(i)} \mathrm{d}t = \int_0^{iL} \frac{\mathrm{d}\,x}{\sqrt{v_{\text{initial}}^2 - \frac{x}{L}\frac{2}{m}2a_1 \sin(\phi_0)}}\,, \tag{3.32}$$

$t(i)$ denotes the time at which the $i^{\,\text{th}}$ switching position is reached and $t(0)$ denotes the onset of the switching sequence and is usually set to zero. The time difference between two subsequent stages is obtained by evaluating $t(i) - t(i-1)$ [70].

3.2.5 Transverse stability

So far, expressions for the longitudinal equation of motion have been derived. While phase stability keeps the molecular package together in the longitudinal direction, transverse forces ensure the lateral focussing and confinement of the OH package. The theory for describing the transverse stability in a decelerator is well known and the discussion presented in this chapter is based on references [61, 70, 77, 82]. The closer a molecule flies towards the centre of the HV-electrodes, the stronger is the transverse focussing force it experiences. For the successful operation of a Stark decelerator, transverse focussing forces are as important as the longitudinal restoring forces towards the synchronous molecule within the phase stable "bucket". Under the influence of transverse forces, molecules with an off-axis position follow oscillatory trajectories around the decelerator's principle axis [70, 77]. As depicted in Fig. 3.6, a Stark decelerator employs alternating vertical and horizontal electrode pairs, which provide focussing forces acting almost normal to the electrode extension. In Fig. 3.6, the vertical electrode pairs running parallel to the y-direction are switched to high voltage. Consequently, restoring forces acting along the z-direction are present and focus the OH package towards the decelerator axis. The transverse confinement of the Stark potential can be perceived from Fig. 3.6 a), where the energy increases along the z-direction for positions close to the electrodes. Along the y-direction, restoring forces are almost absent for the voltage configuration in Fig. 3.6.

Like in the model for the longitudinal motion through the decelerator, one would like to define an average force $\bar{F}_{y,z}$, which characterises the motion of the molecules in the transverse directions y and z. Generally, the transverse force experienced by a particle in

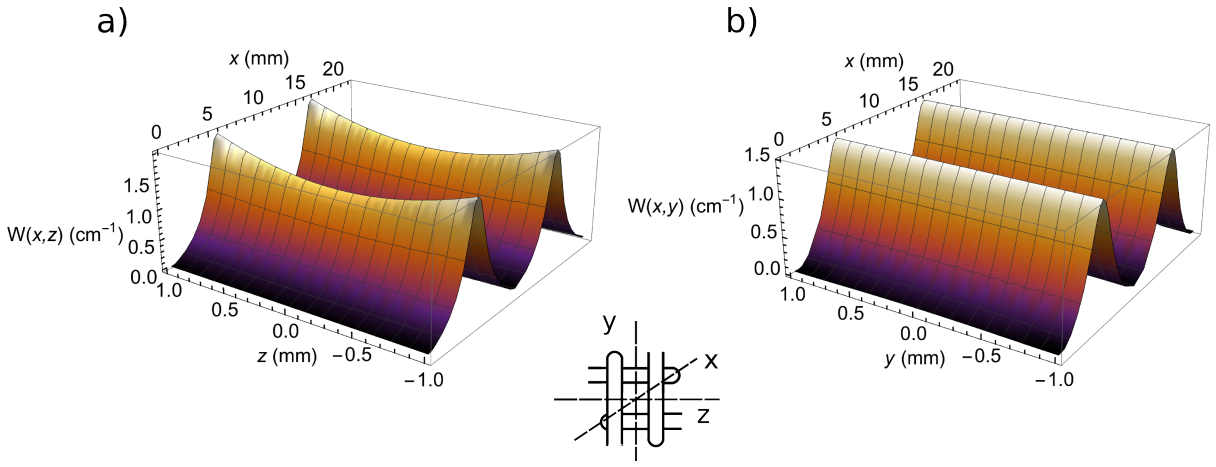

Figure 3.6: **a)** $2L$-periodic Stark potential energy profile for OH in the $J = 3/2, M_J\Omega = -9/4$ state around electrode pairs at ± 10 kV. The longitudinal separation between two subsequent electrodes amounts to $L = 5.5$ mm and the separation between two electrode sets at high voltage is $2L = 11$ mm. The electrode configuration is depicted in the diagram between graphs a) and b). Here, HV is applied to the rods running parallel to the y-axis. The electrode diameter amounts to 3 mm and the horizontal and vertical electrodes form a 2×2 mm^2 square opening when looking along the centre line x. Along x, the origin is located at the centre of a grounded electrode pair. The origin of the y, z-directions coincides with the decelerator axis. **a)** $W(x, z)$ Stark potential profile as a function of the longitudinal direction x and the transverse direction z. Close to the electrodes $x \approx L$, the potential is confining along the z-direction. **b)** $W(x, y)$ Stark potential profile as a function of the longitudinal direction x and the transverse direction y. Lateral confinement is almost absent along y.

the low-field seeking state depends on its position (or phase angle ϕ) within the decelerator and the time at which this position is reached in the switching sequence [61, 77]. When deviating only slightly from the main axis of the decelerator, the transverse force is not very strong and the transverse oscillation frequency $\omega_{y,z}$ is so low that the time for a transverse oscillation is larger than the time required for the molecules to fly through two deceleration stages, which can be written as $2\pi/\omega_t >> 2L/v_x$ [70]. As molecules close to the centre line are expected to experience only weak restoring forces over the course of two stages, the offset from the beam remains approximately constant. Like in the longitudinal model, we assume a non-synchronous molecule with a phase difference $\Delta\phi$ relative to the synchronous molecule. Furthermore, it is requested, that the non-synchronous molecule is travelling at a velocity identical to one of the synchronous molecule, i.e. $v_0 = L/\Delta T$, where ΔT is the time between two subsequent switching events and L denotes the length of one stage [61]. Following refs. [70, 75, 77, 82], the average transverse force $\bar{F}_{y,z}(\phi)$

along the y, z-direction can be expressed as:

$$\begin{aligned}\bar{F}_{y,z}(\phi) = \bar{F}_{y,z}(\phi_0 + \Delta\phi) &= \frac{1}{2L}\int_{\phi L/\pi}^{(\phi+2\pi)L/\pi} F_{y,z}(x)\mathrm{d}\,x \\ &= \frac{1}{2L}\left[\int_{(\phi_0+\Delta\phi)L/\pi}^{(\phi_0+\Delta\phi+\pi)L/\pi} F_{y,z}(x)\mathrm{d}\,x + \int_{(\phi_0+\Delta\phi+\pi)L/\pi}^{(\phi_0+\Delta\phi+2\pi)L/\pi} F_{y,z}(x)\mathrm{d}\,x\right]. \end{aligned} \tag{3.33}$$

The subindices y, z in Eqn. 3.33 denote that the expression applies to the calculation of both transverse forces and that the deviations from the beam axis along y and z are assumed to be constant. For convenience, only the z-coordinate is treated further. Compared to the longitudinal model, where the averaging of the force takes place over a single stage only, the calculation of the transverse force requires averaging over two stages of the decelerator. Therefore, the integral in Eqn. 3.33 can be split up into two terms, the first of which pertains to the transverse force during the first switching cycle and the second term corresponds to the transverse force during the second part of the switching cycle, thereby finishing the deceleration period [82, 111].

Numerical differentiation of the Stark potential depicted in Fig. 3.6 reveals that the acceleration is linear along the z-direction for a wide range of x-values. Therefore, a molecule at an off-centre position can be described as a spring-loaded particle with a deflection z relative to the principle axis and Hook's spring constant k_z relates the average force $\bar{F}_z(\phi)$ to the deflection [70, 77]:

$$\bar{F}_z(\phi) = -k_z z = -m\,\omega_z^2(\phi)\,z = -m\,\omega_z^2(\phi_0 + \Delta\phi)z\,. \tag{3.34}$$

Subtle effects arise when the longitudinal and transversal motion are coupled. As the longitudinal (Eqn. 3.20) and transversal (Eqn. 3.34) oscillation frequencies can become similar, parametric amplification leads to non-stable regions within the separatrix [77]. Furthermore, the transverse forces a molecular package experiences during deceleration depend on the phase angle ϕ_0. In guiding mode ($\phi_0 = 0$), the synchronous molecule is located a maximum distance from the high voltage electrodes. Therefore, molecules located close to the synchronous molecule experience reduced transverse focussing and the transverse oscillation frequency is insufficient for keeping the trajectories within the 2×2 mm^2 transversal window of the decelerator [77]. The reduced transversal acceptance in guiding mode can be perceived from Fig. 5.16 a), where the number of molecules is lower in the vicinity of the synchronous molecule. Hence, the acceptance at low phase angles is slightly lower than predicted by the area of the separatrix, which was demonstrated in references [61, 77].

While in this section, the transverse focussing properties of the decelerator have been discussed only briefly, extended models for the description of the transverse stability in a decelerator are available in the literature [77]. S.Y.T. van de Meerakker and co-workers have extended the transverse stability model to higher order resonances and have demonstrated that the phase-space acceptance of the Stark decelerator is more uniformly filled in the $s = 3$ (third overtone) mode of operation at low phase angles [76, 77]. An improved Stark deceleration switching scheme based on the optimisation of the transverse forces has been demonstrated by D. Zhang and co-workers [82].

3.3 Monte Carlo trajectory simulations

The Stark deceleration process is modelled with realistic Monte-Carlo trajectory simulations taking into account the geometry of the apparatus as well as all externally adjustable parameters such as the phase angle, the deceleration potentials, the incoupling time and the quantities characterising the molecular beam. The simulation code employed in this thesis was adapted from a preexisting version D. Zhang used during his stay in the research group of G. Meijer. In part, the original program was similar to the one outlined in references [70, 112]. The program was adjusted to our decelerator geometry and the code was extended to allow for simulating the trap loading and trapping process. Furthermore, the trapping code was restructured to allow for the numerical optimisation of the trap loading process with a mesh adaptive direct search algorithm [113].

3.3.1 Electric fields and Stark shift

The electric fields generated by the periodic electrode structure of the decelerator were simulated using SIMION [114]. As the electric field in a Stark decelerator results from electrode pairs which are alternatingly grounded or set to high voltage, it is necessary to include several deceleration stages to correctly account for the field contribution arising from high voltage bearing electrodes located one full period $2L$ from a specific point. The electrode structure programmed into SIMION is depicted in Fig. 3.7 a) and the resulting potentials in the x, y-plane are depicted in panel b). The potential was calculated on a grid with a resolution of 20 points/mm. The electric field was obtained by numerical differentiation of the potential and the Stark shift experienced by OH molecules within a deceleration stage was calculated according to [35]:

$$E_{\mathrm{Stark}}(x,y,z) = \frac{E_\Lambda}{2} \pm \sqrt{\left(\frac{E_\Lambda}{2}\right)^2 + \left(\mu^{\mathrm{e}}|E(x,y,z)| \cdot \frac{M\Omega_{\mathrm{eff}}}{J(J+1)}\right)^2}, \qquad (3.35)$$

where $\mu^e EM\Omega_{\text{eff}}/J(J+1)$ represents the linear Stark shift, E_Λ is the Λ-doublet energy splitting and $|E|$ represents the magnitude of the local electric field. Ω_{eff} denotes the effective value of the Ω quantum number, which is ± 1.46 for OH in the $X^2\Pi_{3/2}, J = 3/2$ state and deviates from $\pm 3/2$ due to mixing between the $X^2\Pi_{3/2}$ and $X^2\Pi_{1/2}$ spin-orbit manifolds [35, 64]. The Stark potential energy surfaces obtained from evaluating Eqn. 3.35 are depicted in Fig. 3.6. When applying a potential of ± 10 kV on the electrodes, a maximum of 1.43 cm^{-1} in kinetic energy can be removed per stage at a phase angle of 90°. At a typical phase angle of $\phi = 55.468°$, which results in a final velocity of 28.8 m/s after 123 stages ($v_0 = 425$ m/s), the deceleration process removes a kinetic energy of 1.04 cm^{-1} per stage. The acceleration of an OH molecule under the influence of the electric field is calculated by

$$\vec{a}(x, y, z) = -\vec{\nabla}\frac{E_{\text{Stark}}}{m_{\text{OH}}}. \tag{3.36}$$

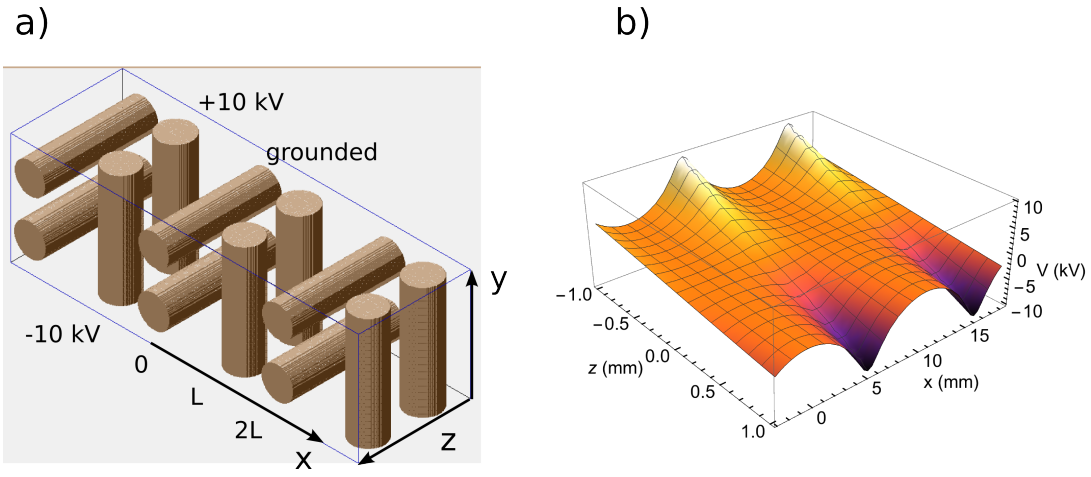

Figure 3.7: **a)** Electrode structure exported from SIMION [114]. Electrode pairs running parallel to the y-direction are at ± 10 kV and electrode pairs running parallel to the z-direction are grounded. **b)** Resulting potential in the x, z-plane, while keeping the y-axis values fixed to $y = 0$.

3.3.2 Switching sequence calculation

Knowledge of the position-dependent acceleration inside the decelerator allows for the calculation of the time sequence according to which the electric fields have to be switched. The synchronous particle always travels to the same reduced longitudinal position ϕ_0 before switching the fields [35]. A numerical integrator is used to propagate the synchronous molecule under the influence of the Stark potential depicted in Fig. 3.6. A one-dimensional trajectory along the x-direction ($y, z = 0$) is calculated in the absence of transverse forces. The time at which the switching points ϕ_0 are reached is determined and written to disk.

The computed deceleration sequence is programmed into the memory of a Pulse Blaster card and is directly used to trigger the HV-switches of the experiment. Initially, the switching between electrodes is fast due to the large velocity of the synchronous molecule. Towards later stages, the velocity of the synchronous molecule is lowered and the electric fields have to be left on for a longer duration until the position of switching is reached. This only applies if the phase angle is non-zero. In guiding mode ($\phi = 0$), the velocity of the synchronous molecule remains unchanged and the duration of a switching cycle is identical for all stages. An exemplary deceleration sequence measured on one of the positive HV electrodes of the experiment is depicted in Fig. 5.7 a).

3.3.3 Propagation of molecular beams through the decelerator

While the synchronous molecule is an idealised particle, a Stark decelerator selects a finite volume of the molecular beam to be transported through the electrode assembly within a phase-space stable region defined by the equations of motion [35]. A successful deceleration presumes careful incoupling of the molecular beam, which requires prior knowledge of the molecular beam velocity and the time required for the molecules to fly from the source to the decelerator entrance [81]. Optimised incoupling schemes have been devised to increase the density after the decelerator [78, 102] and are discussed in chapter 5. In order to obtain an accurate six-dimensional phase-space distribution of decelerated molecules by means of computer simulation, an ensemble of particles was generated around the synchronous molecule at the source location. The molecules were drawn from an initial phase-space distribution resembling the one present in the expanded molecular beam. The longitudinal and radial spreads of velocity as well as position were taken into account. After a free-flight distance to the decelerator entrance, the individual particles were subjected to the acceleration caused by the Stark potential depicted in Fig. 3.6 and the trajectories were integrated for a duration given by the switching sequence determined from the synchronous particle (see section 3.3.2). Upon switching, the acceleration fields were shifted by half a repetition period of the electrodes (L or π radians) and the trajectory integration under the influence of the shifted acceleration was resumed. During the entire simulation process, the flight path of the molecules was checked against geometric constraints imposed by solid structures of the experiment such as the skimmer, the decelerator rods and the trap. Molecules hitting a surface were removed from the simulation. After leaving the decelerator, the particles were propagated to the LIF laser volume in the absence of acceleration. Binning of the arrival time yielded time of flight (TOF) profiles, which can directly be compared to the experiment. The computer code allowed for the extraction of phase-space information at any desirable location and point in time. The simulations took into account contributions from both low-field-seeking com-

ponents $M_J\Omega = -9/4$ and $M_J\Omega = -3/4$, which are transported through the decelerator. This is important especially in guiding mode, where the $M_J\Omega = -3/4$ component contributes significantly to the signal level when employing a switching sequence designed for $M_J\Omega = -9/4$.

Figure 3.8 was obtained by making use of the Monte Carlo trajectory simulation described above and depicts the (x, v_x) phase-space evolution of OH particles flying through the decelerator. The phase-space distribution was extracted from the simulation after an increasing number of deceleration stages have been surpassed. As described in sec. 3.2.1, the phase-space distribution tilts between the free flight from the source (black distribution) to the first deceleration stage (red distribution). The position spread of the molecular beam extends over three phase-stable acceptance regions upon coupling into the decelerator. Throughout the entire simulation, Liouville's theorem applies and the phase-space density is preserved, as described in sec. 3.2.1. Non-phase-stable molecules outside the separatrix spread out according to their velocity components and the phase-space distribution is modulated by the switching sequence and the contour lines depicted in Fig. 3.3. The inset of Fig. 3.8 displays the central phase-stable "bucket" at a final velocity of 28.8 m/s, which is required for the trap loading experiments in chpt. 6.

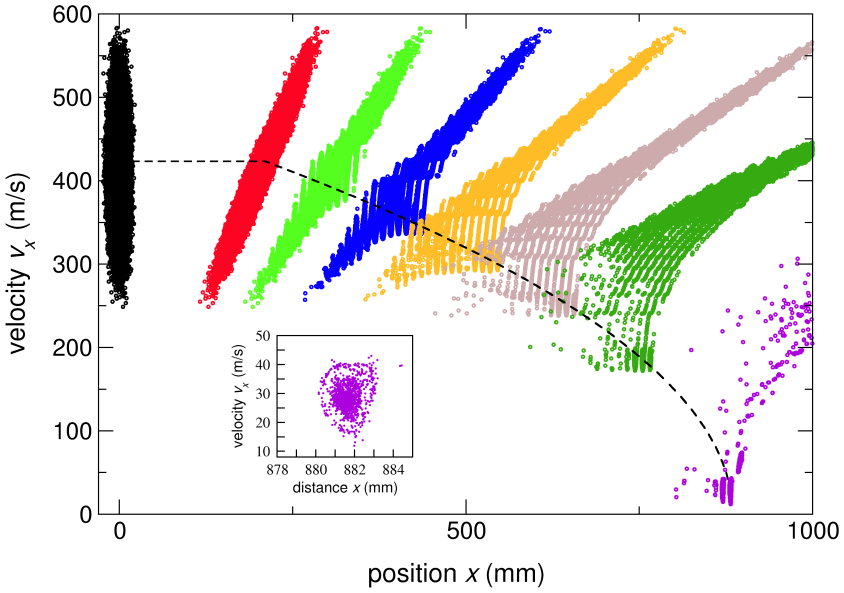

Figure 3.8: (x, v_x) phase-space evolution of OH particles in the $M_J\Omega = -9/4$ low-field seeking states after an increasing number of deceleration stages (black: source, red: first stage, light green: 20 stages, blue: 40 stages, orange: 60 stages, brown: 80 stages, dark green: 100 stages, violet: 123 stages). The dashed line represents the velocity of the synchronous particle. The initial switching velocity was set to $v_s = 425$ m/s and the trajectory simulation was conducted at a phase angle of $\phi_0 = 55.468°$, which results in a final velocity of 28.8 m/s after 123 switching cycles. In analogy to [115].

Chapter 4

The generation of cold and intense OH radical beams

4.1 Introduction

The first effusive beam of directed atomic and molecular rays was generated more than 100 years ago by Dunoyer in 1911 [116]. Beam techniques have paved the way for important technological and scientific achievements, as they offer the possibility to introduce atoms and molecules into a virtually collision free vacuum environment. Otto Stern provided experimental proof for the Maxwell-Boltzmann distribution [117, 118] and demonstrated the space quantisation of spin together with Walther Gerlach in 1922 [119]. Beam methods played a key role in the development of NMR spectroscopy by Isidor Rabi in the late 1930s [120]. Molecular beams of ammonia were of great importance for the development of masers by Charles Townes [121] in the 1950s. In 1951 Kantrowitz and Grey [122] suggested the formation of molecular beams by expanding gas through nozzles, which led to a significant increase in beam intensity compared to effusive sources. Advances in vacuum technology led to improved pumping speeds which allowed for higher backing pressures and supersonic expansions were achieved from the 1960s onwards. At around this time, the development of lasers and improved detection instrumentation led to a branching of molecular beam related research into several new disciplines which experienced rapid growth and are still prospering today. A more complete historic overview of the molecular beam method and the research branches relying on it can be found in references [123, 124].

Cold and intense beams of atoms and molecules are the starting points for a wide range of different experiments. High resolution spectroscopy profits from the low vibrational

Based on: L. Ploenes*, D. Haas*, D. Zhang, S. Y. T. van de Meerakker, S. Willitsch, Cold and intense OH radical beam sources, *Rev. Sci. Instrum.*, 2016, **87**, 053305.

* These authors contributed equally to this work.

and rotational temperatures in molecular beams, which results in the decongestion of molecular spectra [125]. Furthermore, the uniform motion of particles within molecular beams significantly reduces the Doppler spreading of transitions. Crossed beam experiments rely on nozzle beams, which provide dense molecular packages with a high velocity resolution, good state purity and low divergence in a vacuum environment with low background collision rates. The molecular beams are either intersecting at an angle [126, 127] or are merged [128]. Such experiments seek to unravel quantum effects in the dynamics of molecular systems associated with elastic, inelastic or reactive scattering events. Neutral molecules entrained in a gas beam can be deflected or focused in static electric or magnetic fields, provided the molecules display an electric or magnetic dipole moment. Stark and Zeeman decelerators employ switched inhomogeneous fields, which offers full six-dimensional control over the molecule's motion in phase space and it can be brought to an almost complete standstill in the laboratory frame. This opens up the perspective for trapping neutral molecules [35]. In recent years, cold molecules provided by nozzle beams have become the subject of intense study, as their rich internal energy structure renders them interesting subjects for high-precision experiments [5]. Moreover, the molecular beam technique has proven to be an invaluable tool for the study of cluster beams, molecular beam epitaxy and the investigation of gas-surface interactions [129]. The widespread use of the molecular beam method and the versatility it offers demonstrate its significance.

4.1.1 Types of molecular beam valves

The last 50 years have seen very active development of atomic and molecular beam sources [124]. While all types of sources expand gases from a high pressure reservoir into a vacuum chamber, the operation modes can be divided into continuous and pulsed beam sources. Today, very few experiments employ continuous sources due to the high demand in pumping capacity. An example of an experiment utilising continuous molecular beams is the CRESU technique, where a molecular beam is expanded from a de Laval nozzle [130] into a flow tube. The focus of this thesis lies on pulsed molecular beams, which greatly reduce the demand for pumping capacity and the lower background pressures result in more favourable expansion conditions for the molecular beam. Furthermore, pulsed beam sources provide larger densities, narrower velocity profiles and colder molecular beams than continuous sources [123, 131]. In addition to this, the sample consumption is lower in pulsed beams. Another advantage of pulsed valves is that the opening rate can be synchronised with a pulsed laser system, which facilitates the spectroscopic probing of the expanded gas. From a technical and engineering standpoint, pulsed beam sources are more challenging to construct, as a reliable opening and closing mechanism has to be implemented at the interface between the vacuum and the gas reservoir. It is

therefore convenient to classify the different pulsed sources by their opening mechanism. Table 4.1 summarises the most commonly employed pulsed valve types categorised by opening mechanism.

As early as in 1978, Gentry and Giese [132] designed a pulsed valve with a current loop opening mechanism relying on the repulsion between two metal strips through which large opposing currents are pulsed. This valve offers very narrow pulse widths, but the repetition frequency is limited by the high heat load originating from the large currents required for opening the valve. The Jordan valve [133] is an improved, commercially available version of the valve by Gentry and Giese. A similar valve opening mechanism is based on the Lorentz force of a current conducting strip in a homogeneous magnetic field generated by two NdFeB bar magnets. The Nijmegen pulsed valve [50] employed in this thesis makes use of such an opening mechanism. From the 1980s onwards, piezo elements became available and allowed for opening mechanisms with repetition rates as high as 5 kHz. A common piezo-valve is the commercially available Amsterdam valve developed in the group of M. Janssen [134, 135]. This valve is based on an earlier variant developed by D. Gerlich and coworkers [136]. The rapid deformation of piezo crystals has the advantage of being very energy efficient, which prevents heating of the gas reservoir. Another popular opening mechanism is based on an electromagnet, which sets a magnetic plunger into motion. The closing mechanism is realised by a loaded spring pushing the plunger towards the sealing surface once the electromagnet is turned off. By far the best known representatives of these so-called solenoid valves are the Even-Lavie valve [137, 138] and the General valve series 9 produced by the Parker-Hannifin corporation [139].

When looking at the development of the pulsed valve performance over the years, (see Table 4.1) it becomes clear that repetition rates in the kHz regime have been achieved and the pressure and temperature range of operation has been increased significantly. Above all, a modern pulsed valve should be capable of delivering short pulses at a high peak density and provide a good energy resolution of the molecular beam (i.e. high speed ratios). Amongst the listed valves, the Even-Lavie valve [137, 138] stands out, as it excels in almost every category. This valve can be operated at repetition rates up to 1 kHz with backing pressures as high as 100 bar and the temperature range extends from -263 °C to 230 °C. Pulse widths as short as 20 μs can be reached in combination with high speed ratios of the molecular beam. The vast parameter space of operation renders the valve suitable for cluster experiments and the formation of helium nanodroplets [137, 140].

Operation mechanism	orifice (mm)	$f_{\text{rep.}}$ (Hz)	p (bar)	T (°C)	speed ratio S	density (cm^{-3})	pulse Δt (μs)	T_{rot} (K)	species	year	Ref.
Current loop	0.6	1	2	RT	20, 15	$7 \cdot 10^{13}$	13, 30	-	H_2, He	1978	[132]
	0.5	10	< 41	RT	-	-	> 100	25	ACT in He	1981	[141]
	0.25×7.4	< 20	< 6	RT	-	10^{10}	45-50	4.8	CS_2 in He	1998	[142]
	0.5	< 10	< 10	< 70	-	$2 \cdot 10^{13}$ [50]	20-60	-	He		[133]
Lorentz-force	0.45	< 120	1	< 120	-	-	17-45	15	CS_2 in N_2	1986	[143]
	< 1	< 30	1-10	< 80	50	10^{14}	24-50	1	NO in He	2013	[50]
Piezo	< 1.8	< 750	< 14	RT	-	$2 \cdot 10^{15}$	100-10^4	19	CH_4	1982	[144]
	0.5	< 300	< 8	RT	19,34,34	-	-	-	He,Ne,Ar	1985	[145]
	< 1	$< 10^3$	< 30	-196-200	-	-	150-250	-	N_2	1988	[146]
	0.1-0.5	$> 10^3$	< 10	-50-177	-	-	< 20	-	-	1990	[136]
	0.1-0.3	$< 5 \cdot 10^3$	< 30	RT	55-83	10^{16}	7,16	-	NO in He,Ne	2009	[134]
	1	< 100	6	RT	4-11	-	20	-	DMF in He	2014	[147]
Electromag.	< 0.1-0.8	-	< 25	RT	26,22,41	-	-	-	H_2,He,Ne	1981	[148]
	0.8	< 35	-	RT	-	-	70	25	NO in He	1981	[149]
	0.12	> 10	< 300	< 200	-	-	50-75	20	benzene in Ar	1990	[150]
	-	< 100	< 10	< 220	-	-	20-100	-	indole	1994	[151]
	0.5	14	< 4	RT	5-18	-	-	15,18	N_2,CH_4	1995	[152]
	-	$< 10^3$	< 100	-263-230	170,70,30,20	-	20	-	He,Ne,Ar,Kr	2000	[137, 138]
	0.5	50	< 40	-265-27	167	-	32-46	-	He	2002	[153]
	0.1-1.0	< 250	< 86	4-105	-	$2 \cdot 10^{13}$ [50]	300	-	He		[133]

Table 4.1: Characteristics of different molecular beam valves categorised by their opening mechanism. While operation parameters such as the orifice, the repetition rate, the pressure and the temperature do not depend on the species, the resulting molecular beam characteristics are dependent on the gas composition and location of probing. Therefore, the beam characteristics listed here serve as a rough aid in assessing the valve performance, but the comparability between different valves is limited. The table includes the most common valve types but is by no means complete. RT = room temperature, DMF = 2,5-dimethylfuran, ACT = acetylene. The meaning of the symbols is: repetition frequency $f_{\text{rep.}}$, stagnation pressure p, reservoir temperature T, pulse duration Δt, rotational temperature T_{rot}.

According to Table 4.1, opening mechanisms have been optimised for faster opening and closing cycles, which results in reduced pulse durations and shorter travel distances of the sealing plunger. Ultimately, this raises the issue of how long a nozzle must remain open in order to reach full development of the supersonic expansion. Whenever information about the beam temperature and the flow velocity are to be inferred from molecular beams, it is essential that the continuous steady state region of the beam is probed [154]. Only then are the measured values comparable with the theoretical models developed in section 4.2. A molecular beam valve is operated in the choked flow regime if opened sufficiently wide such that the flow characteristics are no longer disturbed by the opening mechanism, but are solely limited by the orifice diameter [109, 155]. The realisation of choked flow operation is accompanied by a flat-top time of flight profile [141, 155]. Theoretical models for estimating the minimum opening time required to establish a continuous flow have been devised by K. Saenger and B. Fenn [156, 157]. As a simple guideline, the authors of reference [157] suggest a minimum opening time of $t_{\min} \geq 4d/a_0$ for a fully developed flow, where d denotes the opening diameter of the valve and a_0 is the speed of sound in the reservoir. For the noble gas series He, Ne, Ar, Kr and xenon, minimum opening times of at least 2, 4, 6, 9, 11 µs are required when assuming a nozzle diameter of 0.5 mm and a reservoir at $T_0 = 300$ K. This indicates that most of the molecular beam sources listed in Table 4.1 operate in the regime of stationary flow conditions, except for a few with very short opening time capabilities [158]. A more recent study by W. Christen [154] on the stationary flow conditions of high pressure He expansions from an Even-Lavie source suggests that significantly longer opening times are required than assumed previously. The opening and closing time of the valve plunger significantly contribute to the pulse duration and if chosen too short, the hindrance of the flow can be described by employing a reduced effective diameter [154, 158]. Likewise, irregularities in the plunger position at long opening times can result in similar effects [154].

Another parameter set of great importance to all valve types is the backing pressure of the reservoir p_0 and the opening diameter of the nozzle d. Hence, these parameters need careful consideration when designing and operating the valve. The mass flow rate is proportional to $p_0 \cdot d^2$ and has to be adjusted to the pumping capacity [129, 131]. The number of two-body collisions is proportional to $p_0 \cdot d$, which implies that cold beams and large terminal Mach numbers are obtained for large product values of $p_0 \cdot d$. The number of three-body collisions is proportional to $p_0^2 \cdot d$ and controls the extent of cluster formation, in which a collision with a third particle is needed to remove the condensation energy released upon the formation of a van der Waals complex [109, 123, 129, 131]. The formation of clusters also depends on the nozzle temperature and the shape of the nozzle

geometry. Confining nozzles result in larger densities in the early part of the expansion, which increases the likelihood of three-body collisions [131, 159].

4.1.2 Types of radical sources

As has been discussed in the previous section, modern day molecular beam researchers have a wide variety of excellent pulsed valves at hand. While the valve performance has been perfected over the years, these sources are limited to the expansion of stable gas species, either pure or in mixture. It is desirable to extend the chemical space of the molecular beam technique to radicals and meta-stable species. The high reactivities of free radicals make them major players in a wide range of chemical processes and they are important reaction agents in atmospheric, interstellar, combustion and biological environments. Laboratory studies characterizing the fundamental properties of free radicals demand for an efficient, reliable and controllable method for their generation [160]. Diatomic open shell radicals such as OH, NH or SH are suitable molecules for Stark deceleration and trapping experiments [35]. Bond dissociation in combination with molecular beams is not limited to the generation of diatomic radical species. It is also possible to generate atoms from diatomic precursors [161] as well as cationic or anionic fragments [162].

The molecular beam technique is particularly suitable for the generation of free radicals under well–defined conditions [163]. Due to their high chemical reactivity, radicals and meta stable species have to be generated at the vacuum interface of the molecular beam valve, as the collision free environment inside a vacuum chamber ensures their longevity. The formation of radicals is an endothermic process as bonds have to be cleaved. Therefore, energy is transferred into the gas during the early stages of expansion, which leads to local heating. The ongoing expansion ensures that the radicals are re–cooled to rotational temperatures below 10 K [160, 164]. Furthermore, molecular beams are directional and allow to deliver the produced radicals to a target zone with sufficient density for further investigations. Often, the precursor molecules are seeded in a carrier gas, which accelerates the re-thermalisation of the radicals after dissociation and acts as a suppressor for radical recombination [123, 160].

In molecular beams, the dissociation of precursors can be achieved by several different methods, such as photolysis [165], chemical reactions [166, 167] and electrical discharges [168–170]. More unconventional radical sources have also been devised, such as the laser ablation of graphite into molecular beams [171] or the installation of a flash pyrolysis chamber in front of the nozzle [172, 173], which is also referred to as "Chen nozzle". A comprehensive summary on the radical sources available for the molecular beam technique

has been compiled by P. C. Engelking [164]. Of all these methods, photolysis and electrical discharges are by far the most widely applied techniques, where the discharge method is the most cost–efficient, simplest and offers the widest scope of application.

A wide variety of different electric discharge sources has been developed. In the presence of a precursor gas pulse, HV is applied to an electrode structure resulting in the formation of a plasma, which is a suitable medium for the formation of atomic or molecular radicals, ionic species and metastable atoms. Depending on the electrode geometry and the type of applied voltage, the different electrical discharge sources can be categorised as pinhole discharges (also referred to as plate discharges) [161, 168–170, 174–179], corona discharges [180–182], hollow cathode discharges [183], RF discharges [184, 185] and dielectric barrier discharges [162, 178, 179]. While RF, Corona and hollow cathode discharges are mostly encountered in continuous sources, plate discharges and the dielectric barrier discharge method have been optimised to fit the outer end of nozzles in pulsed valves. A summary over different discharge types and typical molecular beam parameters of the dissociation products is given in Table 4.2. This thesis is solely concerned with the pinhole discharge and the dielectric barrier discharge types, which have been adapted to fit the Nijmegen pulsed valve.

A pinhole discharge consists of at least two electrode plates, which are electrically insulated from the valve chassis and form a part of the expansion channel. Alternatively, discharge geometries where a circular cathode is located a few mm in front of the valve have also been constructed [168, 174]. The duration and amplitude of the applied potential are of paramount importance, as they control the amount of energy imparted on the expanding gas cloud. According to Table 4.2, potential differences between -0.3 and -2 kV are employed for pinhole discharges. The circular ring cathodes located outside the valve nozzle require higher ignition voltages of up to -3.0 kV. Often, current limiting resistors are employed to prevent excessive heating of the molecular beam [175–177]. Some discharge sources apply a potential over a duration longer than the gas pulse. The discharge ignites when the pressure between the electrode plates rises and the breakdown voltage decreases to a sufficiently low value [168, 169, 176, 178, 179]. On the other hand, pulsing the discharge voltage with a narrow gate offers maximum control over the discharge duration and the location of the discharge within the expanding gas package [161, 170]. Shorter discharge durations allow for reduced heating and the mean speed of the pulse correlates with the discharge duration. In addition to this, short discharge pulses have been reported to reduce the translational and rotational temperature of the beam [170]. At low discharge voltages and short pulse durations of around 2 µs, a glowing tungsten filament has been employed by Lewandowski et al. [170] to reliably ignite the discharge.

Discharge type	Discharge geom.	species	precursor	$V_{\text{discharge}}$ (kV)	$\Delta t_{\text{disch.}}$ (µs)	T_{rot} (K)	density ($\cdot 10^{12}$ cm^{-3})	v_{beam} (m/s)	FWHM (%)	Ref.
Corona	W-wire	OH ($^2\Sigma^+$)	H_2O in He	15	∞	11	-	-	-	[180]
Corona	Pt-needle	OH	1% H_2O in Ar	2.4	∞	-	-	685	9.4	[182]
RF	RF-coil	OH	H_2O in He		∞	-	-	$>$ 3000	20 %	[185]
Hollow cath.	needle in res.	He*,Ne*,Ar*	He,Ne,Ar	-5	∞	-	-	-	-	[183]
Glow,ring	ring el.	ArOH	H_2O in Ar	3	$<$ 1	3-15	-	-	-	[174]
Glow, ring	ring el.	OH	H_2O in Ar	2.4	∞	$J = 3/2$	2.7	885	-	[168]
Glow, plate	slit	OH	H_2O in He	0.3	$>$ pulse	30	3.9	-	-	[175]
Glow, plate	slit	OH	H_2O in Ar	0.3-1	$>$ pulse	5-10	8	500	-	[176]
Glow, plate	concentric	OH	H_2O in Ar	$<$ 2.5	2500	$J = 3/2$	0.08	760	26.3%	[169]
Glow, plate	conical	OH	H_2O in Xe	1.4-1.9	1-200	28-195	1.6	265-470	16%	[170]
Glow, plate	concentric	F	F_2 in He	0.85	10 & 1	-	-	-	13.8	[177]
Glow, plate	conical	O	O_2 in He	0.7-1.2	10	-	-	-	20.8-27.8	[161]
Glow, plate	conical	OH	H_2O in Ar,Kr,Xe	0.9	$>$ pulse	$J = 3/2$	7.5,7.3,2.3	671,484,385	9.8,13.1,9.2	[178]
Glow, plate	conical	CH_3	CH_4 in Kr	0.6-1.7	$>$ pulse	$<$ 15	-	510-560	17-35	[179]
DBD	concentric	He*,NH_4^+,NH_2^-	NH_3 in He	6, 2 MHz	8 osc.	-	-	-	-	[162]
DBD	conical	OH	H_2O in Ar,Kr,Xe	4, 1 MHz	-	$J = 3/2$	2.5,2.3,0.8	646,490,397	11.2,17.2,12.6	[178]
DBD	parabolic	CH_3	CH_4 in Kr	1.5-2.2, 1 MHz	8-120 osc.	$<$ 15	-	550	28-30	[179]

Table 4.2: Different types of discharges employed for the generation of molecular and atomic radical species and the resulting molecular beam characteristics. An infinitely long discharge duration indicates a continuous source, where the discharge is left on over the entire duration of the expansion. Discharge durations longer than the gas pulse are attributed to pulsed sources. As the DBD requires pulsed voltage bursts, the 0-peak potential $V_{0-\text{pk}}$ is reported along with the oscillation frequency. The density scales with $\rho(r) \propto 1/r^2$ for circular nozzles and with $\rho(r) \propto 1/r$ for slit nozzles, where r denotes the distance between the nozzle opening and the location of the density measurement. For better comparability all densities have been scaled to $r = 1$ cm using the aforementioned scaling relations. $J = 3/2$ in the rotational temperature section indicates efficient cooling into the lowest rotational state of OH in the $X^2\Pi_{3/2}$ state. The meaning of the symbols is: discharge voltage $V_{\text{discharge}}$, discharge duration $\Delta t_{\text{disch.}}$, rotational temperature T_{rot}, beam velocity v_{beam}, full width at half maximum velocity spread FWHM.

Another ignition aid has been devised by Lu et al. [161], where a sharp ridge is placed on the cathode. Especially when using discharge sources in combination with a Stark decelerator, a sufficiently dense and cold molecular beam is a prerequisite. In addition, the spatial and velocity spread should be sufficiently small and the discharge location as well as the point in time of radical generation should be accurately known. The operation at high discharge potentials is usually undesirable due to arcing and the abrasion of electrodes caused by sputtering [186]. The physics of pinhole discharges is treated in section 4.6.1.

The dielectric barrier discharge (DBD) was introduced to pulsed beam valves by K. Luria, N. Lavie and U. Even in 2009 [162]. The dielectric barrier discharge is a particularly soft dissociation method which relies on the application of a $V_{0\text{-pk}} = 4$ kV pulse train in the low MHz regime onto an electrode structure with an interposed dielectric material. In a DBD, discharge filaments charge the dielectric insulator and the micro-filamentary discharge channels spread over the entire insulator. This ensures a uniform coverage of the discharge region with low energy electrons, thereby preventing arcing [162, 187, 188]. DBDs are well suited for the generation of metastable atoms, diatomic radicals and the generation of cationic and anionic fragments [162]. Due to the low energy requirement of this discharge process, translationally and rotationally cold radical beams are obtainable. Despite the preferential beam properties accessible by the DBD method, only few beam sources have been equipped with a DBD unit [162, 178, 179] due to the more complex electrode structure and the high frequency range the discharge electronics is required to operate in. This chapter describes the development of a DBD assembly as well as a pinhole discharge unit for the Nijmegen pulsed valve (NPV) [50] with the intention of comparing the resulting beam properties obtainable from each method. OH radicals were generated from H_2O with the objective of assessing the suitability of the two sources for Stark deceleration and trapping experiments.

4.2 Background on atomic and molecular beams

Fig. 4.1 depicts the basic components of an atomic/molecular beam apparatus. A gas beam originates from a reservoir which is kept at a backing pressure p_0 and temperature T_0. The gas is expanded through a nozzle with diameter d into a vacuum system with background pressure p_b, thereby forming a supersonic isentropic jet. Further downstream, the dense part of the jet is extracted and collimated using a skimmer, which improves the vacuum in the adjacent experiment chamber [109, 131]. Typical background pressures are indicated in Fig. 4.1. Molecular beams can either be expanded from a pure molecular gas source or the molecules can be seeded in an atomic carrier gas, e.g. Ar, Kr, Xe,

which allows to tune the resulting forward velocity of the beam. Sometimes even inert molecular carrier gases such as SF_6 are employed due to their large molecular mass. When low concentrations of molecular species are seeded in a monoatomic carrier gas, the resulting flow properties are dominated by the carrier gas to a large extent [109]. It is therefore convenient to start the development of the theory underlying the formation of seeded molecular beams by considering atomic species. The expansion of pure molecular species requires only slight adaptations.

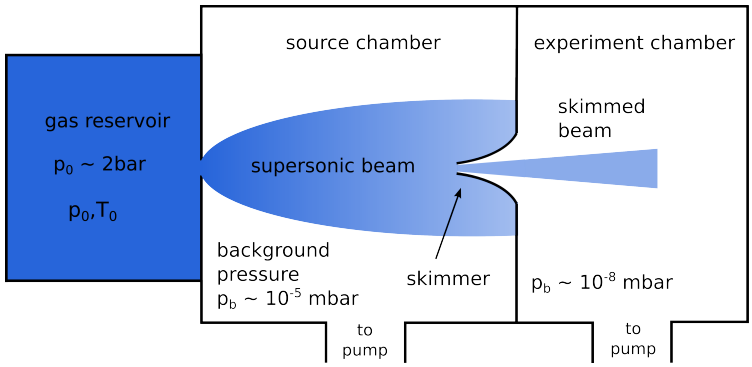

Figure 4.1: Scheme of a supersonic beam source. A typical atomic/molecular beam setup consists of a gas reservoir from which the gas is expanded into vacuum through a narrow channel [103, 189, 190].

4.2.1 Gas flow regimes

Depending on the stagnation conditions in the gas reservoir and the geometric shape of the expansion zone, different gas flow regimes can prevail. The regimes are described in terms of the dimensionless Knudsen number Kn, which is defined as the ratio between the mean free path inside the reservoir λ_0 and the opening diameter of the orifice d [109, 131, 191].

$$Kn = \frac{\lambda_0}{d} \approx \frac{Z_{\text{gas}}}{Z_{\text{wall}}} \,. \tag{4.1}$$

The Knudsen number may serve as an order of magnitude estimate for the ratio between the gas-gas particle collision rates and the gas-reservoir wall collision rates [109]. At low backing pressures, the mean free path inside the reservoir is large compared to the orifice diameter ($\lambda_0 \gg d$) and hardly any collisions between gas particles take place in the vicinity of the expansion duct (see Fig. 4.2 a)) [131, 191]. Consequently, this regime is denoted free molecular or effusive regime and is established for $Kn > 3$ [109, 131]. On the other hand, the mean free path inside the reservoir can become much lower than the orifice diameter ($\lambda_0 \ll d$) at high backing pressures p_0. Under these conditions, the expanding gas experiences many collisions (see Fig. 4.2 b)) and the corresponding gas flow regime is referred to as hydrodynamic, continuous or supersonic regime [32, 109, 191]. Typically,

the continuous regime prevails for Knudsen numbers $Kn < 10^{-3}$ and the gas flow behaves like a compressible fluid [32].

If we assume that the gas inside the reservoir behaves like an ideal gas in thermal equilibrium, the absolute velocity follows a Maxwell-Boltzmann distribution

$$f(v) = 4\pi \left(\frac{m}{2\pi k_\mathrm{B} T} \right)^{3/2} v^2 \, e^{-\frac{m\,v^2}{2\,k_\mathrm{B}\,T}} \, , \tag{4.2}$$

where the mean velocity $\overline{v}$ and the most probable velocity v_mp are given by [32, 109]

$$\overline{v} = \sqrt{\frac{8 k_\mathrm{B} T}{\pi m}} \text{ and } v_\mathrm{mp} = \sqrt{\frac{2 k_\mathrm{B} T}{m}} \, . \tag{4.3}$$

m denotes the mass of the gas, v is the absolute velocity and k_B refers to the Boltzmann constant. Before opening the valve, the gas has no net flow, which is equivalent to stating that the average velocity of the gas is zero [5].

At sufficiently large Knudsen numbers, the expansion of gas from a low-pressure reservoir leads to the formation of an effusive beam. Due to the lack of collisions near the orifice (see Fig. 4.2 a)), the temperature after the expansion is comparable to the temperature T_0 inside the reservoir and the beam samples the velocity distribution inside the cell [32, 131]. The velocity distribution of an effusive source is given by the superposition of a Maxwell distribution with the mean flow

$$f_\mathrm{beam}(v) = (v/\overline{v}) \cdot f(v) = \frac{1}{2} \, \frac{m^2}{(k_\mathrm{B} T_0)^2} \, v^3 \, \mathrm{e}^{-\frac{m\,v^2}{2\,k_\mathrm{B}\,T_0}} \, , \tag{4.4}$$

where v denotes the velocity, m is the mass of the gas and k_B is Boltzmann's constant [32, 131]. The mean forward velocity of the beam $\overline{v}_{\parallel,\mathrm{eff}}$ is obtained by

$$\overline{v}_{\parallel,\mathrm{eff}} = \int_0^\infty v \cdot f_\mathrm{beam}(v) \, \mathrm{d}v = \frac{3\pi}{8} \, \overline{v} \approx 1.2 \, \overline{v} \, , \tag{4.5}$$

as described in ref. [32]. According to Fig. 4.2 a), gas particles have to hit the aperture in order to leave the reservoir. Since faster particles display a larger collision frequency with the reservoir walls Z_wall, they have an increased probability of exiting the aperture and the velocity distribution is slightly shifted to higher velocities [191]. Effusive beams usually emanate from low-pressure gas sources and are mostly employed in the formation of metal atom beams or beams incorporating species that can be ablated at low pressures. Heating the source can help to increase the vapour pressure of the species to be expanded [32, 191].

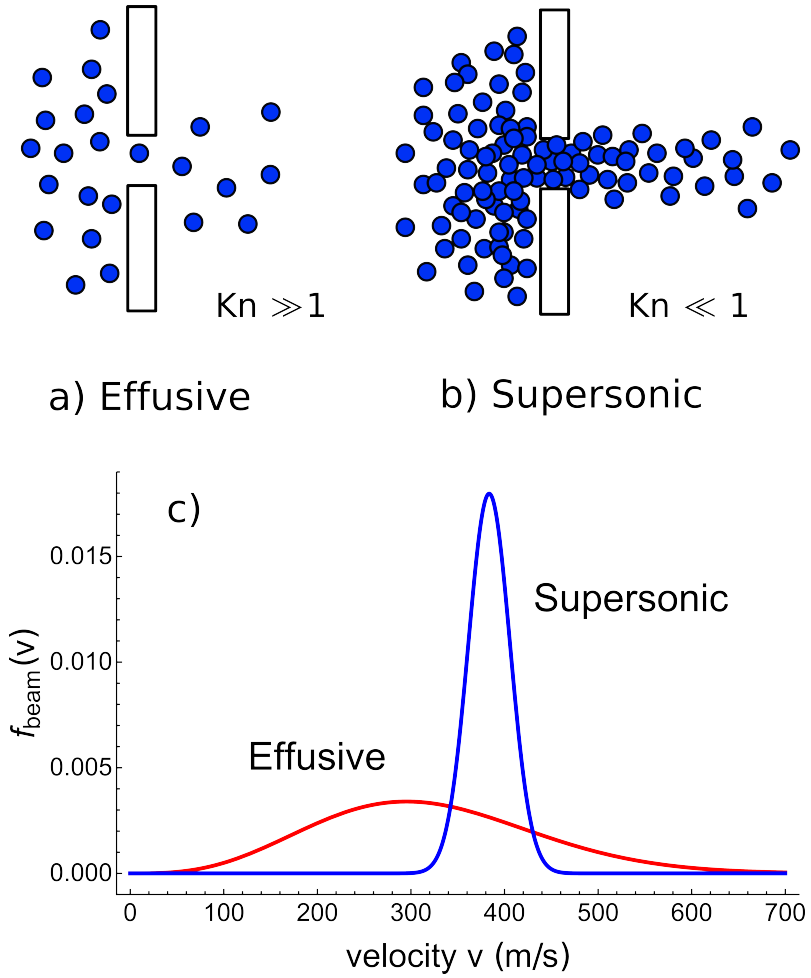

Figure 4.2: Illustration of the different gas flow regimes in **a)** effusive ($Kn \gg 1$) and **b)** supersonic beams ($Kn \ll 1$) [191]. **c)** Velocity distributions for an effusive (red) and a supersonic (blue) Kr beam. A reservoir temperature of $T_0 = 293$ K was assumed for the effusive beam, whereas a translational temperature of $T = 5$ K was assigned to the supersonic expansion and the average beam velocity is 381 m/s [32, 103].

In the limit of high stagnation pressures p_0 and small opening diameters, the Knudsen number is much smaller than unity and a supersonic beam is formed. Typically, $Kn < 10^{-3}$ applies [32] and the beam properties are governed by the flow characteristics of the gas. The resulting gas flows belong to the hydrodynamic regime and obey the laws of compressible fluid dynamics [109, 192]. Due to the high particle density, many collision events take place inside the expansion channel. As depicted in Fig. 4.2 b), collisions in proximity to the orifice occur predominantly along the forward direction and the gas particles are continuously pushed out of the reservoir [32, 191]. The collisions transfer random thermal motion from the reservoir into directed forward velocity. While the gas beam is accelerated to velocities beyond the speed of sound along the beam axis in the lab-fixed frame, the relative velocities of the gas particles in the moving frame are reduced during the free adiabatic and isentropic expansion. The small velocity spread in the moving

frame is synonymous with the low temperatures of the expanded species. Translational temperatures as low as a couple of Kelvin can routinely be achieved in supersonic beams. When molecular gases are expanded, not only the thermal energy associated with the motion of the gas is reduced (translational cooling), but also the internal degrees of freedom such as the rotational and to a lesser extent the vibrational levels are deexcited and the energy is converted into forward motion [32, 191]. The longitudinal velocity distribution of a supersonic beam is similar to a Maxwell-Boltzmann distribution [109, 131], except that the velocity u of the moving frame has to be taken into account.

$$f_{\mathrm{beam}}(v) = \sqrt{\frac{m}{2\pi\, k_{\mathrm{B}}\, T}}\, \mathbf{v}^2\, \mathrm{e}^{\frac{-m\,(\mathbf{v}^2-\mathbf{u}^2)}{2\,k_{\mathrm{B}}\,T}} \quad . \tag{4.6}$$

After having left the nozzle region, the gas continues to expand until the density is so low that collisions no longer take place and the terminal velocity and temperature are reached. This condition is referred to as "freezing" or "quitting" and occurs when the number of collisions in the beam drops to such low values that thermalisation of the gas no longer takes place [32]. A comparison between the different parallel velocity distributions resulting from effusive and supersonic expansions is given in Fig. 4.2 c), where equations 4.4 and 4.6 have been employed. Compared to effusive sources, supersonic molecular beams result in enhanced cooling of translational and internal degrees of freedom. The resulting supersonic jet displays a large forward velocity and the gas load imposed on the vacuum system is much larger than for effusive beams. Consequently, supersonic beam sources are often operated in pulsed mode to facilitate pumping of the chamber [32, 123]. Especially when using molecular beam sources in combination with deceleration techniques, the low beam temperatures, good state purity and the high density of the beam are appealing properties. Throughout the remainder of this chapter we will therefore be dealing with supersonic expansions exclusively. In the next section, the expansion process is described from a thermodynamic point of view.

4.2.2 Thermodynamics of supersonic beams

The aim of this chapter is to derive thermodynamic expressions for free jet flow variables such as pressure p, temperature T, velocity v and density ρ in terms of the Mach number prevailing at arbitrary positions within a supersonic expansion. There are several excellent sources on the topic and the approaches outlined in refs. [103, 109, 123, 131, 192] are followed. At high stagnation pressures, heat transfer processes to the channel walls can be neglected and the expansion is adiabatic. Furthermore, heat conduction effects due to viscosity are negligible at sufficiently high Reynolds numbers and in the absence of shock waves the flow is isentropic. Taking into account the above assumptions on the

flow conditions, the total energy of the gas has to be conserved according to the first law of thermodynamics. The total energy of a gas consists of the internal energy U, the potential energy associated with the state of the gas ($p \cdot V$) and the kinetic energy $1/2\, m\, u^2$, where m denotes the mass of the molecule. Conservation of energy before and after the expansion results in the following expression, where the subscript zero refers to conditions in the gas reservoir [5, 193].

$$U_0 + p_0\, V_0 + 1/2\, m\, u_0^2 = U + p\, V + 1/2\, m\, u^2\,. \tag{4.7}$$

Inside the reservoir, the average velocity of the gas is zero, hence $u_0 = 0$. As the flow is driven by a pressure gradient and expands, it is convenient to reformulate expression 4.7 in terms of the specific enthalpy $h = \frac{1}{m} \cdot (U + pV)$ [5], thereby accounting for the expansion work. Equation 4.7 is then cast into the following form:

$$h_0 = h + \frac{1}{2}\, u^2\,. \tag{4.8}$$

The difference in specific enthalpy before and after the expansion is equivalent to the kinetic energy associated with the mass flow of the expanded gas. Therefore, energy stored within the reservoir in the form of internal and potential energy is converted into forward motion. Complete energy conversion results if $h \to 0$, which is a reasonable assumption, as the internal energy U is significantly reduced during the expansion and the pressure in the vacuum chamber is small ($p \approx 0$). The specific heat capacity at constant pressure $c_p(T)$ relates the specific enthalpy h to the temperature T via $\mathrm{d}h = c_p(T)\,\mathrm{d}T$. For an ideal gas, c_p can be approximated by

$$c_p = \frac{\gamma}{\gamma - 1}\frac{k_\mathrm{B}}{m} \text{ and } \gamma = \frac{c_p}{c_v}\,, \tag{4.9}$$

where γ is the ratio between the specific heat capacities at constant pressure and volume. For an ideal monoatomic gas, $\gamma = 5/3$ [5]. Replacing the change in specific enthalpy by an expression taking into account the specific heat capacity and the temperature results in

$$1/2\, u^2 = h_0 - h = \int_T^{T_0} c_p(T)\,\mathrm{d}T\,. \tag{4.10}$$

For a monoatomic gas, the assumption of a constant heat capacity is justified and Eqn. 4.10 can be rearranged for the beam velocity u, where c_p has been replaced by the expression in Eqn. 4.9 [5].

$$u = \sqrt{2c_p(T_0 - T)} = \sqrt{\frac{2k_\mathrm{B}}{m}\frac{\gamma}{\gamma - 1}(T_0 - T)}\,. \tag{4.11}$$

The terminal flow velocity u_∞ arises upon complete energy transfer, which implies that the final temperature T of the beam approaches zero and the entire specific reservoir enthalpy h_0 is converted into forward flow.

$$u_\infty = \sqrt{2c_pT_0} = \sqrt{\frac{2k_\mathrm{B}}{m}\frac{\gamma}{\gamma-1}T_0}\,. \tag{4.12}$$

The terminal velocities for various noble gases with $\gamma = 5/3$ and a reservoir temperature of $T_0 = 293$ K are depicted in Fig. 4.3. Eqn. 4.12 implies that the forward velocity of

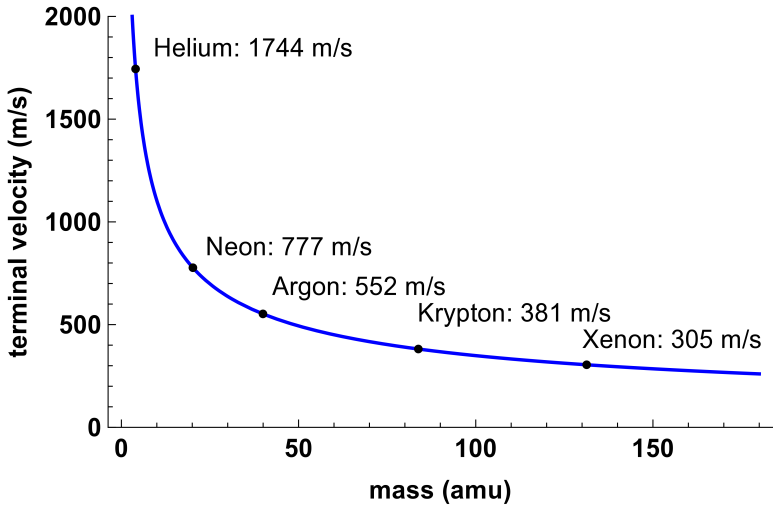

Figure 4.3: Terminal velocities of noble gas atomic beams according to Eqn. 4.12. A reservoir temperature of $T_0 = 293$ K was assumed [103].

the molecular beam can be controlled either by changing the reservoir temperature or by choosing a carrier gas with a different molecule mass m. This property of molecular beams is exploited in experiments which are sensitive towards the velocity of the molecular beam such as Stark or Zeeman deceleration [35]. Cooling of the reservoir has the disadvantage that species with a low vapour pressure might not enter the gas phase with sufficient abundance. It is important to notice that in Eqn. 4.12, $\gamma = 5/3$ is a valid approximation only as long as the backing pressure is not too high. For beam expansions with high backing pressures (the Even-Lavie valve supports up to $p_0 = 100$ bar) it becomes necessary to take into account the pressure and temperature dependence of the heat capacity ratio, as $\gamma(T_0, p_0)$ starts varying considerably close to the critical point. $\gamma(T_0, p_0)$ increases at higher pressures and the terminal velocity for Xe is reduced by as much as 30% when increasing the pressure from 0 to 70 bar at 300 K [194].

In gas dynamics it is customary to express the beam velocity u in terms of the Mach number M. This number is the ratio between the beam velocity and local speed of sound

a, which is defined as

$$a = \sqrt{\frac{\gamma k_{\mathrm{B}} T}{m}} \text{ and } M = \frac{u}{a}\,. \tag{4.13}$$

Rearranging Eqn. 4.11 into the following form

$$u = \sqrt{\frac{\gamma k_{\mathrm{B}} T}{m}} \sqrt{\frac{2}{\gamma - 1}\left(\frac{T_0}{T} - 1\right)} \tag{4.14}$$

and replacing the first square root term by a, the speed of sound at temperature T, allows to deduce the following expression for the Mach number

$$\frac{u}{a} = M = \sqrt{\frac{2}{\gamma - 1}\left(\frac{T_0}{T} - 1\right)}\,. \tag{4.15}$$

Rearranging for the temperature ratio T/T_0 yields a valuable expression which relates the temperature T at the centreline of the expanded beam to the reservoir temperature T_0 via the Mach number

$$\frac{T}{T_0} = \left(\frac{\gamma - 1}{2} M^2 + 1\right)^{-1}\,. \tag{4.16}$$

Retaining to the assumption of a calorically perfect gas, which is expanded under adiabatic isentropic conditions, the following standard thermodynamic relations can be used to relate the source conditions (p_0, T_0, ρ_0) to conditions after the expansion (p, T, ρ) [131].

$$\frac{T}{T_0} = \left(\frac{p}{p_0}\right)^{\frac{\gamma-1}{\gamma}} \text{ and } \frac{\rho}{\rho_0} = \left(\frac{p}{p_0}\right)^{\frac{1}{\gamma}} \text{ and } \frac{\rho}{\rho_0} = \left(\frac{T}{T_0}\right)^{\frac{1}{\gamma-1}}\,. \tag{4.17}$$

In combination with Eqn. 4.16, the above relations result in the following expressions:

$$\left(\frac{p}{p_0}\right) = \left(\frac{T}{T_0}\right)^{\frac{\gamma}{\gamma-1}} = \left(1 + \frac{\gamma - 1}{2} M^2\right)^{\frac{-\gamma}{\gamma-1}} \tag{4.18}$$

and

$$\left(\frac{\rho}{\rho_0}\right) = \left(\frac{n}{n_0}\right) = \left(\frac{T}{T_0}\right)^{\frac{1}{\gamma-1}} = \left(1 + \frac{\gamma - 1}{2} M^2\right)^{\frac{-1}{\gamma-1}}\,. \tag{4.19}$$

Equations 4.18 and 4.19 are of great importance for the gas dynamics of molecular beams and the centreline properties of a free jet are plotted in Fig. 4.4. A striking feature of Fig. 4.4 is that the mean velocity increases quickly and the terminal velocity u_∞ is reached very early in the expansion. Already at a distance of 5 nozzle diameters, the centre-line velocity reaches 98% of u_∞. The velocity ratios plotted in black and red asymptotically approach unity for u/u_∞ and $\sqrt{3}$ for $u_\infty/a(T_0)$ [109]. The temperature

decreases continuously with increasing distance from the orifice until the quitting surface is reached and the number of collisions is insufficient to maintain a continuum flow and thermalisation of the motional degrees of freedom within the beam ceases. The point at which the transition to the free molecular flow occurs marks the breakdown of the treatment based on continuum mechanics [192] and the Mach number is no longer well defined. A kinetic theory for the prediction of the freezing region onset can be found in ref. [123].

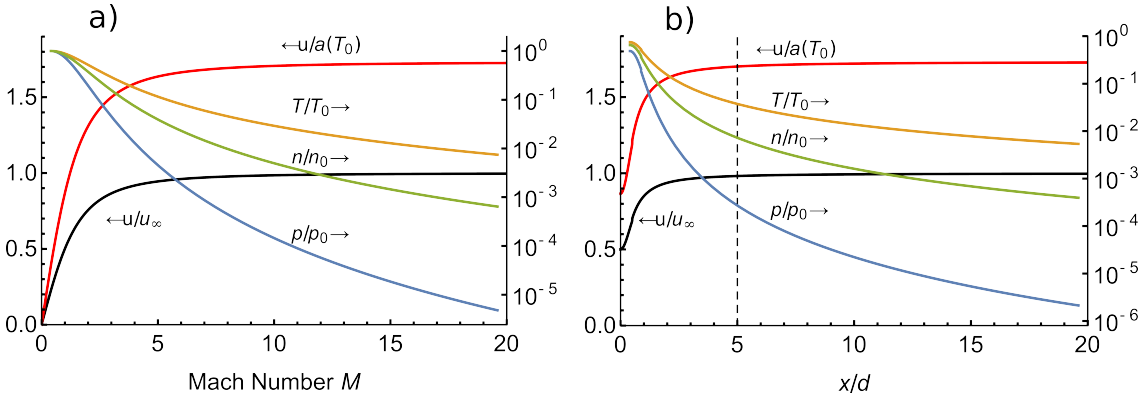

Figure 4.4: **a)** Centreline properties of a free jet as a function of the local Mach number M [192]. **b)** Centreline properties of a free jet as a function of distance from the orifice expressed in fractions of nozzle diameters. For this plot an analytic form for the flow field based on the method of characteristics (MOC) has been employed according to Eqns. 4.21, 4.22 and the first row of Tab. 4.3 [192, 195]. In both plots, the arrows indicate the corresponding vertical axis. Equations 4.18 and 4.19 have been evaluated for $\gamma = 5/3$, which applies to ideal monoatomic gases.

As a last step we now seek to obtain an expression for the centreline velocity, which only depends on the Mach number and the temperature of the reservoir, but not on the local temperature of the expanded beam. The beam velocity is obtained by $u = M \cdot \sqrt{\frac{\gamma k_\mathrm{B} T}{m}}$ and making use of Eqn. 4.16 to substitute T results in [192]

$$u = M \sqrt{\frac{\gamma k_\mathrm{B} T_0}{m} \left(1 + \frac{\gamma - 1}{2} M^2\right)^{-1}} . \tag{4.20}$$

In this chapter all flow properties under expanded conditions have been linked to the stagnation conditions via expressions involving the local Mach number. In order to express the variation of flow properties as a function of the distance from the nozzle orifice, the dependence of the Mach number on the position along the expansion coordinate has to be known. Based on the method of characteristics (MOC) [109, 123, 192], Ashkenas and Sherman have developed an accurate model, which relates the Mach number M to a position in the flow field [192, 196]. A more refined model, which offers better reliability

at short distances from the nozzle, has been worked out by Murphy and Miller [192, 195]. According to their model, the variation of M is given by the following expression:

$$M = \left(\frac{x}{d}\right)^{(\gamma-1)/j} \left[C_1 + \frac{C_2}{\left(\frac{x}{d}\right)} + \frac{C_3}{\left(\frac{x}{d}\right)^2} + \frac{C_4}{\left(\frac{x}{d}\right)^3}\right] \text{ for } x/d > 0.5 \tag{4.21}$$

$$M = 1.0 + A\left(\frac{x}{d}\right)^2 + B\left(\frac{x}{d}\right)^3 \text{ for } 0 < x/d < 1.0 \tag{4.22}$$

In the above expression, A, B,C_{1-4} are fitting parameters and $j = 1, 2$ stands for three-dimensional axisymmetric and two-dimensional planar flow fields. The three dimensional axisymmetric flow-field arises when expanding gas from a circular nozzle. In the far field, the streamlines appear to emanate from a point source. A two dimensional flow-field results when expanding gas from a slit nozzle [123, 192]. The fitting parameters are given in table 4.3. While this model does not require any information on the source, the

Source	j	γ	C_1	C_2	C_3	C_4	A	B
3D	1	5/3	3.232	-0.7563	0.3937	-0.0729	3.337	-1.541
3D	1	7/5	3.606	-1.742	0.9226	-0.2069	3.190	-1.610
3D	1	9/7	3.971	-2.327	1.326	-0.311	3.609	-1.950
2D	2	5/3	3.038	-1.629	0.9587	-0.2229	2.339	-1.194
2D	2	7/5	3.185	-2.195	1.391	-0.3436	2.261	-1.224
2D	2	9/7	3.252	-2.437	1.616	-0.4068	2.219	-1.231

Table 4.3: Fitting parameters for the centreline Mach number model by Murphy and Miller [192, 195]. The parameters are to be used with Eqns. 4.21, 4.22 and cover axisymmetric 3D and planar 2D flow profiles.

background conditions or the molecular weight, it is based on the MOC method and as such assumes the sonic ($M = 1$) surface to be located at the exit of the nozzle. It has been shown that the geometry of the exit channel can affect the location of the sonic surface significantly [159, 192]. The fitting model is also prone to break down in the case of nonisentropic effects such as relaxation of internal energy, cluster formation or chemical reactions [192].

4.2.3 Flow profile and structure of a supersonic beam

While the thermodynamic treatment of a supersonic molecular beam allows to deduce parameters along the centreline of the expansion, the two-dimensional axisymmetric nature of jets expanded from circular orifices is not accounted for. The discussion in this chapter is based on references [109, 123, 131, 192]. Fig. 4.5 displays the flow structure emanating from a converging nozzle, where the reservoir is constantly kept at a pressure

p_0 and temperature T_0. Upon opening the orifice, the pressure difference between the reservoir and the background ($p_0 - p_b$) establishes an accelerating mass flow. Assuming an incompressible gas flow, the continuity condition demands for an increase in forward velocity due to the decreasing flow cross section inside the converging nozzle. It can be perceived from Eqn. 4.18 that the flow reaches the local speed of sound ($M = 1$) at the nozzle exit if the following condition is satisfied [109, 123, 192]:

$$\frac{p_0}{p_b} \geq \left(\frac{\gamma+1}{2}\right)^{\left(\frac{\gamma}{\gamma-1}\right)} = G_c\,, \tag{4.23}$$

where p_0/p_b denotes the ratio between the stagnation and the background pressure. For a monoatomic gas, G_c adopts a value of approximately 2.1. As soon as the sonic surface is established at the orifice exit, the flow rate reaches its maximum value and stagnates, which is also referred to as a choked condition [109]. For non-diverging nozzles, the location of the sonic surface depends on the nozzle geometry. Murphy and Miller [159] reported that for a sharp-edged orifice the sonic surface is convex and the transition to a supersonic flow occurs outside of the nozzle. On the other hand, the sonic surface inside a long capillary is concave and the transition to the supersonic regime occurs within the duct. In case the p_0/p_b ratio is smaller than the critical value G_c, the beam leaves the nozzle with $M < 1$ and the pressure at the orifice exit is roughly p_b. Otherwise, upon increasing the p_0/p_b pressure ratio beyond G_c, the exit pressure p_e is rendered independent on the background pressure p_b and reaches $p_e = p_0/G_c$, while $M = 1$ still applies at the nozzle exit. The flow is termed "underexpanded", as the background pressure p_b is lower than the pressure at the nozzle exit p_e [192].

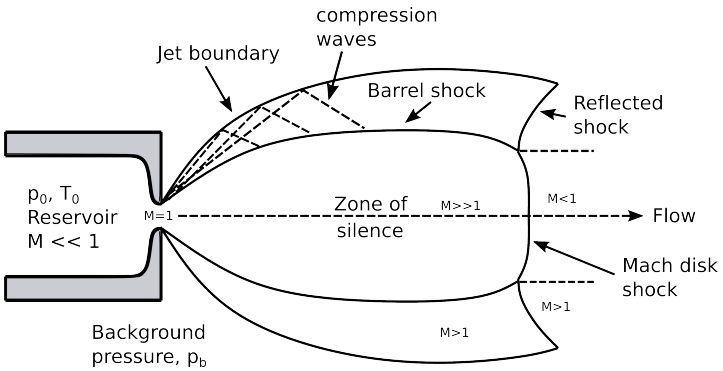

Figure 4.5: Flow profile of a two-dimensional, axisymmetric and strongly under-expanded jet displaying main features such as the jet boundary, the barrel shock, the Mach disk and the zone of silence. All structures shown have revolution symmetry [109, 192].

After having left the nozzle, the beam continues to expand and the Mach number increases beyond unity. At the same time the beam spreads radially and the jet cross section

increases. Along the radial direction, the density decrease is proportional to $1/r^2$, where r denotes the longitudinal distance from the orifice [123, 131]. During the advancing expansion, the pressure inside the flow plume decreases below p_b and an "overexpanded" region emerges. Eventually, the gas is driven back towards the axis of the flow due to radial pressure differences. Consequently, the jet boundary does not have a cylindrical shape, but is bulgy along the edge. As the beam is travelling faster than the local speed of sound, the bulk moves faster than the propagation of downstream information and the expanding beam does not encounter boundary conditions such as the chamber wall and pressure gradients. The central part of flow is therefore also referred to as "zone of silence". However, it is imperative that the boundary conditions are met and shock waves start emerging. A shock wave is a thin nonisentropic region with large density, temperature, velocity and pressure gradients [192]. Shock waves can either alter the flow direction or lower the velocity to subsonic values in order to meet boundary conditions. As soon as the gas exits the nozzle, the flow has to adapt to the background conditions, which results in the formation of expansion fans at the nozzle rim. Reflections of the expansion waves from the jet boundary give rise to compression waves, see Fig. 4.5. If the background pressure p_b is sufficiently low, the compression waves form an envelope structure, which is referred to as barrel shock. The barrel shock at the sides and the Mach disk shock normal to the centreline of the flow limit the expansion of the jet and lead to recompression of the flow. The region between the barrel shock and the jet boundary consists of a non-isentropic region [109, 192]. Experimentally, the formation point of the Mach disk shock is of great importance, as interactions with the molecular beam usually happen in the downstream region. The location of the Mach disk is quite insensitive to γ and can be approximated by

$$\left(\frac{x}{d}\right) = 0.67 \cdot \sqrt{\frac{p_0}{p_\mathrm{b}}}\,, \tag{4.24}$$

where the distance is given in multiples of the nozzle diameter [131, 192, 196]. The width of the Mach disk usually amounts to several mean free paths at p_b [109]. Depending on the p_0/p_b ratio two different scenarios can arise. If p_0/p_b is low, then the Mach disk is located not too far from the nozzle. The upstream flow is continuous and is abruptly stopped at the Mach disk location. Once the jet molecules arrive at the Mach disk their velocities are randomised by collisions and the entropy increases [131]. Hence, the jet is terminated before the transition to the free molecular regime has occurred. In the past, the pumping capacity was limited and this operation regime was encountered frequently. In a supersonic beam experiment one seeks to probe the gas within the zone of silence and skimmers can be installed to extract a part of the supersonic beam's isentropic core [192]. On the other hand, if p_b is sufficiently low, the Mach disk is located very far out in the expansion. In this case, the Mach disk as well as the barrel shock are broadened to such an extent

that they become diffuse shocks [109]. If p_b is lowered even more, the shock structures disappear completely. The only disturbance to the gradually forming free molecular flow are collisions between jet molecules and molecules from the chamber background. An even more significant source of interference is caused by collisions between the jet and reflected jet molecules from the skimmer or the chamber walls [109, 192]. Typically, skimmers are still used to extract molecular beams in the free molecular regime, although the range of use has shifted from selecting the isentropic core to differential pumping as discussed in section 4.2.5.

While the discussion given above applies to a converging nozzle, the far-field flow profile depicted in Fig. 4.5 is also developed in the case of a converging-diverging nozzle profile at sufficiently low background pressures [109]. In a converging nozzle, the flow cross section decreases towards the orifice, whereas for a diverging nozzle the flow duct widens towards the vacuum interface, see Fig. 4.6 a) and b). For such profiles, the $M = 1$ sonic surface is formed at the narrowest point of the gas duct if the pressure condition in Eqn. 4.23 is satisfied and no longer forms at the nozzle exit. The diverging section accelerates the gas to $M > 1$ already within the nozzle. If the background pressure p_b is low, there can be shocks within the diverging section of the nozzle and the exit pressure is adapted to the background pressure $p_b = p_e$. Diverging nozzles promote the formation of subsonic boundary layers close to the nozzle walls due to the viscosity of the gas. This can lead to jet detachment within the diverging nozzle [109]. The confinement of the exiting beam by the channel walls enhances the formation of clusters as the gas density is kept high within the nozzle and three-body collisions are more frequent [131].

Generally, the flow profile and the beam properties strongly depend on the shape of the nozzle. A lot of nozzle shape optimisation studies have been conducted in the context of cluster formation enhancement [197–199]. Other nozzles have been tailored to deliver molecular beams suitable for special applications such as laser targets [200] or for microwave spectroscopy [201], with the latter application involving 3D-printing of nozzles for faster prototyping. A comparison of different conical nozzle shapes with respect to maximising the downstream on-axis beam density and reducing the radial divergence has been conducted by U. Even and co-workers [138, 202, 203]. The density of a pinhole (sonic) nozzle drops rapidly with increasing distance, which is caused by the lacking confinement of the nozzle walls. Due to ease of manufacturing, a conical nozzle with an opening angle between 40-50° it the best compromise for optimising the density while still ensuring adequate cooling of the molecular beam [202]. This finding represents an important guideline for the design of valve nozzles. Compared to a sonic (see Fig. 4.6 c)) nozzle, the downstream density achievable with conical nozzles (see Fig. 4.6 b)) is almost

an order of magnitude larger [202]. If a more accurate model for a given nozzle geometry is required, the gas flow from a nozzle can be simulated using the direct simulation Monte Carlo (DSMC) code by G. A. Bird [204, 205].

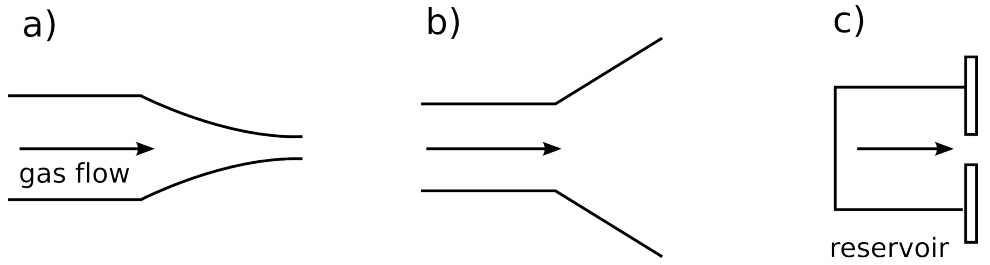

Figure 4.6: Different nozzle geometries. The direction of gas flow is indicated by an arrow. **a)** In a converging nozzle the flow cross section bounded by the walls decreases towards the opening. **b)** Cross sectional view of a diverging conical nozzle. The flow cross section increases towards the orifice. **c)** A pinhole source consists of a reservoir with a circular bore hole through which the gas emanates into the vacuum.

4.2.4 Velocity distribution in supersonic molecular beams

In close proximity to the valve exit the continuous regime prevails and there are enough collisions to equilibrate the transverse and longitudinal velocity distributions. Consequently, the parallel and perpendicular temperatures are characterised by a single value $T = T_{\parallel} = T_{\perp}$. The velocity distribution is centred around the mean beam velocity $u =< v_{\parallel} >$ in the longitudinal direction [109].

$$f(v_{\parallel}, v_{\perp})\,\mathrm{d}v_{\parallel}\,\mathrm{d}^2v_{\perp} = n \cdot \left(\frac{m}{2\pi k_{\mathrm{B}}T}\right)^{1/2} \left(\frac{m}{2\pi k_{\mathrm{B}}T}\right) e^{-\frac{m}{2k_{\mathrm{B}}T}(v_{\parallel}-u)^2}\, e^{-\frac{m}{2k_{\mathrm{B}}T}v_{\perp}^2}\,\mathrm{d}v_{\parallel}\,\mathrm{d}^2v_{\perp}. \quad (4.25)$$

m denotes the molecular mass, $v_{\parallel}$ designates the velocity parallel to the beam axis, u is the mean velocity of the mass flow and $v_{\perp}$ represents the vertical velocity component at right angles to the molecular beam axis. The number density of the beam is expressed by n. As the expansion proceeds, the velocity spread of the molecular beam is reduced. The collision frequency decreases during the expansion and the cooling becomes less efficient further downstream. The parallel and orthogonal velocity distributions drop out of equilibrium and need to be considered separately [109]. While the longitudinal velocity distribution is frozen, the radial velocity distribution continues to decrease further, which is due to geometrical cooling. In a collision-free environment, atoms with large radial velocities leave the jet axis after a short flight time, whereas atoms with small radial velocities tend to stay close to the axis even at large distances from the nozzle [109]. The combined velocity distribution under non-equilibrium conditions for the longitudinal and

radial distributions is given by an "ellipsoidical Maxwell distribution" [109, 123].

$$f(v_\parallel, v_\perp)\,\mathrm{d}v_\parallel\,\mathrm{d}^2v_\perp = n\cdot\left(\frac{m}{2\pi k_\mathrm{B}T_\parallel}\right)^{1/2}\left(\frac{m}{2\pi k_\mathrm{B}T_\perp}\right)e^{-\frac{m}{2k_\mathrm{B}T_\parallel}(v_\parallel-u)^2}\,e^{-\frac{m}{2k_\mathrm{B}T_\perp}v_\perp^2}\,\mathrm{d}v_\parallel\,\mathrm{d}^2v_\perp. \tag{4.26}$$

$T_\parallel$ and $T_\perp$ denote the longitudinal and radial temperatures, which characterise the spread of the distribution. It is therefore possible to express the parallel and perpendicular velocity spreads as

$$\sigma_{v,\parallel} = \frac{1}{\sqrt{2}}\cdot\sqrt{\frac{2k_\mathrm{B}T_\parallel}{m}} = \frac{v_{\mathrm{mp},\parallel}}{\sqrt{2}} \text{ and } \sigma_{v,\perp} = \frac{1}{\sqrt{2}}\cdot\sqrt{\frac{2k_\mathrm{B}T_\perp}{m}} = \frac{v_{\mathrm{mp},\perp}}{\sqrt{2}}\,. \tag{4.27}$$

Here, $v_{\mathrm{mp},\parallel}$ and $v_{\mathrm{mp},\perp}$ denote the parallel and perpendicular velocities, which can be attributed to the kinetic energy at a given temperature $T_\parallel$ and $T_\perp$. In addition to this, $v_{\mathrm{mp},\parallel}$ and $v_{\mathrm{mp},\perp}$ are the most probable velocities of the Maxwell-Boltzmann distribution in Eqn. 4.2.

Generally, the velocity distribution depends on the position at which the molecular beam is probed and with that on the velocity and flight time of the beam up to the probe location. Most experimental determinations of the velocity distribution scan the longitudinal density variation of the molecular beam at different time delays. The determination of the transverse profile is more challenging, as it often involves two-dimensional imaging [206]. An alternative way of probing the radial density distribution in the molecular beam would be to use the pinhole-setup depicted in Fig. 4.14 and determine the density at different horizontal positions along the laser beam without changing the height of the valve orifice relative to the laser beam. For the remainder of this section we solely focus on the longitudinal velocity distribution given by

$$f(v_\parallel)\,\mathrm{d}v_\parallel = n\cdot\left(\frac{m}{2\pi k_\mathrm{B}T_\parallel}\right)^{1/2} v_\parallel^2\,e^{-\frac{m}{2k_\mathrm{B}T_\parallel}(v_\parallel-u)^2}\,\mathrm{d}v_\parallel\,. \tag{4.28}$$

Equation 4.28 can be reformulated such that a time of flight (TOF) distribution is obtained [207]. The arrival time of an individual particle at the detection site is given by $v_\parallel = L/t$, where L is the distance between the source and the detection region and t denotes the required flight time. At $t = t_0$ the flow's mass average passes through the detection region. Substituting $v_\parallel$ by L/t in Eqn. 4.28 and making use of $\mathrm{d}v_\parallel = -L/t^2\mathrm{d}t$ results in

$$f_\mathrm{TOF}(t)\,\mathrm{d}t = f(v_\parallel)\,\mathrm{d}v_\parallel = n\cdot\left(\frac{m}{2\pi k_\mathrm{B}T_\parallel}\right)^{1/2}\frac{L^3}{t^4}\,e^{-\frac{m}{2k_\mathrm{B}T_\parallel}(\frac{L}{t}-\frac{L}{t_0})^2}\,\mathrm{d}t\,, \tag{4.29}$$

where the minus sign has been omitted. Similar expressions have been obtained in [103, 208, 209].

In gas beam dynamics it is common practice to state the width of the velocity distribution in terms of the full width at half maximum (FWHM), which is linked to the velocity spread $\sigma_{v,\parallel}$ by the following relation:

$$\mathrm{FWHM}_v = 2 \cdot \sqrt{2 \cdot \ln(2)} \cdot \sigma_{v,\parallel} \; . \tag{4.30}$$

Like $\sigma_{v,\parallel}$, the FWHM_v parameter can be related to the local temperature in the expansion. In the free molecular regime, the velocity spread is best characterised by the speed ratio S, which is defined as the ratio between the flow velocity u and the most probable velocity of thermal motion $v_{\mathrm{mp},\parallel}$. By making use of equations 4.13, 4.27 and 4.30 the speed ratio can be calculated from several quantities [109, 123].

$$S = \frac{u}{v_{\mathrm{mp},\parallel}} = \frac{u}{\sqrt{2} \cdot \sigma_{v,\parallel}} = \frac{u}{\sqrt{\frac{2k_\mathrm{B}T_\parallel}{m}}} = \frac{u \cdot 2 \cdot \sqrt{ln(2)}}{\mathrm{FWHM}_v} = M \left(\frac{\gamma}{2}\right)^{1/2} \; . \tag{4.31}$$

Alternatively, the speed ratio can also be considered as the energy resolution of the molecular beam. High speed ratios relate to fast beams with a narrow velocity distribution, which implies that the velocity profile in the moving frame is particularly narrow and hence a good energy resolution has been achieved. The energy resolution of molecular beams is a critical quantity in crossed molecular beams [210].

4.2.5 Skimmer

Following the formation of a molecular beam it can either directly be employed in the source chamber or alternatively be passed on to different sections of the experimental setup. In the latter case it is often desirable to insert a skimmer into the beam path with the objective of collimating the beam and selecting the dense and cold part for subsequent experiments. In addition to this, placing a skimmer between the source chamber and the adjacent vacuum chamber leads to a significant reduction in the gas load as the remaining part of the molecular beam is rejected. Especially crossed molecular beam setups will benefit from the lower background pressure in the collision chamber. A schematic drawing of a supersonic beam source incorporating a skimmer is depicted in Fig. 4.1. Usually, the valve-skimmer distance can be adjusted according to experimental needs, but the distance should be chosen such that there is no equilibration between the molecular beam and the background gas. Two different operation regimes can be distinguished in which the skimmer is employed differently and has to meet different demands. [109, 129, 131]

The first case is by far the less common operation type in which the molecular beam source is operated at high background pressures ($p_b = 10^{-2} - 1$ mbar). Under these conditions, which are also referred to as an expansion of the Campargue type [129], the expanding gas remains in the continuous regime at all times and a pronounced Mach shock disc is formed, the location of which can be calculated using Eqn. 4.24. At sufficiently large backing pressures the surrounding shock layers protect the overexpanding zone of silence from collisions with the background gas [129]. However, the large shock system poses a problem when one seeks to extract molecules from the zone of silence. In this case, the purpose of the skimmer is to puncture the Mach shock disc (see Fig. 4.5) and to select molecules from the zone of silence with minimal beam deterioration. As the Mach shock disc is formed early in the expansion, the distance between the valve and the skimmer has to be kept relatively short. This beam extraction method requires careful optimisation of the skimmer shape in order to prevent the formation of shock waves at the skimmer entrance and the interior of the skimmer, which would impede the throughput of the supersonic flow. The skimmer geometry is chosen such that the normal shock of the Mach disc is transformed into an oblique shock wave and remains attached to the outer surface of the skimmer cone. In reference [129], several conical skimmer geometries for operating the valve close to the skimmer at high background pressures were tested. While the extracted beam intensity is high for this method, the degree of collimation is inferior to skimming at low background pressures and the beam throughput deteriorates quickly if the skimmer shape is not adapted to the operation conditions [109].

Due to the above mentioned difficulties and the availability of turbo-molecular pumps, most modern molecular beam apparatus now operate at low background pressures ($p_b < 10^{-6}$ mbar). This operation regime also applies to the molecular beam experiments described in this thesis. As discussed in section 4.2.3, the spatial dimensions of the zone of silence increase at low background pressures and the Mach and barrel shocks turn into diffuse shocks. Upon lowering the background pressure even further, the molecular beam passes through the freezing surface and a transition to the free molecular regime occurs [109]. Under these conditions, the skimmer is located downstream of the quitting surface and the valve-skimmer distance is much larger compared to the high background pressure regime and can reach several hundred nozzle diameters ($x/d > 100$) [123]. Operating a skimmer at low background pressures results in better collimation, larger speed ratios and better cooling of the transmitted beam [109]. On the other hand, the intensity of the skimmed beam is reduced due to the large distance between the valve and the skimmer [109].

Imposing the surfaces of a skimmer into a dense molecular beam can lead to the formation of shock waves caused by particles reflected from the outer and inner walls of the skimmer. These shock waves are non-isentropic layers with appreciable density and temperature gradients and their thickness is on the order of several mean free paths. The interaction with shock waves leads to heating of the molecular beam and to a reduction in the flux intensity [211]. Besides reflections from the interior walls of the skimmer, shock waves originating from the lip of the skimmer can combine in the entrance channel, which leads to skimmer clogging [212]. Once a skimmer is clogged, increasing the backing pressure of the valve or bringing the valve closer to the skimmer does not lead to a gain in beam density after the skimmer [211–213]. These skimmer interference effects are undesirable and can be reduced by lowering the backing pressure, placing the valve at a larger distance from the skimmer [212] and optimising the geometry of the skimmer. Guidelines for the skimmer shape at low background pressures and manufacturing directions have been reported by W.R. Gentry and C.F. Giese [214]. According to them, a molecular beam skimmer should possess the following features:

- The edge of the orifice should be as sharp as possible to prevent skimmer interference.
- The exterior angle should be small to ensure that the shock wave remains attached to the outer surface of the skimmer. This reduces the amount of molecules that are back-reflected from the outer skimmer wall. An optimum value of $\theta_e = 30°$ has been reported for the exterior full cone angle (see Fig. 4.7 a)).
- The interior angle should be as large as possible to reduce scattering from the interior skimmer walls back into the beam. This design guideline conflicts with the external angle requirement and a good compromise is $\theta_i = 25°$. The opposing angle requirements can be alleviated by keeping the angles small at the apex and increasing the angles towards the skimmer base, which gives rise to a trumpet-like shape (see Fig. 4.7 b)).
- The skimmer opening is chosen based on pumping speed considerations and the degree of collimation required.

The valve-skimmer distance is a critical experimental parameter, which determines the density at the skimmer entrance and with that the severity of skimmer interference. By making use of the DSMC method [204, 216], it has been shown that skimmer interference in the free molecular regime is negligible if the Knudsen number at the skimmer entrance obeys $Kn = \lambda_s/d_s \geq 2$ and it deteriorates drastically for Kn values approaching unity, where λ_s denotes the mean free path and d_s is the diameter of the skimmer orifice [213, 217]. The applicability of the Knudsen number criterion for predicting the onset

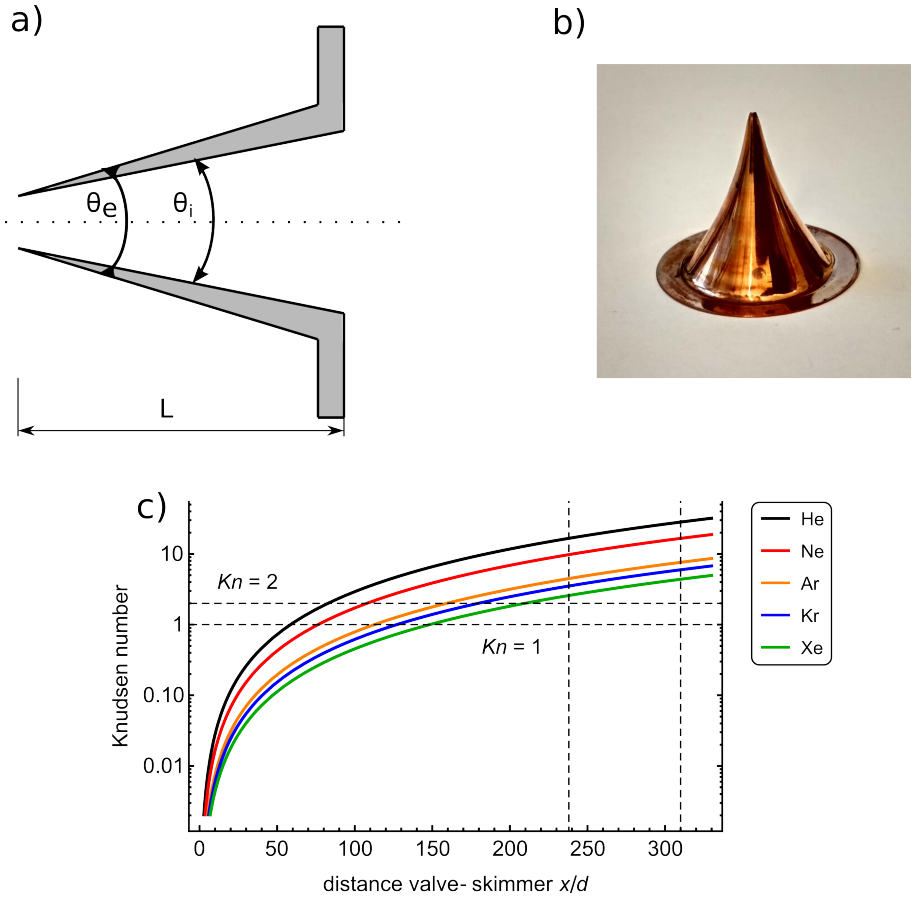

Figure 4.7: **a)** Cross section of a conical skimmer illustrating the interior θ_i and exterior θ_e full angles as well as the sharp apex of the skimmer. **b)** Image of a commercially available trumpet shaped skimmer [215], which offers a good compromise between a small exterior angle at the entrance and a large interior angle at the base. **c)** [103] Knudsen number of different noble gases at the skimmer apex calculated according to Eqn. 4.32. $Kn = 1$ and $Kn = 2$ are indicated by dashed horizontal lines. These Kn-values are of interest, as they span the transition region between skimmer interference and the interference-free regime. Typical operation parameters of the NPV valve were employed: nozzle diameter $d = 500$ µm, backing pressure $p_0 = 1.5$ bar, skimmer temperature $T_s = 293.15$ K, skimmer diameter $d_{sk} = 3$ mm. In the experiment, the nozzle-skimmer distance amounts to $x/d = 238 - 310$, which is indicated by dashed vertical lines. The noble gas integral collision cross sections were taken from reference [192].

of skimmer interference has been verified experimentally [217, 218]. While the mean free path between molecules in the molecular beam is large and the beam temperature T_{beam} is low, collisions between cold molecules in the beam and hot reflected molecules from the skimmer surface are detrimental to a high skimmer throughput [103, 109, 212]. Therefore, the mean free path between molecules in the beam and reflected hot molecules is defined by

$$\lambda_s = \left[5.3\, n_s \left(\frac{C_6}{k_B T_s} \right)^{1/3} \right]^{-1}, \tag{4.32}$$

where n_s denotes the density at the skimmer apex, T_s is the temperature of the skimmer and $5.3\left(\frac{C_6}{k_B T_s}\right)^{1/3}$ is proportional to the integral collision cross section [192, 217]. The density can be calculated making use of relations 4.19, 4.21 and the resulting mean free paths for different noble gases are depicted in Fig. 4.7 c). Of particular interest is the intersection of the Knudsen number curves with the $Kn = 2$ line, which marks the transition into the interference-free regime. Heavier gases possess a larger collision cross section, which results in larger Knudsen numbers. Consequently, larger nozzle-skimmer distances are required for heavier carrier gases [103]. Further insight on conditions leading to skimmer interference and skimmer clogging can be gained by employing the DSMC method [138, 202, 203]. For krypton, the skimmer should be located at least 170 nozzle diameters downstream, which corresponds to a distance of 85 mm when assuming a nozzle diameter $d = 0.5$ mm, and for xenon a minimal distance of 100 mm is required. These considerations are useful when designing the source chamber of a molecular beam experiment, as they give reference values for the required chamber dimension and the travel of the translation stage onto which the valve is mounted.

Quite recently, tremendous progress has been achieved in the skimming of molecular beams by cryogenic cooling of the skimmer [211, 212]. The advantage of such a procedure is that less thermal energy is imparted onto molecules reflected from the skimmer surface, which lowers their mean free path when reflected back into the beam. At lower temperatures, molecules interacting with the skimmer surface are adsorbed and can no longer contribute to skimmer interference. Moreover, the angle and the thickness of the shock front, which is present on the skimmer surface, is greatly reduced. The unclogging temperature of the skimmer is dependent on the carrier gas and is 60 K, 40 K and 20 K for krypton, argon and neon, respectively [212]. An increase in the transmitted beam flux by a factor 8 has been reported [212]. Skimmer cooling has been demonstrated to be applicable to molecular beams of OH radicals generated by discharging water vapour and a density gain of a factor 30 could be achieved in ref. [211]. The gain is composed of a geometric factor achieved by placing the valve much closer to the skimmer and an enhanced state purity due to evaded collisions with reflected molecules [211]. While skimmer cooling allows for an order of magnitude improvement in the densities available after the skimmer, one needs to exercise great care not to relocate the problematic back-scattering of beam particles from the skimmer to structures further downstream such as the entrances of hexapole guides, Stark or Zeeman decelerators.

4.3 The Nijmegen pulsed Valve (NPV)

The Nijmegen pulsed valve (NPV) is a novel molecular beam valve, which is capable of producing temporally short molecular beam pulses at high densities. The valve was developed and thoroughly characterised by B. Yan, P. H. F. Claus and coworkers [50]. The opening mechanism of the NPV is based on the Lorentz force retracting an aluminium strip located between two bar magnets by pulsing a high current through the strip. According to the classification schemes discussed in section 4.1.1, the opening mechanism of the NPV is similar to a valve introduced by Barry et. al. in 1986 [143]. The NPV has proven to be a reliable and robust pulsed gas source, which is inexpensive to build, easy to maintain and yet displays excellent beam characteristics [50]. Vogels et al. [81] have reviewed the suitability of the NPV and other beam sources for Stark deceleration in the context of collision experiments. Building on the favourable beam characteristics, pinhole discharge plates have been developed for the NPV [178], which forms a part of this thesis. Equipping the NPV with discharge plates greatly enhances the chemical space of species that can be expanded into vacuum. Before addressing the development of the discharge units, the NPV source is described in this section.

As displayed in Figure 4.8 a), the NPV consists of a valve body and a front plate incorporating the valve opening mechanism. The valve body serves as a gas reservoir and allows for mounting of the valve. Gas lines can be connected via 1/4" Swagelok connectors. The two black circular openings serve as feedthroughs for the valve electrodes and fix the position of the electrodes relative to the valve body. When closing the valve, the front plate is screwed onto the valve body, thereby pushing against a rubber ring, which establishes a firm seal. The entire valve assembly can then be mounted inside a vacuum chamber. Under vacuum conditions, the valve housing was found to be tight up to backing pressures of 5 bar. If the valve body is kept at atmospheric pressure, backing pressures up to 10 bars have been reported [50].

Figure 4.8 b) depicts the current electrodes and the spring with the magnet holders removed for better visualisation. The spring is spanned between the electrodes using retainer plates, which serve as electrical connectors at the same time. The spring consists of an aluminium strip with a Torr Seal droplet pushing against a rubber ring, thereby sealing the valve. The electrodes are mounted on a threaded PEEK insulator, which is screwed into the front plate. This allows to adjust the distance between the spring head and the rubber sealing ring. It is important to notice that the opening point of the valve depends on the force with which the plug pushes against the sealing ring. If the PEEK plate is screwed into the front plate too far, the valve does not open and if the contact

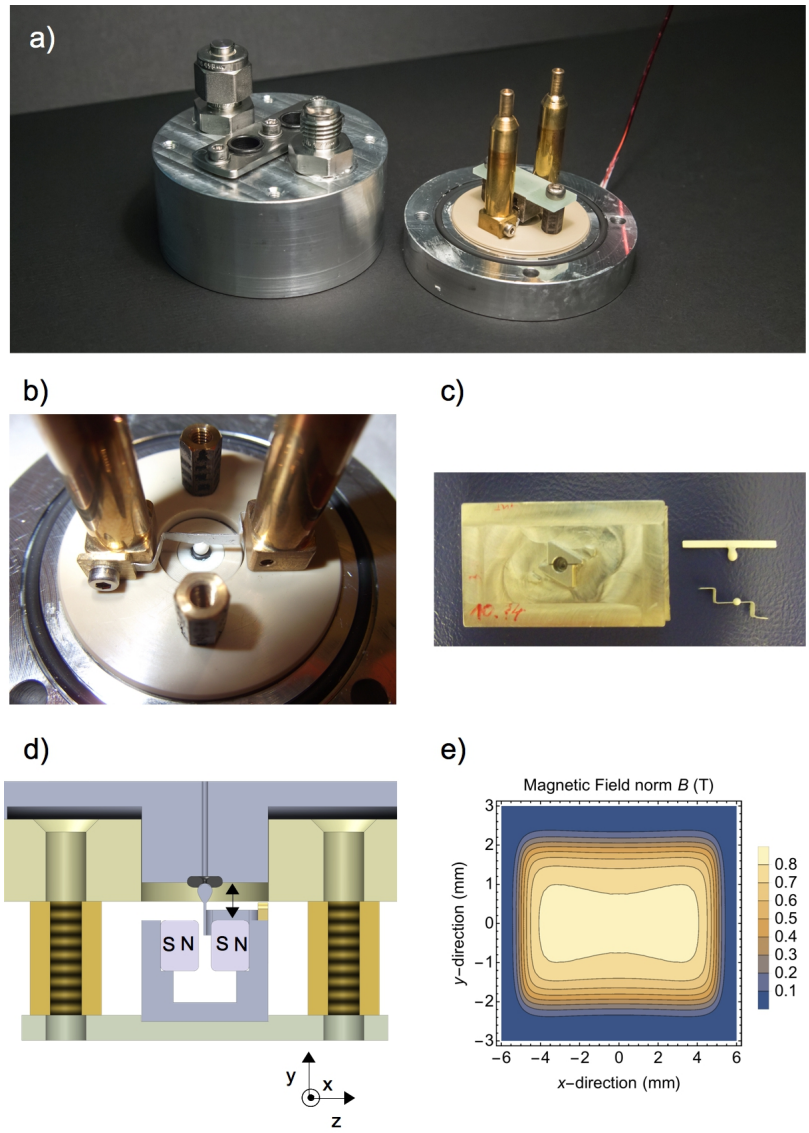

Figure 4.8: **a)** Picture of the Nijmegen pulsed valve body and the front plate incorporating the valve opening mechanism. The valve body serves as a gas reservoir and allows for mounting of the valve. **b)** Close-up of the current electrodes and the spring with the magnet holders removed. The spring is spanned between the electrodes using retainer plates, which serve as electrical connectors at the same time. The spring consists of an aluminium ribbon with a Torr Seal poppet pushing against a rubber rig, thereby sealing the valve. **c)** Spring bending gauge with a spring in original and bent form on the right hand side. **d)** NdFeB bar magnet arrangement with the spring located in the shaft formed by the front surfaces of the magnets. **e)** Magnetic field generated by the bar magnet configuration in d) for $z = 0$ mm. The origin is located at the centre of the shaft.

pressure is too low, the seal is not established correctly, which leads to leaking of the valve. Two Nickel coated NdFeB bar magnets (1.45 T, 10 x 4 x 3 mm) are mounted to the left and right of the spring as depicted in Figure 4.8 d). The opposing surfaces of the magnets are separated by a distance of 1 mm. As indicated by the plot in Figure 4.8 e), the straight, 10 mm long midsection of the spring is exposed to an almost uniform magnetic field. By pulsing a large current (400-1100 A) through the spring, the Lorentz-force $\vec{F} = (\vec{I} \times \vec{B}) \cdot l$ lifts the spring upwards and the valve opens for a short time (30-90 µs). Assuming a magnetic field strength of 0.82 T and a current of 1000 A, the spring experiences a force of 8.2 N over the length of interaction. Employing NdFeB bar magnets as the source of the magnetic field limits the maximum admissible operating temperature to 80 °C, as the magnets demagnetise above the Curie temperature. Due to the Nickel coating of the bar magnets, the valve is not suitable for molecular hydrogen.

As the spring is moving up and down rapidly, it is important to keep the weight as low as possible. Typically, an Aluminium spring weighs around 20 mg and the thickness of the band is 0.2 mm. Additionally, the spring has to be sturdy and flexible enough to endure many opening and closing cycles. The NPV can be operated at repetition rates up to 30 Hz. In the context of this thesis, the valve was mostly operated at repetition rates of 10 Hz. A good spring can easily last for a year ($> 10^8$ shots) before rupturing due to metal fatigue. The springs are cut out from a thin Aluminium foil using a punch, which allows for maximum reproducibility. A drop of Torr Seal is applied to the midsection and heated slightly such that the viscosity is temporarily reduced and a plug is formed under the influence of gravity. The shape of the Torr Seal droplet is crucial for the successful operation of the valve. The droplet is required to have a symmetric shape and should not be too large compared to the sealing ring such that it is guided towards the centre even if it impacts at a slightly off-centre position. Before insertion into the valve, the spring is bent into a Z-shaped form using the bending gauge depicted in Figure 4.8 c).

A schematic diagram for the NPV current pulse generation electronics is depicted in Fig. 4.9 and discussed in more detail in ref. [50]. The electrolytic capacitor bank with a total capacitance of 10 mF is charged by a floating power supply with an adjustable voltage between 0–20 V. A TTL pulse initiates the discharge of the capacitors via four parallel MOSFETs. During the current pulse, the capacitor bank is directly connected to the spring and peak currents of up to 1 kA are achieved. The circuit is designed such that the inductance and the resistance of the high current carrying components are low. When the valve is placed inside a vacuum chamber, the distance between the capacitor bank and the spring increases. In this case, conductors with a large cross section have to be employed to ensure a sufficiently low resistance. Over the course of a year it can become necessary

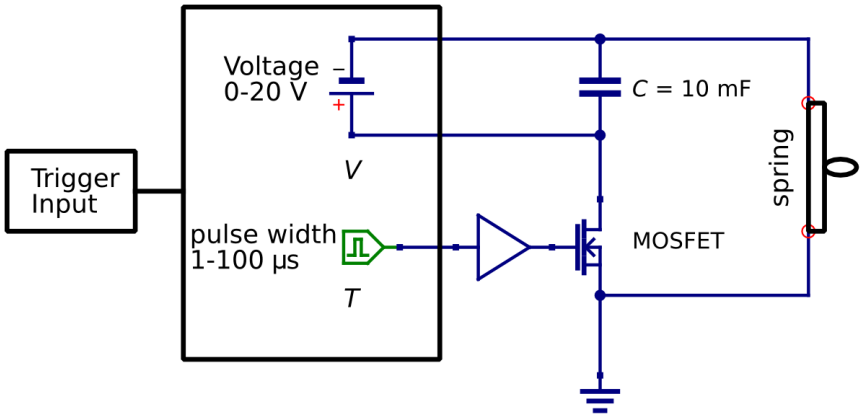

Figure 4.9: Schematic diagram of the NPV valve electronics used for the generation of current pulses, adapted from [50].

to replace the capacitors if a degradation of the valve opening performance is observed. Due to the large number of fast loading and discharging cycles, the capacitor's ability to store charge is gradually reduced. As both the current pulse duration (T-setting) and the charging potential across the capacitor bank (V-setting) are adjustable parameters, the effective opening time of the valve depends on the combined setting of these parameters. In order to relate the V- and T- potentiometer settings to more physically meaningful quantities such as the peak current and the current pulse duration, I-profiles were recorded with a current probe (Pearson current monitor, model 101). The current measurements were performed with the valve mounted on the translation stage so that the current path is identical to the one under typical experimental conditions. This includes thick audio-grade copper braid cables ($\varnothing$ = 8 mm) with a total length of 80 cm for transporting the current from the feedthrough port of the vacuum chamber to the valve. The current profiles are depicted in Fig. 4.10, where graph a) displays the current profiles for different V-settings at T = 4. If the voltage on the capacitor bank is too low, the charge is drained before the next loading cycle starts and the pulse is shorter than the T = 4 setting would allow. Typical operation conditions of the valve were found to be V = 6.4 and T = 3-5. The duration of the current pulses is given in Fig. 4.10 b), which is an upper estimate on the valve opening duration as the current has to surmount a certain threshold for the Lorentz-force to compensate the spring tension before the valve opens. The maxima of the current running through the spring are given in Fig. 4.10 c). From the graphs displaying the current duration and the current maximum it is apparent that the values are roughly mirrored along a diagonal running from the bottom left to the top right across the graph. It is therefore possible to obtain comparable expansion conditions for different sets of V,T-settings. This is in good agreement with the experimental finding that different

combinations of V and T lead to the same increase in source chamber pressure and to comparable beam profiles.

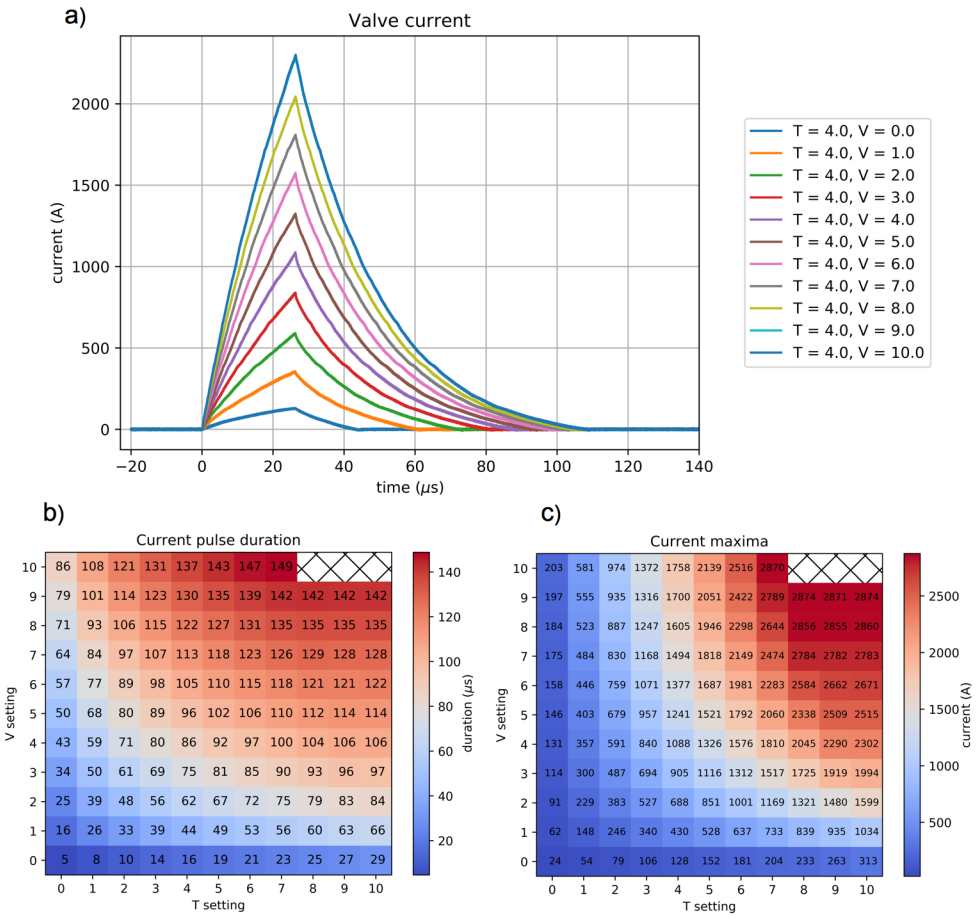

Figure 4.10: Current characteristics of the NPV valve driver for different V,T-settings. **a)** Current profiles at T = 4.0 and variable V-values. **b)** Current pulse durations for all V,T-combinations. **c)** Current maxima for all V,T-combinations. The crossed out fields could not be measured, as the spring ruptured at large opening parameters.

4.4 Experimental setup

In order to ascertain direct comparability between the two discharge sources, the characterisation of both valves was carried out on the experimental setup depicted in Figure 4.11. An xyz-translation stage (Thermionics, EC-B450C-T275T-1.87-4) allowed for reproducible and accurate positioning of the valve relative to the laser beam with a step size of 0.01 mm and an overall travel distance of 12.5 mm in the y- and z-direction. Along the x-direction, the total travel distance measured 101.6 mm and a step resolution of 0.0254 mm was provided by the translation stage. The valve was mounted inside a vacuum chamber, which is pumped by a 1000 $\mathrm{l\,s^{-1}}$ turbo molecular pump (Leybold-Oerlikon,

Turbovac 1000 C). The opening rate of the NPV was set to 10 Hz and a short gas pulse of a few tens of µs duration was formed [50]. As indicated in Fig. 4.13, each measurement was preceded by a trigger pulse of 10 µs duration, which initiated the opening of the valve and served as a time reference. For the valve characterisation experiments described in this chapter, Ar, Kr and Xe were employed as carrier gases. At room temperature one percent of H_2O was seeded in the carrier gas by leading the gas through a water bubbler. A discharge pulse dissociated the water molecules within the expansion channel of the valve and the resulting OH radicals were cooled by a subsequent supersonic expansion into high vacuum. Typically, a stagnation pressure of 2.5 bar was applied. During operation of the valve, the pressure in the source chamber was kept at around $1.5 \cdot 10^{-5}$ mbar. In a final step, the radicals were detected by laser-induced fluorescence (LIF) with an excitation wavelength centred at 282 nm [168–170].

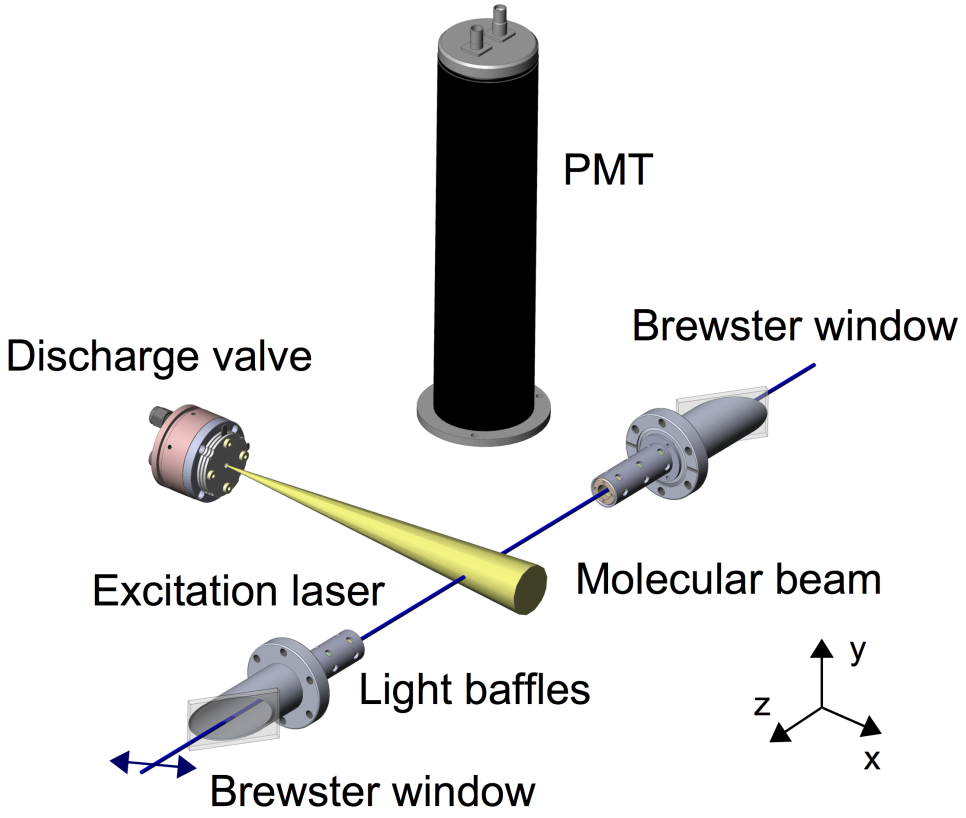

Figure 4.11: Experimental setup for the characterisation of both discharge sources. The OH molecules were detected 5 cm downstream from the nozzle by laser-induced fluorescence (LIF). The blue arrow represents the p-polarised component of the 282 nm laser beam (see text for details).

As depicted in Figure 4.11, light baffles with a circular hole ($\varnothing$= 3 mm) were mounted at the entrance and exit points of the UV laser beam to minimise the amount of stray light

detected by the photomultiplier tube (PMT). Additionally, the laser beam was guided through Brewster windows, which only allow horizontally polarised light to enter the chamber. The windows consisted of UV-fused silica plates and were inclined towards the optical axis at an angle of 56.2°. In this way, the amount of ambient light entering the chamber could be reduced. The intersection region between the laser beam and the molecular beam was located 5 cm downstream from the nozzle opening. OH molecules in the ground state $X^2\Pi(v = 0)$ were excited to the first excited electronic state $A^2\Sigma(v = 1)$, where v denotes the vibrational quantum number. A frequency-doubled Rhodamine 6G dye laser (Fine Adjustment, Pulsare) was pumped by the second harmonic (532 nm) of a Nd:YAG laser (Continuum, Surelite II) to generate laser radiation at 282 nm. The wavelength of the dye laser was calibrated using a wavelength meter (High Finesse, WS−8). The output energy at this wavelength amounted to 10.0 mJ/pulse with a pulse length of 10 ns. It was found that a power of 1.5 mJ/pulse is enough to saturate the OH X-A transition. The $A^2\Sigma(v = 1)$ state relaxes via the $A^2\Sigma(v = 1)$-$X^2\Pi(v = 1)$ transition under the emission of off-resonant fluorescence at 313 nm. The fluorescence was collected by a UV lens ($\varnothing$= 50.8 mm, f = 50 mm) and was detected by a calibrated PMT (Electron Tubes, B2/RFI 9813 QB, C638AFN1). Further stray light suppression was achieved by inserting two bandpass interference filters (Melles Griot, F10-310.0-3-50.0M) and one dichroic long pass mirror (Omega Optical, 305Alp Version 1) in front of the PMT. Both of these filters block radiation at 282 nm, while displaying a high transmittance at 313 nm. Stray light can be caused by ambient light entering the source chamber, the improper alignment of the excitation laser, wavelength shifted reflections of the excitation laser due to photon scattering at surfaces [111] or by the glow accompanying the discharge process. Successful detection of OH was confirmed by the observation of the fluorescence signal depicted in Figure 4.12. A fluorescence lifetime of 717 ± 18 ns was determined by fitting an exponential decay model to the data. The fluorescence lifetime is in agreement with previous results of 712 ns [219] and 717 ns [220]. In order to improve the signal to noise ratio, the data points in Figure 4.12 represent averages over 50 experimental cycles.

The timing sequence of the experimental setup depicted in Figure 4.11 was controlled via a LabView-based software compiling the desired trigger sequence and programming a pulse generation card (Spincore, Pulse Blaster). A typical pulse sequence used for the experiments described in this chapter is illustrated in Figure 4.13. The experiment starts by retracting the valve plunger, which is initiated by the rising edge of the valve trigger. The duration of the valve trigger has no influence on the opening time, which is determined by the settings of the valve electronics. The discharge is initiated a time $t_{\text{disc.}}$ after the valve trigger on CH1. $t_{\text{disc.}}$ is referred to as discharge delay and usually lies within a range of 30-150 µs. In order to measure the temporal profile of the OH beam,

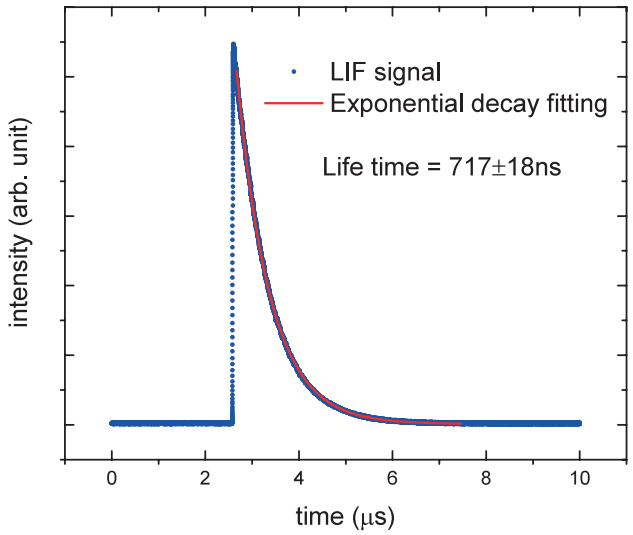

Figure 4.12: Laser-induced fluorescence (LIF) signal of OH radicals inside the molecular beam. Fitting an exponential decay model to the signal leads to a lifetime of 717±18 ns, which is in agreement with previous results [219, 220]. Reprinted from [178], with the permission of AIP Publishing.

the integrated LIF signal is recorded at varying trigger delays t_{delay} between the discharge and the dye laser pulse. The flash lamp of the Nd:YAG laser is triggered a time t_{QSW} before the emission of the laser pulse and allows to adjust the intensity of the emitted laser pulse. Additionally, an oscilloscope trigger can be defined relative to CH4 in order to control the onset of signal acquisition.

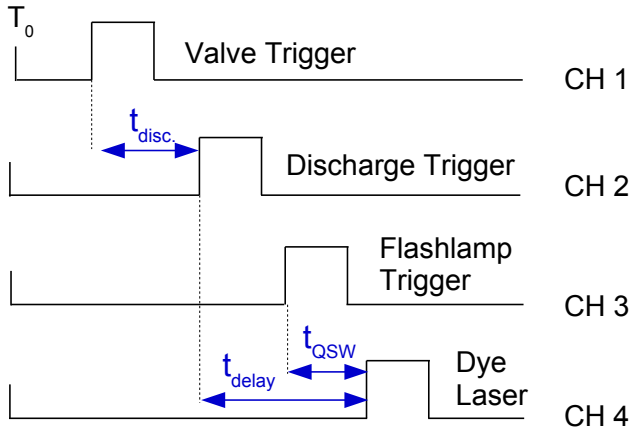

Figure 4.13: Typical trigger sequence corresponding to one experimental cycle. The valve trigger initiates the opening of the valve and HV is applied onto the discharge plates in a subsequent step. The laser beam is emitted a time t_{delay} after the discharge has fired and the laser intensity can be controlled by the t_{QSW} delay.

4.5 Density measurement of molecular beams

An important quantity for characterizing molecular beams is the density. The density of OH radicals produced by the discharge is of particular interest, as it provides information on the discharge efficiency and serves as a starting point for subsequent density estimations after the decelerator outlined in section 5.6. The accurate determination of the density is a challenging task [92, 221, 222] as the number of OH radicals has to be determined within the detection volume at the crossing point between the expanding gas cloud and the laser beam (see Fig. 4.11). Experimental conditions were chosen such that the $A^2\Sigma(v = 1)$-$X^2\Pi(v = 1)$ $Q_1(1)$ and $Q_{21}(1)$ transitions were saturated (1.5 mJ/pulse [178]) throughout the density determination procedure. Working under saturated conditions is desirable as this results in larger LIF signals [223] and the excitation rate factors adopt the simple form given in equation 4.36. The density determination by LIF photon counting followed here is similar to the method presented in the thesis of M. Kirste [221]. The CELIF technique provides an alternative approach to measuring the absolute densities in molecular beams by simultaneously acquiring cavity ring-down (CRD) and light induced fluorescence (LIF) signals on a shot to shot basis [222, 224].

In a first step, the PMT voltage signal $V_{\mathrm{LIF}}(t)$ corresponding to the LIF trace of the non-resolved $Q_1(1)$ and $Q_{21}(1)$ transitions was acquired on an oscilloscope. Subsequently, this signal was related to the number of photons detected at the PMT N_{photons}, which is described by the following expression:

$$N_{\mathrm{photons}} = \frac{\int_{t_{\mathrm{start}}}^{t_{\mathrm{end}}} V_{\mathrm{LIF}}(t)\,\mathrm{d}t}{R_{\mathrm{L}}\,G_{\mathrm{PMT}}\,e}\,. \tag{4.33}$$

R_{L} is the output load resistance of the PMT, G_{PMT} denotes the PMT gain and e is the elementary charge of the electron. In a subsequent step, the number of photons at the PMT was converted to the total number of OH radicals N_{OH} via the following expression:

$$N_{\mathrm{OH}} = \frac{4\pi\,N_{\mathrm{photons}}}{\Omega\,T\,Q\,\varepsilon}\,. \tag{4.34}$$

The factor $4\pi/\Omega$ corrects for the fraction of solid angle under which the photons are collected by the PMT. The emission of fluorescence is considered homogeneous as the laser pulse is significantly shorter than the excited state lifetime of 717 ns [178]. Furthermore, it is assumed that polarisation effects of the excitation laser and the fluorescence do not play a role. Q denotes the quantum efficiency of the PMT, T is the transmission coefficient of the optics and ε represents the excitation rate factor at saturated conditions. In the limit of saturated conditions, the LIF intensity is directly proportional to the product between

the excitation rate factor and the initial state population N_i with rotational degeneracy g_i [223, 225, 226].

$$I_\mathrm{LIF} \propto \varepsilon \cdot N_\mathrm{i} \quad \text{where} \tag{4.35}$$

$$\varepsilon = \frac{g_\mathrm{e}}{g_\mathrm{e} + g_\mathrm{i}} = \frac{(2J'+1)}{(2J'+1)+(2J''+1)}\,. \tag{4.36}$$

The upper and lower state populations reach an equilibrium, which depends on the rotational degeneracies of these states. Consequently, $\varepsilon = \frac{1}{3}$ for the $P_1(1)$ transition and $\varepsilon = \frac{3}{5}$ for the combined $Q_1(1)$ and the $Q_{21}(1)$ transitions (the bandwidth of 0.1 cm^{-1} of our laser system is insufficient to resolve the transition). Equation 4.36 is part of a more general expression for the LIF intensity in the saturated regime given by D. R. Guyer et al. [226] and has the following form:

$$I_{LIF}\,(v'', J''; v', J') \propto \left\{ N_{v''J''} \frac{(2J'+1)}{(2J'+1)+(2J''+1)} \right\} \sum_{v''} \nu^4_{v''v'}\, q_{v''v}\, P(\nu)\,. \tag{4.37}$$

$N_{v''J''}$ is the population in the v'', J'' levels and $\nu_{v''v'}$ represents the frequency between the upper and lower vibrational states. $q_{v''v}$ accounts for the Franck-Condon factor associated with a ν'',ν' transition and $P(\nu)$ takes into account the dimensionless PMT sensitivity and filter transmission. The term in curly brackets describes the absorption process, whereas the terms of the sum pertain to emission. Compared to equation 4.35, equation 4.37 accounts for vibrational branching during emission and takes into account the wavelength dependence of the filter plates. When determining the density in the absence of filters or when employing filter plates with a transmission bandwidth narrower than the vibrational spacing, equation 4.35 holds. Otherwise, equation 4.37 relates the LIF intensity to the number of photons detected and a Franck-Condon factor corrected ε-factor would have to be used in equation 4.34.

During an LIF-based density determination under saturated conditions, it is crucial that the laser power is constant to prevent spreading of the beam profile. Furthermore, the laser beam volume and the detection volume should be constant throughout the measurement. Usually, the detection volume V_det and the solid angle Ω are known with least accuracy. In order to define these two quantities, the collection lens was replaced by two pinhole plates. The first pinhole plate had a $r_1 = 0.5$ mm bore hole and was located directly in front of the PMT. The second plate was machined with a radius of $r_2 = 0.155$ mm and was located 5 mm above the laser beam with a diameter of $d_\mathrm{laser} = 3.0$ mm. Measurement of the separation between the two plates resulted in $d = 193.84$ mm for chapter 4 and $d = 239.5$ mm for chapter 5 (see Fig. 4.14), depending on how the pinhole holder was

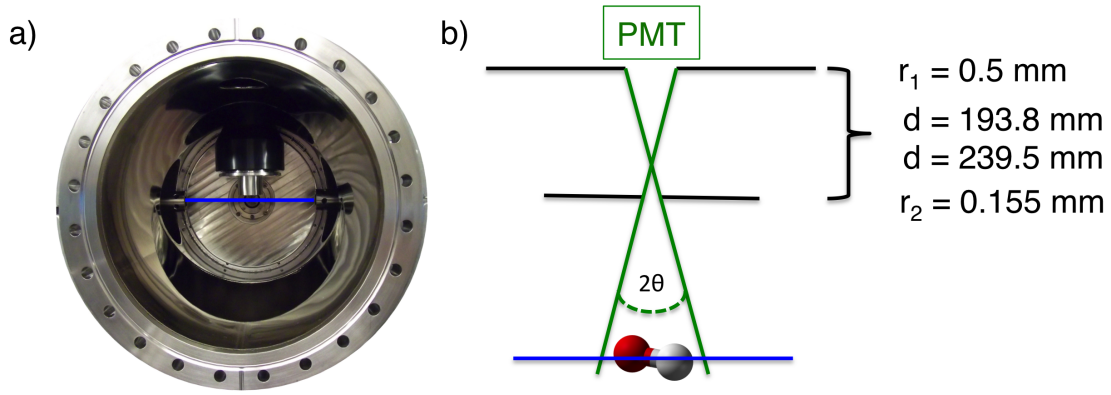

Figure 4.14: **a)** Experimental density measurement setup in the source chamber. The direction of view is that of the expanding gas cloud. The laser beam is indicated in blue and the 0.31 mm diameter pinhole is mounted 5 mm above the laser beam. The pinhole plate is inserted into an adapter piece which fits the lens holder. **b)** Schematic illustration of the detection region covered by the PMT. $d = 193.8$ mm applies to chapter 4 and $d = 239.5$ mm holds in chapter 5.

inserted. The solid angle of the detection cone under which photons were collected is given by the following expression:

$$\Omega = 2\pi\left(1 - \cos(\theta)\right) = 2\pi\left(1 - \frac{d \cdot \frac{1}{1+\frac{r_2}{r_1}}}{\sqrt{r_1^2 + \left(\frac{d}{1+\frac{r_2}{r_1}}\right)^2}}\right). \tag{4.38}$$

As the lower pinhole-plate was mounted directly above the laser beam and the bore hole diameter is small, we can assume the detection volume to be a cylinder with a length equivalent to the laser beam diameter and a radius equal to r_2. The OH radical density within the detection volume is then expressed by

$$\rho_{\mathrm{OH}} = \frac{N_{\mathrm{OH}}}{V_{\mathrm{det}}} = \frac{N_{\mathrm{OH}}}{\pi {r_1}^2 d_{\mathrm{laser}}}. \tag{4.39}$$

The density value obtained in this way represents the average density within the detection volume V_{det}. As the detection volume at the crossing point between the molecular beam and the laser is rather small ($V = (2.3 \pm 0.1) \cdot 10^{-4}$ cm^3), the density value reflects a local density within the molecular beam and it can safely be assumed that the density is constant throughout the whole detection volume. As mentioned in section 4.2.4, the molecular beam displays a longitudinal as well as a transversal density distribution. It is therefore necessary to adjust the valve position relative to the laser beam axis such that the density is probed from the dense core of the expanded molecular beam.

Due to the small opening diameter of the lower pinhole plate, the OH molecules leave the detection zone within less than 300 ns for the fast beam velocities in Tables 4.4 and 4.7. Hence, the transit time through the detection zone is less than the 1/e-lifetime of 717 ns (see Fig. 4.12). However, the laser beam diameter provides a sufficiently wide band of excited OH radicals at identical densities such that the detection zone is replenished with OH radicals from behind and constant density values can be assumed.

4.6 Pinhole discharge source

4.6.1 The physics of pinhole discharges

As motivated in section 4.1.2, the introduction of plasma generating elements to molecular beam valves allows for the dissociation of molecules and the generation of meta-stable species. Ideally, the discharge should not heat the expanding gas [170], while providing a suitable environment for achieving high dissociation efficiencies. Depending on the breakdown mechanism and the pathway of providing energy to the gas, a wide variety of plasma sources exist. Operation mechanisms are based on inductively coupled radio frequency (RF), microwaves, capacitively coupled RF and direct current (DC) [227]. The applications for modern plasma technology are very diverse and have been reviewed in ref. [186].

Plasmas are composed of ionised gases and are also referred to as the fourth state of matter. In plasmas, a large number of electrons is detached from the cores and varying degrees of ionisation can be obtained [186]. While overall electrically neutral, plasmas are conductive and contain a large number of both positively and negatively charged species which are free to move [227, 228]. It is insightful to classify plasmas by their energy and by the electron density, see Fig. 4.15 a) [227]. Furthermore, plasmas can either be in thermal or non-thermal equilibrium depending on whether the constituents (neutral species, ions, electrons) possess the same temperature [186, 227]. Which case applies depends to a large extent on the gas density and on the length over which the discharge takes place. Thermal equilibrium plasmas require very high temperatures and pressures, as the equilibration is mediated by collisions. On the other hand, in a non-thermal equilibrium plasma at lower pressure, the electrons are far more energetic than the remaining constituents, as they are light and experience accelerations by the applied electromagnetic fields. It is this type of plasma which is ideal for the spectroscopic investigation of dissociated radicals due to the low heating of the gas. Furthermore, the large kinetic energy of electrons allows for inelastic scattering, thereby ensuring efficient dissociation and the generation of secondary electrons, which keeps the plasma sustained [186, 227].

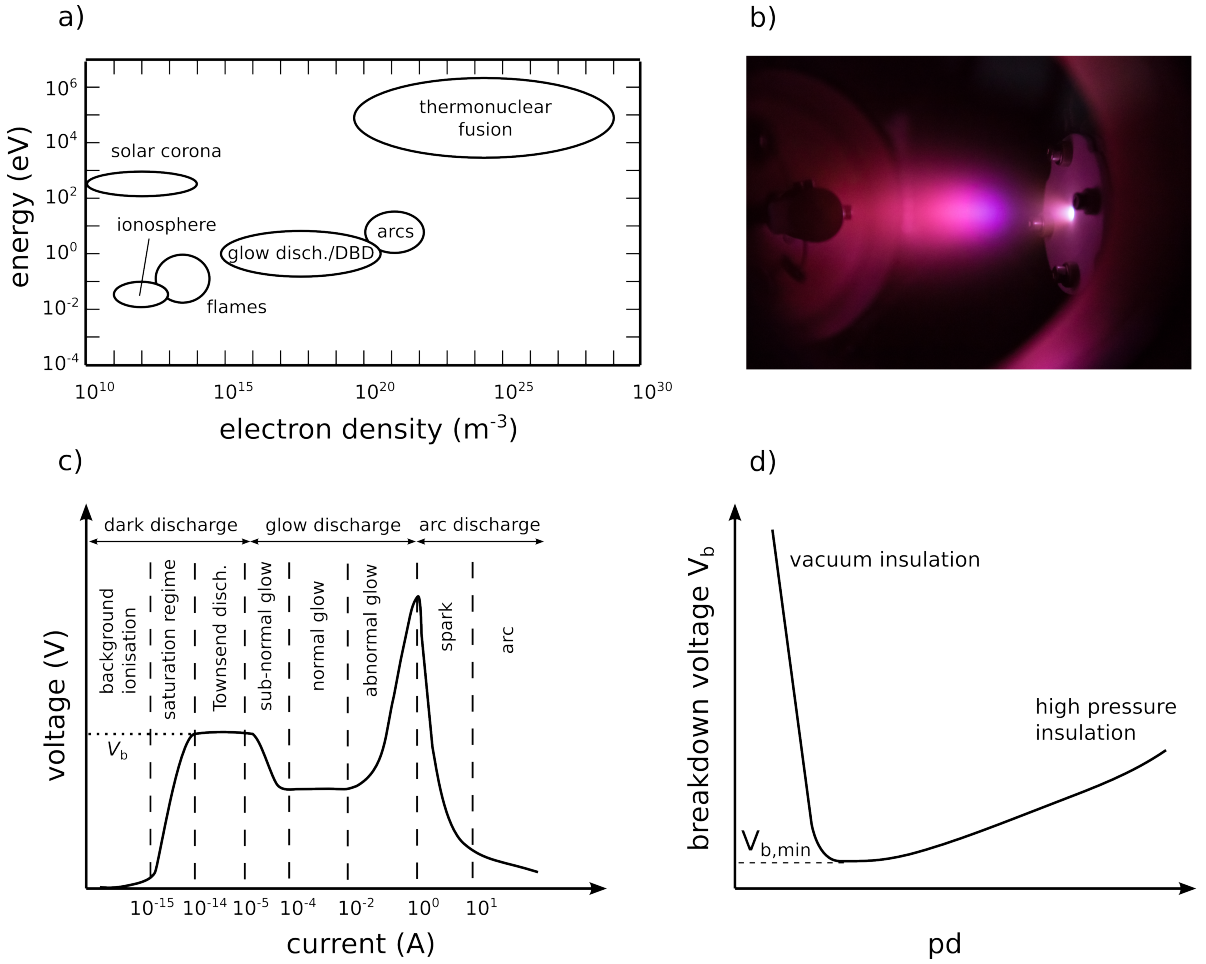

Figure 4.15: **a)** Classification of plasmas according to their energy and electron density [227, 229]. **b)** Operation of the pinhole plate discharge in the glow regime, where glowing metastable Ar atoms allow for the visualisation of the expansion plume. The plasma cloud is propagating towards a microphone (circular dark structure on the left part of the image), which allows to probe the arriving gas package. **c)** Sketch of the current-voltage diagram of a plate discharge indicating the different operation regimes. Under low current conditions the discharge is dark, whereas at moderate currents a visible glow develops. In analogy to [228, 230, 231]. The pinhole discharge source was operated in the normal and abnormal glow regime. **d)** Breakdown potential for a plate discharge as a function of the product between the gap size d and the pressure p [227].

The direct current glow discharge can be observed in very simple discharge cells consisting of two parallel electrode plates surrounded by a gas [186, 227]. In fact, such a setup is geometrically quite similar to the discharge front assembly for the Nijmegen pulsed valve depicted in Fig. 4.17. The different characteristic operation regimes of a plate discharge are assigned according to the current-voltage diagram in Fig. 4.15 c). At low potential differences between the electrodes, the gas is a good insulator. Nonetheless, a very small current is still detectable due to ionisation of the gas by cosmic radiation or by field emission caused by irregularities in the electrode structure. Under these conditions, the

current and the discharge are subjected to statistical fluctuations and the discharge is not self-sustaining [186, 227, 230]. Electrons located within the electrode gap are accelerated by the electric field. While travelling towards the anode, an electron can ionise gas atoms through inelastic collisions, which results in the formation of a second electron and a cationic fragment. Increasing the voltage on the discharge plates leads to a strong increase in current by several orders of magnitude. The current rise in the saturation regime is due to ionisation and persists until the breakdown voltage of the gas V_b is reached [230]. At this point, the gas becomes conductive and no longer acts as a dielectric insulator. Cations are accelerated towards the cathode and knock out secondary electrons. This process is of great importance for sustaining the discharge, as lost electrons are replenished. The Townsend region marks the beginning of self-sustainability [186, 227, 228, 232]. Increasing the current further results in a transition to the glow discharge regime and the buildup of considerable positive space charge in front of the cathode. Close to the cathode surface the electric field strength is very high and the adjacent positive space charge results in a strong potential drop of several hundred volts, which is referred to as cathode fall [232]. At the same time, collisions with electrons lead to excitation of the gas atoms, which de-excite via the emission of visible light, hence the name glow regime [186, 227]. The normal glow regime is situated in the current range from 10^{-4} to 10^{-2} A [230, 231]. In this region, the current can vary over a wide range for identical discharge potentials. Increasing the discharge potential V results in a more complete coverage of the area through which the current flows [228, 232]. Once the entire cathode is covered in glow, a further enhancement of the discharge current only results for larger potentials, which denotes the beginning of the abnormal glow regime. At sufficiently large currents, the abnormal glow transits into the spark regime [228, 232].

The discussion of the different discharge regimes in the previous paragraph has important practical implications for the operation of plasma sources incorporated into molecular beam valves. The discharge is only self-sustained once the breakdown voltage is reached. This determines how readily a discharge can be ignited upon every opening cycle of the valve. As indicated in Fig. 4.15 d), the breakdown voltage is a function of the product between the pressure p and the discharge plate separation d. Provided the discharge gap size is fixed, the gas acts as a high pressure insulator at elevated background pressures. On the other hand, if the pressure is too low, a state of vacuum insulation is reached. A quantitative expression for the breakdown voltage is available from Paschen's law [227]. From Eqn. 4.18 it can be deduced that the pressure at the sonic surface ($M = 1$) is approximately 0.5 times the stagnation pressure ($p/p_0 \approx 0.5$) for monoatomic gases. Ideally, the experimental discharge potential is chosen as low as possible to prevent heating of the beam while still ensuring reliable ignition [170]. As pointed out by

Lewandowski et al. [170], a glowing filament helps to ignite the discharge. Another point in need of consideration is the polarity of the discharge potential with regard to the propagation direction of the gas inside the expansion channel. The discharge stability can be enhanced by choosing the location of the cathode such that the electron flow between the cathode and the anode opposes the direction of the expanding gas [170, 175, 176]. The drift velocities of electrons are much larger than those of the heavier cationic fragments. It is beneficial to align the cation drift direction with the flow velocity, as sustained discharges rely on the secondary emission of electrons from the cathode by incident cationic fragments. This effect was reported in ref. [176], where a "non-linear diode-like" behaviour has been ascribed to supersonic gas flows. In addition to this, control over the operation regime of the discharge can be exercised by adjusting the current with the help of a ballast resistor R_{ballast}, provided that the breakdown voltage has been surmounted [103, 175, 176]. The actual operation point is located at the intersection between the current-voltage profile in Fig. 4.15 c) and the load line, which is defined by [228, 232]:

$$V_{\mathrm{supply}} = V_{\mathrm{gap}} + I \cdot R_{\mathrm{ballast}} = I \cdot R_{\mathrm{disch.}} + I \cdot R_{\mathrm{ballast}} = I \cdot R_{\mathrm{tot}} \,. \tag{4.40}$$

Here, V_{supply} denotes the voltage on the power supply, V_{gap} is the voltage drop across the discharge gap and $I \cdot R_{\mathrm{ballast}}$ takes into account the voltage drop over the resistance R_{ballast}. A final point which needs consideration is sputtering. At sufficiently high voltages, the bombardment of the cathode not only releases secondary electrodes, but also charged cathode fragments. This effect is referred to as sputtering and can lead to electrode deterioration over time [186].

In a glow discharge plasma the main constituents of interest are the electrons, as they allow for a rich plasma chemistry [186]. Typically, the glow discharge plasmas employed for molecular beams belong to the thermally non-equilibrated type, where the electron temperature ($T_{\mathrm{e}} \approx 1 - 3$ eV [228]) is much larger than the temperature of the remaining components [186]. This ensures cold molecular beams, while still allowing for efficient radical production. Glow discharges are capable of operating over a wide pressure range, which typically lies between 0.01 bar and atmospheric pressures. Typical breakdown voltages range from a few hundred volts up to 2 kV, where the current is situated in the mA-regime [186, 228, 232]. In glow discharges the degree of ionisation is rather low with $f_{\mathrm{i}} = n_{\mathrm{e}}/n_0 = 10^{-8} - 10^{-5}$, where n_{e} denotes the electron density ($10^9 - 10^{11}$ cm^{-3}) and n_0 is the density of neutral gas particles [228].

4.6.2 Dissociation of water in glow discharges

In the electronic ground state $\tilde{X}(^1A_1)$ water translates in the C_{2v} point group and adopts a θ(H–O–H) = 104.5° bond angle and r_{OH} = 0.95792 Å bond length. The ionisation energy amounts to $E_i = 12.621 \pm 0.002$ eV and the H-OH bond dissociation energy has been reported as $D(H - OH) = 5.0992 \pm 0.0030$ eV [233]. The dissociation of H_2O into OH is the result of inelastic collisions between water precursor molecules and plasma electrons. The dissociation rate is proportional to the collision cross section, which displays a strong dependence on the collision energy. However, the electron energy distribution inside a plasma is often unknown, which makes it difficult to predict the contributing discharge pathways [176]. Elastic and inelastic cross sections for the collisions between water molecules and electrons have been reported in the literature [233, 234]. An inelastic scattering event between an energetic electron and a single water molecule can result in the following electron impact processes [235]:

$$\begin{aligned} e^- + H_2O &\rightarrow OH(X) + H + e^- \ (7\,eV) && \text{(a)} \\ &\rightarrow OH(A) + H + e^- \ (8.9\,eV) \xrightarrow{h\nu} OH(X) && \text{(b)} \\ &\rightarrow H_2O^- \rightarrow OH(X) + H^- . && \text{(c)} \end{aligned}$$

Pathway (a) is referred to as direct dissociation pathway and results in the formation of OH(X) radicals [176, 235]. The dissociation can either occur from the ground $\tilde{X}(^1A_1)$ state across the dissociation threshold or via excitation to the $\tilde{A}(^1B_1)$ or $\tilde{a}(^3B_1)$ states, which connect to OH(X) via dissociative channels. This pathway is active above a threshold of 7 eV [235]. Pathway (b) is initiated via the collisional excitation of ground state water into $\tilde{B}(^1A_1)$ or $\tilde{b}(^3A_1)$ states, which dissociate into OH(A). Subsequently, the de-excitation from OH(A) to OH(X) occurs radiatively. This pathway is operative above a threshold of 8.9 eV [235]. Dissociative electron attachment (c) represents another route leading to OH(X) with a cross section peak value at 6.5 eV attributed to a resonance [234]. Based on the magnitude of the collision cross sections, the major contribution to OH production is ascribed to channel (a) [234]. Cross sections for the reaction paths involving collisions between water and electrons are depicted in Fig. 4.16.

Penning dissociation represents an alternative dissociation pathway, which takes place according to the following scheme [176]:

$$\begin{aligned} e^- + Rg &\rightarrow Rg^* + e^- \\ Rg^* + H_2O &\rightarrow OH + H + Rg\,. \end{aligned} \qquad \text{(d)}$$

Furthermore, the encounter of electrons and water molecules can lead to ionisation giving rise to the following cationic fragments, where the threshold energy for occurrence is given in parenthesis [233, 234]:

$$\begin{aligned} e^- + H_2O &\rightarrow H_2O^+ + 2\,e^- && \text{(e)} \\ &\rightarrow OH^+ + H + 2\,e^- \ (18.116\,\text{eV}) && \text{(f)} \\ &\rightarrow O^+ + H_2 + 2\,e^- \ (19.0\,\text{eV}) && \text{(g)} \\ &\rightarrow H^+ + OH^- + e^- \ (16.95\,\text{eV})\,. && \text{(h)} \end{aligned}$$

As pointed out by P. Bruggeman and D. C. Schram [236], the presence of cationic fragments can lead to electron-ion dissociative recombinations and positive-negative ion recombinations, which significantly contribute to the overall OH formation rate in plasmas with a high ionisation fraction f_i. However, in a glow discharge the degree of ionisation ($f_i = 10^{-8} - 10^{-5}$ [228]) is too low for ionic recombinations to contribute much. Therefore, it is sufficient to take into account only processes (a)-(d) for the plasma formation in case of a pinhole discharge source. Additionally, it is important to consider the expanding nature of the plasma cloud upon leaving the valve duct. The gas expansion and the missing confinement lead to rapid quenching of the radical chemistry as the collision

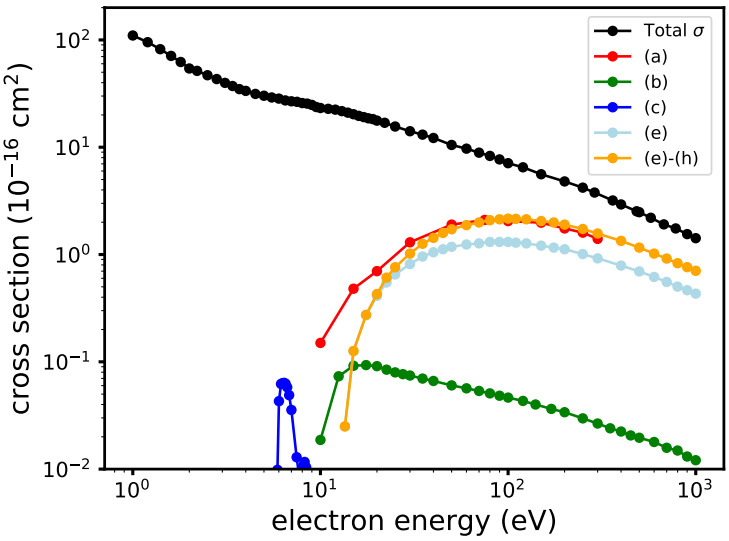

Figure 4.16: Cross sections for collisions between H_2O and e^- based on the data available in [233, 234]. The black curve represents the total collision cross section and also incorporates elastic collisions whose cross section decreases with increasing collision energy. The remaining curves are labelled according to the processes described in the main text. There is some uncertainty regarding the quality of the data used for (a), as it is quite challenging to determine cross sections leading to the electronic ground state OH(X), see [233–235]. The orange curve represents the overall ionisation cross section of the processes described in (e)-(h).

frequency and the density drop. While this prevents the plasma chemistry from reaching an equilibrium state, OH loss via radical-radical recombinations is effectively suppressed [176]. Moreover, the discharge plates are only 2 mm apart, which limits the transit time of the gas in the discharge section to approx. 10 µs for krypton (Eqn. 4.13 was employed for calculating the velocity).

4.6.3 Construction of the pinhole discharge source

The pinhole-discharge source is based on the design by Lewandowski *et al.* [170]. A cross-sectional view of the pinhole-discharge assembly mounted onto the NPV valve body is depicted in Figure 4.17. The valve expansion channel consists of a circular bore hole with a diameter of 0.5 mm. The thickness of the stainless steel discharge plates and the Macor ® insulators is 1.0 mm and 2.0 mm, respectively. The electrode and the insulator closest to the valve possess a 0.5 mm diameter hole to match the valve nozzle. The conical orifice of the nozzle starts from the midpoint of the second insulator and features a 60° opening angle [202]. H_2O molecules are dissociated into OH radicals between the two high-voltage plates. Typically, a potential difference of 800-1000 V between the two electrodes is sufficient to invoke a stable discharge without the use of a tungsten filament. By grounding the electrode in proximity to the valve body and applying a negative potential to the electrode at the end of the expansion channel, the flow of electrons is directed in such a way that it opposes the direction of the expanding gas. As discussed in the previous section, this voltage configuration results in a more stable discharge. The electrode configuration and the resulting potential are depicted in Fig. 4.19 a).

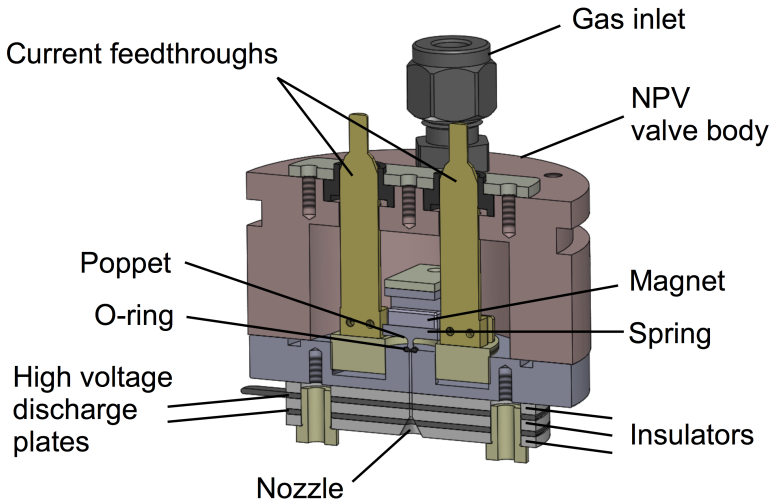

Figure 4.17: Schematic illustration of the pinhole-discharge valve (see text for details).

The circuit diagram of the discharge electronics employed for the experiments involving the pinhole discharge source is depicted in Fig. 4.18 a). A ballast resistor ($R = 385\ \Omega$) was incorporated into the circuit to limit the discharge current [175–177] and to ensure operation in the glow discharge regime [103, 228, 232]. The discharge unit is represented by an equivalent circuit taking into account the capacitance of the discharge electrodes and the resistance of the plasma once the discharge is ignited, which is represented by the discharge switch in the closed position. A high voltage switch (Behlke, HTS-31-06) connects the discharge to a capacitor bank with an overall capacitance of 30 µF which stores enough energy to operate the discharge reliably. The discharge current was monitored making use of a split-core current probe (Tektronix, TM502A, A6302). Depending on the temporal overlap and duration of the gas pulse and the TTL discharge trigger, three different operation modes can be distinguished according to the sketches in Fig. 4.18 b) cases i)-iii). In each case, the voltage across the discharge gap is monitored. In case i), the TTL pulse is longer than the gas pulse and the two pulses overlap in time. As soon as the gas density in the expansion channel is large enough, an electric breakdown takes place and the discharge is ignited (see Fig. 4.15 b) and d)). The breakdown is accompanied by a voltage drop across the discharge gap, which is caused by the discharge current flowing through the discharge and the ballast resistors [176]. The discharge remains active while the gas pressure is sufficiently large and extinguishes on the falling edge of the gas pulse. The voltage does not drop significantly after opening the HV switch due to the capacitance of the discharge plate structure and the floating end of the open switch terminal. Case ii) represents the opposite of case i), with a long gas pulse and a short, temporally coinciding discharge pulse. The discharge ignites and continues to burn even after the discharge TTL pulse has reached low logic levels. In the end, the potential decays exponentially as the discharge is withdrawing charge from the capacitance of the discharge plates. This scenario allows to sample the gas pulse by placing the discharge window at different positions within the gas pulse. In case iii) there is no temporal overlap between the discharge pulse and the gas package. The charge remaining on the discharge plates suffices to ignite the discharge. Experimentally, all three cases could be addressed by adjusting the discharge trigger duration and the opening settings of the valve. Operation in mode iii) is not recommended, as the amount of energy available for driving the discharge is reduced.

To a certain degree, the discharge characteristics depend on the cone geometry. The electric fields and the potentials along the centre line of different discharge channel geometries are depicted in Fig. 4.19 b). For a fully cylindrical channel and the Y-shaped cone, the maximum field strengths achievable in the middle of the channel are close to the values expected for parallel plates, i.e. $E_{\mathrm{max}} = 500$ V/mm. Similar electric field profiles have been

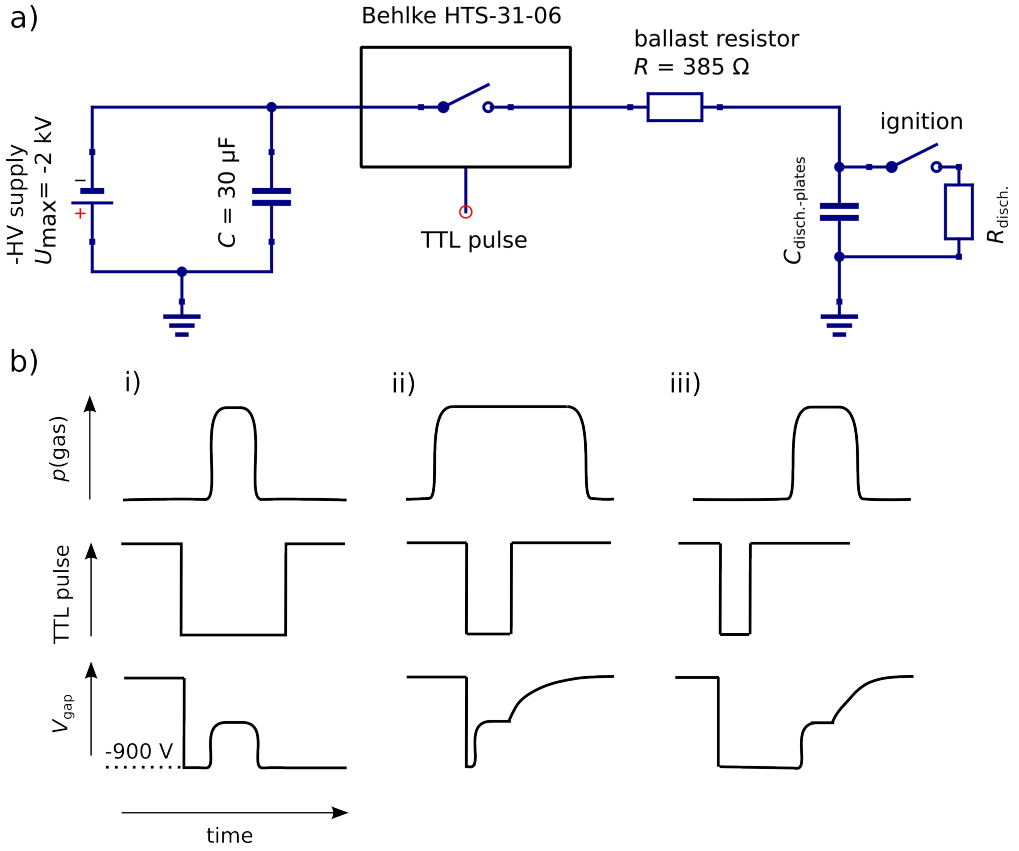

Figure 4.18: **a)** Circuit diagram of the discharge electronics. The switching box was built and conceived by G. Holderied. **b)** Schematic dependence of the temporal voltage profile on the relative time delay between the discharge TTL pulse and the rising edge of the gas pressure in the discharge channel [176]. **i)** Short gas pulse temporally overlapping with a longer discharge trigger signal. **ii)** Short discharge pulse window combined with a long gas package. **iii)** Discharge in the absence of a temporal overlap between the discharge pulse and the gas package.

reported in ref. [103], where a discharge stack with a larger bore hole has been characterised. From a gas dynamic point of view, the cone-shaped exit channel is advantageous, as it reduces the radial spreading of the package, which results in larger on-axis densities than is the case for pinhole nozzles [138, 202, 203]. Electrode structures displaying a fully conical expansion channel with an identical thickness of the electrode stack components suffer from reduced field strengths along the centre line. This could lead to discharge ignition issues. The reduced field strengths are a result of increased divergence within the fully conical channels. The electron density likely shifts towards the cone boundary resulting in inhomogeneous dissociation. Thus, the pinhole discharge geometry depicted in Fig. 4.19 a) with a cone opening up far downstream offers the best compromise between minimising the radial divergence of the expanded beam and providing a strong and tightly confined electric field region.

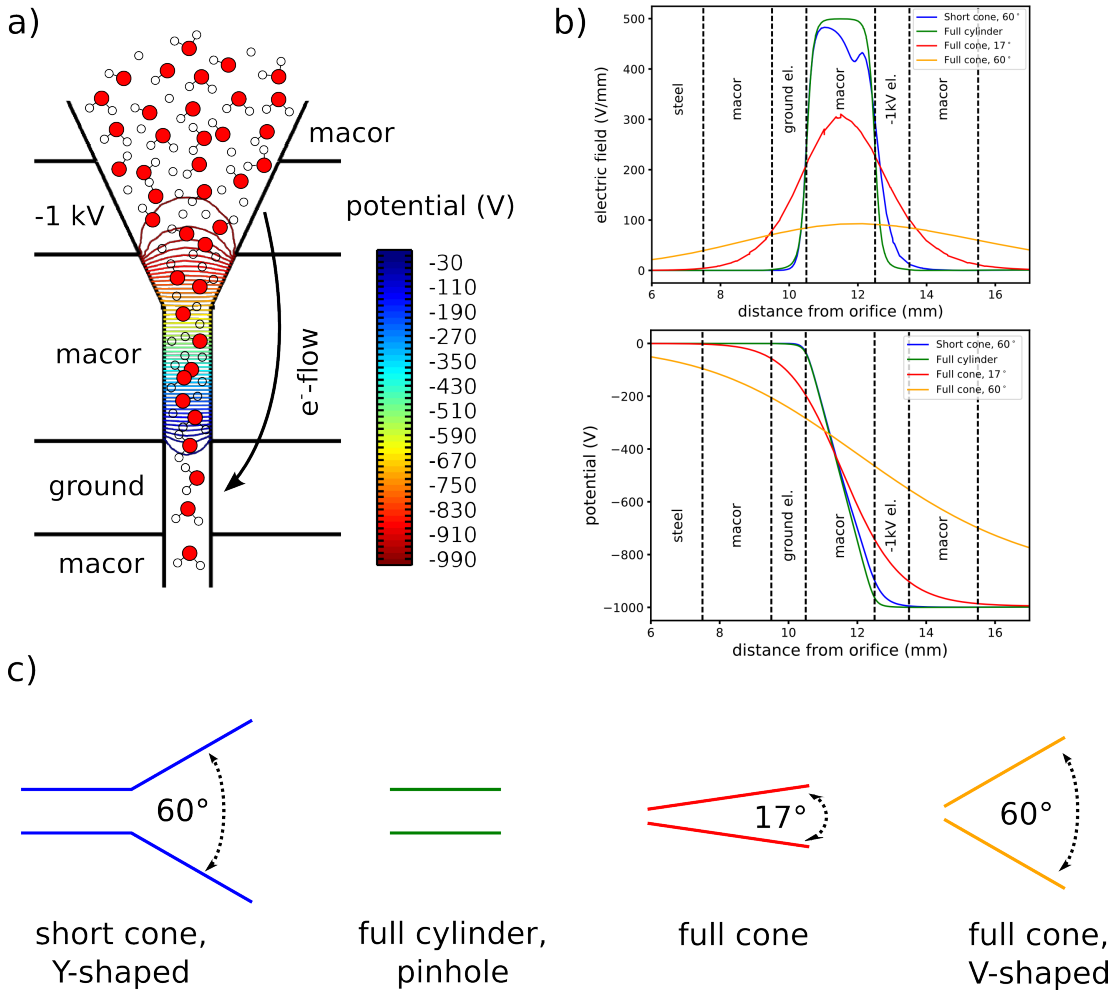

Figure 4.19: **a)** Discharge potential inside the circular expansion channel when applying -1 kV on the outer electrode. The electrode structure is indicated, as well as the electron flow direction [176]. This geometry was characterised experimentally. **b)** Comparison of the electric field and the potential for different discharge channel geometries. The fields were simulated with Comsol [237] and a potential of -1 kV was applied on the outer electrode. The data traces represent the values along the centre line through the channel. The blue curve corresponds to the geometry depicted in a). **c)** Cross sectional view of the discharge geometries employed in b). The color scheme from the graphs in b) applies.

In his master thesis [238] D. Ostermayer characterised the OH beam properties obtainable from the Y-shaped discharge nozzle, the pinhole nozzle and the fully conical V-shaped nozzle (see Fig. 4.19 c)) under comparable conditions. In brief, his findings are that varying the discharge settings of the pinhole source (full cylinder) offered only very limited control over the molecular beam properties. Furthermore, the discharge was not very stable with this type of source. On the other hand, good performance in terms of cooling and density was found for the Y- and V-shaped nozzles. The V-shaped nozzle provided slightly colder beams than the Y-shaped source, which is presumably due to the longer conical expansion section of the V-shaped source and the larger separation of the electrode

surfaces from the centre line. Consequently, the discharge seems to be less violent in a V-shaped nozzle, which is in accordance with the lower electric field strength depicted in Fig. 4.19 b). D. Ostermayer found the Y-shaped source to yield denser OH beams in comparison to the V-shaped nozzle [238].

4.6.4 Results and Discussion

The pinhole discharge valve was characterised using Ar, Kr, and Xe as carrier gases. Typical beam profiles for OH co-expanded with the three different noble gases are given in Figure 4.20. The mean velocity and the longitudinal velocity spread can be deduced

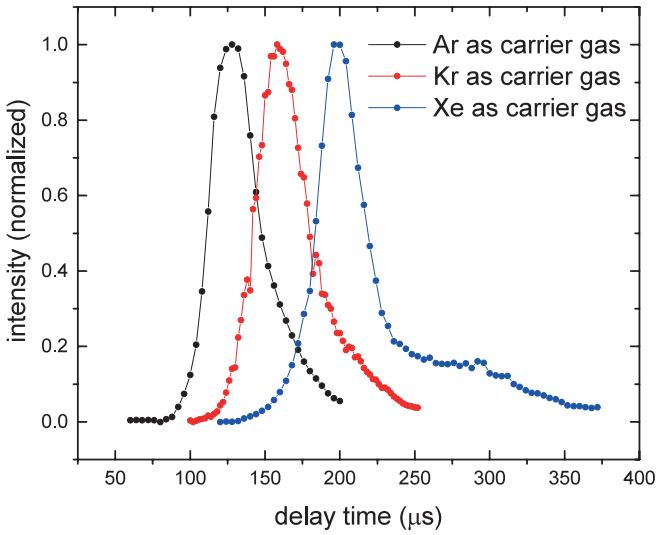

Figure 4.20: Temporal profiles of the OH beam generated by the pinhole discharge for Ar, Kr and Xe as carrier gases. The amplitude of the profiles has been normalised for better comparison. Reprinted from [178], with the permission of AIP Publishing.

from the beam profiles. For the determination of the longitudinal velocity distribution, the effect of the valve opening time and the laser excitation volume was taken into account. To eliminate any influence from the valve opening time, it was reduced until the temporal beam profile no longer changed. For Ar, Kr, and Xe, the mean velocities of the OH beam were determined as 670.5±6.3 $\mathrm{m\,s^{-1}}$, 483.5±5.0 $\mathrm{m\,s^{-1}}$ and 385.1±4.0 $\mathrm{m\,s^{-1}}$, respectively. Compared to the terminal velocities u_∞ calculated for pure noble gases (see Eqn. 4.12 and Fig. 4.3), the OH velocities after the discharge are significantly larger. The differences between the OH mean velocity and the terminal velocity for each of the three noble gas species are: $\Delta v_{\mathrm{Ar}} = 119$ m/s, $\Delta v_{\mathrm{Kr}} = 103$ m/s and $\Delta v_{\mathrm{Xe}} = 80$ m/s. To a certain degree the molecular beam is faster due to the presence of comparatively light species such as H_2O and OH. However, as the concentration of light species is low and only accounts for a few percent of the total stagnation pressure, it is clear that the largest contribution to the increased kinetic energy of the beam must originate from the heat

released during the discharge. The longitudinal velocity spreads were determined to be (9.8±0.5)%, (13.1±0.6)% and (9.2±0.8)% for Ar, Kr and Xe, respectively. The cause for the broadening of the velocity spread when using Kr as carrier gas is not clear, but it was a common observation in all our measurements. Similar observations have been reported previously [239]. The favourable beam profiles render the NPV-based discharge valve an ideal source for deceleration and trapping experiments [35, 38, 39, 81, 240, 241].

In order to determine the rotational state population of the OH radicals, the laser wavelength of transitions from $J'' = 3/2$ to $J'' = 9/2$ between the electronic ground state $X^2\Pi(v = 0)$ and the first excited state $A^2\Sigma(v = 1)$ were scanned, where J denotes the total angular momentum quantum number. The resulting spectrum is depicted in Figure 4.21 and the assignment of the spectral peaks is based on the LIFBASE program [242]. The $P_1(1)$ and $Q_1(1)$ (and $Q_{21}(1)$) transitions originating from the $J'' = 3/2$ rotational ground state and the $P_1(2)$ and $Q_1(2)$ (and $Q_{21}(2)$) transitions starting from the first rotationally excited $J'' = 5/2$ state are clearly resolved. Since our dye laser has a bandwidth of about 0.1 cm^{-1}, the $Q_1(1)$ and $Q_{21}(1)$ lines as well as the combined $Q_1(2)$ and $Q_{21}(2)$ transitions are overlapped and not resolvable. Integration over the spectral features reveals that around 98% of the OH molecules are in the rotational ground state. From the results in Table 4.4 it can be perceived that changing the carrier gas does not influence the rotational state distribution. Furthermore, changing the backing pressure from 0.5 bar to 5 bar did not significantly change the population in the rotational ground

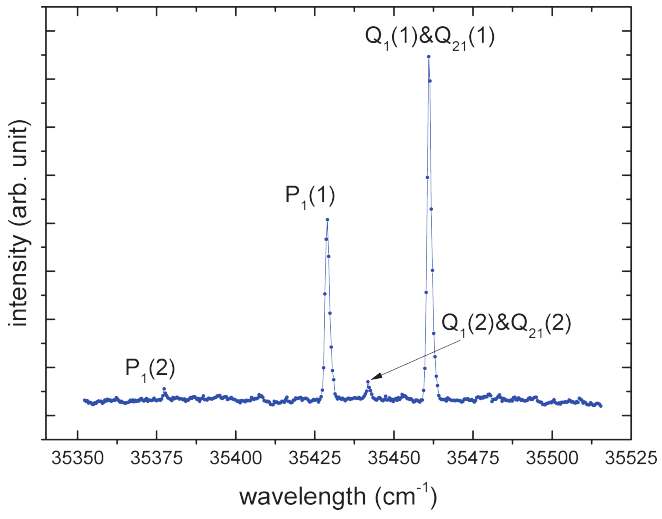

Figure 4.21: Rotationally resolved electronic spectrum of OH generated from the pinhole-discharge source. The carrier gas is Ar. The $P_1(1)$ and $Q_1(1)$ ($Q_{21}(1)$) transitions from the $J''= 3/2$ ground state and the $P_1(2)$ and $Q_1(2)$ ($Q_{21}(2)$) transitions from the first rotationally excited state $J''= 5/2$ are clearly resolved. The x-axis is the excitation laser wavelength measured in vacuum. Reprinted from [178], with the permission of AIP Publishing.

state. The high degree of state purity achieved after the expansion is a direct result of the optimised shape of the nozzle geometry [50] and the discharge plate arrangement [170]. The discharge occurs towards the end of the expansion duct where the local gas density is still high. Consequently, the expanding OH radicals can take part in a large number of collisions, which efficiently convert rotational energy into translational motion.

carrier gas	mean velocity ($m\,s^{-1}$)	velocity spread FWHM (%)	population in rotational ground state (%)	density $\times 10^{10}$ (cm^{-3})
Ar	670.5±6.3	(9.8±0.5)	> 98	10.7±4.1
Kr	483.5±5.0	(13.1±0.6)	> 98	4.2±1.6
Xe	385.1±4.0	(9.2±0.8)	> 98	3.0±1.2

Table 4.4: OH radical beam properties generated by the pinhole-discharge source. The densities were measured 5 cm downstream of the valve. The data was acquired by L. Ploenes and D. Zhang conducted the analysis.

The general procedure for determining the density has been described in section 4.5. The greatest difficulty associated with the OH density measurement lies in the accurate determination of the solid angle under which the fluorescence photon emitting volume is detected and the determination of the laser detection volume contributing to the signal. In order to better define these two quantities, the collection lens was replaced by two pinholes. The first pinhole had a diameter of 0.31 mm and was placed 5 mm above the intersection point of the OH and laser beam. The second pinhole had a circular opening of 1.0 mm and was located directly in front of the PMT. This arrangement allowed for an accurate definition of the solid angle ($\Omega = (2.1 \pm 0.3) \cdot 10^{-5}$ sr) and the detection volume ($V = (2.3 \pm 0.1) \cdot 10^{-4}$ cm^3). To compensate for the reduction in signal, all filters were removed. The stray light contribution was determined to be less than 5%. The measurements were performed under saturated conditions, where the excitation extinction ratio $\varepsilon = 1/3$ for the $P_1(1)$ transition [168, 223]. Under these conditions, the $|e\rangle$-state OH densities 5 cm downstream of the nozzle were determined to be (1.1±0.4)×10^{11} cm^{-3} for Ar, (4.2±1.6)×10^{10} cm^{-3} for Kr and (3.0±1.2)×10^{10} cm^{-3} for Xe. The Xe density is similar to the one reported in ref. [170] and demonstrates the suitability of the NPV for radical production. The cold and intense radical beams produced by the NPV discharge valve are particularly useful in experiments where the particle density is crucial, for example collision, deceleration and trapping experiments [243].

The electric properties of the discharge were characterised using argon. The discharge voltage present at the electrodes was monitored using a HV-probe and the discharge current was measured with the help of a de-gaussed current probe. The time of flight and current profiles depicted in Fig. 4.22 pertain to case i) in Fig. 4.18, where the discharge voltage pulse is applied over the entire duration of the gas pulse. The duration of the HV discharge pulse was set to 200 µs and the discharge was ignited 30 µs after opening the valve. The time of flight in trace a) is given relative to the discharge delay and the corresponding current pulse is depicted in trace b). The TOF profile is very broad, as the entire gas pulse was discharged. The discharge current peaks 71 µs after the application of the HV pulse and reaches 24 mA. The first spike close to the time origin was caused by noise pickup due to switching the discharge voltage. The origin of the second current peak at 175 µs is not clear. As it lies within the discharge pulse duration of 200 µs, it could be that residual gas remaining in the valve channel was discharged or that the valve plunger rebounced slightly upon closing, which resulted in the emission of a secondary gas pulse.

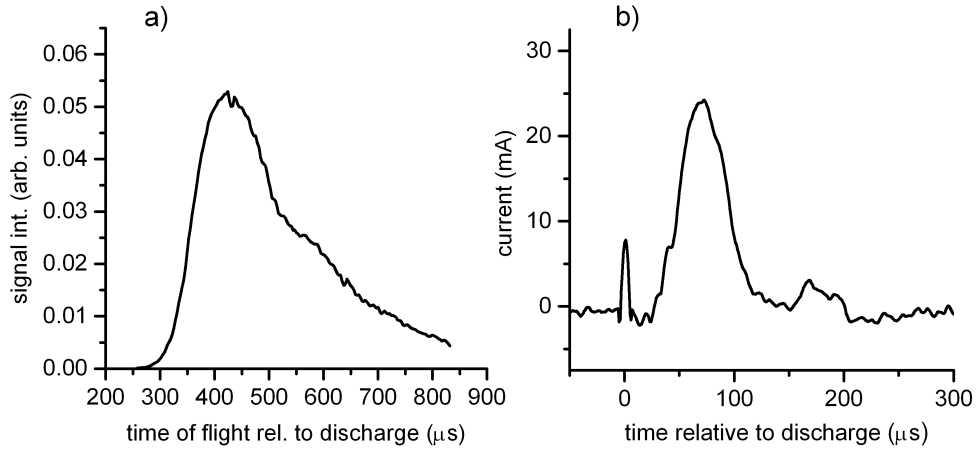

Figure 4.22: Illustration of case i) in Fig. 4.18. The valve was operated at V = 6.44 and T = 6.0 (see Fig. 4.10), which resulted in a chamber pressure of $p = 1.9 \cdot 10^{-4}$ mbar. A discharge potential of -800 V was applied and the discharge delay was set to 30 µs. A discharge duration of 200 µs was chosen. **a)** Time of flight profiles recorded 256 mm downstream of the valve. The flight time is given relative to the onset of the discharge pulse. **b)** Current profile corresponding to the pulse depicted in a).

Setting the discharge duration to 30 µs allowed to dissociate and sample different sections of the gas pulse in the expansion channel. The constellation of using a discharge pulse which is shorter than the width of the gas pulse corresponds to case ii) in Fig. 4.18 and the experimental data is depicted in Fig. 4.23. From trace b) it is evident that the densest part of the gas package has not reached the discharge zone yet when placing the discharge window 70 µs after the valve opening trigger. At a delay of 70-90 µs, the discharge does not

ignite for another 20 µs until the gas pressure in the channel has reached levels at which a gas breakdown can occur. At a discharge delay of 100 µs the idle time decreases and the discharge ignites with a delay of only 10 µs relative to the initiation of the HV-pulse. The prolonged on-time of the discharge is accompanied by an increase in the discharge current and a rise in the intensity of the integrated LIF time of flight profiles depicted in 4.23 a). At discharge delays of 120 µs and above, the discharge ignites with almost no delay. The TOF profiles reach maximum values between discharge delays of 120-130 µs, which has proven to be the preferred range for stable generation of OH radicals. At long discharge delays the current profiles map out the dropping pressure of the gas package in the discharge channel. The current reversal after the extinction of the discharge is thought to originate from the transport of negative charge along with the expanding gas. Compared to case i), the TOF signal levels in case ii) reach similar intensities. However, the peak currents in case ii) were found to be almost twice as high when operating the discharge for a shorter duration. Current probes have proven to be invaluable devices, as they allow to characterise the discharge behaviour at the nozzle and facilitate choosing stable discharge settings.

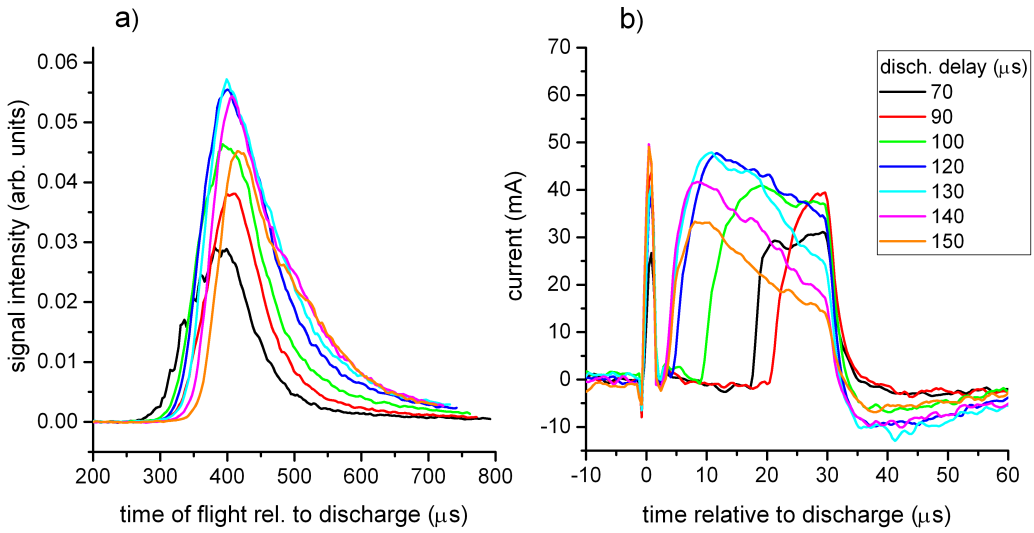

Figure 4.23: Illustration of case ii) in Fig. 4.18. The valve was operated at V = 6.44 and T = 6.0 (see Fig. 4.10), which resulted in a chamber pressure of $p = 2.0 \cdot 10^{-4}$ mbar. A discharge potential of -800 V was applied and different discharge delays were investigated, while fixing the duration at 30 µs. **a)** Time of flight profiles were recorded 265 mm downstream of the valve. The flight time is given relative to the onset of the discharge pulse. **b)** Current profiles corresponding to the TOF curves depicted in a).

The possibility of igniting the discharge utilising the energy stored in the capacitance of the electrode stack was demonstrated using krypton as carrier gas. This scenario belongs to case iii) in Fig. 4.18 and the discharge duration was set to 10 µs. Figure 4.24 displays

current and voltage data at different discharge delays relative to the valve opening trigger. The delays were chosen such that the discharge does not start within the closed state of the HV-switch. As the expansion velocity of krypton is slower than that of argon, the onset of the discharge lies approx. 158 µs after the valve trigger. The voltage drop coincides with the rising edge of the current and decays exponentially as the gas removes charge from the discharge plates. The current maxima are comparable to those in case ii), but the width of the current peak is narrow and does not form a plateau. This suggests that the capacitance of the stack is not sufficiently large for igniting the discharge over longer periods. Generally, operation of the discharge in accordance with case ii) is recommended. It is desirable to discharge the dense part of the gas package in the channel over a limited timespan to reduce heating of the beam, but still provide enough energy for efficient dissociation.

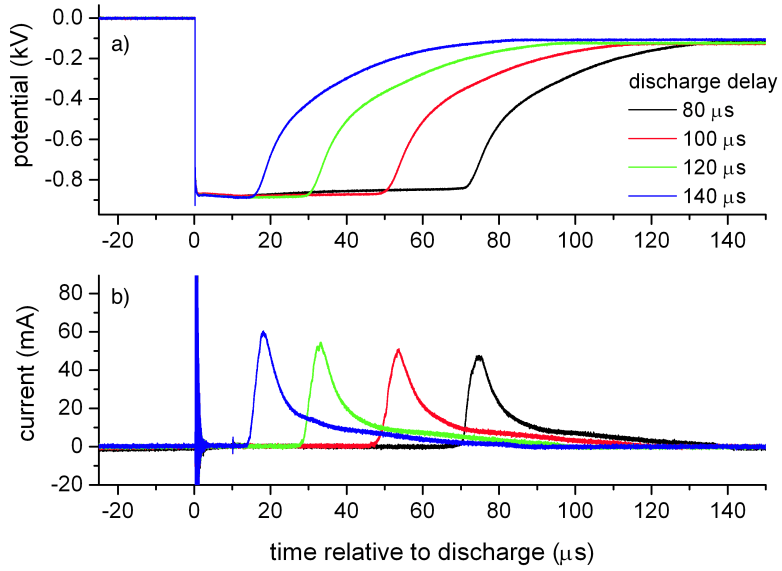

Figure 4.24: Data illustrating the ignition of the discharge source by the energy stored in the capacitance of the discharge stack, see case iii) in Fig. 4.18. The discharge was operated at -900 V and different discharge delays were investigated while keeping the duration fixed at 10 µs. The data shown was recorded with krypton as carrier gas. **a)** Voltage profiles indicating the onset of the discharge by an exponential drop in the potential across the discharge plates. **b)** Current profiles corresponding to the voltage traces depicted in a).

Another parameter of great importance for the operation of every discharge source is the discharge potential. The dependence of the time of flight profiles and the discharge current on the potential is depicted in Fig. 4.25 a) and b). The data was recorded at a discharge delay of 120 µs and argon was used as a carrier gas. The onset of OH production was found to lie at around -500 V. The discharge current displays a delayed

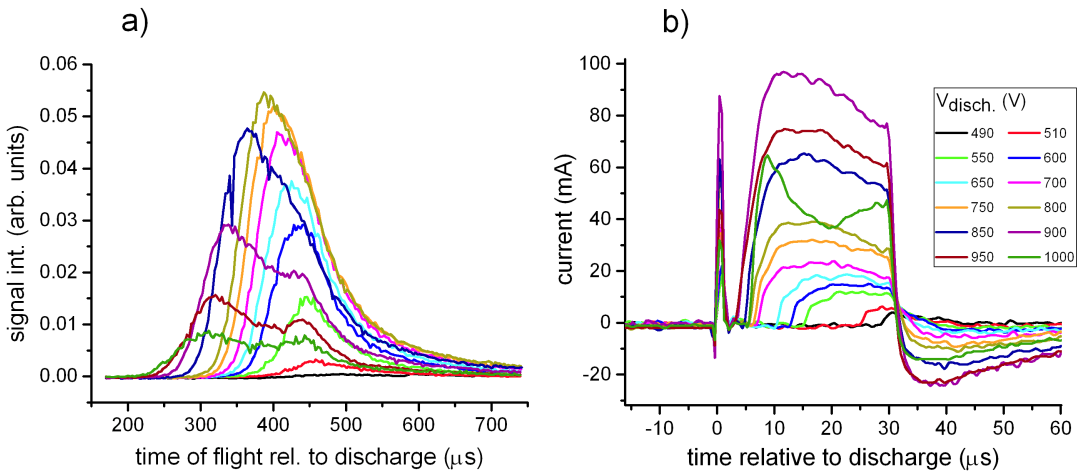

Figure 4.25: Dependence of the molecular beam properties and the discharge current on the discharge potential. The valve was operated at V = 6.44 and T = 6.0 (see Fig. 4.10), which resulted in a chamber pressure of $p = 2.0 \cdot 10^{-4}$ mbar. The discharge was operated with a delay of 120 µs relative to the valve opening and the discharge duration was set to 30 µs. The data was recorded with argon as carrier gas. **a)** TOF profiles indicating an increased velocity spread and faster beam velocities at large absolute discharge potentials. The legend in part b) applies. **b)** Current profiles corresponding to the TOF curves depicted in a).

onset relative to the initiation of the discharge trigger at low absolute discharge voltages (−510 V to −650 V). Under such conditions, the required breakdown voltage cannot be reached until the densest part of the package arrives. This suggests that the combination of an insufficient gas pressure in the discharge channel and the application of a low potential difference pertains to the vacuum insulation regime in Paschen's model, which is depicted in Fig. 4.15 d). Increasing the magnitude of the discharge potential allows for ignition at lower pressures and the discharge onset appears earlier. Besides increasing discharge currents, the discharge duration is also enhanced at higher potential differences between the ground electrode and the electrode bearing a negative potential. Accordingly, the TOF signal intensity increases up to a value of -800 V and then decreases again. Most likely, the decrease in OH LIF signal is due to an unfavourable shift in the energy distribution of the electrons in the plasma and pathways not leading to the formation of the hydroxyl radical start absorbing the discharge energy. It was observed that applying large potential differences results in a poor OH yield, while intensifying the glow of meta-stable noble gas species in the gas plume. Consequently, the largest current does not coincide with the voltage setting resulting in a maximum LIF curve. When tuning the velocity of a molecular beam, the discharge potential is of great importance, as it controls the amount of energy transferred to the discharge cell. Large discharge potentials lead to fast molecular beams, which is indicated by the shift of the maximum LIF signal towards shorter arrival times.

In addition to this, the FWHM velocity spread is increased. A detailed analysis of the changes in the beam profile and the beam velocity as a function of the discharge voltage are given in Table 4.5. The energy per ignition cycle was determined from current-voltage curves. Besides the valve opening parameters V and T, the discharge potential had the largest influence on the beam velocity. Especially for applications which are sensitive to the beam velocity and require sufficient OH density, the discharge voltage has to be chosen carefully, as large signal intensities with moderate heating of the beam can only be achieved in a narrow discharge voltage window.

voltage (V)	mean velocity (m/s)	velocity spread FWHM (%)	Energy (µJ)
-510	559.1 ± 8.9	20.5 ± 1.0	-
-550	572.1 ± 9.0	18.2 ± 0.9	90
-600	586.0 ± 9.2	20.6 ± 1.0	140
-650	598.2 ± 9.4	22.6 ± 1.1	200
-700	609.6 ± 9.6	24.5 ± 1.2	310
-750	623.1 ± 10.0	26.6 ± 1.3	460
-800	639.3 ± 10.7	28.8 ± 1.4	570
-850	726.8 ± 11.7	-	1064
-900	-	-	1730

Table 4.5: Evolution of the mean velocity and the FWHM velocity spread as a function of the discharge potential. The corresponding energy per ignition cycle is stated alongside. An analysis of the beam shape at large discharge delays was not possible due to its deterioration. An error of 5% is assumed for the FWHM values.

4.7 DBD discharge source

4.7.1 The physics of dielectric barrier discharges

The dielectric barrier discharge (DBD), also referred to as silent discharge, was first observed by Werner Siemens in 1857 [244]. It was soon realised that this type of discharge is particularly suitable for ozone generation, which is exploited in industrial processes such as the disinfection of drinking water and the bleaching of paper. Ozone reactors reaching capacities of several tons per day have been devised. Furthermore, DBD technology has found widespread usage in other applications such as pumping of CO_2 lasers, surface treatment, gas decontamination cells, UV excimer lamps and plasma screens. The DBD-process is readily maintained and cost effective, while offering excellent scalability from small laboratory usage to industrial scales. Dielectric barrier discharges have been reviewed in several comprehensive articles [187, 188, 245, 246].

A key feature common to all DBD cells is the presence of at least one dielectric surface interposed between or directly in contact with the electrodes. Depending on the application, a wide range of electrode geometries exist [246]. For illustration purposes common planar and radial DBD cell configurations are depicted in Fig. 4.26 a). Various dielectric materials such as glass, quartz, polymers or ceramics have been utilised. The width of the discharge gap ranges from 0.1 mm to a few cm. The presence of the dielectric layers minimises the metal electrode surface exposure to the gas, which reduces the risk of electrode corrosion and sputtering [246]. Due to the non-conductive nature of the dielectric material, alternating voltages are required for driving the discharge. Typically, voltage sources providing 1-100 kV and operating between 50 Hz to a few MHz are required. DBDs are capable of igniting over a wide pressure range from 0.1–5 bar, with the preferred working pressure often lying at around 1 bar. Below 0.001 bar a transition to RF glow discharges, which display different behaviours, is observed. Depending on the gas and the electrode geometry, transitions to more homogeneous atmospheric pressure glow discharges (APGD) have also been observed [247]. The discharge cells can either be implemented as closed systems or in an open geometry, which allows for gas flows.

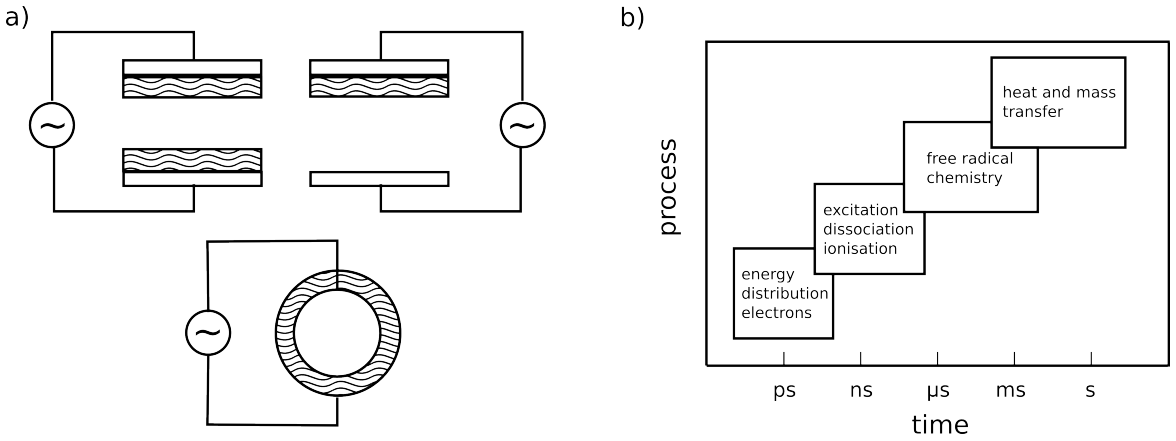

Figure 4.26: **a)** Common dielectric barrier discharge configurations [246]. The dielectric layer is indicated by wavy lines and covers at least one electrode. The electrodes are connected to a high-voltage waveform generator. **b)** Chronology of the processes taking place in a filamentary DBD [245].

In a DBD configuration, the discharge is formed by a multitude of narrow (radius ≈ 0.1 mm) microdischarge filaments that last for a few nanoseconds. During the course of a discharge cycle, the formation of such a filament involves several steps [187, 188, 245]. As the magnitude of the oscillating voltage rises during a half-period, the electric field increases beyond the breakdown field of the gap. This results in electron avalanches leading to the formation of streamers, which are highly ionised channels rapidly propagating between the electrodes [228]. Considerable space charge induces high electric field strengths at

the streamer tip, thereby causing an ionisation wave travelling towards the anode's dielectric layer. Subsequently, the ionisation wave is reflected back from the anode towards the cathode, where a cathode fall layer develops. At the dielectric surface the discharge filament widens up and acts like a surface discharge covering a much larger area than the width of the filament diameter eclipses. Deposition of charge on the anode dielectric leads to a reduction of the electric field, which quenches the ionisation and the discharge is choked. Upon the next voltage half-cycle the process is inverted. A part of the negative charge deposited by the surface discharge remains on the dielectric plate, which causes neighbouring discharges to strike outside of this region in case the applied voltage is above the breakdown point. Hence, the purpose of the dielectric is not only to limit the current, energy and the duration of the discharge, but also to distribute the discharge filaments evenly across the electrode and dielectric structures. Therefore, dielectric barrier discharges fall into the category of non-equilibrium low temperature plasmas, where the gas surrounding the plasma channels is hardly heated. It is these properties which render the DBD particularly desirable for the application in molecular beam techniques, as the low energy dissipation results in cold molecular beams with low forward velocities. The generated radicals and excited species will therefore propagate at velocities similar to the surrounding carrier gas [162].

The characteristics of a plasma filament resemble that of a transient glow discharge and the key properties are listed in Table 4.6 [187]. The diameter of the streamers depends on the density and the electronegativity of the gas. Based on experimental findings, microdischarge channel radii for noble gases have been reported in decreasing order as He $>$ Ne $>$ Ar $>$ Kr [247]. The amount of charge transported is proportional to the gap width and the ratio ε/g, where ε denotes the relative permittivity of the dielectric material and g is the thickness. As an individual microdischarge filament is active for a short duration on the nanosecond timescale, many filaments are formed during one half-wave of the oscillating potential. The surface coverage with microdischarges depends on the power density and it has been reported that irradiation of the DBD's active zone with UV light results in an augmented number of microdischarges which are spread out more evenly [248]. At high water concentrations the irradiation of the DBD with UV-light increases the overall OH radical yield, as it counteracts the depletion of microdischarges caused by the reduced surface resistance of the dielectric in the presence of water [248].

In barrier discharges charged particles decay relatively fast and the discharge chemistry is mostly dominated by radical reactions [188, 245]. The relevant timescales following the ignition of a filament are depicted in Fig. 4.26 b). The filamentary discharge forms on the nanosecond timescale and acts like a chemical reactor providing electron density

Duration: 1-10 ns	Charge transferred: 0.1-1 nC
Radius filament: ≈ 0.1 mm	Electron density: $10^{14} - 10^{15}$ cm^{-3}
Peak current: 0.1 A	Electron energy: 1-10 eV
Current density: $10^6 - 10^7$ A/m^2	Temperature: close to surrounding gas

Table 4.6: Properties of a microdischarge streamer as reported in ref. [187].

and energy for dissociation and excitation processes. The initiated free radical chemistry lasts from the microsecond up to the millisecond timescale. It is important to notice that in molecular beams the expanding gas package clears the discharge region within tens of microseconds, which effectively quenches the radical reactions due to the dropping collision rate. The transit time is not sufficient for a chemical equilibrium to be established. The main pathways involved in the production of the OH radical in mixtures of noble gases and water are identical to pathways (a) and (d) in section 4.6.2. However, upon the addition of small amounts of oxygen, alternative pathways for OH formation need to be taken into consideration as well [249, 250]:

$$O_2 + e^- \rightarrow O(^3P) + O(^1D) + e^- \quad \text{(i)}$$

$$O(^1D) + H_2O \rightarrow 2\,OH\,. \quad \text{(j)}$$

4.7.2 Construction of the DBD discharge source

The dielectric barrier discharge is modelled after the design introduced by Even et al. [162] and has been adapted to fit the NPV. A schematic illustration of the NPV valve with a mounted DBD assembly is depicted in Figure 4.27. The DBD electrode consists of a NdFeB-ring magnet with an inner diameter of 9 mm, an outer diameter of 12 mm, and a thickness of 2 mm. The ring magnet electrode is contacted via an electrode washer soldered onto a wire running through a duct in the discharge front plate. Once assembled, the duct is sealed by applying TorrSeal. The diameter of the valve nozzle measures 0.3 mm and the dielectric inset joins smoothly with the front plate of the valve to form a 50° opening angle. The discharge takes place along the inner surface of the dielectric channel head between the DBD electrode and the grounded stainless steel valve body. The location of the interface between the grounded front plate and the dielectric cone inset was chosen to lie close to the valve orifice. This ensures sufficiently large gas pressures at the dielectric channel head and allows for reliable ignition of the discharge. The DBD is initiated by applying an alternating-current high-voltage pulse with a fixed frequency of around 1 MHz and an amplitude of roughly 4 kV to the DBD electrode. The electronic schematic of the DBD power supply is depicted in Fig. 4.28 a) and incorporates the equivalent circuit of a dielectric barrier discharge cell consisting of one dielectric layer. The equivalent circuit

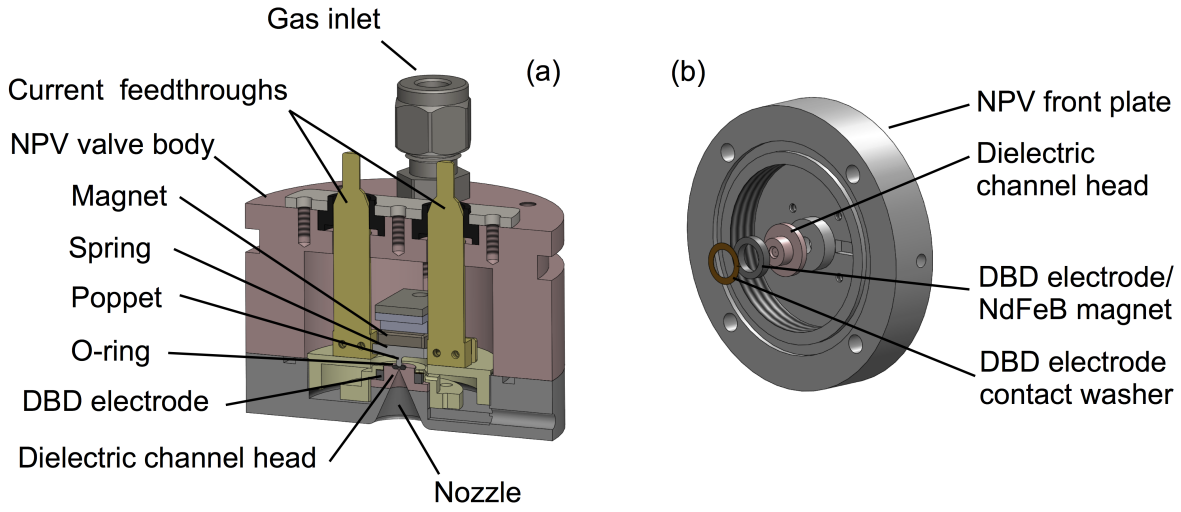

Figure 4.27: Schematic illustration of the DBD valve with mounted discharge assembly **(a)** and a detailed view of the electrodes and insulators taking part in the dielectric barrier discharge process **(b)**.

takes into account the capacitance of the dielectric C_d, the capacitance of the gas gap C_g, as well as the variable resistance R_g once the discharge is ignited. A detailed analysis of the electronic characteristics of DBDs can be found in references [245, 246]. However, an important result which deserves mentioning is that the power available to the discharge is proportional to the frequency. During each period the number of microdischarge filaments remains identical and increasing the number of cycles per second consequently results in an increased discharge activity. Hence, it is beneficial to operate the discharge at high frequencies. A typical voltage profile for a discharge duration of 10 µs is depicted in Fig. 4.28 b). The circuit displays a rather long ring-down time of 30 µs as the discharge electronics was characterised with the valve detached.

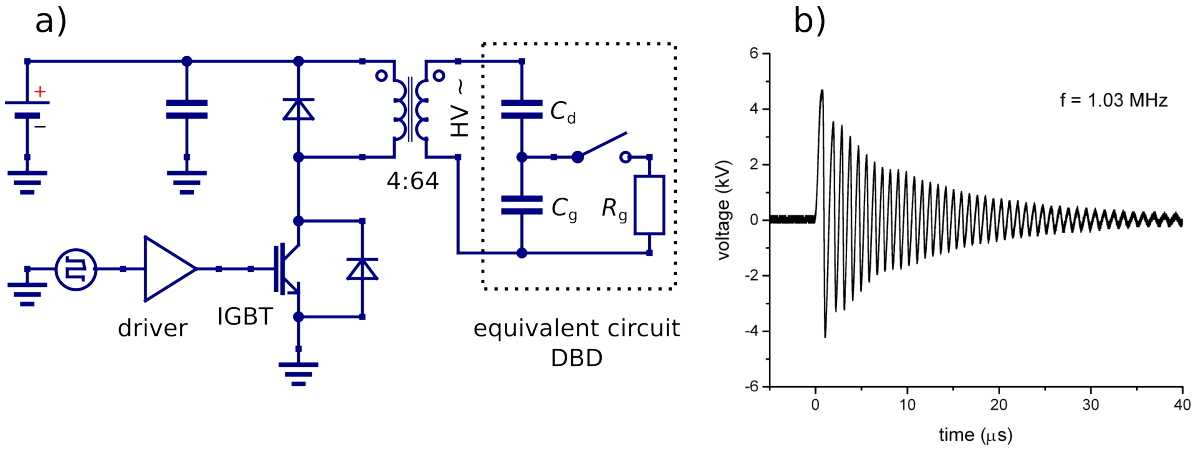

Figure 4.28: **a)** Simplified circuit diagram of the discharge electronics, which was built and conceived by N. Janssen. The DBD driver is based on an IGBT switch in combination with a 4:64 step up transformer. **b)** Typical HV burst pulse at around 1 MHz.

4.7.3 Results and Discussion

The DBD discharge source has been characterised under conditions identical to the ones prevailing during the pinhole discharge in order to ascertain maximum comparability between the two different discharge techniques. The main characteristics of the OH beam generated via the DBD method are given in Table 4.7. Furthermore, for some experiments O_2 was added to the backing gas to improve the discharge stability and the OH production efficiency.

The mean velocity and the velocity spread are comparable to the results of the pinhole-discharge source. The DBD source, however, seems to exhibit improved cooling characteristics. More than 99 % of the OH radicals were found to be in the ro-vibrational ground state. This can be deduced from the rotationally resolved electronic transition spectrum (Figure 4.29), in which no signals due to transitions starting from $J''= 5/2$ could be detected within our sensitivity limits. We ascribe the lower rotational beam temperature to the gentler discharge process. Hence, the DBD source is to be given preference when colder species are required.

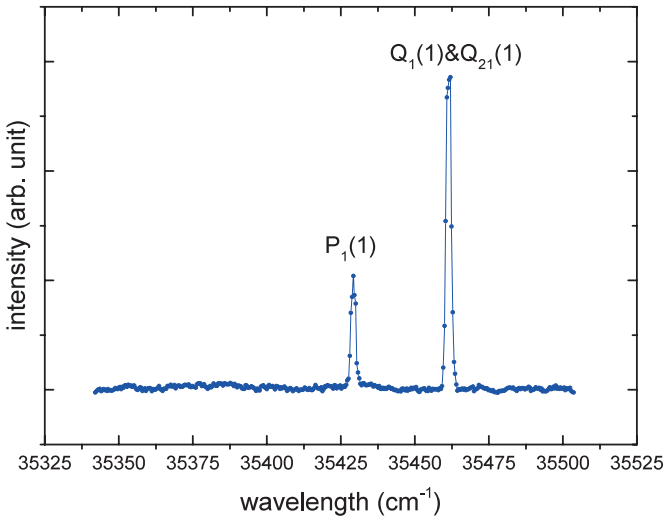

Figure 4.29: Rotationally resolved electronic spectrum of OH generated by the DBD source. The carrier gas is Ar. The $P_1(1)$ and $Q_1(1)$ ($Q_{21}(1)$) transitions from the $J''= 3/2$ ground state are observed. No indication of the $P_1(2)$ and $Q_1(2)$ transition from the first excited rotational state $J''= 5/2$ can be found. The x-axis is the excitation laser wavelength measured in vacuum. Reprinted from [178], with the permission of AIP Publishing.

On the other hand, the OH density yield of the DBD process is a factor 3 lower for all carrier gases when compared to the OH densities achieved with the pinhole discharge valve. In part, the decrease is caused by the differing nozzle shapes. The DBD source features a nozzle diameter of 0.3 mm, whereas the pinhole discharge source possesses a

nozzle with an opening of 0.5 mm in diameter. The conventional pinhole-discharge valve has a 60° full cone angle, whereas the DBD valve is equipped with a 50° cone. Another important difference between the two valves is the geometry of the section in the expansion channel at which the discharge strikes. The DBD source has a through-cone structure, whereas the pinhole discharge expansion channel exhibits a straight and narrow initial section. The gas density in the pinhole channel is therefore higher than in the DBD source upon initiation of the discharge. The larger gas density in the pinhole channel not only helps with igniting the discharge, but the conversion into radicals is also more complete at augmented pressures, as the dissociation process is mediated by collisions.

Furthermore, we observed that the addition of O_2 molecules to the molecular beam enhanced the radical density of the DBD source by a factor of around 2.5, as listed in Table 4.7. Adding O_2 not only increased the radical density, but also improved the discharge stability. The shot-shot noise was reduced to variations of a few percent. Interestingly, a similar performance enhancement was not observed by adding O_2 to the gas mixture in the conventional discharge valve. Upon the addition of O_2, the combined reaction pathways (i) and (j) given in section 4.7.1 contribute to the formation of OH radicals. Amongst gases subjected to dissociation via electron impact, molecular oxygen plays a special role as it allows for very high dissociation efficiencies. It has been reported that a large fraction of the available electron energy ($< 85\%$) can be employed for the dissociation of O_2, provided that the energy distribution covers the region from 4 to 8 eV [188, 251]. This effect is due to excitation of $O_2(X\ ^3\Sigma_g^-)$ from the ground state to the electronically excited $O_2(A\ ^3\Sigma_u^+)$ and $O_2(B\ ^3\Sigma_u^-)$, which dissociate into $O(^3P) + O(^3P)$ and $O(^3P) + O(^1D)$, respectively[188, 251]. Presumably, it is the increased energy uptake in the presence of O_2, which stabilises the discharge and allows for the distribution of this energy within the gas via subsequent radical reactions. The discharge structure and the electron energy distribution in a pinhole discharge are considerably different from those in a dielectric barrier discharge. Pinhole discharges are more violent and cause more heating. When adding O_2 to the pinhole discharge source no enhancement of the OH radical production was observed, which could be due to an unsuitable energy distribution of the electrons.

In a supersonic expansion, the mean beam velocity depends on the average mass of the gas mixture [109, 131]. Since the molecular mass of O_2 is smaller than that of the carrier gases, the beam velocity can be tuned by varying the O_2 concentration. By changing the O_2 concentration from 40 % to 10 %, the velocity of the OH beam could be altered from 510 $\mathrm{m\,s^{-1}}$ to 495 $\mathrm{m\,s^{-1}}$. This provides additional flexibility for experiments in which the

carrier gas	mean velocity ($m\,s^{-1}$)	velocity spread FWHM (%)	population in rotational ground state (%)	density $\times 10^{10}$ (cm^{-3})
Ar	646.2±7.1	(11.2±0.7)	> 99	3.7±2.3
Ar+20%O_2	693.8±7.3	(12.8±1.1)	> 99	9.3±5.8
Kr	489.9±5.6	(17.2±1.5)	> 99	1.3±0.8
Kr+16%O_2	509.3±5.9	–	> 99	3.4±2.1
Xe	396.5±4.5	(12.6±0.7)	> 99	1.1±0.7
Xe+4%O_2	475.0±5.2	–	> 99	2.3±1.5

Table 4.7: OH radical beam properties generated by the DBD source. The densities were measured 5 cm downstream of the valve. The data was acquired by myself and D. Zhang conducted the analysis.

velocity of the incoming molecular beam plays a crucial role. Compared to the pinhole discharge source, the DBD source provides molecular beams which are slower.

4.8 Conclusion and Outlook

In this chapter two high–performance discharge sources providing an efficient and reliable method for the generation of cold and intense free radical beams have been introduced. The discharge heads are very versatile and can be employed with a wide range of experiments. Combining state–of–the–art discharge technology with the high density and short pulses offered by the Nijmegen pulsed valve allows for the generation of dense OH beams with favourable beam profiles. While the hydroxyl radical has proven to be suitable for the characterisation of the discharge source, the formation of radicals is by no means limited to this species and NH radicals have successfully been generated from NH_3 in the Basel labs. Both the conventional pinhole–discharge and the DBD sources display superior beam properties compared to previous sources. The two implementations succeed in the generation of translationally and rotationally cold and intense OH radical beams. Deceleration and trapping experiments will benefit from the high density and low translational temperature achievable.

The discharge physics of both the pinhole source and the dielectric barrier discharge (DBD) source have been discussed. The underlying discharge processes are of fundamentally different nature and result in unlike beam properties. The pinhole discharge source yields high radical densities. However, the beam experiences rotational as well as translational heating due to more violent discharges. In contrast, the gentle nature of the discharge in the DBD source results in a ground state population exceeding 99%.

Addition of O_2 to the gas mixture increases the OH radical density as well as the discharge stability and allows to tune the mean beam velocity. To a certain degree, the two sources offer complementary properties. Which source is best chosen depends on the application. Spectroscopic investigations or collision experiments involving radicals in a molecular beam would certainly profit from the high rotational state purity and could cope with the slightly lower densities offered by the DBD source. For applications such as Stark or Zeeman deceleration in conjunction with trapping of neutral molecules, the pinhole source is deemed superior. The deceleration process itself offers rotational state selection and it is therefore desirable to choose the denser radical source, as neither deceleration technique allows for the compression of phase space. Hence, the plate discharge source was chosen for the deceleration and trapping experiments described in the following chapters. The influence of the discharge delay and the discharge potential on the beam profile and the velocity have been investigated in more detail for the pinhole discharge due to the importance of these parameters for deceleration.

Both sources still provide room for further improvement. It would be interesting to compare the suitability of different discharge nozzle geometries for the generation of radical species. In addition to this, the DBD source would benefit from an enhanced power supply allowing for the adjustment of the oscillation frequency and the number of oscillation cycles, similar to the DBD driver presented in references [162, 252]. An adjustable oscillation frequency would allow to better match the impedance between the driver and the discharge head.

Chapter 5

Optimised Stark deceleration of OH radicals to low final velocities

5.1 Introduction

Translationally cold molecules have become an attractive subject of research in recent years. A number of techniques for the generation of cold molecules has been developed [1, 5, 35, 87, 253], among which Stark deceleration is one of the most important [34, 35, 70, 190]. This method finds a wide range of applications in spectroscopy [90, 254–256], collision-dynamics studies [14, 55, 81, 88, 92, 93, 257–264] and trap loading experiments [28, 49, 54, 74, 240, 265, 266]. The principle of Stark deceleration has been well documented [35, 87], and a number of operation schemes have been developed for the optimization of Stark-decelerated molecular beams in different types of experiments [78–80, 82].

The operation principle of a Stark decelerator has been described in section 3.2. In brief, a Stark decelerator employs time-varying inhomogeneous electric fields produced by an array of dipolar electrodes to slow down pulsed beams of polar molecules [34, 35]. When a package of molecules approaches a set of electrodes, they are switched to high electric potential. Molecules in low-field-seeking Stark states experience a force which reduces their kinetic energy. The voltages on the electrodes are switched off before the molecules reach the maximum of the dipole potential in order to prevent their re-acceleration after they have passed the electrodes. This procedure is repeated at every pair of electrodes along the decelerator until the molecules have reached their target velocity at the exit of the assembly.

Based on: D. Haas, S. Scherb, D. Zhang, S. Willitsch, Optimizing the density of Stark decelerated radicals at low final velocities: a tutorial review, *EPJ Tech. Instrum.*, 2017, **4**, 6.

The final velocity of the package of molecules is controlled by a parameter referred to as phase angle Φ_0, which corresponds to a scaled position of a "synchronous molecule" at which the high voltages on the electrodes of the decelerator are switched. Successful deceleration of the molecules to the target velocity requires careful coupling of the molecular cloud into a stable phase-space volume determined by the phase angle [77, 78, 80]. Successful coupling requires prior knowledge of the initial velocity of the molecular package and the incoupling time, i.e. the time required for the molecules to fly from their point of generation to the entrance of the Stark decelerator. Efficient coupling leads to an optimised beam density after Stark deceleration [78].

In this chapter, the assembly of the Stark decelerator and its integration into the experimental setup will be discussed. These more technical aspects of Stark deceleration are followed by a comprehensive introduction on how to optimise our decelerator to achieve a maximum density of decelerated radicals at velocities below 50 m/s. Such optimisations are of particular interest for trapping experiments [28, 74, 240, 265] and low-energy scattering applications [267, 268]. As every Stark deceleration experiment commences at the source, guidelines for adjusting the relevant parameters leading to high-density molecular beams of radicals are discussed. Subsequently, procedures for optimising the number density of molecules after the Stark decelerator and guidelines for improving the signal-to-noise ratio of the experiment by enhancing the detection efficiency are considered in detail. The optimisation can therefore take place along three different routes and a classification scheme for the optimisation parameters is introduced. Class I optimization comprises all the parameters resulting in an increased number density of the decelerated radical package, which includes optimising the radical source as well as the operation of the Stark decelerator. Class II optimization seeks to increase the signal-to-noise ratio of the experiment and thus improve the duty cycle. Finally, a procedure for the determination of the density after the decelerator is outlined. As the discharge assembly of the Nijmegen pulsed valve (NPV) has been characterised with OH (hydroxyl) radicals and this species is frequently used in deceleration experiments [28, 74], it serves the purpose of an exemplary species well. The deceleration and trapping experiments described in the next chapter will profit from the optimisation procedures introduced here.

5.2 Experimental setup

Our experimental setup is displayed in Fig. 5.1. The first part allows for the determination of molecular beam properties in the source chamber and is identical to the experimental scheme introduced in section 4.4. The NPV body is mounted onto an xyz-translation stage such that the position of the valve can be adjusted relative to the detection laser

beam and to the central axis of the decelerator. The interior of the valve body acts as a gas reservoir. Normally, the valve is operated at backing pressures in the range of 1-3 bar including about 1-2% water vapour at room temperature (17.535 torr, 2.337 kPa at 20° [269]). The NPV generates short gas pulses of a few ten µs duration at a repetition rate of 10 Hz. The pressure in the source chamber during operation of the valve is on the order of $1{\cdot}10^{-5}$ mbar. Depending on the choice of noble gas, molecular beams in different velocity regimes can be produced. For our Stark decelerator, Kr and Xe yield beams of sufficiently low initial velocity enabling the generation of dense OH beams at low final velocities. A full characterization of the molecular beam properties is given in Table 4.4.

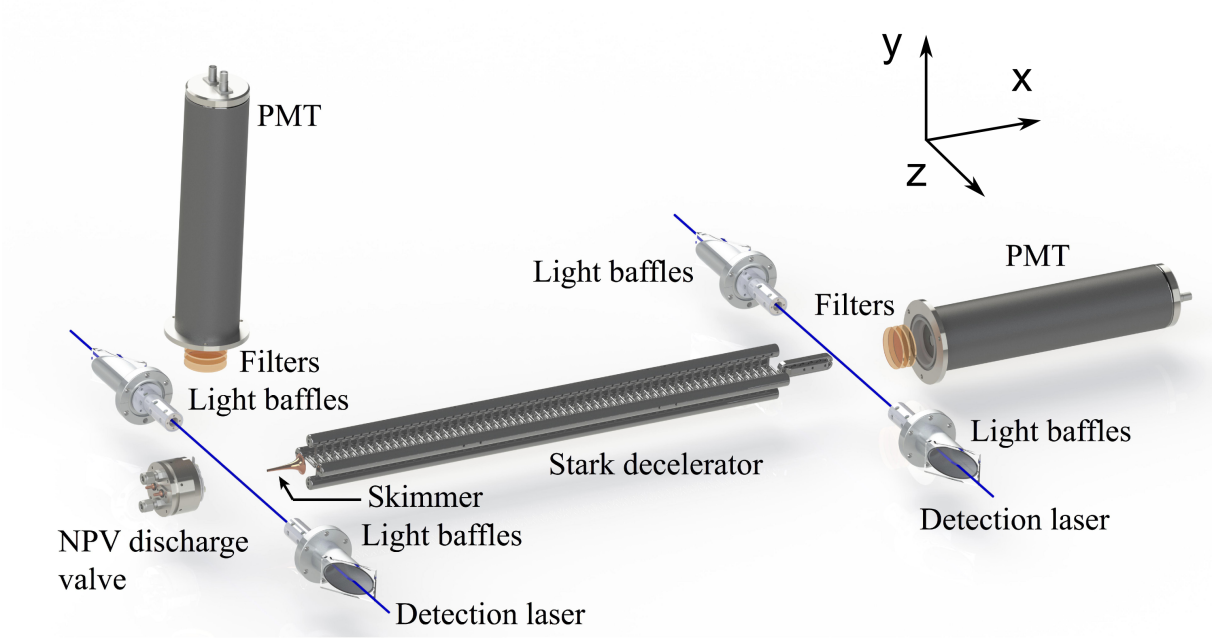

Figure 5.1: Schematic representation of the experimental setup. The NPV discharge valve is used for the production of molecular beams containing internally cold OH radicals. A skimmer with an orifice of 3 mm diameter is placed between the valve and the Stark decelerator. The beam of OH molecules is detected by laser-induced fluorescence (LIF) either 101–137 mm downstream from the nozzle or 11.5 mm after the exit of the 124-stage Stark decelerator. Stray light is reduced by aligning the 282 nm-excitation laser beam through Brewster windows and light baffles ($\varnothing$= 3 mm). LIF at 313 nm is collected on a photomultiplier tube (PMT) using a lens and a stack of bandpass optical filters.

The OH beam was probed using a 282 nm excitation laser crossing the expanded gas package 101–137 mm downstream of the valve opening or 84.8 mm from the entrance of the Stark decelerator. The laser excites OH radicals in their $X\ ^2\Pi(v = 0)$ ground state to the first electronically excited state $A\ ^2\Sigma(v = 1)$, where v denotes the vibrational quantum number. The 282 nm laser radiation was generated using a frequency doubled dye laser

(Pulsare, Fine Adjustment) pumped by a Nd:YAG laser (Surelite II, Continuum). The output energy of the LIF excitation laser was measured to be approx. 2.0 mJ/pulse and the pulse duration is 10 ns. The $A - X$ transition was experimentally found to be saturated at a laser intensity of 0.2 mJ/(mm^2 pulse). Off-resonance fluorescence at 313 nm from the $A\ ^2\Sigma(v = 1) - X\ ^2\Pi(v = 1)$ transition was collected by a lens coupled to a calibrated photomultiplier tube (PMT) (Electron Tubes B2/RFI, 9813 QB). In order to limit the amount of stray light in the chamber, the laser beam was guided through Brewster windows and through pinholes with a diameter of 3 mm. Further stray light suppression from the discharge process or the excitation laser was achieved by installing bandpass filters in front of the PMT, as indicated in Fig. 5.1. After having passed the LIF detection region of the source chamber, the molecular beam was guided through a skimmer (Beam Dynamics, model 50.8) with an opening diameter of 3 mm and a length of 50.8 mm. The total interior angle at the apex amounts to 25° [215]. The skimmer is located 18.2 mm from the laser beam, which results in valve-skimmer distances of 119–155 mm. In accordance with the skimmer clogging criteria ($Kn \geq 2$) introduced in section 4.2.5, these distances should allow for operation of the decelerator without being affected by too severe skimmer clogging. In this experimental setting, the skimmer primarily serves as a differential pumping barrier and the pressure in the decelerator chamber increased from the low 10^{-8} mbar regime by an order of magnitude when operating the molecular beam source. After having passed the skimmer, the package of OH radicals is coupled into a 124-stage Stark decelerator and the velocity in the forward direction is reduced to the desired value. The high-voltage switching sequence applied on the decelerator electrodes is directly calculated by the trajectory simulation code introduced in chapter 3. A pulse generation card (Spincore, Pulse Blaster) is programmed with the simulation output and the resulting TTL trigger burst sequence is sent to the high-voltage switching boxes. After having left the decelerator, the OH package is probed by a LIF excitation laser located 11.5 mm from the decelerator exit. The detection setup after the decelerator is equipped with the same precautions against stray light as in the source chamber. Scanning the delay of the laser pulse relative to the discharge allows for the recording of time of flight (TOF) profiles after the decelerator.

5.2.1 Decelerator structure

A Stark decelerator consists of alternating horizontal and vertical dipolar electrode pairs, which allow for the generation of switched inhomogeneous electric fields. The appearance of the repetitive and highly symmetric electrode structure is tightly linked with its purpose, namely the repeated removal of a fixed amount of kinetic energy from a package of OH molecules. Within an electrode pair, the centre-to-centre distance amounts to 5 mm

and the diameter of the electrode pins was chosen to be 3 mm. The electrode pairs are typically operated at ±10 kV, which results in a mean electric field strength of 10 kV/mm at an electrode pair surface-to-surface separation of 2 mm. This configuration provides a maximum deceleration energy of 1.43 cm^{-1} per stage for OH molecules. In order to prevent arcing via field emission of electrons from rough edges, the entire high voltage structure is highly polished. Due to electropolishing of the electrode pins, their diameter ranges from 2.8–2.92 mm instead of the envisaged 3 mm. The effective diameters are accounted for in the trajectory simulations and electrode pairs are formed from thicker and thinner electrodes to compensate differences in the electrode separation. The longitudinal centre-to-centre separation between two subsequent electrode pairs measures 5.5 mm. An additional 13 stages have been realised in the form of a more compact mini-decelerator. This 13-stage extension uses the same electrode spacing and rod diameter (see Fig. 5.4) as the main decelerator. In total, the decelerator consists of 124 electrode pairs, which results in a total length of 676.5 mm.

As depicted in Figs. 5.2 and 5.3, the decelerator consists of four parallel and highly polished HV-rods into which the electrode pins are mounted. The supporting rods are held in place by a hanger assembly consisting of two circular disks which are interconnected by four supporting bars. Together, the disks and the bars form a frame, which allows for safe handling of the delicate electrode structure. The HV bearing structures are electrically insulated from the frame using Macor rods. The hanger assembly acts as a stabilisation frame, which allows for mounting and aligning the decelerator inside the vacuum chamber. The assembly of the electrode structure is depicted in Fig. 5.2. Before mounting the electrodes onto the frame, the HV-rods were pre-fitted with 55 and 56 electrode pairs, respectively. The diametrically opposite pairs bearing 55 electrode pins were inserted first. Great care had to be exercised not to scratch the electrodes when inserting the last HV-rod into the limited central space of the frame. The electrodes were adjusted such that the horizontal and vertical pairs interlock and the desired electrode opening and longitudinal spacing was achieved. The final alignment was verified with the help of an alignment mask, which fits onto the front bore holes of the decelerator as depicted in Fig. 5.3 a). After insertion of the hanger assembly into the vacuum chamber, the electrodes were connected to the HV feedthroughs of the chamber, see Fig. 5.3 b).

5.2.2 Vacuum chamber

As depicted in Fig. 5.4, the experimental setup consists of three stainless steel vacuum chambers which house the valve, the decelerator and the trap (not shown here). In order to improve the expansion conditions for the molecular beam and to cope with the high gas

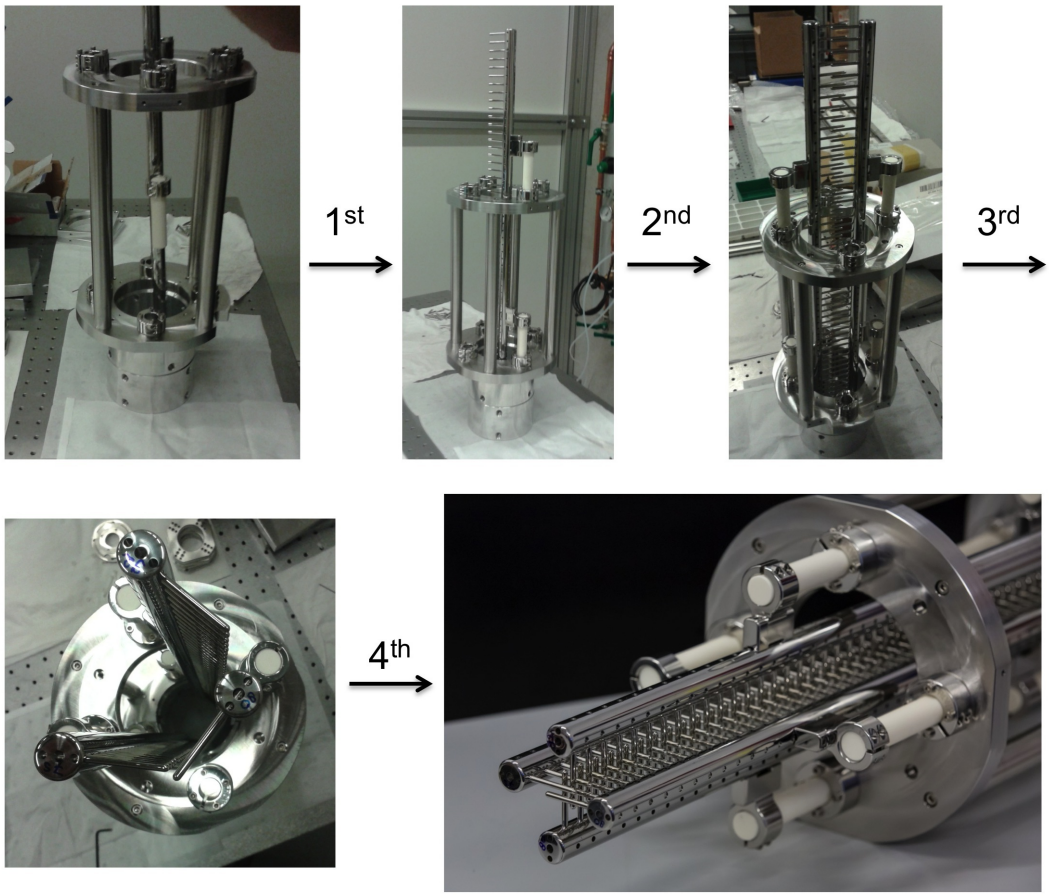

Figure 5.2: Stepwise insertion of the pre-assembled HV-rods and electrode pins into the hanger assembly.

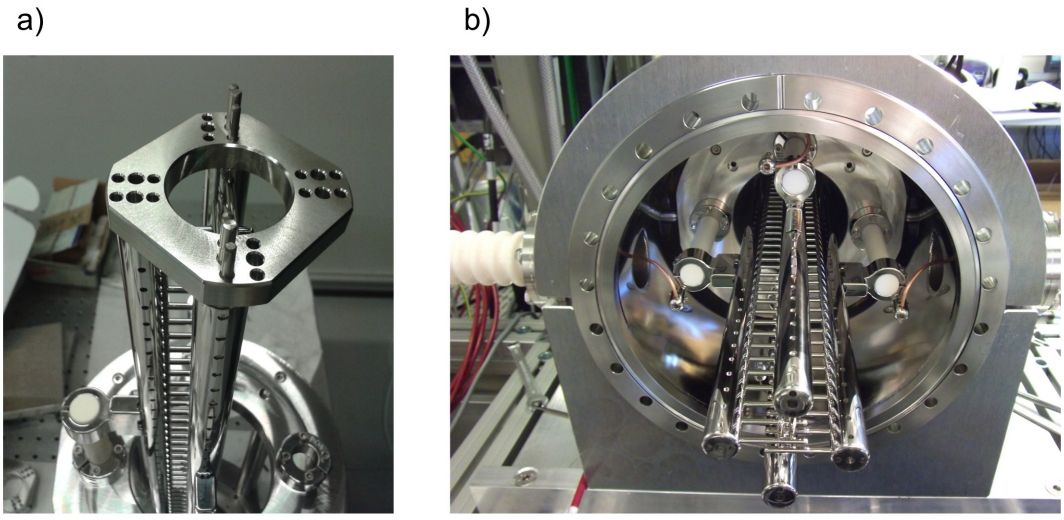

Figure 5.3: **a)** Alignment mask guaranteeing correct relative alignment of the electrode pins on both sides of the decelerator. **b)** Application of electrical contact to the HV electrodes after positioning the decelerator inside the vacuum chamber.

load when operating the valve, the pumping capacity in the source chamber is enhanced compared to the remaining chambers. A magnetically suspended turbo molecular pump (TMP) (Leybold Oerlikon, Mag W 1300 iP) with a pumping speed of 1050 l/s for argon is employed in the source chamber. Smaller pumps with an argon pumping capacity of 520 l/s (Leybold Oerlikon, Mag W 600 iP) are mounted onto the decelerator and trap chamber. After a few days of pumping, pressures in the low 10^{-8} mbar range can be achieved. Each of the chambers is equipped with a pressure gauge and the composition of the gas background in the trap chamber can be determined with a residual gas analyser (RGA) (SRS, RGA200).

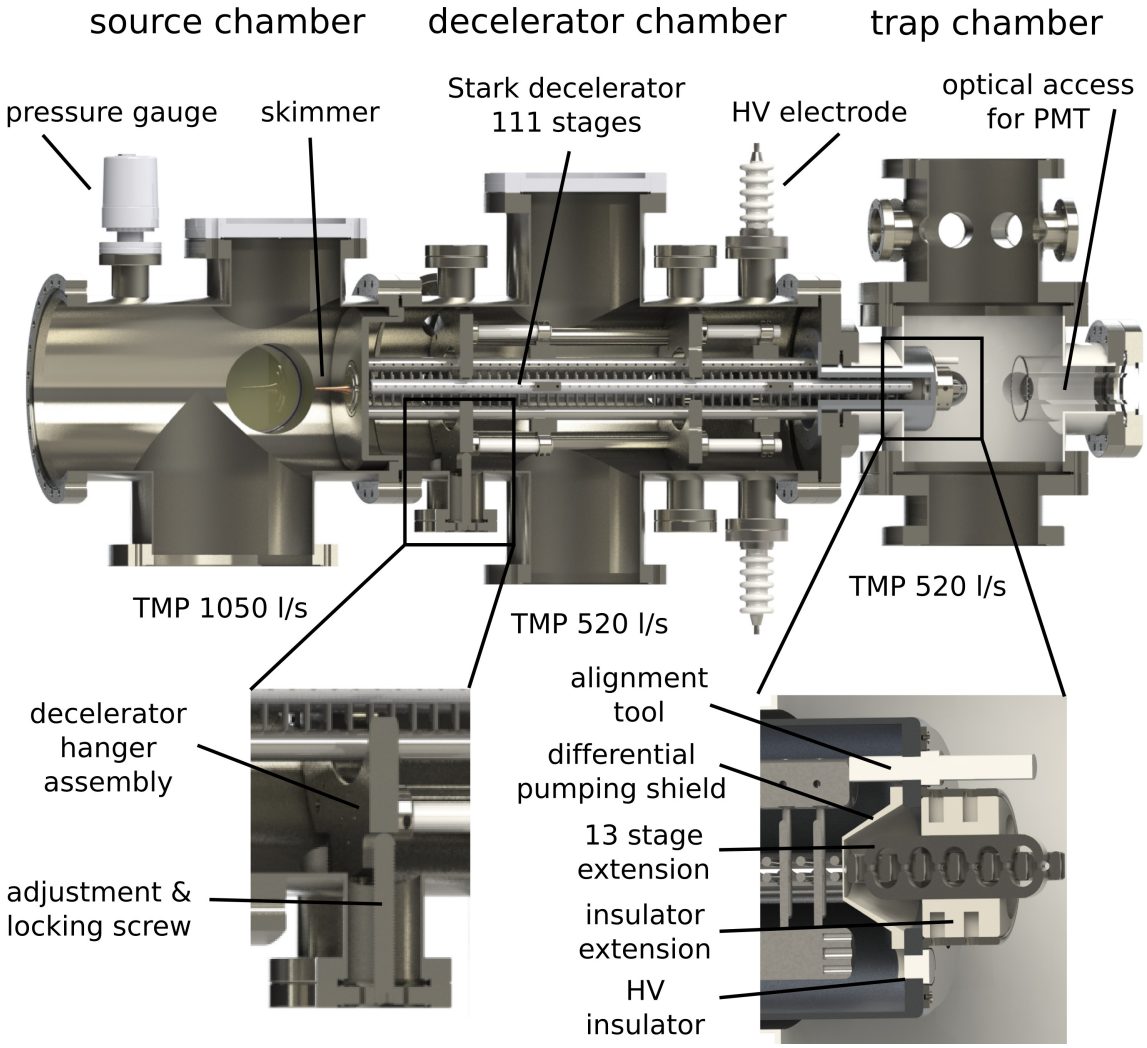

Figure 5.4: Cross sectional view of the vacuum chamber consisting of the source, decelerator and trap chamber. The decelerator consists of 124 stages and ranges from the decelerator chamber into the trap chamber. The enlarged section on the left displays the adjustment and locking screw for the hanger assembly. The right inset figure depicts the coupling of the more compact 13-stage extension to the main decelerator. The Ar pumping speeds are stated below each pump.

As depicted in the left inset of Fig. 5.4, the circular discs of the decelerator hanger assembly rest on adjustment and locking screws, which allow for reproducible positioning of the decelerator. Each of the two discs is held in place by sets of 2 horizontal and 4 vertical locking screws. The 2×2 mm^2 opening of the decelerator needs to be aligned to the skimmer and the valve opening such that the OH flight path lies along a direct line of sight through the entire setup. Initially, the decelerator was aligned with the help of a theodolite. Over the course of time, the alignment was confirmed several times using an adjustment laser travelling from the trap chamber towards the valve opening. Alternatively, one can also check the alignment via optical inspection. The decelerator opening is large enough for looking through the entire assembly. The 111-stage section of the main-decelerator ranges into the trap chamber and is continued by a 13-stage extension, which uses the same electrode spacing and diameter, but allows for a more compact construction. This design is desirable if a trap is to be placed close to the end of the electrode structure. Furthermore, the extension mounting allows for differential pumping between the decelerator and the trap chamber. The differential pumping can be improved further by inserting a shield with a circular hole between the two sections of the decelerator. As depicted in Fig. 5.4, the 13-stage extension is mounted onto a cylinder enclosing the end of the main-decelerator. The opening of the extension needs to be aligned to the opening of the main-decelerator and the longitudinal distance between the last main-decelerator electrode and the beginning of the extension is required to measure one stage separation (5.5 mm). The slackness of the screw holes in the extension's mounting plate is sufficient for the in-plane alignment. The longitudinal alignment was facilitated by inserting a removable spacer tool. The extension is electrically connected to the main decelerator via HV-insulator insets machined out of Macor.

5.2.3 Conditioning

Prior to operating the decelerator, the HV-electrodes have to be conditioned. During the conditioning procedure, the DC-voltage applied on an electrode pair is increased successively. The purpose of conditioning is to ensure that the electrodes are capable of withstanding the applied potential difference without the occurrence of discharges. To a certain degree, the conditioning process can improve the surface quality of the electrodes. Small unevenness in the electrode structure may be smoothed out by discharges. Furthermore, dust particles sticking to the electrode surface charge up and are removed from the electrode via Coulomb repulsion. As most discharges result in the release of particles into the vacuum, a discharge event can reliably be detected by a pressure spike. Alternatively, an ampere meter connected in series between the HV-supply and the electrode can be employed for monitoring the conditioning process. A typical conditioning setup is depicted

in Fig. 5.5. In order to protect the decelerator from violent and abrasive discharges, the discharge current was limited by large conditioning resistors (100 MΩ). Furthermore, the discharge voltage was increased slowly, such that discharges occur at the lowest voltage threshold which triggers them [111]. Up to potential differences of ±5 kV, the discharge voltage was increased at a rate of 1.0 kV every 5 minutes in the absence of discharges. If a discharge was detected, the voltage was kept constant until no further discharges occurred over a period of 5 minutes. Above ±5 kV the step size was halved. It is recommended to condition to potential differences which are larger than the intended operation range. Consequently, the decelerator was conditioned to 11.5 kV for operation at ±10 kV. Failure to condition can be due to damaged electrode surfaces or the accumulation of dust on the electrodes. It was found helpful to invert the polarity of the applied potentials if an excessive number of discharges was experienced. Permanent creeping currents, which are accompanied by a lasting increase of the background pressure, indicate an insulator breakdown. In such cases the chamber has to be opened and the insulators need to be screened for discolouration spots and holes. It might be necessary to re-polish defective regions. At large potential differences, i.e. above ±20 kV, the formation of potentially hazardous Bremsstrahlung X-rays could occur, as the free electrons in a discharge are accelerated by the electric fields, which has been reported in ref. [270]. The following references were found to be useful for troubleshooting and understanding conditioning problems [111, 271, 272].

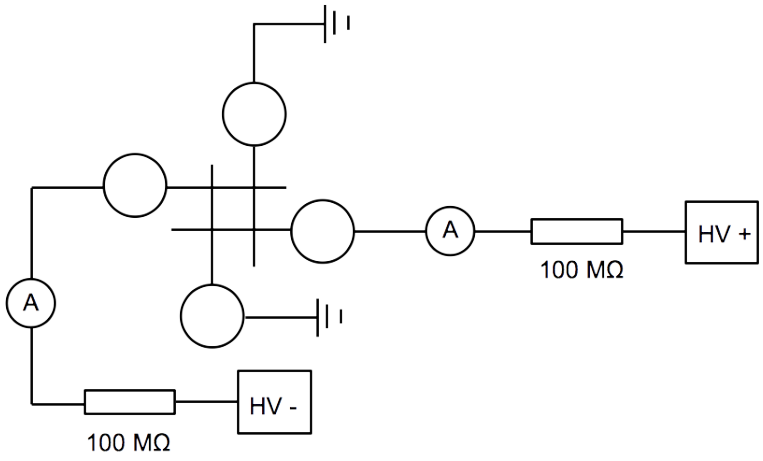

Figure 5.5: HV-conditioning scheme applied on the horizontal electrode pair. The large resistors limit the discharge current to the µA-regime. The vertical electrodes are grounded and the scheme is reversed for conditioning the vertical electrode pair.

5.2.4 HV-switching electronics

Due to the large initial velocities of the molecular package upon incoupling, the time required for traversing an electrode stage is around 10 µs. Therefore, guiding molecular packages through the decelerator or reducing their velocity requires fast switching of the applied potential from one electrode pair to the subsequent. The switching is accomplished using four fast high voltage transistor switches (Behlke, HTS 301-03-GSM HFB option). These switches can operate up to 30 kV with a minimum pulse width of 200 ns and maximum burst frequencies of 2.5 MHz [273]. The circuit diagram of the HV-switching equipment is depicted in Fig. 5.6. The black circles in the middle represent the four HV-rods onto which the electrode pins are attached. Each HV-rod is connected to a HV-switch. Depending on the state of the switch, the rods are either grounded or connected to 0.5 µF backing capacitors (Hivolt Capacitors Ltd, PPR200-504), which are rated up to 20 kV. The backing capacitors are continuously recharged by HV-power supplies. The capacitors are required to prevent voltage drops during the switching scheme due to the non-negligible capacitance of the decelerator structure, which is estimated to be around 100 pF [61, 111]. Upon every switching cycle this capacitance has to be charged anew. As a safety precaution, 80 MΩ drain resistors are connected parallel to the capacitors and ensure complete discharging of the capacitors after turning off the power supplies. Alternatively, the capacitors can be drained via a shiftable, smaller 20 MΩ resistor, which is ideal for maintenance tasks. To prevent ringing, 330 Ω resistors are installed before and after the switch [111]. It is important to utilise low-inductance resistors to prevent damaging the HV-switches.

An exemplary +10 kV HV-burst sequence for a 111-stage deceleration cycle slowing an OH package from 450 m/s to 64.1 m/s at a phase angle of $\Phi = 70°$ is depicted in Fig. 5.7 a). Initially, the OH packet is travelling fast and the HV pulses are closely spaced, whereas towards the end the switching frequency decreases. During the depicted pulse sequence, the voltage across the backing capacitor only drops between 3–4%. The 1/e fall- and rise times of the pulses depend on the capacitance of the electrodes and were determined to be $\tau_{\text{fall}} = 88$ ns and $\tau_{\text{rise}} = 47$ ns, respectively. The trigger sequence for the pulses in Fig. 5.7 was generated with a pulse generation card and was sent to the HV-switches over a BNC network. During the operation of the switches, the pressure in the source chamber was continuously monitored and the trigger signal was inhibited if a predefined pressure threshold was surpassed in the trap or decelerator chamber. Similar electronic circuitry has been described in refs. [61, 111].

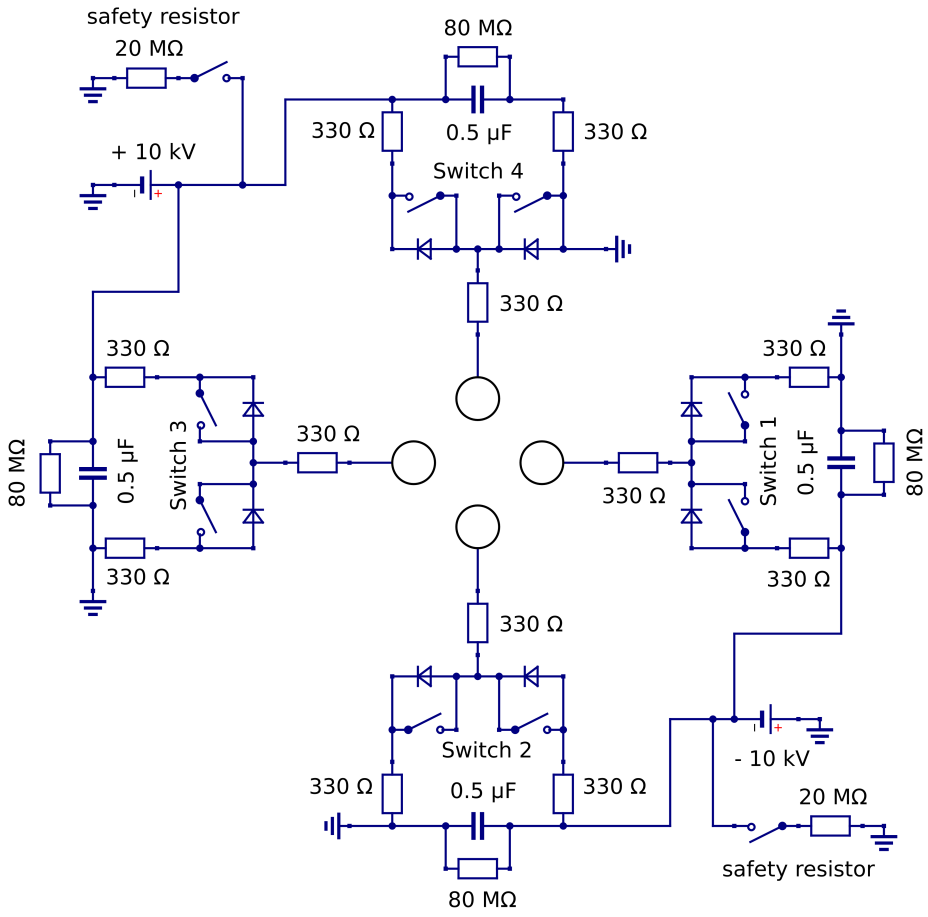

Figure 5.6: Circuit diagram of the HV-switching equipment. The four black circles at the centre represent the HV-rods with the attached electrode pins [61].

5.3 Optimising the radical source for Stark deceleration

A Stark deceleration experiment is preceded by the formation of a molecular beam of vibrationally and rotationally cold polar molecules. The number density of molecules exiting the Stark decelerator critically depends on the initial phase-space distribution and evolution of the expanding gas pulse. In turn, these properties strongly depend on the characteristics of the gas valve in use and its operation conditions. A wide variety of valves exist and the performance of the pinhole-discharge variant of the Nijmegen pulsed valve (NPV) has been assessed in chapter 4 and ref. [178]. Vogels et al. [81] have reviewed the suitability of different beam sources for Stark deceleration in the context of collision experiments.

5.3.1 Introduction

As Stark decelerators rely on conservative forces, the phase-space volume of the molecule packets cannot be compressed and the decelerator can only preserve the phase-space den-

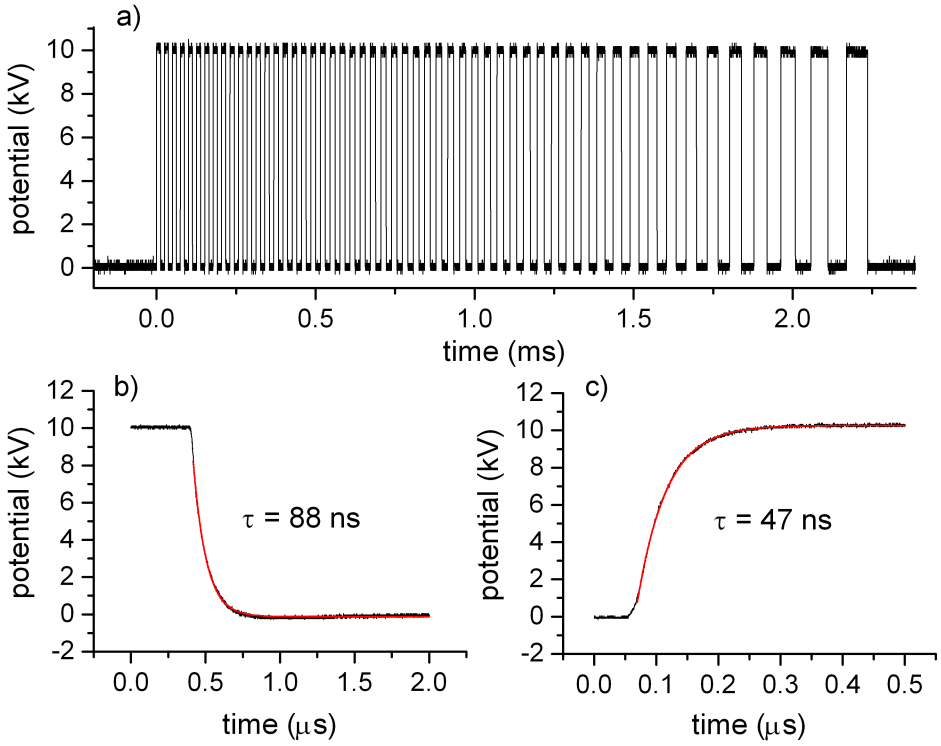

Figure 5.7: **a)** HV-pulse sequence measured at the HV-feedthrough. The $\Phi = 70°$ sequence corresponds to the deceleration of an OH package from 450 m/s to 61.4 m/s on a 111-stage decelerator. **b)** Fall time of an individual HV-pulse. **c)** Rise time of a HV pulse.

sity of the initial molecular beam [35]. This underlines the necessity to optimise conditions at the source as much as possible to maximise the number density of molecules decelerated to target velocity. Optimising the radical source pertains to class I optimisation. As discussed in sec. 5.1, class I optimisation includes all parameters the adjustment of which results in an augmented density of decelerated radicals. There are several parameters relating to the initial molecular beam which are relevant for Stark deceleration experiments, primarily its mean velocity v, its velocity spread Δv (expressed as the full-width-at-half-maximum (FWHM) of the velocity distribution), its longitudinal spatial spread Δx and its initial radical density n after exiting the valve. These parameters are strongly correlated with each other. It is often difficult or even impossible to tune only one parameter without changing one or all of the others. This imposes challenges to experimentalists, and compromises have to be made to maximise the beam density after deceleration.

5.3.2 Velocity of the molecular beam

Generally, higher initial beam velocities demand for higher phase angles Φ_0 when targeting a specific final velocity after Stark deceleration [35, 70]. In turn, high phase angles result in a reduced phase-space acceptance of the decelerator leading to reduced number densities

at the exit of the decelerator [35]. It is thus advantageous to start with a molecular beam which is as slow as possible. Before starting a deceleration experiment, mean velocities were measured by correlating different longitudinal valve positions to maxima in the corresponding time-of-flight (TOF) profiles of the OH radicals (see Fig. 5.12 a)).

The velocity of a radical beam can be coarse-tuned by using different carrier gases. As discussed in chapter 4, OH beam velocities around 670 m/s, 485 m/s and 385 m/s can be obtained with Ar, Kr and Xe as carrier gases in the NPV discharge source. The carrier gas also influences the properties and plasma chemistry of the discharge and therefore the density of radicals produced. As listed in Tab. 4.4, the density decreases for heavier carrier gases. Furthermore, by tuning the delay between striking the discharge and opening the valve, the velocity of the radical beam can be fine-tuned at the cost of decreasing the beam density [170] (see also Fig. 5.10 below). As discussed in sec. 4.6.4, the discharge potential has a profound impact on the beam velocity and needs to be adjusted with great care.

The velocity of the molecular beam in a Stark deceleration experiment should be chosen according to the specifications of the Stark decelerator. The decelerator consists of 124 stages and the electrode structure has been described in section 5.2.1. At a typical operating voltage of ± 10 kV, the decelerator provides a maximum deceleration energy of 1.43 cm^{-1} per stage for OH molecules. Therefore, the maximum initial velocity of OH molecules is limited to $\simeq$500 m/s if a target velocity of 35 m/s is to be reached (see Fig. 3.5 b)). This restriction excludes the use of Ar as carrier gas in our case.

The effect of using different carrier gases on the Stark deceleration process is illustrated in Fig. 5.8, where the TOF profiles of OH radicals exiting the decelerator are depicted. The experimental TOF profiles (upper traces) are compared with simulated traces (lower traces) extracted from Monte-Carlo trajectory simulations of the decelerated molecules [112]. The initial mean velocities of the OH beam seeded in Xe (Fig. 5.8 a)) and Kr (Fig. 5.8 b)) are 415 m/s and 465 m/s, respectively. The relative velocity spreads $\Delta v/v$ were determined from TOF profiles and $\Delta v/v$=12% was found for both carrier gases. These values deviate slightly from the results given in Tab. 4.4. The characteristics of the beam slowly varied over time, as wear parts such as the spring of the valve and the discharge electrodes aged. Thus, the experiment had to be re-optimised periodically to account for the changing beam characteristics. The spatial spreads were deduced to be 12.5 mm for Kr and 11.0 mm for Xe by comparing experiments and simulations.

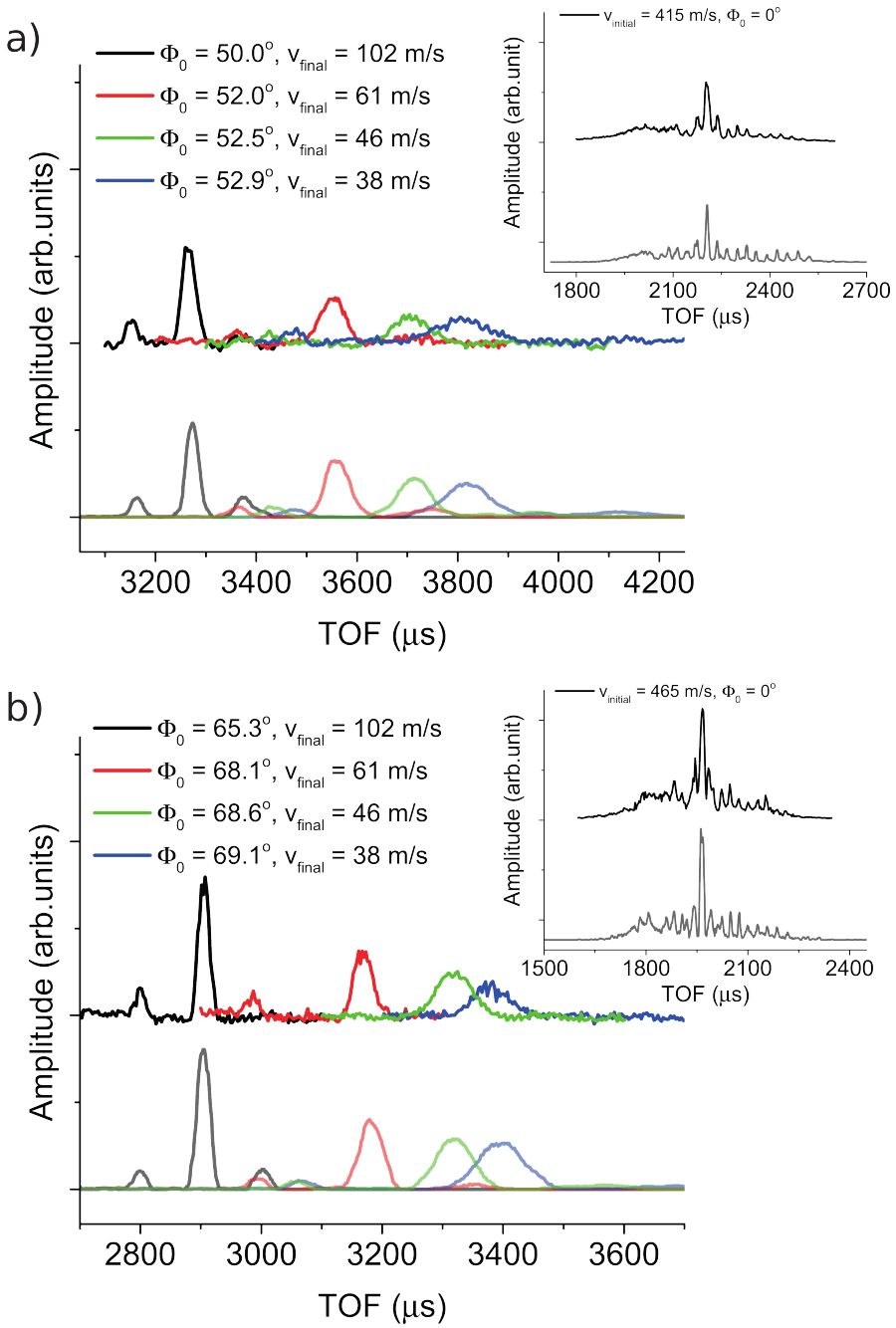

Figure 5.8: Time-of-flight (TOF) profiles of OH radicals recorded 11.5 mm downstream from the exit of the Stark decelerator using **a)** Xe and **b)** Kr as carrier gas. The synchronous velocity was set to the mean velocity of the initial OH beam. The phase angles for deceleration and resulting final velocities of the OH package exiting the Stark decelerator are indicated for each experiment. The dark solid lines (upper traces) are experimental results and the light solid lines (lower traces) represent Monte-Carlo trajectory simulations of the experiments. All traces are normalised to the signal obtained in guiding mode ($\Phi_0 = 0$, insets) using Kr as a carrier gas. The scales of **a)** and **b)** are identical. The insets of **a)** and **b)** depict the guiding signal when the Stark decelerator is operated with $\Phi_0 = 0$. In the simulations, the contributions from both $M_J\Omega = -9/4$ and $M_J\Omega = -3/4$ low-field-seeking states were taken into account.

As discussed in section 4.6.4, using Kr as carrier gas yields an initial OH beam density a factor 2 to 3 lager than with Xe. When comparing the Kr and Xe TOF profiles obtained in guiding mode (i.e., $\Phi_0 = 0°$), the higher OH densities seeded in Kr molecular beams are directly reflected in the guiding TOF signal intensities depicted in the insets of Fig. 5.8. As Xe carrier gas produces a lower initial OH beam velocity, the same target velocities as with Kr can be achieved while operating at smaller phase angles. The lower phase angles compensate the initially lower density of OH in a Xe beam such that the radical densities achieved after deceleration are similar to those obtainable with Kr. Hence, employing Kr or Xe makes no significant difference in terms of optimising the radical density at low velocities. It is interesting to notice the increased temporal spreading in the TOF profiles as the final velocity decreases. The spreading is due to a prolonged flight time between the decelerator and the point of detection. During the free flight, the package begins to spread out spatially according to the velocity components it contains. One notices that the initial OH beam velocities are higher than one would expect, e.g. from the results presented in ref. [81] or from the terminal velocity u_∞ given by Eqn. 4.12. This is attributed to different gas dynamics in the valve caused by the discharge and the fact that the valve warms up to about 40°C during operation.

5.3.3 Velocity spread and spatial spread of the molecular beam

Velocity spread Δv and spatial spread Δx of the initial beam play quite different roles for the final number density of Stark-decelerated radicals as illustrated with trajectory simulations in Fig. 5.9. All simulations were started with identical particle densities. The left column depicts TOF profiles when the Stark decelerator is operating in guiding mode (phase angle $\Phi_0 = 0°$). The right column displays TOF profiles of OH packages which are decelerated down to 35 m/s employing a phase angle of 62.4°. The initial beam velocity was chosen as 450 m/s, which is typical for Kr as carrier gas. All profiles are normalised to the TOF profile in guiding mode with 10% velocity spread and 10 mm spatial spread.

As can be seen in Fig. 5.9 a), the spatial spread of the initial beam determines the number of adjacent stable phase-space volumes (defined by the periodicity of the Stark decelerator) into which the molecule cloud couples. The coupling into several phase-space volumes results in side peaks around the central peak in the TOF profiles, as observed in the first column. Those side peaks have different velocities compared to the main peak. As the spatial spread increases from 10 mm to 30 mm, the intensity ratio of the main peak and the side peak decreases and more side peaks appear [81]. This effect can be observed when the simulations are running in both guiding and deceleration mode. A large spatial spread is not necessarily detrimental to the deceleration experiments, depending on the intended

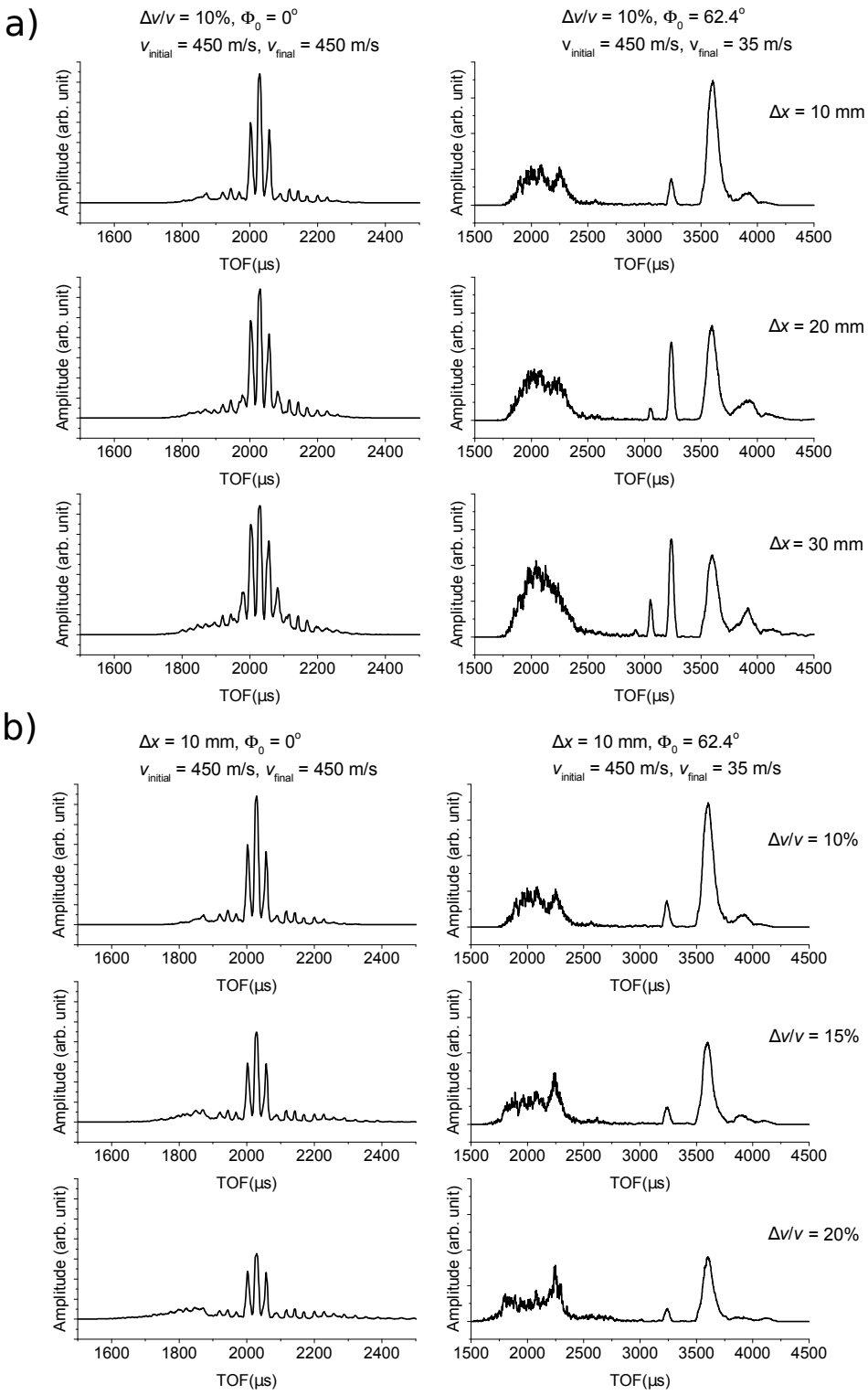

Figure 5.9: Simulated TOF profiles for **a)** different spatial spreads Δx and **b)** different relative velocity spreads $\Delta v/v$ of the initial OH beam. All simulations were performed assuming identical initial OH beam densities. The left column shows the TOF profiles when the Stark decelerator is operated in guiding mode (phase angle $\Phi_0 = 0°$). The right column depicts the TOF profiles as OH beams are decelerated down to 35 m/s at a phase angle of 62.4°. The initial molecular beam velocity was chosen as 450 m/s, which is typical for Kr as carrier gas.

application. For example, in spectroscopic measurements and trap loading experiments, the side peaks will not cause problems, as often one of the peaks can be selected. On the other hand, in collision experiments, each of the transported molecule packets may contribute to the collision process, which complicates the interpretation of the results. It has to be noticed that at low final velocities, the intensity of the side peaks is not increasing symmetrically when increasing the spatial spread. The peaks pertaining to higher velocities increase in intensity more markedly than those relating to low velocities, because molecules with lower velocities are stopped and reversed in the decelerator.

Conversely, the effect of velocity spread is shown in Fig. 5.9 b). An increasing velocity spread not only changes the ratio between the main peak and the side peaks, but also significantly decreases the total number density of molecules transported through the decelerator. In a deceleration experiment the molecular beam usually flies freely over a certain distance before it is coupled into the Stark decelerator. For the simulations in Fig. 5.9, the distance between the valve and the decelerator across two vacuum chambers separated by a skimmer amounts to 232 mm. After this stretch of free flight, the velocity spread has effectively enlarged the spatial spread, thus diluting the beam before entering the decelerator.

It was observed that the time delay $t_{\mathrm{dis.}}$ between opening the valve and striking the discharge has a critical effect on the velocity spread as shown in Fig. 5.10. For low values of $t_{\mathrm{dis.}}$, the beam exhibits a higher velocity and larger velocity spread. The OH beam has a maximum intensity when the discharge pulse is applied around 50 µs after the opening of the valve. At these settings, the beam adopts a minimum velocity spread of 16.1% and a mean velocity of 475.6 m/s. For higher values of $t_{\mathrm{dis.}}$, the beam displays a lower mean velocity, and the inferior expansion conditions result in a lower peak intensity and a larger velocity spread. Similar trends have been observed in previous reports [170, 274]. As discussed in chapter 4, the discharge voltage is another important parameter which needs to be adjusted for optimising the properties of the molecular beam. Ideally, the discharge potential is chosen as low as possible to prevent heating and to reduce the velocity spread. Before each deceleration experiment, the following valve optimisation strategy was employed:

- The valve opening parameters were chosen such that the source pressure was in the range of $(1.0 - 4.0) \cdot 10^{-5}$ mbar. Usually, a valve driver setting of V = 6.44 and T = 4.0 was found to be a good starting point. This setting corresponds to a current pulse of approx. 100 µs with a maximum of 1.4 kA, according to Fig. 4.10.

- The discharge voltage was adjusted to the lowest possible setting without reducing the LIF signal below practical levels. As indicated in Tab. 4.5, the mean beam velocity can change by over 100 m/s upon changing the discharge potential from −700 V to −850 V for Ar. A similar dependence of the beam velocity on the discharge voltage was observed for Kr and Xe as well. The velocity increase is due to heating effects as more energy is supplied to the plasma. Furthermore, operating the discharge at more negative potentials increases the velocity spread. Consequently, the discharge voltage is the parameter affecting the beam properties the most and requires special consideration.

- Fine tuning of the molecular beam velocity and the velocity spread was accomplished by adjusting the discharge delay. As a rule of thumb, it was found that the mean beam velocity decreases by approx. 10 m/s for every 10 µs the discharge delay is increased beyond 100 µs.

- Usually, optimal beam properties for deceleration could not be achieved upon following this procedure just once. In case of unfavourable beam characteristics, the T-parameter of the valve driver was readjusted and the above steps were iterated.

5.4 Optimised operation of the Stark decelerator for low-velocity applications

5.4.1 Incoupling time

The optimal operation of a Stark decelerator depends on its application and different schemes have been proposed [78–80, 82, 85]. In a typical Stark deceleration experiment, a high voltage (HV) pulse sequence is computed based on the synchronous velocity v_s and the target velocity after deceleration. The initial synchronous velocity v_s is chosen from the velocity distribution of the molecular beam and often corresponds to the maximum of the beam profile, but loading from the centre of the distribution is not a requirement. Upon the arrival of a molecular package with the synchronous velocity v_s at the entrance of the Stark decelerator, the calculated HV pulse sequence is applied on the electrodes. The part of the molecular package overlapping with the stable phase-space volume of the decelerator is slowed down to the final velocity. To maximise the incoupling efficiency, it is crucial that the high voltage pulse sequence is applied isochronal to the arrival of the molecular package. The precise determination of the incoupling time $t_{\mathrm{incoupling}}$, i.e., the time delay between the generation of the pulsed beam and the coupling into the Stark decelerator, is essential for a successful deceleration experiment.

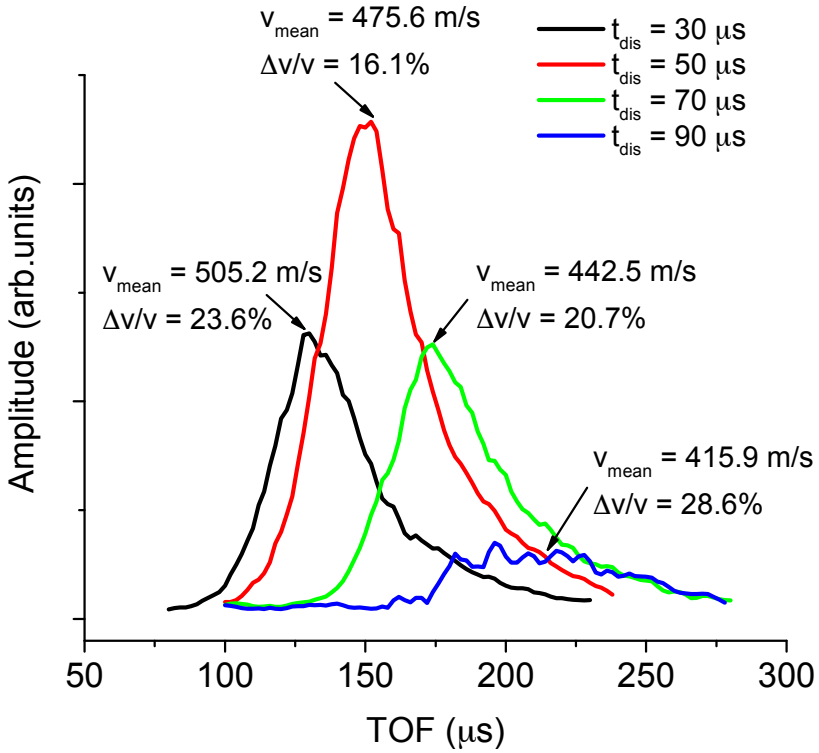

Figure 5.10: TOF profiles as a function of the time delay t_{dis} between the valve opening trigger and striking the discharge. The TOF curves were recorded 5 cm downstream from the nozzle. The mean beam velocity v_{mean} and the relative longitudinal velocity spread $\Delta v/v$ are indicated for each measurement.

A detailed protocol on how to determine the incoupling time has been given by Vogels et al. [81]. In this experimental setup, the first step towards deceleration consists of determining the mean velocity and the velocity spread of the OH beam as described in sections 5.3.3 and 4.2.4. The incoupling time can be estimated by the relation $t_{\mathrm{incoupling}} = L/v_{\mathrm{s}}$, where L denotes the distance between the valve and the Stark decelerator, and v_{s} represents a selected synchronous velocity, which, in this case, is identical to the mean velocity of the molecular beam. Subsequently, the Stark decelerator is operated in guiding mode, i.e., with phase angle $\Phi_0 = 0°$. The incoupling time is fine-tuned until a symmetric TOF profile similar to the one depicted in Fig. 5.8 is achieved. $t_{\mathrm{incoupling}}$ can further be improved by optimising the slow-molecule yield at high phase angles. A final velocity of around 35 m/s was found suitable for the determination of $t_{\mathrm{incoupling}}$. At such low velocities, the stable phase-space volume bounded by the separatrix is significantly smaller then for $\Phi_0 = 0°$, which allows for greater sensitivity in adjusting $t_{\mathrm{incoupling}}$. Even at relatively small incoupling time offsets, the densest part of the molecular beam is shifted to lie outside of the small stable phase-space region at high phase angles. The resulting signal drop is immediately noticeable and the incoupling time can be readjusted.

Finally, the TOF profiles in guiding mode and at low final velocities are compared with TOF curves obtained from Monte Carlo trajectory simulations. Once the experimental TOF profiles are well reproduced by the simulations, $t_{\mathrm{incoupling}}$ is fixed.

The distance L_{det} between the exit of the Stark decelerator and the detection point amounts to 11.5 mm. An uncertainty in L_{det} of $\Delta L_{\mathrm{det}} = 1$ mm translates into an uncertainty of 2 µs in the TOF profile for a guiding velocity of 470 m/s and into an uncertainty of 28 µs for a final velocity of 35 m/s. The distance L_{det} was determined with an uncertainty less than 1 mm. Thus, as a rule of thumb, it can be assumed that the discrepancy between experimental and simulated TOF traces should be smaller than 2 µs for a guiding profile and 20 µs for a profile pertaining to a slow package of OH radicals. By comparing the simulated TOF traces with their experimental counterparts, this rule could indeed be satisfied at both high and low velocities.

5.4.2 Loading at $v_{\mathrm{s}} < v_{\mathrm{mean}}$

Once $t_{\mathrm{incoupling}}$ has been determined, the density of decelerated molecules can further be optimised by selecting different synchronous velocities v_{s} from the velocity distribution of the molecular beam. In general, v_{s} does not have to be identical to the mean beam velocity v_{mean}. Under the premise of keeping the final velocity fixed, choosing a lower synchronous velocity v_{s} allows to operate the decelerator at lower phase angles. This results in a larger addressable phase-space volume for deceleration and leads to an improved deceleration efficiency. If, however, v_{s} deviates too much from v_{mean}, then the density of the molecule package coupled into the Stark decelerator decreases substantially from the maximum value as sparser sections of the gas pulse are sampled. This suggests that there is an optimal value of v_{s} leading to a maximised decelerator throughput for a given velocity distribution.

To illustrate this point, various initial velocities within the velocity profile were selected as synchronous velocities v_{s} and the molecules were decelerated down to 35 m/s. The OH molecules were seeded in Kr yielding a beam of mean velocity $v_{\mathrm{mean}} = 470$ m/s and a velocity spread (FWHM) of about 20%. Fig. 5.11 a) depicts the TOF profiles obtained for OH beams decelerated down to various final velocities with the initial velocity chosen as 450 m/s. The phase angles Φ_0 used to operate the Stark decelerator are indicated together with the final velocities. The effect of choosing a synchronous velocity v_{s} differing from the mean velocity $v_{\mathrm{mean}} = 470$ m/s can be seen by inspecting the TOF profile in guiding mode ($\Phi_0 = 0$) and comparing it with the inset in Fig. 5.8 b), where $v_{\mathrm{s}} = v_{\mathrm{mean}}$ applies. In the latter case, the TOF profile exhibits a symmetric structure and the TOF profile

is skewed for $v_s < v_{mean}$, as depicted in Fig. 5.11 a). Here, the wing of faster molecules to the left of the main peak is more pronounced than the wing of slower molecules to its right. The simulations reproduce these experimental results.

Fig. 5.11 b) depicts the combined effect of the initial package density and phase angle on the density of decelerated molecules by choosing different v_s values. In the experiment, OH molecules were decelerated down to the same final velocity (35 m/s) starting from different initial velocity components of the beam. As v_s decreases relative to v_{mean}, the density of the decelerated OH beam increases due to the larger phase-space acceptance provided by the lower initial velocity. The area bounded by the separatrix is proportional to the longitudinal acceptance of the Stark decelerator. The increasing area of the phase-stable region for the phase angles under consideration is depicted in Fig. 5.11 c). The density of the decelerated radicals reaches a maximum at $v_s = 450$ m/s. Further decreasing v_s lowers the density of decelerated OH molecules, as the gain achieved by using smaller phase angles is not able to compensate the loss in initial beam density further away from the core of the velocity distribution, see Fig. 5.11 d). The simulations (lower traces in Fig. 5.11 b)) faithfully reproduce the trends observed in the experiments. Thus, by optimising the synchronous velocity v_s, the density of decelerated OH radicals could be increased by a factor of 2, which is consistent with previous observations [78].

As a last consideration, the voltage applied on the Stark decelerator is another parameter which can be adjusted to optimise the radical density. A typical applied voltage is ±10 kV. Keeping the operation phase angle fixed, higher potential differences between the electrodes result in a larger phase-space acceptance, thereby increasing the number of decelerated molecules. However, this line of reasoning is valid for high final velocities only. When employing Stark decelerators for low-velocity applications, especially at velocities below 50 m/s, molecules at the slow end of the velocity distribution in a phase-stable package are stopped and reflected inside the Stark decelerator [80], which causes loss. This effect was also observed in our experiment. Consequently, the Stark decelerator was operated at ±10 kV all the time.

5.5 Detection efficiency optimisation

Increasing the fluorescence collection efficiency and the reduction of stray light are essential for sensitive LIF detection. Excitation to the first electronically excited state takes place via the $A^2\Sigma^+(v = 1) \leftarrow X^2\Pi(v = 0)$ transition at 282 nm, whereas fluorescence around 313 nm is collected from the $A^2\Sigma^+(v = 1) \rightarrow X^2\Pi(v = 1)$ transition. As the excited state relaxates into the $X^2\Pi(v = 1)$ state, off-resonant photons are emitted at a

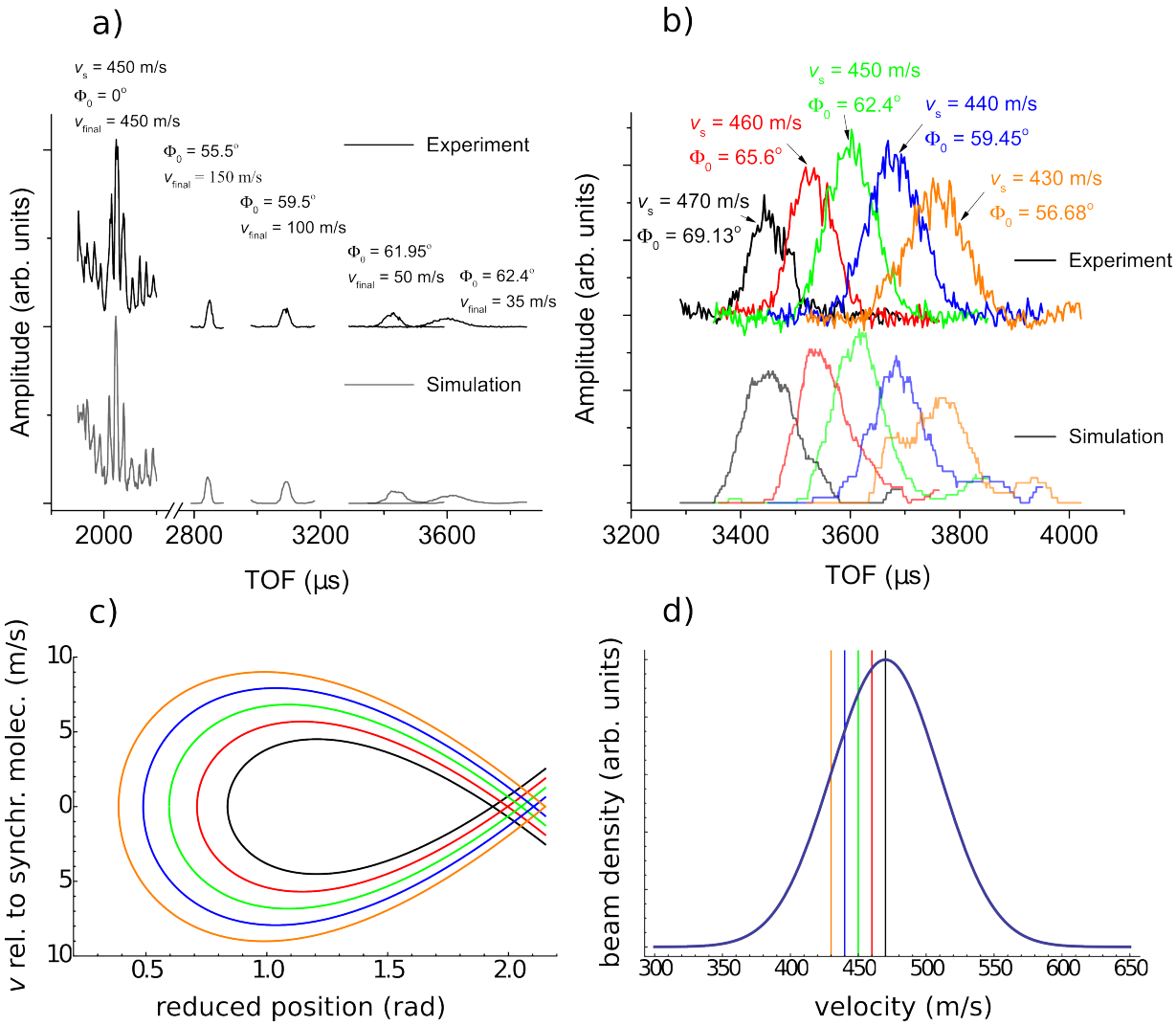

Figure 5.11: Effect of the synchronous velocity v_s on the density of decelerated molecules. **a)** TOF profiles of the decelerated OH beam at various final velocities (carrier gas: Kr, mean beam velocity v_{mean} =470 m/s, velocity spread (FWHM) of $\Delta v/v$ =20%). The synchronous velocity v_s was chosen to be 450 m/s. The employed phase angles Φ_0 and the resulting final velocities v_{final} are indicated above each TOF profile. **b)** OH TOF profiles obtained for deceleration at different initial synchronous velocities to a common final velocity of 35 m/s. All other experimental conditions are identical to those of the experiments in Fig. a). In figures **a)** and **b)**, dark lines represent experimental results and light traces belong to Monte-Carlo trajectory simulations. **c)** Increasing area of the longitudinal phase-stable region bounded by the separatrix for the phase angles under investigation. **d)** Bars indicating the beam density at different synchronous velocities v_s. The velocity distribution is centred around v_{mean} =470 m/s and displays a spread of $\Delta v/v$ =20% (FWHM). For Figs. **c)** and **d)** the color scheme in Fig. b) applies.

lower wavelength, which can conveniently be separated from the excitation wavelength by optical bandpass filters. Furthermore, bandpass filters also play an important role in suppressing "spurious fluorescence", which can arise from light baffles, Brewster windows and other objects located in proximity to the light path [111]. Therefore, it is advantageous to install filter plates with a narrow bandpass region, which only allows fluorescence photons at 313 nm to reach the PMT. To that end, two narrow band pass filters (Asahi Filter, XHQA313 and Semrock, FF01-315/15-25) are used in this setup. At 313 nm, this filter combination provides a transmission of up to 50% centred in a transmission window of 10 nm.

5.6 Estimation of OH densities after the decelerator

5.6.1 Dependence of the signal intensity on the valve position

Before describing procedures for determining the density after the decelerator in guiding mode and at low final velocities, it is insightful to consider the changes in signal level that result for different valve positions. Fig. 5.12 a) depicts time of flight (TOF) profiles recorded at valve orifice-laser distances ranging from 101 mm to 142 mm. As indicated in Fig. 5.16, the laser beam in the source chamber may be approximated by a cylinder with a diameter of 3 mm and the imaging takes place over a total length of approximately 10 mm. Retracting the valve from 101 mm to a distance of 137 mm leads to a decrease in TOF signal intensity by a factor of 2.2. Assuming that radial $1/r^2$-losses lead to the largest density reduction during the increased flight time, the loss factor $137^2/101^2 \approx 1.8$ lies close to the experimental factor of 2.2. The remaining signal reduction is likely due to increased longitudinal spreading during the longer free flight time, which contributes a factor $2.2/1.8 \approx 1.2$. Therefore, the position of the valve has to be taken into account when scaling densities according to the signal height ratio of TOF profiles. The relative signal intensity drop for the TOF maxima is depicted in Fig. 5.12 b).

In a next step, the signal level dependence on the valve position is investigated behind the decelerator exit. Recording guiding TOF profiles after the decelerator provides information on the skimmer throughput as the molecular beam has to pass a skimmer with a 3 mm orifice before entering the decelerator. The skimmer is located 18.2 mm downstream of the source chamber laser beam and features a length of 50.8 mm. Fig. 5.13 a) depicts guiding TOF profiles at different valve-skimmer distances and the incoupling time was readjusted for every valve position. As depicted in Fig. 5.13 a), the valve position only has a minor effect on the TOF signal intensity. For valve-skimmer distances ranging between 119 mm to 165 mm, the TOF maxima are reduced by a factor of 1.2. The pressure in

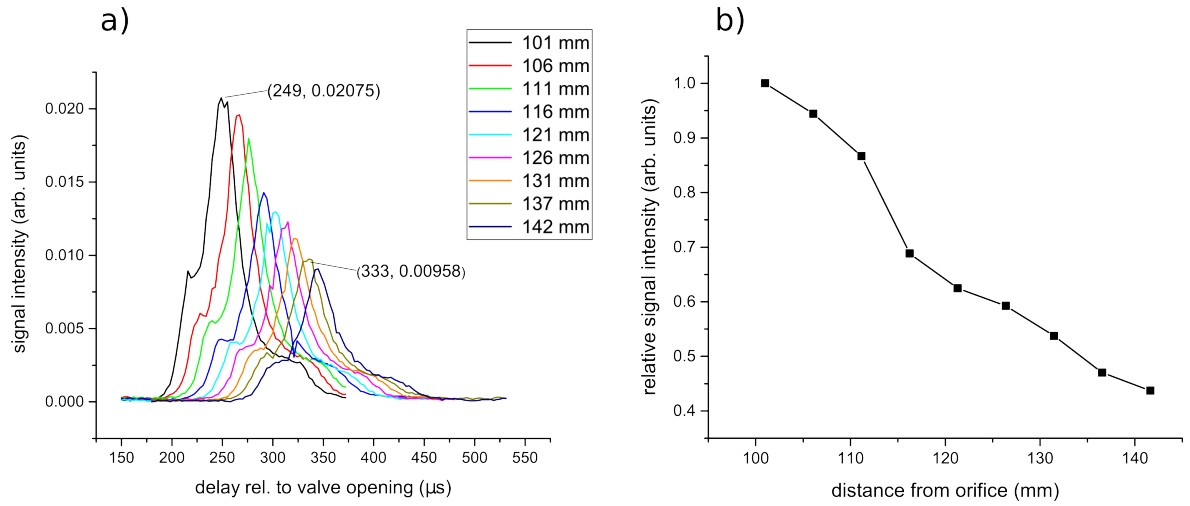

Figure 5.12: Variation of the signal intensity in the source chamber as a function of the valve position. **a)** Time of flight (TOF) profiles recorded at various valve orifice-laser distances ranging from 101 mm to 142 mm. **b)** Relative signal intensity drop as a function of the distance from the orifice. The data points pertain to the TOF maxima in panel a).

the decelerator chamber follows a similar trend and the pressure is reduced by a factor of 1.4 when increasing the valve-skimmer distance from 119 mm to 165 mm. Compared to the signal intensity reduction in the source chamber, the signal reduction after the decelerator chamber is lower when adjusting the valve position over an identical range. This is due to the much narrower radial velocity acceptance of the skimmer compared to the laser beam. While the skimmer has a diameter of 3 mm, the laser beam probes the expanded OH beam over a length of 14 mm. Therefore, the solid angle under which the source is seen through the skimmer is almost identical for all valve settings, which is in contrast to larger range of solid angles spanned by the laser beam and the source. Consequently, there is less density variation over the region in the molecular beam from which the skimmer samples OH radicals compared to the laser excitation volume. As discussed in section 4.2.5, the intensity of the molecular beam is reduced by skimmer interference and skimmer clogging if the valve-skimmer distance is too small [109]. This does not seem to be the case in Fig. 5.13 a) as the signal intensities gradually decrease with increasing distance. This finding is also in agreement with the $Kn > 2$ criterion for krypton in Fig. 4.7 c), where the shortest valve-skimmer distance of 119.2 mm lies above the $Kn > 2$ threshold separation. The signal drop in Fig. 5.13 is therefore likely due to longitudinal spreading of the OH beam before coupling into the decelerator. As the density variation after the decelerator is similar to the one measured by the pressure gauge in the decelerator chamber, interference effects caused by the presence of the decelerator electrodes are unlikely. However, such effects can become important for cryogenic skimmers with a high

particle flux as the decelerator electrodes eclipse part of the $\varnothing = 3$ mm skimmer opening.

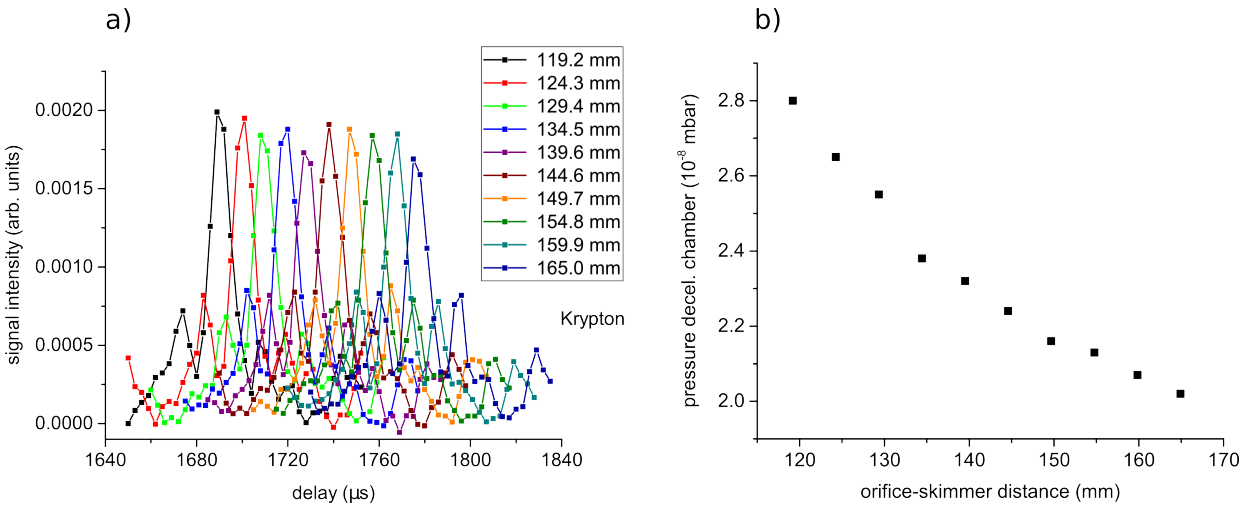

Figure 5.13: **a)** Signal intensity after the decelerator in guiding mode for various orifice-skimmer distances. The incoupling time has been adjusted based on the valve position. **b)** Pressure drop in the decelerator chamber as a function of the valve orifice-skimmer distance.

5.6.2 Density scaling considerations

As a final step involved in the optimisation procedure, the density before and after the decelerator was determined. The procedures described in this section allow to establish an absolute density calibration for TOF signals in guiding mode and at low final velocities. For the present scheme, a density estimation always starts with the determination of an absolute density or photon number from a calibrated LIF measurement in the source chamber, as described in sec. 4.5. The source chamber density is then associated with a TOF profile measured under identical conditions, where the pinhole plates have been substituted with a LIF collection lens. Scaling the density in the source chamber by the ratios of the TOF signal maxima before and after the decelerator allows to infer the density in the trap chamber. It is imperative that the LIF detection setup in the trap chamber is identical to the one installed in the source chamber for this method to work. As the densities between the molecular beam in the source chamber and the OH package travelling at 28 m/s span several orders of magnitude, different filters and PMT gain settings were employed, which has to be considered when scaling the density values by the TOF signal intensities. In general, the signal intensity I is proportional to the PMT gain G, the filter transmission T, the density ρ and the excitation volume $V_{\text{exc.}}$, from which photons are collected.

$$I \propto T \cdot G \cdot \rho \cdot V_{\text{exc.}} \tag{5.1}$$

Under the assumption of identical detection efficiencies, the density reduction ratio r between the source density and the density of the OH package after the decelerator in guiding mode ($\Phi = 0°$) can be cast into the following form:

$$\frac{I(\text{source})}{I(0°)} \cdot \frac{G(0°)}{G(\text{source})} \cdot \frac{T(0°)}{T(\text{source})} \cdot \frac{V_{\text{exc.}}(0°)}{V_{\text{exc.}}(\text{source})} = \frac{\rho(\text{source})}{\rho(0°)} = r_{\text{guiding}} \tag{5.2}$$

The density loss between the guiding mode of operation and deceleration to 28 m/s is expressed by $r_{28\text{ m/s}}$, which can be calculated in the following way:

$$\frac{I(0°)}{I(28\text{ m/s})} \cdot \frac{G(28\text{ m/s})}{G(0°)} \cdot \frac{T(28\text{ m/s})}{T(0°)} \cdot \frac{V_{\text{exc.}}(28\text{ m/s})}{V_{\text{exc.}}(0°)} = \frac{\rho(0°)}{\rho(28\text{ m/s})} = r_{28\text{ m/s}} \tag{5.3}$$

It would certainly be more precise to measure the density of the OH package employing pinhole plates in the trap chamber and to proceed in analogy to section 4.5. However, due to the lower signal levels at the exit of the decelerator, the LIF signals were below the detection limit when collecting LIF photons through two pinhole plates with small diameters, even in guiding mode ($\Phi = 0°$) and at the highest gain settings of the PMT. The procedure described below offers an alternative approach for estimating the density after the decelerator.

5.6.3 Determination of the source chamber density

In a first step, the density in the source chamber was determined by acquiring a LIF signal through two pinhole plates. The first plate had a radius of $r = 0.155$ mm and was positioned 5 mm above the laser beam and a second concentric pinhole plate with $r = 0.5$ mm was mounted a distance $d = 239.5$ mm above the first plate. The valve-laser distance was adjusted to a relatively small value of 101 mm in order to increase the signal levels. No optical filters were employed and the PMT was operated at -2100 V, which corresponds to a gain factor of $G = 7 \cdot 10^7$. Off-resonant fluorescence was collected from the $A\ ^2\Sigma(v = 1) - X\ ^2\Pi(v = 1)$ transition at 313 nm by exciting ground state OH via the $Q_1(1)$ and $Q_{21}(1)$ branches at 282 nm. Hence, an excitation rate coefficient of $\varepsilon = 3/5$ had to be employed for the density calculation. The LIF traces recorded through the pinhole plates are depicted in Fig. 5.14. Due to the absence of optical filters, the laser caused a stray light peak at the beginning of the acquisition window. Therefore, the time gate within which data was considered needed careful adjustment such that the stray light photons were excluded from the density calculation, which is indicated by the green vertical bars in Fig. 5.14. The continuous signal in the left plot a) is the average of 10 traces similar to the one depicted in the right plot b), where spikes caused by individual photons are visible. As each LIF trace in Fig. 5.14 b) represents an average

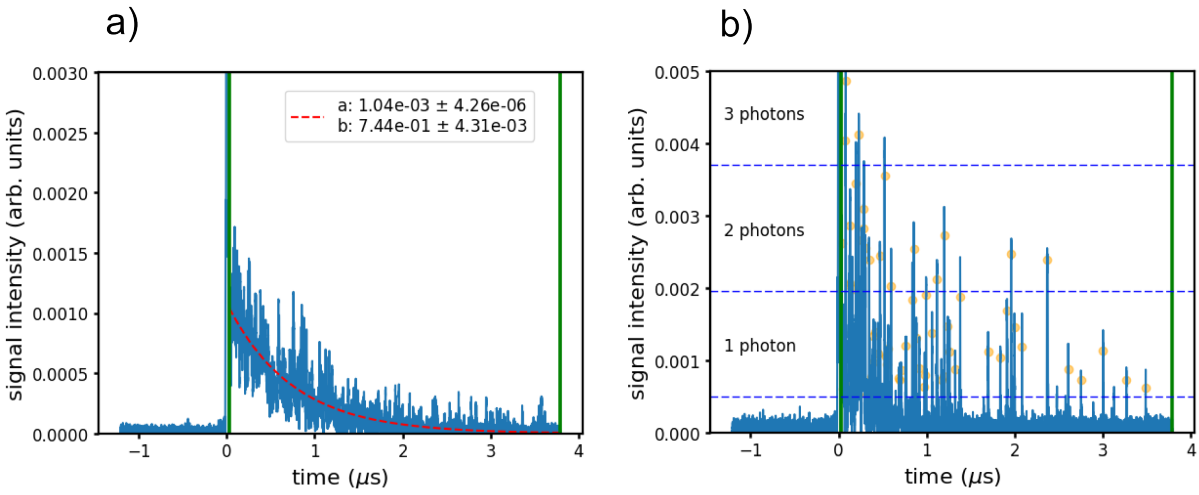

Figure 5.14: OH LIF traces measured through two pinholes ($r_1 = 0.155$ mm, $r_2 = 0.5$ mm) mounted in the source chamber. The valve-laser distance amounts to 101 mm. The PMT was operated at -2100 V, which corresponds to a gain of $G = 7 \cdot 10^7$. The origin of the time axis denotes the arrival of the laser beam at the source chamber. The green vertical bars represent the time gate within which data was considered. **a)** Continuous LIF trace, which represents an average over 800 individual experiments. The curve was fitted to an exponential model: $f(t) = a \cdot \mathrm{e}^{-t/b}$. The lifetime confirms the formation of OH in the molecular beam. **b)** LIF trace representing an average over 80 experimental cycles. Individual photons are visible and the intervals for deciding whether a peak corresponds to a single, two or three photons are indicated by dashed horizontal lines. T. Kierspel kindly provided his peak-finding algorithm.

over 80 experimental cycles, the data presented in a) has an effective average of 800. By subsequently applying Eqns. 4.33 and 4.34 onto the data depicted in curve a), $(5.0 \pm 1.3) \cdot 10^6$ OH molecules could be detected under a solid angle of $\Omega = (2.3 \pm 0.2) \cdot 10^{-5}$ sr within the excitation volume of $V_{exc.} = (2.3 \pm 0.1) \cdot 10^{-4}$ cm^3, which results in a $|f\rangle$-state density of $\rho(\mathrm{source})_\mathrm{a} = (2.2 \pm 0.6) \cdot 10^{10}$ part./cm^3.

While the determination of the density using Fig. 5.14 a) requires numerical integration of the LIF curve and knowledge of the absolute gain factor of the PMT in accordance with Eqn. 4.33, a different approach to determining the density in the source chamber can be pursued by counting the number of photon spikes in Fig. 5.14 b). The expected signal level of a single photon can be estimated by the following expression:

$$V_\mathrm{photon} = \frac{G_\mathrm{PMT} \cdot e \cdot R_\mathrm{L}}{\Delta t_{photon} \cdot N_\mathrm{avg}}, \tag{5.4}$$

where V_photon denotes the signal level in Volts, G_PMT is the PMT gain, R_L stands for the output load resistance of the PMT and Δt_{photon} gives the duration of the signal spike pertaining to a single photon. If the photon traces are recorded on an oscilloscope in

averaging-mode, the signal level becomes inversely proportional to the number of averages, as the photons usually do not coincide temporally within the N_{avg} repetition cycles. Based on Eqn. 5.4, interval regions for counting single, two or three photons have been defined and the levels are indicated by the horizontal lines in Fig. 5.14 b). By counting the number of peaks and taking into account that $N_{\mathrm{avg}} = 80$, a total number of $(3.9 \pm 0.9) \cdot 10^5$ OH molecules was obtained, which corresponds to a $|f\rangle$-state density of $\rho(\mathrm{source})_{\mathrm{b}} = (1.7 \pm 0.4) \cdot 10^{10}$ part./cm^3. The advantage of photon counting is that the noisy baseline can be excluded from the analysis, which renders the method almost background-free. Furthermore, the PMT gain is not required for working out the number of OH molecules and Eqn. 4.33 can be omitted. Consequently, the error associated with the density value is much smaller in photon counting than for the previously described method involving the integration of the signal in Fig. 5.14 a). Nonetheless, within error bars $\rho(\mathrm{source})_{\mathrm{a}}$ and $\rho(\mathrm{source})_{\mathrm{b}}$ agree well. Due to the better uncertainty, $\rho(\mathrm{source})_{\mathrm{b}} = (1.7 \pm 0.4) \cdot 10^{10}$ part./cm^3 will be used as a $|f\rangle$-state source density value, which serves as a starting point for extrapolating the density to the end of the decelerator.

Once the source chamber density has been determined, the next step consists of calculating the density after the decelerator according to Eqns. 5.2 and 5.3. Fig. 5.15 depicts TOF signals of the OH beam in the source chamber and after the decelerator for both the guiding mode of operation ($\Phi = 0°$) and at 28 m/s ($\Phi = 62.544°$). It is important to notice that each point in a TOF profile is obtained by numerically integrating the corresponding LIF trace, which implies that the signal intensity is directly proportional to the density. In Fig. 5.15, the TOF profile in the source chamber has been normalised to unity and the TOF profiles after the decelerator have been scaled by the density reduction factors given in Eqn. 5.2 and Eqn. 5.3 as it is necessary to account for differences in the observable excitation volume, filter transmissions and the PMT gain.

5.6.4 Density after the decelerator in guiding mode ($\phi = 0$)

The TOF trace in the source chamber was recorded at a valve-laser distance of 137 mm, which is larger than the 101 mm used in the absolute density estimation. It was found experimentally that the TOF signal intensity changes by a factor of 2.2 ± 0.2 when moving the valve between the two positions (see Fig. 5.12). Hence, a $|f\rangle$-component density of $(7.8 \pm 2.0) \cdot 10^9$ part./cm^3 can be assigned to the maximum of the TOF profile in the source chamber, which was recorded at a PMT voltage of -1150 V. In the absence of the pinhole plates, optical filters are required for attenuating the stray light and an identical filter combination with a transmission of $T = 32\%$ was installed for recording all three traces in Fig. 5.15. Therefore, $\frac{T(0°)}{T(\mathrm{source})} = 1.0$ applies throughout the density calculation. For

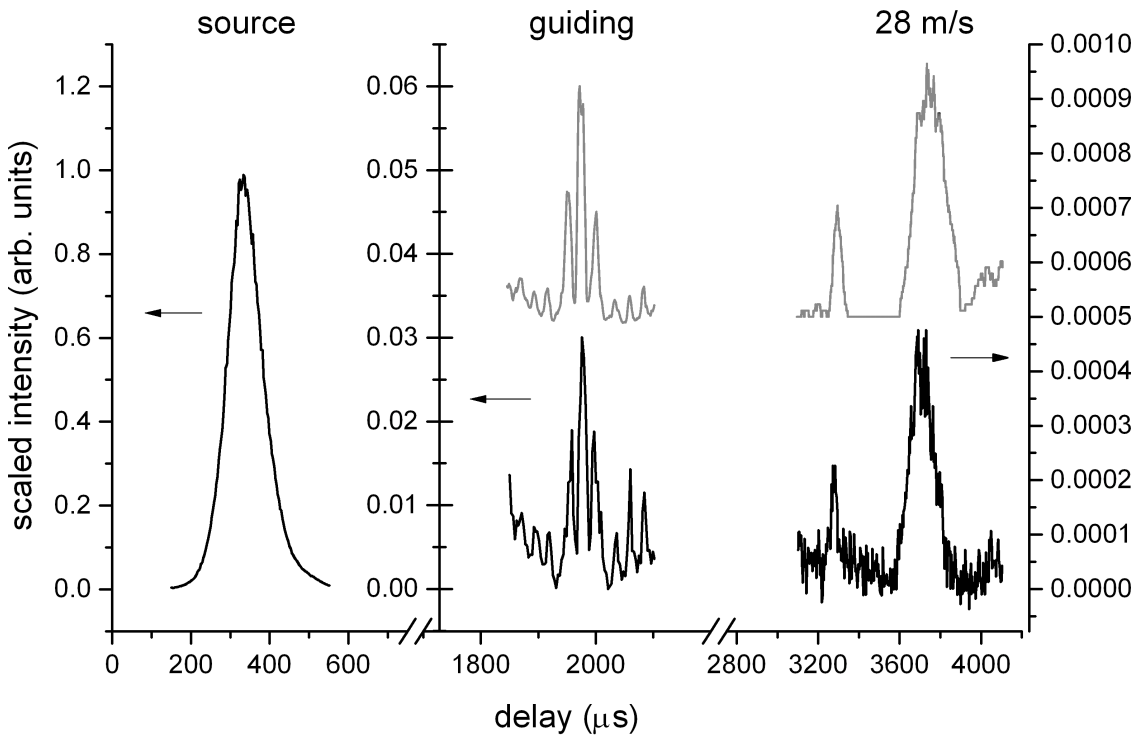

Figure 5.15: TOF profiles recorded in the source chamber ($v_{\mathrm{mean}} = 470$ m/s, $\Delta v/v = 25\%$ FWHM) and after the decelerator for the guiding mode of operation ($v_{\mathrm{mean}} = v_{\mathrm{s}} = 470$ m/s, $\Phi = 0°$) and at 28 m/s ($v_{\mathrm{mean}} = 470$ m/s, $v_{\mathrm{s}} = 450$ m/s, $\Phi = 62.544°$). The source signal is normalised to unity and the signals after the decelerator are scaled such that they reflect the density changes predicted by Eqn. 5.2 and Eqn. 5.3, respectively. The arrows indicate the corresponding vertical axis. The signal levels are reproduced well by trajectory simulations, which are depicted in light grey and are vertically offset for clarity. The simulations take into account both, the $M_J\Omega = -9/4$ and $M_J\Omega = -3/4$ low-field-seeking states.

detecting OH in guiding mode, the PMT was set to -2000 V and the gain correction factor amounts to $\frac{G(0°)}{G(\mathrm{source})} = 590 \pm 170$. The LIF acquisition setup in the source chamber and the trap chamber is identical and consists of a lens with a focal length $f = 50$ mm and a diameter $d = 50$ mm. Therefore, the solid-angle under which LIF photons are collected is identical in both chambers. However, the excitation volume between the source chamber and the trap chamber is different. According to the solid angle calculations introduced in sec. 6.4, the laser beam in the source chamber and the trap chamber is imaged over a length of approx. 14 mm along the propagation direction of the laser beam, which is 3 mm in diameter. The solid angle function within the laser beam domain is depicted in Fig. 5.16 c). From geometric considerations and trajectory simulations in the source chamber it is estimated that the molecular beam spreads out radially by such an extent that the entire length of 14 mm are covered with OH molecules at a constant density of $(7.8 \pm 2.0) \cdot 10^9$ part./cm^3. Consequently, the source excitation volume is estimated to be

$V_{\text{exc.}}(\text{source}) = \pi \cdot 1.5^2 \cdot 14 = 99 \pm 27$ mm^3. On the other hand, the spatial dimension of the OH package after the decelerator is limited by the $\varnothing = 3$ mm diameter of the skimmer and the 2×2 mm^2 opening of the decelerator. The longitudinal extension depends on the phase angle and on the free flight distance at the end of the decelerator. The spatial dimensions of the OH package in guiding mode were obtained from trajectory simulations and are depicted in Fig. 5.16 a). The laser dimensions are indicated by the black vertical lines and an excitation volume of $V_{\text{exc.}}(0°) = 11.0 \pm 2.3$ mm^3 is obtained when considering that not the entire height of the LIF laser is covered by the OH cloud along the y-direction. The geometrical situation is depicted in Eqn. 5.5, where r denotes the radius of the laser beam, y refers to the height of the molecular package contributing to the signal, l is the length of the laser beam under consideration and θ represents the angle subtending the circular outer segment which is to be discarded. The area of the excitation volume is obtained by multiplying the cross section bounded by the circle and the two horizontal lines with the length l.

$$V_{\text{exc.}}(0°) = A \cdot l = \pi r^2 l - 2 \cdot \left(\frac{r^2}{2}(\theta - \sin(\theta)) \right) \cdot l \qquad (5.5)$$

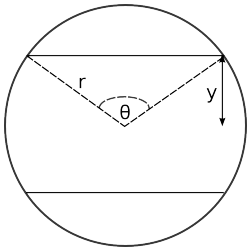

$$\theta = 2 \cdot \cos^{-1}\left(\frac{y}{r}\right)$$

The excitation volume scaling factor amounts to $\frac{V_{\text{exc.}}(0°)}{V_{\text{exc.}}(\text{source})} = 0.112 \pm 0.038$. The last factor required is the ratio between the signal intensity of the experimental TOF profile in the source chamber and in guiding mode: $\frac{I(\text{source})}{I(0°)} = 0.50 \pm 0.13$. The density reduction factor r_{guiding} between source conditions and guiding can then be calculated according to Eqn. 5.2:

$$\frac{I(\text{source})}{I(0°)} \cdot \frac{G(0°)}{G(\text{source})} \cdot \frac{T(0°)}{T(\text{source})} \cdot \frac{V_{\text{exc.}}(0°)}{V_{\text{exc.}}(\text{source})} = \frac{\rho(\text{source})}{\rho(0°)} = r_{\text{guiding}} = \qquad (5.6)$$

$$0.50 \cdot 590 \cdot 1.0 \cdot 0.112 = 33 \pm 17\,.$$

Finally, a $|f\rangle$-component density of $\rho(0°) = (2.4 \pm 1.4) \cdot 10^8$ part./cm^3 can be ascribed to the signal in guiding mode. All densities in chapter 5 were measured on the combined $Q_1(1)$ and $Q_{21}(1)$ transitions and therefore pertain to the $|f\rangle$-state population, which is the low-field seeking component transported through the decelerator upon application of electric fields. Consequently, the quantum states addressed by the LIF laser in the source

chamber and after the decelerator are identical, which ensures comparability of the signal levels.

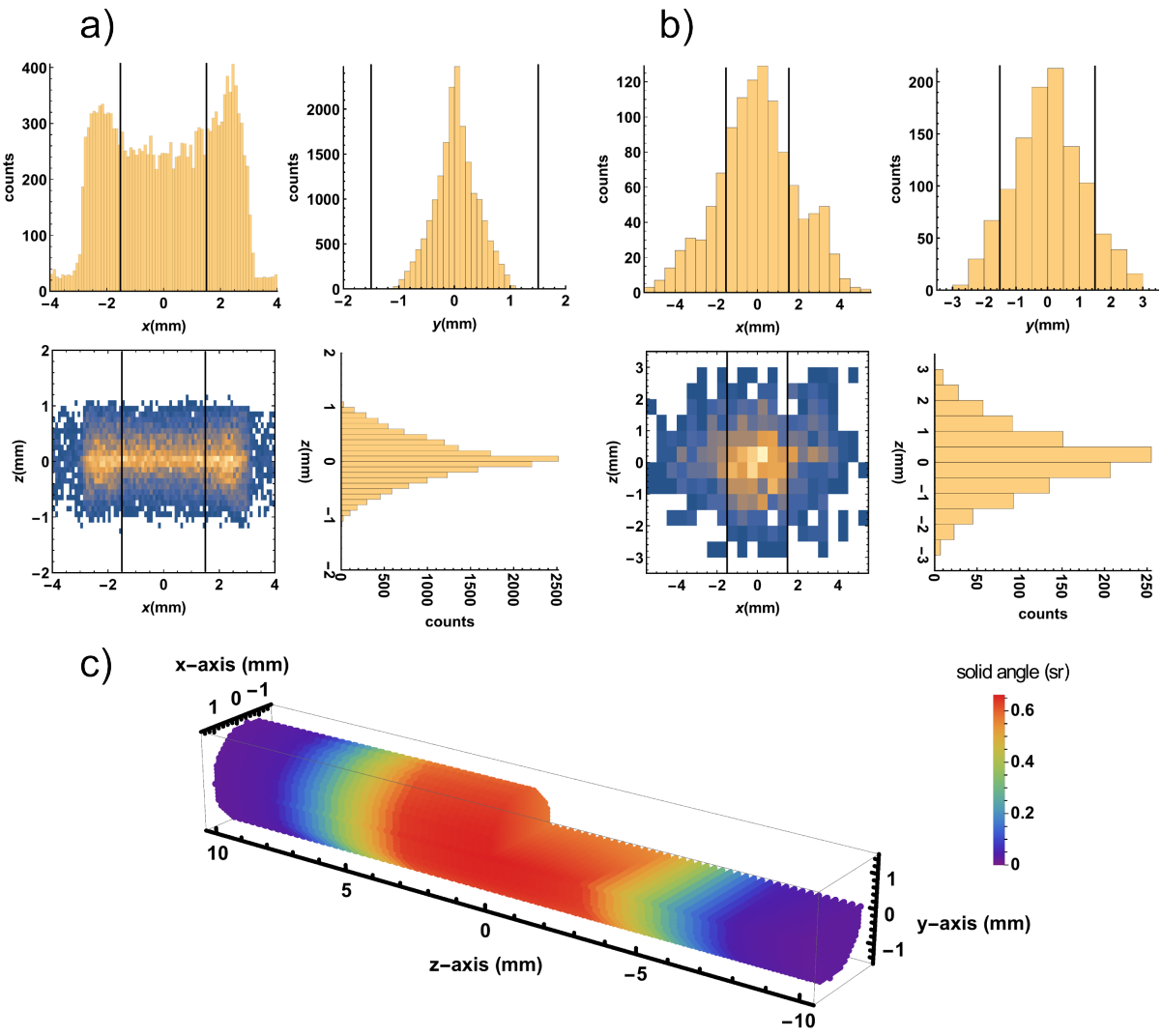

Figure 5.16: Spatial distribution of OH molecules at the laser detection zone after the decelerator for **a)** the guiding mode of operation and **b)** at 28 m/s. The x-direction denotes the axis of deceleration and the z-direction lies along the laser propagation path, as indicated by the coordinate system in Fig. 5.1. The dimensions of the cylindrical laser beam are indicated by the black bars. **c)** Solid angle function under which LIF photons can be detected by the lens (f = 50 mm, $\varnothing$= 50 mm) in the source and trap chamber. The laser beam is assumed to be of cylindrical shape with a diameter of 3 mm.

5.6.5 Density after the decelerator at 28 m/s

Similar procedures as outlined above apply for the determination of the density loss factor between the guiding signal and the slow OH package. For decelerating to a velocity of 28 m/s, the $v_s < v_{\mathrm{mean}}$ scheme from section 5.4.2 was employed. Due to the increased flight time between the end of the decelerator and the detection point, the OH package spreads

out significantly and the density distribution of the package is depicted in Fig. 5.16 b). The slow OH cloud covers the entire laser beam in the x, y-direction and displays an overlap of approx. 4 mm along the longitudinal z-axis of the laser beam. The coordinate system depicted in Fig. 5.1 applies and the following excitation volume at 28 m/s is obtained: $V_{\text{exc.}}(28\text{ m/s}) = 28.3 \pm 7.6\text{ mm}^3$. The density drop between guiding and the package at 28 m/s is then obtained by:

$$\frac{I(0°)}{I(28\text{ m/s})} \cdot \frac{G(28\text{ m/s})}{G(0°)} \cdot \frac{T(28\text{ m/s})}{T(0°)} \cdot \frac{V_{\text{exc.}}(28\text{ m/s})}{V_{\text{exc.}}(0°)} = \frac{\rho(0°)}{\rho(28\text{ m/s})} = r_{28\text{ m/s}} \tag{5.7}$$
$$= 32.9 \cdot 0.76 \cdot 1.0 \cdot 2.56 = 64 \pm 29$$

and the resulting $|f\rangle$-density at 28 m/s is determined to be $(3.7 \pm 2.7) \cdot 10^6$ part./cm^3. While the density obtained in this way is subjected to a relatively large uncertainty of more than 50%, it is nonetheless possible to deduce the correct order of magnitude from the procedure described here. Given a phase angle of $\Phi = 62.544°$ and an initial synchronous velocity of $v_s = 450$ m/s, the density achieved at 28 m/s is sufficiently large to allow for trapping experiments. As the density estimation procedure outlined in this section represents a veritable bookkeeping exercise, the parameters involved in the calculation are summarised in Tab. 5.1 for convenience. The excitation volume from which photons were collected is stated for each density value. The density only applies within this volume and represents an average density over the entire excitation volume as a single PMT does not provide spatial resolution. As can be seen from Fig. 5.16 a) and b), the local densities within the detection volume can vary by almost an order of magnitude and significantly larger peak densities are present within small and localised regions of the OH package. It is also worth noticing that good agreement between the simulation and the experimental

source density	guiding density	density at 28 m/s
	$\frac{I(\text{source})}{I(0°)} = 0.50 \pm 0.13$	$\frac{I(0°)}{I(28\text{ m/s})} = 32.9 \pm 8.8$
	$\frac{G(0°)}{G(\text{source})} = 590 \pm 170$	$\frac{G(28\text{ m/s})}{G(0°)} = 0.76 \pm 0.11$
$V_{\text{exc.}}(\text{sour.}) = 99 \pm 27\text{ mm}^3$	$V_{\text{exc.}}(0°) = 11.0 \pm 2.3\text{ mm}^3$	$V_{\text{exc.}}(28\text{ m/s}) = 28.3 \pm 7.6\text{ mm}^3$
	$\frac{V_{\text{exc.}}(0°)}{V_{\text{exc.}}(\text{source})} = 0.112 \pm 0.038$	$\frac{V_{\text{exc.}}(28\text{ m/s})}{V_{\text{exc.}}(0°)} = 2.56 \pm 0.87$
	$r_{\text{guiding}} = 33 \pm 17$	$r_{28\text{ m/s}} = 64 \pm 29$
$(7.8 \pm 2.0) \cdot 10^9$ part/cm^3	$(2.4 \pm 1.4) \cdot 10^8$ part/cm^3	$(3.7 \pm 2.7) \cdot 10^6$ part/cm^3

Table 5.1: Overview of the parameters employed in the determination of the density in the source chamber as well as after the decelerator for the guiding mode of operation and at 28 m/s. All densities stated pertain to the $|f\rangle$-component.

trace is achieved in Fig. 5.15, where the peak intensities have been scaled such that the changes in density are reflected. Consequently, the trajectory simulations take into account the relevant loss factors and faithfully reproduce the resulting changes in density. This can be utilised to estimate the density by an independent approach, which solely relies on the trajectory simulations.

5.6.6 Density from Monte Carlo trajectory simulations

Fig. 5.17 illustrates the procedure followed for determining the particle densities based entirely on trajectory simulations. In a first step, the molecular beam's longitudinal and radial properties such as the spatial and velocity spread were adjusted until the experimental curves in Fig. 5.15 were reproduced faithfully. A radial velocity spread of $10\% \cdot v_{\mathrm{mean}}$ and a $\Delta v / v_{\mathrm{mean}} = 25$ % FWHM Gaussian velocity distribution for the longitudinal direction were found to reproduce the experimental results best. Moreover, simulation particles were drawn from a Gaussian longitudinal position distribution with a FWHM of 14 mm representing the spatial spread of the package at the source. The radial extension of the starting volume was set to $r = 0.25$ mm, which matches the opening radius of the valve. The particles were then propagated through the setup taking into account all geometric obstacles including the skimmer and the 124 pairs of deceleration electrodes. A more detailed description of the Monte Carlo trajectory simulations is given in section 3.3. The distance between the laser beam and the skimmer amounts to 18.2 mm and the decelerator entrance is located 66.6 mm after the skimmer opening. For the present purpose, the code was adapted such that the number of simulated particles in the source

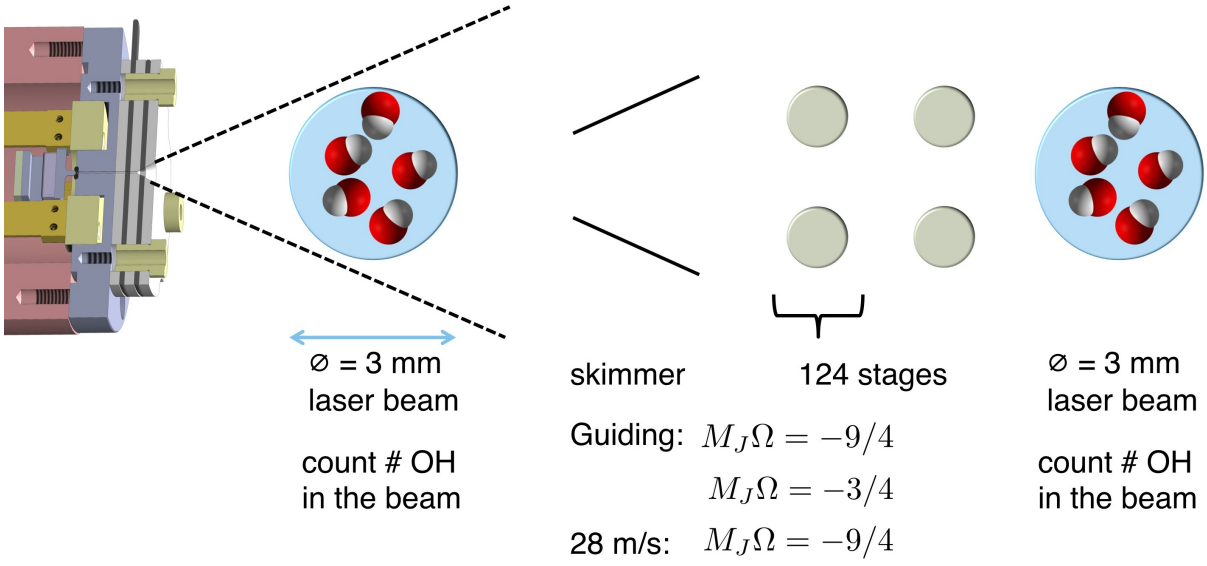

Figure 5.17: Scheme illustrating the simulation procedure for the computational determination of densities after the decelerator.

laser beam could be counted. In the source chamber, the region of counting was adjusted such that an excitation volume identical to the one in the experiment ($V_{\text{exc.}}$(source)) was covered. Additionally, the counting was performed such that only particles were included which were inside the laser beam at the point in time at which the synchronous particle reached the centre of the cylinder. This approach is equivalent to guiding a short laser pulse through the source chamber at a delay leading to a maximum LIF signal intensity and working out the number of OH molecules from the LIF trace. After having passed the laser beam with a length of 14 mm, the molecules hitting the chamber walls or the skimmer surfaces were removed from the simulation. The part of the beam flying through the skimmer opening was propagated through the decelerator under the influence of the forces exerted on the OH molecules by applying ±10 kV on the electrodes. The counting procedure adopted in the source chamber was repeated after the decelerator for excitation volumes identical to $V_{\text{exc.}}(0°)$ or $V_{\text{exc.}}(28\text{ m/s})$, depending on the decelerator's mode of operation.

In guiding mode ($\Phi = 0°$), the $M_J\Omega = -9/4$ and the $M_J\Omega = -3/4$ low field seeking states need to be taken into account. Each state was simulated separately starting with $2 \cdot 10^6$ molecules. After the decelerator, 12605 ($M_J\Omega = -9/4$) and 10545 ($M_J\Omega = -3/4$) molecules were counted within the laser excitation volume in guiding mode. A total of 659 OH molecules were counted within the laser beam for a package leaving the decelerator at 28 m/s. The total number of molecules counted in the laser volume needs to be scaled by $r_{\text{scal.}}$, such that a $|f\rangle$-state source chamber density of $7.8 \cdot 10^9$ part./cm^3 is reached.

$$r_{\text{scal.}} = \frac{\rho(\text{source})}{(N_{\text{OH},1}(\text{source}) + N_{\text{OH},2}(\text{source}))/V_{\text{exc.}}(\text{source})}\,, \tag{5.8}$$

where ρ(source) = 7.8·10^9 part./cm^3 denotes the experimentally determined $|f\rangle$-density in the source chamber and $N_{\text{OH},1}$(source) designates the OH number within the laser beam for the $M_J\Omega = -9/4$ simulation and $N_{\text{OH},2}$(source) for the $M_J\Omega = -3/4$ simulation, respectively. The density in guiding mode is then obtained by the following expression:

$$\rho(0°) = r_{\text{scal.}} \cdot \frac{N_{\text{OH},1}(\Phi = 0°, M_J\Omega = -9/4) + N_{\text{OH},2}(\Phi = 0°, M_J\Omega = -3/4)}{V_{\text{exc.}}(0°)}\,, \tag{5.9}$$

where $N_{\text{OH},1}(\Phi = 0°, M_J\Omega = -9/4)$ and $N_{\text{OH},2}(\Phi = 0°, M_J\Omega = -3/4)$ denote the number of OH molecules counted within the excitation volume $V_{\text{exc.}}(0°)$ after the decelerator. Analogously, the density at 28 m/s is determined by:

$$\rho(28\text{ m/s}) = r_{\text{scal.}} \cdot \frac{N_{\text{OH},1}(28\text{ m/s}, M_J\Omega = -9/4)}{V_{\text{exc.}}(28\text{ m/s})}\,, \tag{5.10}$$

where the $M_J\Omega = -3/4$ state was excluded, as no contribution of this state could be detected at the end of the decelerator at elevated phase angles. The densities obtained via trajectory simulations are listed in Tab. 5.2. The relative uncertainties of the density values obtained from trajectory simulations are smaller than the ones obtainable from experimental data. The only uncertainties employed for calculating the error budget of the simulated densities are the error of the density in the source chamber and a counting uncertainty of 5% for the particles inside the laser beam. The densities from experimental scaling are lower than the simulated densities. This is probably due to the simulation not taking into account skimmer interference, skimmer clogging and small imperfections in the alignment. The advantage of the density estimation by means of trajectory simulations is that the simulation does not require knowledge of the PMT gain curve, which is another source of uncertainty. Additionally, no imaging system is involved, as the OH molecules are directly counted within the laser beam. Hence, errors from imperfect lens alignment, changes in the solid angle and fluctuations of the laser beam profile are not present in the simulation.

method	ρ(source) (part./cm^3)	$\rho(0°)$ (part./cm^3)	ρ(28 m/s) (part./cm^3)
experiment	$(7.8 \pm 2.0) \cdot 10^9$	$(2.4 \pm 1.4) \cdot 10^8$	$(3.7 \pm 2.7) \cdot 10^6$
simulation	$(7.8 \pm 2.0) \cdot 10^9$	$(7.7 \pm 2.3) \cdot 10^8$	$(1.1 \pm 0.3) \cdot 10^7$

Table 5.2: Comparison of the densities in guiding mode and at 28 m/s obtained by either scaling experimental data or via particle counting in Monte Carlo trajectory simulations. All densities stated pertain to the $|f\rangle$-component.

5.7 Conclusion and Outlook

In this chapter, the construction and the commissioning of a 124 stage Stark decelerator have been described. Additionally, the optimisation of relevant experimental parameters for maximising the beam density of Stark-decelerated radicals for low-velocity applications has been discussed. Crucial parameters are the type of carrier gas, the discharge conditions in the radical source, the velocity, velocity spread and spatial spread of the initial molecular beam. The radical density after the decelerator can be improved further by adjusting the synchronous velocity for coupling the beam into the decelerator. For reaching low velocities, the operation of a 2×2 mm^2 decelerator at potentials higher than ±10 kV is not recommended.

Molecular beams of OH radicals seeded in Kr and Xe carrier gases have been characterised and the implications of the different beam properties on Stark deceleration have

been investigated. Higher OH densities are initially achieved using faster Kr beams, but the Stark decelerator has to be operated at a higher phase angle and therefore lower stable phase-space volume in comparison to Xe. Thus, the radical densities achieved after deceleration proved similar.

The effect of velocity spread and spatial spread of the beam on the final number densities has been discussed. An optimised operation scheme has been found by fixing the discharge delay to the maximum density of the beam profile, thereby minimising the velocity spread. Instructions for finding valve and discharge parameters suitable for deceleration have been given.

The synchronous velocity, according to which the switching sequence applied to the Stark decelerator is designed, can be tuned within the beam's velocity profile. By appropriately lowering the synchronous velocity below the mean velocity of the molecular beam, the number density of the decelerated OH radicals can be increased. However, there is a trade-off between decreasing the synchronous velocity (and thus increasing the phase-space acceptance of the decelerator) and the loss of beam density by deviating too far from the mean velocity of the beam.

Finally, procedures for the determination of the density in the source chamber and after the decelerator have been outlined. In a first step, a density of $(7.8\pm2.0)\cdot10^9$ part./cm^3 was determined in the source chamber by installing two pinhole plates. When correcting for the PMT gain, the filter transmission and the excitation volume, the source chamber density can be scaled by the measured signal intensities in order to deduce the density behind the decelerator in guiding mode and at 28 m/s. Alternatively, the density can be estimated by means of Monte Carlo trajectory simulations. Satisfactory agreement between the two methods was found and the density in guiding mode amounts to $(2.4\pm1.4)\cdot10^8$ part./cm^3, whereas the density is reduced to $(3.7 \pm 2.7) \cdot 10^6$ part./cm^3 at 28 m/s.

The focus of this chapter lies on optimising OH radical densities of molecular packages decelerated to low final velocities. Therefore, it represents an important milestone in fulfilling fundamental requirements for the magnetic trapping of OH. With the present trap design, loading velocities below 30 m/s are required for successfully loading OH molecules into the trap. As the final loading and stopping process involves density losses, it is of paramount importance to optimise the molecular beam source and the deceleration process up front. It is also worth mentioning that for achieving even lower velocities, it is advantageous to couple a conventional Stark decelerator (as employed here) with a

ring Stark decelerator [98]. The latter decelerator type offers an improved deceleration performance for very slow molecules. Such a scheme has been demonstrated in ref. [90].

Chapter 6

Cryogenic Magnetic Trapping of cold polar molecules

6.1 Introduction

6.1.1 Trapping neutral molecules

The "conventional" Stark decelerator consisting of alternating vertical and horizontal electrode pairs offers longitudinal confinement as well as alternating focussing forces along the transverse directions. However, once a slow package of OH molecules is obtained, the type of decelerator employed in this thesis cannot retain the molecular cloud and a trap is required for storing the slowed molecules over prolonged periods of time. Due to the complexity of molecular species and their rich internal energy structure, the trapping of slow neutral molecules offers appealing prospects such as the study of quantum-state resolved collisions and chemical reactions at low temperatures [88, 275, 276], the determination of radiative lifetimes [240, 266, 277] and evaporative cooling from a trapped ensemble [28]. Furthermore, cold molecules are considered ideal candidates in the search for physics beyond the standard model [5, 255]. All of the above-mentioned applications can benefit from the long interrogation time offered by trapping environments. Trap lifetimes are limited by collisions with energetic background gas particles leading to ejection from the trap and by the black body radiation (BBR) induced pumping out of trappable states [278].

A wide range of trapping experiments involving neutral molecules have been reported in the literature and ref. [279] (see Tab. I therein) provides a comprehensive summary on the different trap loading and trapping schemes which have been devised up to the year 2013.

Based on: D. Haas*, C. von Planta*, T. Kierspel, D. Zhang, S. Willitsch, Long-term trapping of Stark-decelerated molecules, *Comms. Phys.*, 2019, **2**, 101. * These authors contributed equally.

Usually, the trap geometry and with that the type of the confining potential is adapted to the characteristics of the slow molecule source to ensure optimal coupling of the molecule package to the trap. In this section, the focus is put on the confinement of molecules by the Zeeman or Stark shifts caused by field gradients emanating from the trap's high-voltage electrodes or magnets. For static traps, Maxwell's equations solely allow for the formation of a three-dimensional field minimum, but not a maximum [279, 280]. Consequently, only molecules in their electrically or magnetically low field-seeking states can be confined [279]. The confinement of high-field seeking molecules has been accomplished in an AC trap [281], however.

Despite being limited to molecules with a magnetic moment, magnetic traps are quite common and have been employed in a wide range of experiments. A variety of magnetic traps has been implemented involving permanent magnets [49, 88, 282–285], electromagnets [54, 286, 287], superconducting magnets [286, 288, 289] and cryogenic permanent magnets, as is the case in this thesis. The first magnetic trapping of a neutral molecule was demonstrated by Weinstein and coworkers [31]. In their experiment CaH was laser ablated and buffer gas loaded into a superconducting magnetic trap. The advantage of such a scheme is that the buffer gas offers continuous collision-mediated cooling while the paramagnetic species approaches the trap centre. On the other hand, careful control over the background gas level is required if loading from cryogenic buffer gas beams to ensure the longevity of the trapped ensemble [286]. Additionally, magnetic traps have successfully been loaded from Stark [49, 54, 88] and Zeeman [283, 285, 289] decelerators.

The loading of permanent magnetic traps from Zeeman decelerators requires opening of the trap by eliminating the entrance hump of the Zeeman potential to prevent reflection of the incoming slow molecule package. Frequently, the field-compensation is accomplished with pulsed electromagnetic coils [283, 285, 289]. Alternatively, the loading of electromagnetic traps can be realised by activating the downstream rear electromagnet first such that it acts as a last deceleration stage. Subsequently, the trap is closed by activating the electromagnet closer to the decelerator exit once the slowed package is entirely within the trap [54, 287].

When loading a magnetic trap from a Stark decelerator, a different strategy is usually adopted. The molecular package approaches the trap at kinetic energies surmounting the shoulder of the confining Zeeman potential and electric fields are applied to the magnets as a final deceleration stage to remove the surplus of kinetic energy once the package is in the vicinity of the trap centre [49, 54, 88]. As discussed in section 6.2.2, this scheme also applies to the trapping experiments described in this chapter. Moreover, magnetic

traps have also been loaded with SH radicals brought to a near standstill at the trap centre via photodissociation of SH_2 [284]. As superconducting traps are operated in cryogenic environments, the BBR pumping out of trappable states is largely suppressed and enhanced storage times of $\approx$ 25 s have been reported for buffer gas loaded NH molecules [286] and very recently trapped O_2 molecules have been observed for as long as 90 s by Y. Segev and coworkers [289].

Electrostatic trapping of polar molecules has been conducted from Stark decelerated species [55, 74, 75, 100, 266, 278, 290], photoassociation [291] and velocity selection in combination with adiabatic [292] and Sisyphus cooling [29, 30]. Most traps have been implemented in the form of electrostatic quadrupole traps [55, 74, 75, 266, 278, 290] placed after the decelerator exit. Furthermore, static trapping of NH_3 and ND_3 molecules within a travelling wave decelerator has been reported in ref. [100]. As travelling wave decelerators provide improved transverse focussing properties at low velocities and the trapping takes place within the decelerator, a large portion of the molecular package can be confined. Other types of electric traps include the trapping of CO molecules on a chip trap [95] and the trapping of NaCs molecules between thin wire loops producing a quadrupolar field [291]. M. Schnell and coworkers have developed an AC electric trap allowing for the confinement of electrically high-field seeking $^{15}ND_3$ [281]. Long 1/e-storage lifetimes of 12 s (CH_3F) [292], 27 s (CH_3F) [29] and 57 s (H_2CO) [30] have been achieved in a micro-structured electrostatic trap.

6.1.2 A new type of hybrid trap

Hybrid systems of cold atoms and ions have been studied intensively in recent years. The simultaneous trapping of atoms with ions has opened up new possibilities for the investigation of interactions between the two species and has greatly contributed to the understanding of collisional and chemical processes at low temperatures [7, 51, 293, 294].

The cryogenic magnetic trapping scheme described in this thesis forms part of an advanced hybrid trapping technique which aims at trapping neutral molecules and molecular ions simultaneously [51]. The principle of the hybrid trapping scheme is depicted in Fig. 6.1. A translationally cold package of neutral molecules (red ellipsoid in Fig. 6.1) is produced by means of Stark deceleration [35] and the optimised operation of our Stark decelerator at low final velocities has been discussed in chapter 5. During the last deceleration stage, a translationally cold package of OH radicals is loaded into a magnetic trap, which is incorporated into an RF thin wire ion trap [295]. A Coulomb crystal (blue ellipsoid in Fig. 6.1) is loaded into the ion trap, which is located on the same principle axis as

the magnetic trap. A Coulomb crystal is an ordered and localised arrangement of laser-cooled ions within an ion trap. Due to laser cooling, the translational motion of the ions lies in the low mK-regime [6, 296]. Molecular ions can be cooled sympathetically to $T < 10$ mK by exchanging kinetic energy with the laser-cooled atomic ions [296]. By sliding the bar magnets along the principle axis, the two traps are superimposed, which renders the setup a hybrid trap. While ions can be stored inside an ion trap for timescales reaching minutes and even hours [296], the lifetime of trapped polar diatomic molecules is limited by the blackbody radiation (BBR) pumping OH out of trappable states. Hence, the hybrid trapping scheme is surrounded by a cryogenic shield in order to suppress the BBR intensity reaching the trap centre and to increase the trap lifetime of the neutral species. Additionally, the pumping capacity of the cryogenic shield improves the background pressure, which is crucial for maintaining a good state purity over the course of collision experiments.

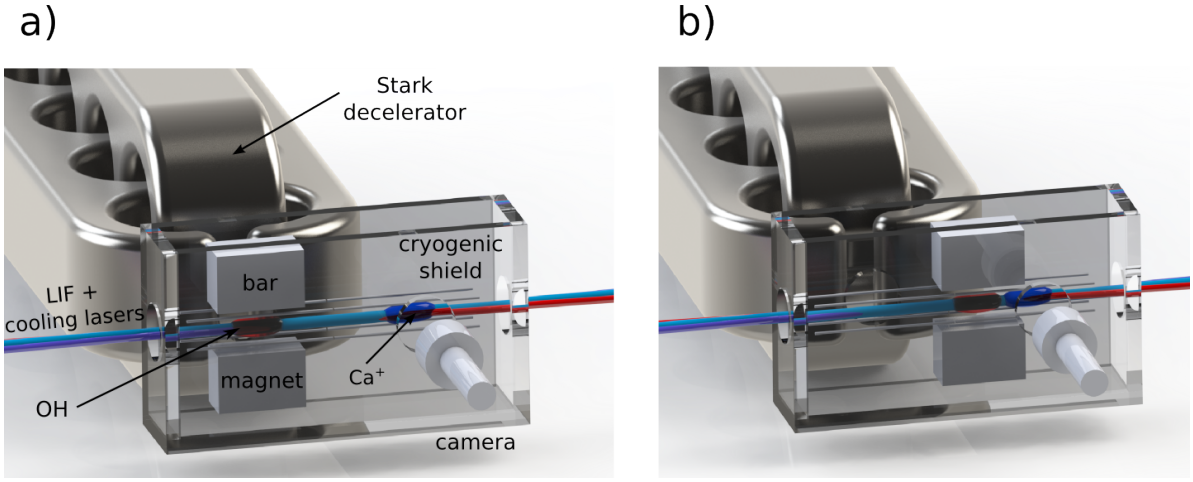

Figure 6.1: Scheme of an ion-molecule hybrid trap setup consisting of a Stark decelerator coupled to a magnetic trap encompassing a cryogenic ion trap. The box around the trap structure represents a cryogenic shield, which prevents blackbody radiation from reaching the trapped molecules. **a)** A package of translationally cold molecules (red ellipsoid) is loaded into a magnetic trap. The presence of the OH radicals is monitored using a 282 nm LIF laser. A Ca^+ Coulomb crystal (blue ellipsoid) is loaded into the thin wire ion trap lying on the same principle axis as the magnetic trap. The Ca^+ ions are laser-cooled using a 397 nm laser and a 866 nm repumper laser. **b)** Sliding the bar magnets along the trap axis allows for the superposition of the trapped neutral molecules with the Coulomb crystal. Fluorescence of the Coulomb crystal is detected using a CCD camera.

The molecular ion-neutral hybrid trap widens the chemical space of the hybrid trapping technique and paves the way for the investigation of quantum-state selective elastic, inelastic and reactive collisions at low translational energies $E_{\text{coll.}} < 30$ mK. Interesting target systems are OH + Ca^+, OH + N_2^+ and OH + H_2O^+. However, the hybrid trap is

by no means limited to OH and other radicals such as NH and SH are suitable for deceleration and trap loading [35]. The study of ion-molecule reactions at low temperatures is of great interest for attaining a better understanding of the chemical processes taking place in interstellar clouds [297–299]. Under these conditions ion-molecule reactions are often barrierless and the reaction rate is dominated by long-range interactions between the reactants [297, 300]. Furthermore, ion-molecule reactions play an important role in plasma and combustion chemistry [297]. At very low collision energies, reactions are often governed by few partial waves and the dependence on the collision's angular momentum allows for the observation of quantum phenomena such as scattering resonances and the tunnelling through centrifugal barriers [3, 18, 300]. The present hybrid trapping scheme was developed with the prospect of observing the aforementioned quantum mechanical effects in ion-molecule systems. The field of ion-molecule chemistry has recently been reviewed by D. Zhang and S. Willitsch [300].

While the hybrid trap functionality is not demonstrated in this chapter, the loading and cryogenic long-term trapping of hydroxyl radicals described here represent an important prerequisite for the superposition of cold neutral molecules with molecular ions. The trap loading measurements were conducted with a fully implemented version of the hybrid trap. Furthermore, detailed accounts on the design and optimisation of the trap loading process are given.

6.2 Trap loading simulations

Prior to construction of the hybrid trap, the loading process was modelled by Monte Carlo trajectory simulations in order to determine ideal trap parameters such as the dimensions of the trapping volume as well as the shape and magnitude of the stopping and trapping potentials. Moreover, the simulations allow for detailed insights on the phase space distribution and dynamics of the trapped OH cloud. Binning of the particles within a laser volume region allows for the computation of time of flight (TOF) profiles, which can directly be compared with experimental TOF traces. Therefore, the simulation of Monte Carlo trajectories from the source to the trap region provides an invaluable tool for validating and interpreting experimental results. In this section, technical details on the implementation of the trap loading simulations will be discussed. The general principles of the loading strategy are elucidated and the implementation of the algorithm is described. The successful application of a mesh adaptive direct search optimisation algorithm for achieving improved loading efficiencies is reported. A detailed description of the phase-space considerations during loading and the subsequent phase-space dynamics inside the trap has been relegated to section 6.5.3 as it represents a key result of this thesis.

6.2.1 Coupling the Stark decelerator to a magnetic trap

Efficient transfer of the decelerated OH package into the magnetic trap required careful minimisation of particle losses during the loading procedure. Successful trap loading necessitates minimising the volumetric mismatch between the phase stable region of the decelerator and the trap [301, 302]. During free flight after exiting the decelerator, the molecular package starts expanding in both, the longitudinal and transversal directions. Therefore, placing the trap close to the decelerator helps to prevent losses. In practice, this requirement is mitigated by the presence of the two cryogenic shields and a safety distance that has to be held towards the last high voltage electrode of the decelerator. Currently, the distance between the end of the decelerator and the trap centre amounts to 11.5 mm. As illustrated in Fig. 6.2, the loading process was designed such that the bar magnets forming the magnetic trap also serve as a last electrostatic deceleration stage. Since an additional and final deceleration step occurs in close proximity to the trap centre [54, 88, 301], this scheme allows for loading the trap with molecules leaving the decelerator at velocities exceeding the trap's acceptance velocity. Furthermore, loading at increased velocities ($29 < v < 38$ m/s) reduces the amount of transversal spreading as the flight time towards the trap centre is reduced. The loading of comparatively fast packages also leads to a diminution of particle loss caused by reflection on the entrance shoulder of the Zeeman potential. In addition, four wire electrodes were spanned in between the magnets to introduce further degrees of freedom in shaping the stopping fields. The stopping wires allow to match the Stark potential to the velocity distribution of the incoming package. The resulting stopping and trapping fields are depicted in Fig. 6.3.

6.2.2 Modelling the trap loading process

6.2.2.1 Electric and magnetic fields

For simulating the trap loading, which involves a final electrostatic deceleration step, the electric fields of the trap structure were computed using COMSOL [237]. The Stark energy and the acceleration of the OH particles were calculated according to equation 3.35 and 3.36, respectively. The Stark energy experienced by OH in the $X^2\Pi_{3/2}(J = 3/2,\ M_J = \pm 3/2,\ f)$ states is depicted in Fig. 6.3 a) and the distances indicated in Fig. 6.2 apply. For a voltage configuration of ± 2.3 kV on the front stopping wires and ± 5.8 kV on the bar magnets and rear stopping wires, the maximum amount of energy that can be removed from an OH package approaching along the x-direction ($y, z = 0$) amounts to 0.76 cm^{-1}. The kinetic energy of a molecule reaching the trap centre is reduced by 0.59 cm^{-1}. Along y, the stopping potential is weakly confining and along the z-direction confining forces are absent.

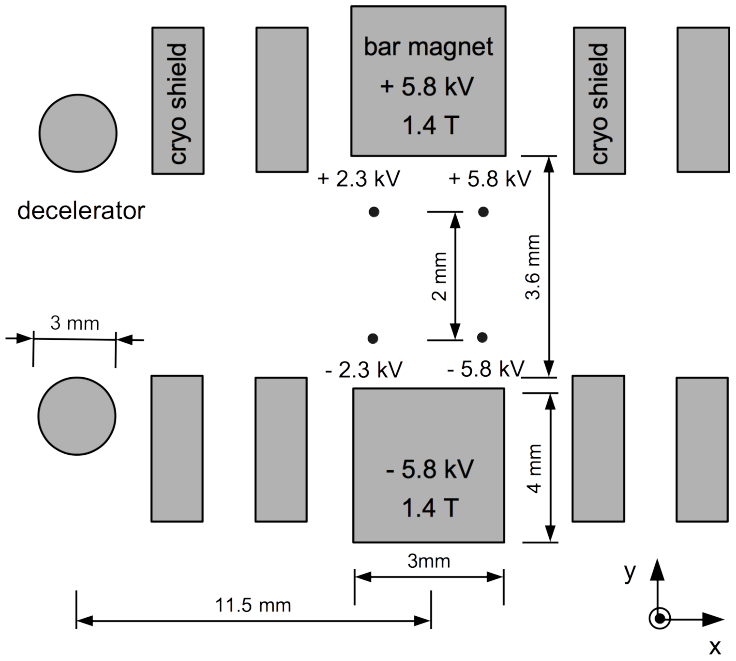

Figure 6.2: Cross sectional view through the hybrid trap illustrating the electrode geometry required for loading. The stopping wires are 0.2 mm in diameter and a potential of ±2.3 kV is applied to the front wires and ±5.8 kV to the rear stopping wires. The bar magnets are pulsed at a potential difference of ±5.8 kV. Except for the opening holes, the grounded cryogenic shields form a Faraday cage around the hybrid trap.

The magnetic fields generated by the two bar magnets forming the permanent magnetic trap were obtained from analytical expressions outlined in ref. [303]. The Zeeman energy of OH in the $X^2\Pi_{3/2}(J = 3/2,\ M_J = +3/2,\ f)$ state inside the magnetic trap is depicted in Fig. 6.3 and was obtained from

$$E_{\text{Zeeman}} = \mu_B \left| \vec{B}(x, y, z) \right| \frac{M_J \Omega (\Lambda + g_e \Sigma)}{J(J+1)}, \tag{6.1}$$

where μ_B is the Bohr magneton, g_e denotes the free electron g-factor, $J, \Omega, \Lambda, \Sigma$ are the Hund's case (a) quantum numbers and M_J is the projection of J onto the space-fixed axis. The Zeeman trapping potential E_{Zm} for the $X^2\Pi_{3/2}(J = 3/2,\ M_J = +3/2,\ f)$ state in between the two 1.64 T PrFeB magnets is depicted in Fig. 6.3 b). The resulting magnetic trap has a depth of 0.14 cm^{-1} (corresponding to a maximum velocity of 13.9 m/s for OH radicals in this state) along the longitudinal x-direction as well as 0.33 cm^{-1} (21.7 m/s) and 0.13 cm^{-1} (13.3 m/s) along the transverse y- and z-directions, respectively. Under room temperature conditions, the remanescence of the bar magnets is reduced to 1.4 T. Consequently, the trap is shallower and the trap depth along the x-direction amounts to 0.12 cm^{-1} (12.8 m/s) and the transverse trap depths are 0.29 cm^{-1} (20.0 m/s) along y and 0.11 cm^{-1} (12.3 m/s) along z. From the packet of decelerated molecules, only those

in the low field seeking $J = 3/2,\ M_J = +3/2,\ f$ Zeeman component can be confined magnetically [54, 88]. This comprises half of the molecules in the decelerated ensemble.

While the magnetic field was permanent and reached into the last decelerator stage, the electric field was usually switched on once the synchronous molecule reached the cryogenic shields and was switched off at the time the synchronous molecule arrived at the trap centre. The exact timing of the electric field was optimised by the procedures described in section 6.2.3. As depicted in Fig. 6.3 c), the Stark energy slope extends beyond the trap centre and allows for matching the deceleration in Fig. 6.3 d) to the velocity distribution of the incoming OH package. This field configuration allows to stop molecules that are slightly faster than the synchronous molecule, which enhances the loading efficiency. Trajectory simulations confirm that at low velocities, the greatest loss of molecules during the loading procedure is caused by the reflection of slower molecules from the stopping fields.

6.2.2.2 Trajectory simulations

The Monte Carlo trajectory simulations for the Stark decelerator have been described in section 3.3. For the simulation of the trap loading process, the code was modified such that interactions with the Stark and Zeeman potentials depicted in Fig. 6.3 could be included. The permanent magnetic field reached into the first deceleration stage. The molecules exiting the decelerator were propagated to the switchon point of the stopping field and the trajectories were continued under the influence of the combined Stark and Zeeman potentials. Upon reaching the trap centre, the stopping fields were switched off and the decelerated package was left to evolve within the trap potential. The geometry depicted in Fig. 6.3 was taken into account in the simulations. After every integration timestep, the position of each simulated particle was checked against the geometry and particles hitting solid objects were removed from the simulation.

The trap loading simulation covers the $J = 3/2,\ M_J = \pm 3/2,\ f$ states of which the $M_J = -3/2$ component is magnetically high-field seeking and is lost during the loading process. Consequently, the remaining signal of trapped molecules was a factor of two lower than the signal intensity after the last deceleration stage. After completion of the loading process, the trajectories of the molecules in the trap potential were propagated up to 0.1 s. Details of the trap dynamics including the full six-dimensional evolution of the phase-space volume were extracted from the simulations and are depicted in Fig. 6.16. Furthermore, the simulation also took into account the laser beam through the trap centre. Binning the arrival times of the particles at the excitation volume limited to a radius of

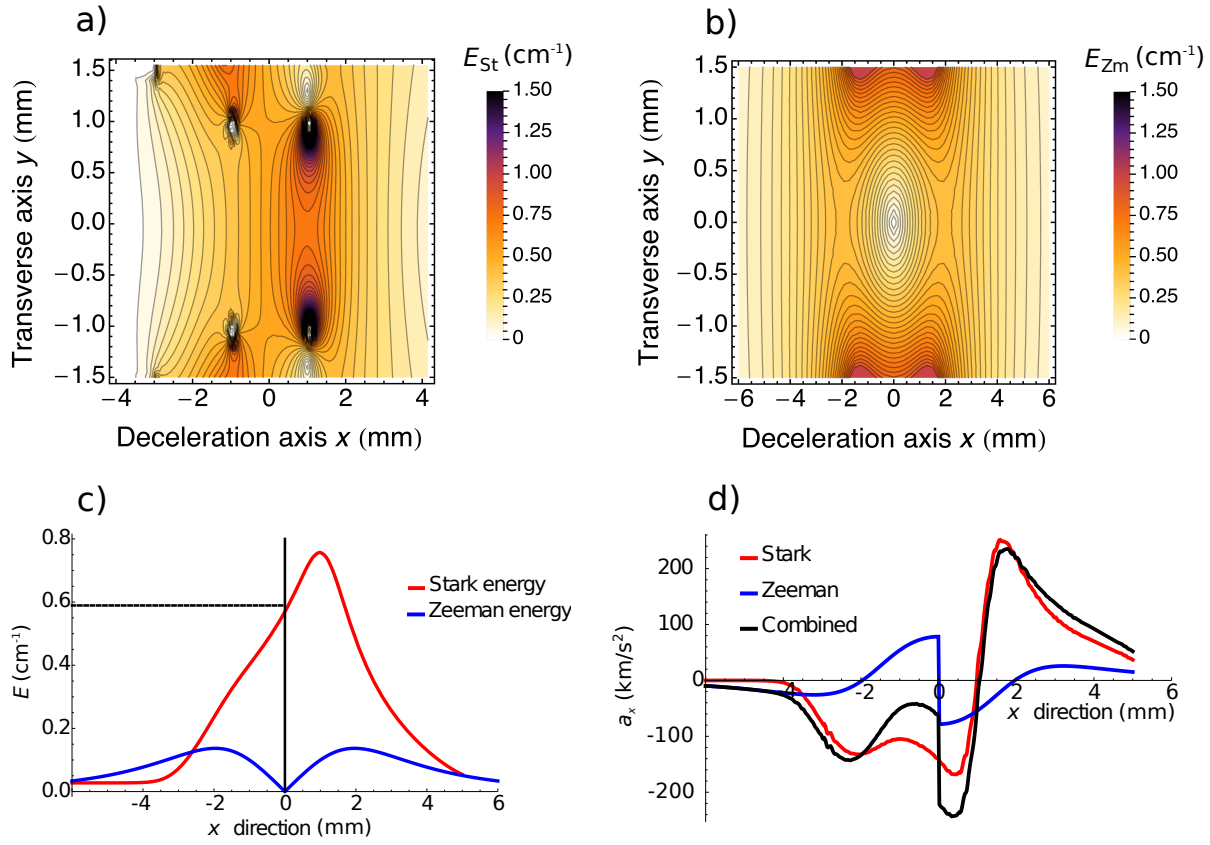

Figure 6.3: Stopping and trapping potentials. **a)** Stark energies E_{St} for OH in the $J = 3/2,\ M_J = \pm 3/2,\ f$ state resulting from applying an electric potential of ± 5.8 kV on the bar magnets and the rear stopping wires. The stopping wires closer to the decelerator exit are kept at ± 2.3 kV. **b)** Zeeman energies E_{Zm} for OH in the $J = 3/2,\ M_J = +3/2,\ f$ state, where the bar magnets display a remanescence of 1.64 T. **c)** Stark/Zeeman energy profile along the stopping direction $(y, z = 0)$. The black vertical bar represents the trap centre and the horizontal dashed line corresponds to the kinetic energy of the synchronous molecule at the decelerator exit (28.8 m/s, 0.59 cm^{-1}). **d)** Longitudinal acceleration a_x for OH molecules according to the Stark and Zeeman energies from c). The x-direction lies along the deceleration axis and the y-direction lies normal to the magnet surfaces enclosing the OH cloud. All distances are given relative to the trap centre.

0.7 mm and weighting the counts allowed for simulating TOF profiles which could be compared with experimental TOF traces, see Fig. 6.12.

6.2.3 NOMAD optimisations

The complexity of the stopping geometry and the many parameters influencing the loading efficiency make it difficult to optimise the loading conditions manually. Instead, a numerical optimisation procedure (the NOMAD direct search algorithm [113, 304]) was implemented in the trajectory simulations to predict optimised experimental parameters and to facilitate the elucidation of the best loading strategy. Here, the loading efficiency is

defined as the fraction of molecules remaining in the trap after 0.1 s relative to the number of phase-space stable molecules leaving the decelerator. The loading efficiency was taken as a figure of merit and the optimisation was performed with respect to the phase angle ϕ and the stopping potentials V_{front} on the front stopping wires, V_{bar} on the bar magnets and V_{rear} on the rear stopping wires. During the initial design stages of the hybrid trap additional parameters such as the switchon/switchoff points of the electric fields and the distance between the decelerator exit and the trap centre were taken into account. With progressing construction of the experiment, the distance between the decelerator exit and the trap centre had to be fixed to 11.5 mm. Compared to the previously assumed distance of 6.5 mm, the optimised loading efficiencies dropped by a factor of 1.5 at 11.5 mm. The decrease in loading efficiency is due to the increased flight time towards the trap centre, which fosters spatial spreading of the package.

The implementation of the optimisation algorithm into the Monte Carlo trajectory simulations is depicted in Fig. 6.4. The NOMAD direct search algorithm [113, 304] can be utilised as a blackbox optimiser, which makes it ideally suited for interacting with the Monte Carlo trajectory computer code. Initially, a molecule sample consisting of 10^6 particles with a velocity spread of 12% (FWHM) was generated. Each optimisation run was conducted from an identical starting distribution. The NOMAD optimiser controlled the parameter space of each individual run and the stopping potentials were scaled according to $V_{\text{front}}, V_{\text{bar}}$ and V_{back}. Subsequently, a burst sequence was calculated with the phase angle ϕ_0 determined by the optimiser. The trajectories were then propagated according to the procedures outlined in section 6.2.2. After switching the stopping fields off and propagating the trajectories inside the trap for 0.1 s, the number of OH particles remaining in the trap was counted. In a final step, the loading efficiency was computed and written to a table and the NOMAD optimiser was updated with the outcome of the simulation. This procedure was found to be very helpful in designing the loading process as the search for optimum parameters was automated and did not require manual intervention.

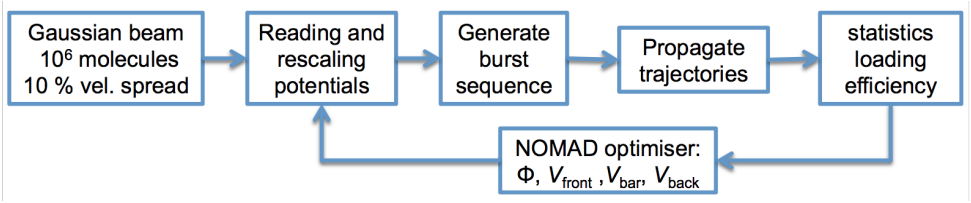

Figure 6.4: Graphical visualisation illustrating the incorporation of the optimisation algorithm into the Monte Carlo trajectory simulation discussed in section 6.2.2.

It was found that the loading efficiency is optimal if the stopping field is switched on once the synchronous particle reaches the circular opening in the outer cryogenic shield and the fields are switched off by the time the synchronous particle reaches the trap centre. The trap loading process was optimised under the restriction that $V_{\mathrm{bar}} = V_{\mathrm{rear}}$ as the two electrode pairs share high-voltage switches in the experiment. In order to map out the optimised working range of the hybrid trap, loading efficiency optimisations have been conducted for 5 different sets of potential ranges. Due to electrostatic breakdown of the trap, the experimental potentials on the bar magnets and the rear stopping wires were limited to ± 5.8 kV and the ± 2.3 kV on the front wires were obtained from a 40% voltage divider.

The best operational parameters and corresponding loading efficiencies are listed in Tab. 6.1 along with the experimental operation conditions. The loading efficiencies under cryogenic conditions were quite similar. The efficiencies stated in Tab. 6.1 already include a reduction by a factor 2 due to the loss of the magnetically high-field seeking $J = 3/2,\ M_J = -3/2,\ f$ state. Table 6.1 displays an increase in loading efficiency at larger stopping potentials, which allows for the removal of more kinetic energy during the trap loading process. Consequently, the velocity after the decelerator v_{decel}, which is still amenable to trapping, is increased. The flight time between the exit of the decelerator and the cryogenic shields is reduced at larger velocities, which leads to a reduction of the transversal spread of the OH package and an improved phase-space density at the switch-on point of the electric stopping field. The second reason for the gain in loading efficiency at higher potentials lies in the operation of the decelerator with a reduced phase angle which results in a larger phase-space stable deceleration volume leading to improved densities after the decelerator. The experimental operating parameters lead to a loading efficiency which is reduced by 2 percentage points compared to the optimised operation conditions of the lowest potential range. Currently, the reliable operation of the hybrid trap at lower potential differences outweighs the gain in loading efficiency that could be achieved at higher potentials.

In the end, the experiment imposed a stringent reduction on the degrees of freedom which are amenable to optimisation. The phase angle ϕ_0 and the stopping potential of the bar magnets and the rear stopping wires ($V_{\mathrm{bar}} = V_{\mathrm{rear}}$) were the only remaining parameters. The potential on the front wires was set to 40% of V_{bar}, in accordance with the voltage divider setting of the switching box. The low number of parameters renders it feasible to evaluate the loading efficiency function on a grid. The resulting loading efficiencies at stopping potentials between $5.5 - 7.5$ kV and phase angles lying in the range of $55.40 - 55.48°$ are depicted in Fig. 6.5. The loading efficiency was only evaluated

V_{range} (kV)	$V_{\text{bar,rear}}$ (kV)	V_{front} (kV)	phase ϕ (deg)	$v_{\text{decel}} \rightarrow v_{\text{trap}}$ (m/s)	efficiency (%)
10.5-9.5	10.5	4.4	55.276	38.2 → 3.3	16.8
9.5-8.5	9.4	4.1	55.309	36.6 → 6.1	15.7
8.5-7.5	8.2	3.4	55.371	33.7 → 4.3	14.9
7.5-6.5	7.4	2.9	55.412	31.8 → 3.7	13.4
6.5-5.5	6.5	1.9	55.452	29.7 → 7.0	11.7
experiment	5.8	2.3	55.468	28.8 → 7.2	9.9

Table 6.1: Optimised loading efficiencies at 1.4 T remanescence of the bar magnets. A total of 5 potential ranges is optimised for maximum loading efficiency. A complete loss of the $J = 3/2,\ M_J = -3/2,\ f$ magnetically high-field seeking states is taken into account. Besides the optimum operation parameters for each voltage range, the velocity reduction for the synchronous molecule during the final stopping pulse is indicated. The current permissible experimental operating conditions are indicated as well. The distance between the decelerator exit and the trap centre amounts to 11.5 mm and the switchon point coincides with the synchronous particle reaching the first cryogenic shield and the stopping fields are switched off as soon as the trap centre is reached.

if the velocity of the synchronous particle was not reflected back from the stopping field, where a velocity of -9 m/s was chosen as a cut-off criterion. The black region in the upper panels and the rightmost blue regions of the lower panels pertain to these cases. From the upper panels it can be perceived that the optimal loading conditions lie on a ridge with residual velocities between 5-7 m/s for the synchronous molecule. As indicated by the lower panels, the loading efficiency increases with increasing stopping potentials as the decelerator can be operated at lower phase angles.

6.3 Experimental realisation of the hybrid trap

6.3.1 Overview of the experimental setup

The experimental setup employed for the trapping experiments is depicted in Fig. 6.6. A pinhole discharge variant of the Nijmegen pulsed valve (see Chpt. 4) was utilised for obtaining a dense and internally cold beam of OH radicals seeded in Kr. After having passed a ⌀ 3 mm skimmer, the OH beam was coupled into a 124-stage Stark decelerator (see Chpt. 5). By making use of the source chamber's LIF detection setup, a mean velocity of 425 m/s could be assigned to the molecular beam. Subsequently, the decelerator was programmed such that the molecular package within the phase stable volume was decelerated form 425 m/s to 28.8 m/s at a phase angle $\Phi = 55.468°$. The decelerator comprises two sections, a main section of 111 stages which is housed in the decelerator chamber and a geometrically more compact 13-stage extension, also referred to as mini-decelerator, ranging from the decelerator chamber into the trap chamber, see Fig. 5.4.

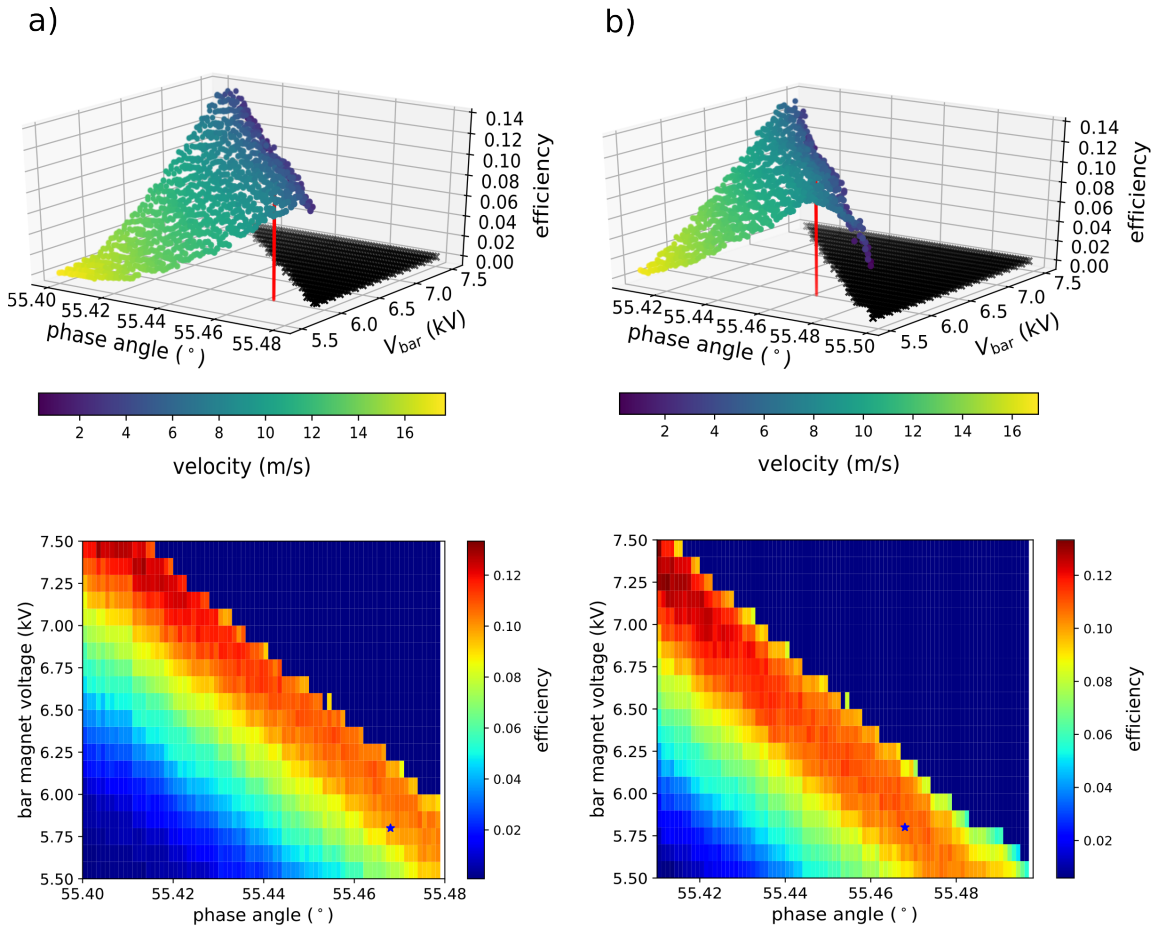

Figure 6.5: Loading efficiency as a function of the phase angle ϕ_0 and the stopping potential on the bar magnets and rear stopping wires, where $V_{\mathrm{bar}} = V_{\mathrm{rear}}$ applies. The potential on the front wires was set to 40% of V_{bar}. The distance between the decelerator exit and the trap centre amounts to 11.5 mm. The switchon/switchoff point coincides with the position of the synchronous molecule at the first cryogenic shield and the trap centre. The top panels depict optimisations for a bar magnet remanescence of **a)** 1.4 T and **b)** 1.64 T. The final velocity of the synchronous molecule is color-coded and the current experimental operation parameters are indicated by the red bar. For better visibility, the loading efficiencies are depicted as scatter plots in the lower panels and the blue asterisk denotes the experimental operating conditions.

The 13-stage extension allowed for differential pumping between the decelerator chamber and the trap chamber. Additionally, the space saving shape of the extension proved to be essential for minimising the free flight distance between the exit of the decelerator and the trap centre, which helped to reduce the loss of slow OH molecules due to spatial spreading. The hybrid trap was surrounded by two cryogenic copper shields connected to a two-stage closed-cycle Gifford-McMahon cryocooler (Sumitomo, DE-204SL, HC-4E1) with a cooling power of 13.5 W at the first stage (at 80 K) and 6.7 W at the second stage (at 20 K). The two stages were equipped with silicon temperature diodes (Lake Shore cryotronics, DT-670). The closed-cycle refrigerator was spring-loaded in order to dampen

the vibrations exerted onto the experimental setup during the helium compression and expansion cycles. Temperatures of 17 K on the inner shield and 53 K on the outer shield could be achieved. The cryogenic shields depicted in Fig. 6.6 b) feature a total of 6 holes, two of which allow a 282 nm LIF excitation laser to be guided through the trap centre. Another set of diametrically opposite holes allows for loading the ion trap with Ca^+ ions and for collecting fluorescence photons emitted by the laser cooled ions. The remaining two openings serve for loading the magnetic trap with OH molecules and for collecting 313 nm off-resonant fluorescence from the $A^2\Sigma(v = 1)$-$X^2\Pi(v = 1)$ transition with a PMT. As the alignment of the trap centre relative to the decelerator exit is crucial for an optimal trapping performance, the cryogenic hybrid trap was mounted to an x, y, z-translation stage via a hanger assembly. The alignment was optimised by visual inspection, during which the PMT was removed such that a direct line of sight through the magnetic trap onto the last deceleration stage could be achieved. The coupling between the magnetic trap and the mini-decelerator is depicted in Fig. 6.7 b).

6.3.2 Considerations on ion-neutral hybrid traps

The hybrid trap structure located behind the two cryogenic shields is depicted in Fig. 6.7 and consist of a trapping section for magnetically low-field seeking neutral molecules and a thin wire ion trap for trapping atomic or molecular ions. The salient feature of this type of trap lies in the possibility of spatially overlapping the cloud of magnetically trapped neutral molecules with the species captured inside the ion trap, thereby turning this setup into a true hybrid trap. Due to the vastly different operation regimes of the two types of traps, demanding engineering challenges arise upon their combination as either one of them should remain operational at all times [51].

The trapping of OH molecules is preceded by Stark deceleration and the magnetic trap also serves as a last deceleration stage, which requires the application of several kilovolts on the trap structure such that the Stark effect can be exploited for slowing the incoming package. Applying such high voltages to small electrode structures can lead to discharges and the surface breakdown of insulators. On the other hand, the ions in an ion trap are confined using electrostatic interactions. Ion traps typically operate by applying sinusoidal voltages of a few 100 kHz and peak-to-peak potentials of several hundred volts onto the ion trap electrodes [6, 296]. The trajectories of trapped ionic particles are very sensitive towards changes in the electric fields. Therefore, the high-voltage requirements of an electrostatic trap for neutral molecules cannot be reconciled with the required operation conditions of an ion trap. Hence, the neutral trap was implemented as a magnetic trap. Furthermore, the spatial dimensions of a decelerated package after 11.5 mm of free flight

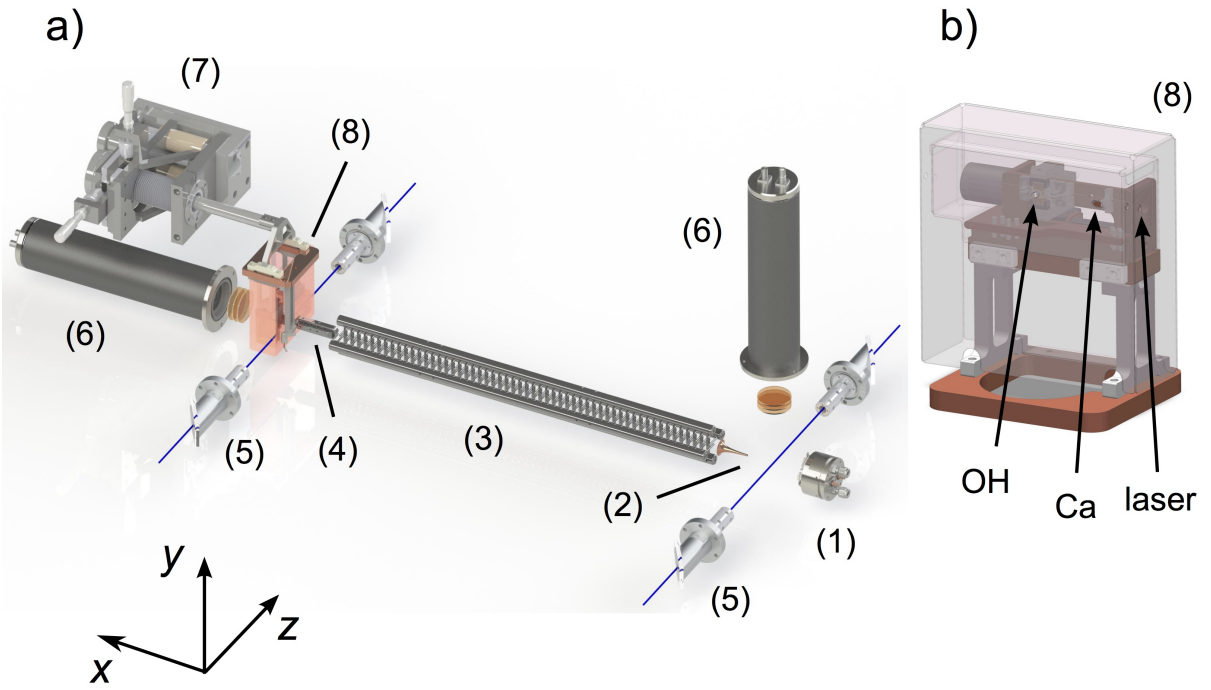

Figure 6.6: **a)** Experimental setup employed for the magnetic trapping of OH radicals. A cold and dense beam of OH radicals was generated by the pinhole discharge variant of the Nijmegen pulsed valve (NPV) (1). The resulting beam was guided through a 3 mm skimmer (2) and coupled into a 124-stage Stark decelerator (3). The last 13 deceleration stages of the mini-decelerator were implemented in a space saving form (4). Brewster windows and light baffles (5) were employed to reduce the amount of stray light detected by the photo-multiplier tube (PMT) (6). The hybrid trap (8) was mounted onto an x, y, z-translation (7) stage as the precise alignment between the decelerator and the centre of the magnetic trap is crucial for a successful loading process. **b)** Close-up of the hybrid trap (8) surrounded by an inner and outer cryogenic shield attached to the cryocooler. Holes in the cryogenic shields allow for directing a laser beam through the trap centre as well as loading the magnetic neutral trap with OH and the ion trap with Ca^+ from a beam of neutral Ca atoms.

are approximately 6×4×4 mm, as indicated in Fig. 5.16. Therefore, relatively small structures are required for confining the package inside a magnetic trap. Aligning the magnetic trap with the ion trap's electrode structure leads to a congested setup. To complicate matters even more, the entire trap needs to be operated at cryogenic conditions to prevent the black body radiation (BBR) from pumping the neutral molecules out of trappable states.

The scheme of the magnetic trap, as depicted in Fig. 6.2, was devised by D. Zhang and myself. C. von Planta designed the ion trap and reconciled the engineering demands of the two traps into the experimental form depicted in Fig. 6.7. Machining of the trap parts and the computer aided design (CAD) drawings of the trap were carried out by P. Knöpfel and

G. Martin from the mechanical workshop. The wire guiding strategy depicted in Fig. 6.7 and the cryogenic engineering was implemented by C. von Planta. Additionally, C. von Planta conducted the conditioning experiments and optimised the insulator geometry until a reliable operation of the trap could be achieved, which is gratefully acknowledged. For a detailed discussion of the trap design, I refer to the thesis of C. von Planta.

6.3.3 Magnetic trap

The confining zone for magnetically low field seeking molecules was formed by installing two PrFeB magnets (Vacuumschmelze, VD 131 DTP) with a 15 µm Ni coating in a quadrupolar configuration. PrFeB was selected as magnetic substrate instead of the more widely used NdFeB, as the latter undergoes a spin-reorientation transition below 135 K [305, 306], which results in a reduction of the magnetisation. Moreover, the magnetisation axis can shift by as much as 30° at 4.2 K [306], which would be detrimental to the shape of the quadrupolar trapping field. Compared to NdFeB magnets, PrFeB based magnets display a reduced coercitivity, which imposes a problem for UHV applications requiring the baking of vacuum chambers as the coercitivity decreases with increasing temperature. Vacuumschmelze have developed a grain-boundary diffusion process for improving the coercitivity of PrFeB magnets [305]. The magnets of type VD 131 DTP employed here possess a coercitivity of 1640 kA/m and a remanence B_r of 1.38 T at room temperature. The remanescence increases from 1.4 T at ambient conditions to 1.64 T in a cryogenic environment, which results in an increased trap depth. The maximum permissible operation temperature lies at 110° [305, 307]. The bar magnet dimensions were chosen to be $(\Delta x, \Delta y, \Delta z) = (3\ \mathrm{mm}, 4\ \mathrm{mm}, 6\ \mathrm{mm})$ and the coordinate system in Fig. 6.7 a) applies. The inner magnet surfaces lying normal to the y-direction were separated a distance of 3.6 mm. This separation represents a good compromise between electrostatic safety as a potential of ±5.8 kV was applied to the bar magnets and sufficiently large magnetic field gradients allowing for trap depths of 0.14 cm^{-1} (13.9 m/s) along x, 0.33 cm^{-1} (21.7 m/s) along y and 0.13 cm^{-1} (13.3 m/s) along the z-direction. Additionally, the space between the two bar magnets needs to be sufficiently large for spanning four stopping wires such that the magnets can slide over the wire guides. Moreover, the magnetic trap also has to fit over the thin wire ion trap. A cryogenic stepper motor (Pythron, VSS 19.200.1.2-UHVC2-KTC, MCC-1 32-48 MINI-USB-H) allows for the superposition of both traps by sliding the bar magnets over the ion trap. This 2-phase stepper motor offers a holding torque of up to 3.5 mNm, a step resolution of 1.8° and is capable of operating at temperatures as low as 3 K [308]. The travel path of the magnetic trap between the two loading apertures is depicted in Fig. 6.7. Moving the neutral trap along the trap axis allows to reposition the OH cloud away from the openings in the cryogenic shields where

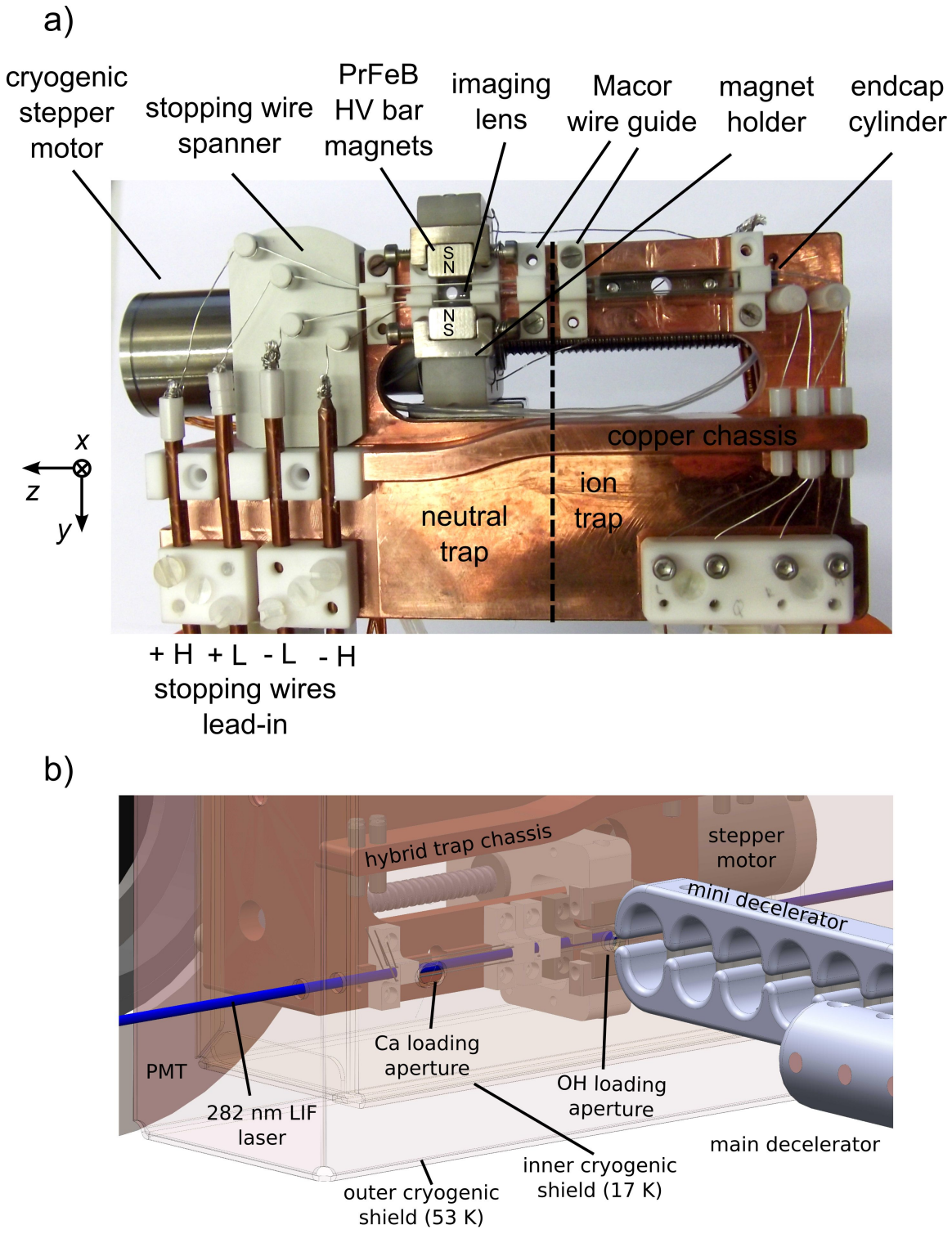

Figure 6.7: Experimental implementation of the hybrid trap. **a)** Front view displaying the neutral trap and the thin wire ion trap. The OH molecules approach the magnetic trap along the x-direction by flying into the page. The wire management for connecting the stopping electrodes of the neutral trap and the thin wire electrodes of the ion trap are visible. **b)** Two cryogenic shields at 53 K and 17 K are attached to the outer and inner stage of the cryocooler. Apertures were drilled into the shields to permit loading of the magnetic and the ion trap. The vertical electrode set was removed from the mini-decelerator for better visibility of the coupling between the trap and the decelerator.

the black-body radiation contribution is largest. Moving the magnetic trap to a BBR-free zone allows to tailor the trapping lifetime.

The four shaping electrodes for the stopping field were implemented in the form of thin stainless steel wires with a diameter of 0.2 mm. As depicted in Fig. 6.7 a), the four stopping wires spanned a square with a centre-to-centre distance of 2 mm in the x, y-plane. The centre of a wire was located approximately 0.8 mm from the surface of the closer bar magnet. The wires in proximity to the decelerator opening were pulsed at potentials of $\pm$L = $\pm$2.32 kV and those located closer to the copper chassis were switched at $\pm$H = $\pm$5.8 kV, where L and H denote low and high potentials, respectively.

Detailed accounts on the construction of the ion trap are given in the thesis of C. von Planta. The only ion trap component relevant in the context of this thesis are the DC-endcap electrodes, which consisted of two hollow tungsten cylinders inserted into the central bore hole of the ion trap's wire guides. The hollow endcap electrodes exhibit an interior diameter of 1.4 mm and represent the narrowest path along the propagation direction of the laser beam. Consequently, a part of the laser beam is clipped at these two sites, which represents a source of stray light within the trap. To increase the photon detection efficiency, a UV lens ($\varnothing$ = 6 mm, f = 6 mm) was mounted into the copper chassis.

6.3.4 HV-switching and conditioning of the Hybrid Trap

An electric scheme identical to the one depicted in Fig. 5.6 was employed for the generation of HV loading pulses, except that only two MOSFET push-pull switches (Behlke Power Electronics, HTS 301-03-GSM) backed by two 0.5µF capacitors (Hivolt Capacitors Ltd., PPR200-504) were required, one for the positive and one for the negative pulses. The lower L-potential of 2.32 kV (see Fig. 6.7 a)) was obtained by installing a low-inductance voltage divider providing 40% of the H-potential (5.8 kV). The application of high-voltage onto small electrode structures is problematic as high electric field gradients arise, which increases the likelihood of discharges and insulator breakdowns.

6.3.5 LIF detection of OH molecules in the trap

The presence of OH molecules in the trap was verified by collecting LIF photons from electronically excited OH radicals. A frequency-doubled Rhodamine 6G dye laser (Fine Adjustment, Pulsare) was pumped by the second harmonic (532 nm) of a Nd:YAG laser (Continuum, Surelite II) to generate laser radiation at 282 nm. Before being directed through the apertures in the cryogenic shield, the laser beam was passed through a gold

plated beam shaper pinhole ($\varnothing$= 10 μm) and was telescoped (M = -5) to a $1/e^2$-radius of 0.5 mm in front of the Brewster windows. After having passed the hybrid trap, a $1/e^2$-radius of 0.8 mm was determined. Therefore, a $1/e^2$-radius in the range of 0.6-0.7 mm is assumed inside the trap. The optical setup for cleaning and collimating the beam profile is depicted in Fig. 6.8.

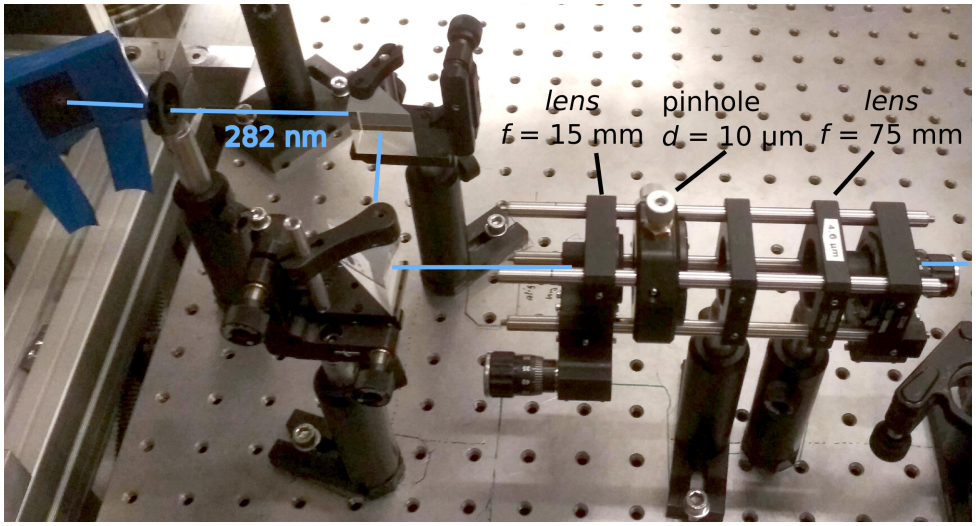

Figure 6.8: Beam shaping and collimation setup consisting of a 10 µm pinhole and a M = -5 Galilei telescope.

The 282 nm laser radiation excited OH molecules in the ground state $X^2\Pi(v = 0)$ to the first excited electronic state $A^2\Sigma(v = 1)$, where v denotes the vibrational quantum number. The output energy at this wavelength was 1.0 mJ/pulse with a pulse length of 10 ns. The $A^2\Sigma(v = 1)$ state relaxes via the $A^2\Sigma(v = 1)$-$X^2\Pi(v = 1)$ transition under the emission of off-resonant fluorescence at 313 nm. The fluorescence was collected by a UV lens ($\varnothing$= 6 mm, f=6 mm) and was detected by a calibrated photomultiplier tube (Electron Tubes, B2/RFI 9813 QB, C638AFN1). The imaging of fluorescence photons took place through a $\varnothing$= 5 mm hole in the AlN magnet holder and the cryogenic shield. Stray light suppression was achieved by inserting narrow band-pass filters (Semrock, FF01-315 and Asahi Spectra, XHQA313) in front of the PMT. A fluorescence lifetime of 717 $\pm$ 18 ns has been determined in earlier experiments [178] and was used for species confirmation. Digitised and averaged LIF traces at a fixed laser delay were integrated within a time-window of 2.31 μs duration, which resulted in an individual point in the TOF curves depicted in Fig. 6.12. The determination of trap densities based on the acquired LIF signal is described in more detail in section 6.5.4.

6.4 OH detection efficiency optimisation, optical simulations

As the cryogenic shields of the hybrid trap impair the optical access to the trap centre and the laser beam diameter is limited to 1.4 mm by the endcap cylinders of the ion trap, the photon collection efficiency needed to be optimised. It was found that installing a lens into the copper mounting bar of the magnetic trap improves the photon collection efficiency. In order to quantify the expected signal gain for different lens diameters and imaging apertures in the cryogenic shield, an optical ray tracer was developed. Geometric obstacles imposed by the hybrid trap were taken into account and the lens was chosen such that the photon throughput is maximised. Additionally, the ability to trace rays through the hybrid trap's imaging system allowed for the determination of the solid angle under which the imaging takes place by means of the Monte Carlo method. First, the ray tracing algorithm will be discussed and modifications to the code required for solid angle computations are addressed in a subsequent section.

6.4.1 Ray tracing routine

Ray tracing is the process of calculating the paths of a given set of rays through an optical setup by considering reflections and refractions [309]. The lecture notes by M. Breining [310] were found to be very useful for developing a Fortran-based ray tracer. The following discussion refers to the light paths depicted in Fig. 6.9. Initiation of the ray tracing routine results in the generation of rays originating from a point source at a location $\vec{P}$. In a subsequent step, unit direction vectors $\vec{r_1}$ are computed such that the surface of the spherical lens is uniformly covered with intersecting light rays. This allows to study the refraction of rays intersecting the spherical lens surface at large polar angles θ. Alternatively, ray tracing can also start from light rays running parallel to the x-axis and the coordinate system depicted in Fig. 6.9 a) applies. In this case, the parallel rays are emitted from point sources located on concentric rings situated around the x-axis. This allows to uniformly distribute the light bundles on the surface of the lens whose rotation symmetry also lies around the x-axis in the absence of an offset. Irrespective of the type of radiation source, the points of intersection between the rays and the spherical surface of the lens were computed by solving the following expression for α:

$$|\vec{P} + \alpha \cdot \vec{r_1} - \vec{C}|^2 = \left\| \begin{bmatrix} x_0 \\ y_0 \\ z_0 \end{bmatrix} + \alpha \cdot \begin{bmatrix} r_{1,x} \\ r_{1,y} \\ r_{1,z} \end{bmatrix} - \begin{bmatrix} C_x \\ C_y \\ C_z \end{bmatrix} \right\|^2 = R_c^2 \,, \tag{6.2}$$

where the parameter α scales the $\vec{r_1}$ unit direction vector such that the intersection point $\vec{I}$ between the ray and the lens surface is reached. $\vec{C}$ denotes the origin of curvature and R_c corresponds to the radius of curvature, as indicated in Fig. 6.9 a).

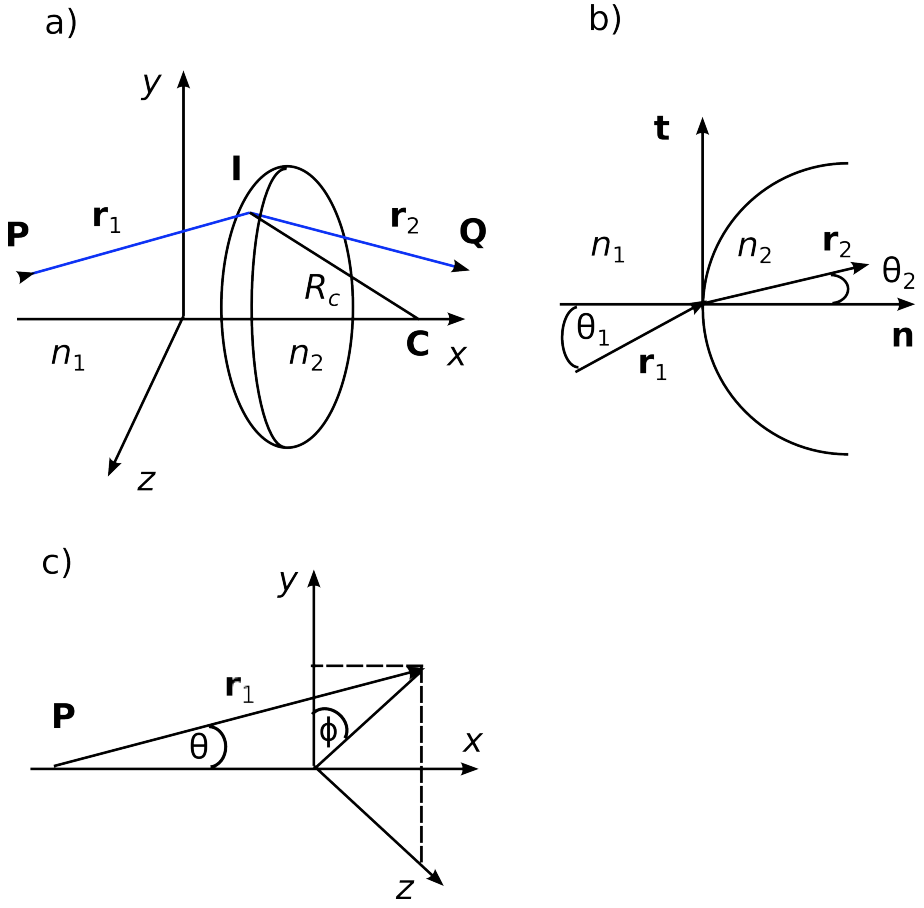

Figure 6.9: **a)** Refraction of a single ray emanating from a point $\vec{P}$ and ending at a point $\vec{Q}$. The light ray is refracted a the intersection point with the lens surface $\vec{I}$. **b)** Closeup of the refraction at the vacuum-glass interface of a spherical lens [310]. **c)** Polar coordinate system used for the generation of unit direction vectors pointing towards the surface of the lens.

Once the points of intersection $\vec{I}$ are known, the angle θ_1 between the surface normal and the incident ray is determined. The geometric situation is depicted in Fig. 6.9 b). Computationally, it is convenient to utilise the dot product between the incoming beam $\vec{r_1}$ and the surface normal on the sphere for the determination of $\cos(\theta_1)$ and the following expression is evaluated:

$$\frac{-\begin{bmatrix} r_{1,x} \\ r_{1,y} \\ r_{1,z} \end{bmatrix} \cdot \begin{bmatrix} I_x - C_x \\ I_y - C_y \\ I_z - C_z \end{bmatrix}}{\sqrt{(I_x - C_x)^2 + (I_y - C_y)^2 + (I_z - C_z)^2}} = \cos(\theta_1)\,. \tag{6.3}$$

The second term in the nominator is equivalent to the surface normal vector and the denominator ensures normalisation. Next, the new direction $\vec{r_2}$ of the light ray is worked out after refraction at the vacuum-glass interface. A relation between the incident light ray $\vec{r_1}$ and the refracted ray $\vec{r_2}$ can be obtained by applying Snell's law, which states that: $n_1 \sin(\theta_1) = n_2 \sin(\theta_2)$, where n_1 is the refractive index of the first medium and n_2 designates the refractive index of the lens. The unit vectors lying tangential $\vec{t}$ and normal $\vec{n}$ to the refraction surface at the intersection point of the ray with the lens serve as a suitable coordinate system for describing the incident as well as the refracted ray. Making use of Snell's law and projecting the incident and refracted unit vectors onto $\vec{t}$ and $\vec{n}$ yields the following expressions:

$$\begin{aligned} n_1\vec{r_1} &= n_1\|\vec{r_1}\|\cos(\theta_1)\cdot\vec{n} + n_1\|\vec{r_1}\|\sin(\theta_1)\cdot\vec{t} = n_1\cos(\theta_1)\cdot\vec{n} + n_1\sin(\theta_1)\cdot\vec{t} \text{ and} \\ n_2\vec{r_2} &= n_2\|\vec{r_2}\|\cos(\theta_2)\cdot\vec{n} + n_2\|\vec{r_2}\|\sin(\theta_2)\cdot\vec{t} = n_2\cos(\theta_2)\cdot\vec{n} + n_2\sin(\theta_2)\cdot\vec{t} \implies \\ \vec{r_2} &= \frac{n_1}{n_2}\vec{r_1} + \left(\cos(\theta_2) - \frac{n_1}{n_2}\cos(\theta_1)\right)\cdot\vec{n} \end{aligned} \tag{6.4}$$

Equation 6.4 is a key equation in ray-tracing [310] through optical elements as it relates the direction vector of the incident ray $\vec{r_1}$ in a medium with n_1 to the direction vector of the refracted ray $\vec{r_2}$ propagating in a medium with a refractive index n_2. The direction cosine $\cos(\theta_1)$ has been determined in Eqn. 6.3 and $\cos(\theta_2)$ can be obtained from $\cos(\theta_1)$ using Snell's law.

$$n_2\cos(\theta_2) = n_2\sqrt{1-\sin^2(\theta_2)} = \sqrt{n_2^2 - n_1^2\sin^2(\theta_1)} = \sqrt{n_2^2 - n_1^2\cdot(1-\cos^2(\theta_1))} \tag{6.5}$$

Once the direction vector of the refracted ray $\vec{r_2}$ is known, the ray is propagated to the next refraction surface, which is either another spherical surface in the case of a biconvex lens or a plain surface in the case of a planoconvex lens. Additionally, refraction from planar glass slabs such as viewports are supported by the code. The ray tracer was written in Fortran and the propagation through several optical elements is possible. Lens parameters such as the lens diameter, center thickness, edge thickness, radius of curvature and the refractive index of the lens material at the wavelength of operation are required as input. Moreover, the distance between the source and the refracting surface has to be specified as well as the distance between the source and the screen on which the image is formed. The intersection coordinates of the rays at refractive surfaces and the direction vectors can be written to disk for further processing. The two- and three-dimensional refraction of rays by several different optical elements is illustrated in Fig. 6.10. It is important to notice, that the refraction model introduced here is not limited by the paraxial approximation as a full trigonometric model has been implemented, which allows for realistic refraction even if the light ray propagates at large angles relative to the optical axis. As the origin of

the light source can be displaced relative to the center of the lens, it is possible to simulate skew rays, which never pass through the optical axis. The ray tracing routine described in this section is capable of taking into account spherical aberration, astigmatism and coma [309]. This is a necessary requirement if a cloud of light emitting particles with an object dimension not much smaller than the lens is to be imaged. The ray tracer was validated by comparing the paths of a few rays originating from different initial positions against the trajectories obtained by manual calculation. The correct implementation of the Monte Carlo routine was verified by reproducing selected entries from Table 1 in ref. [311] in the absence of lenses.

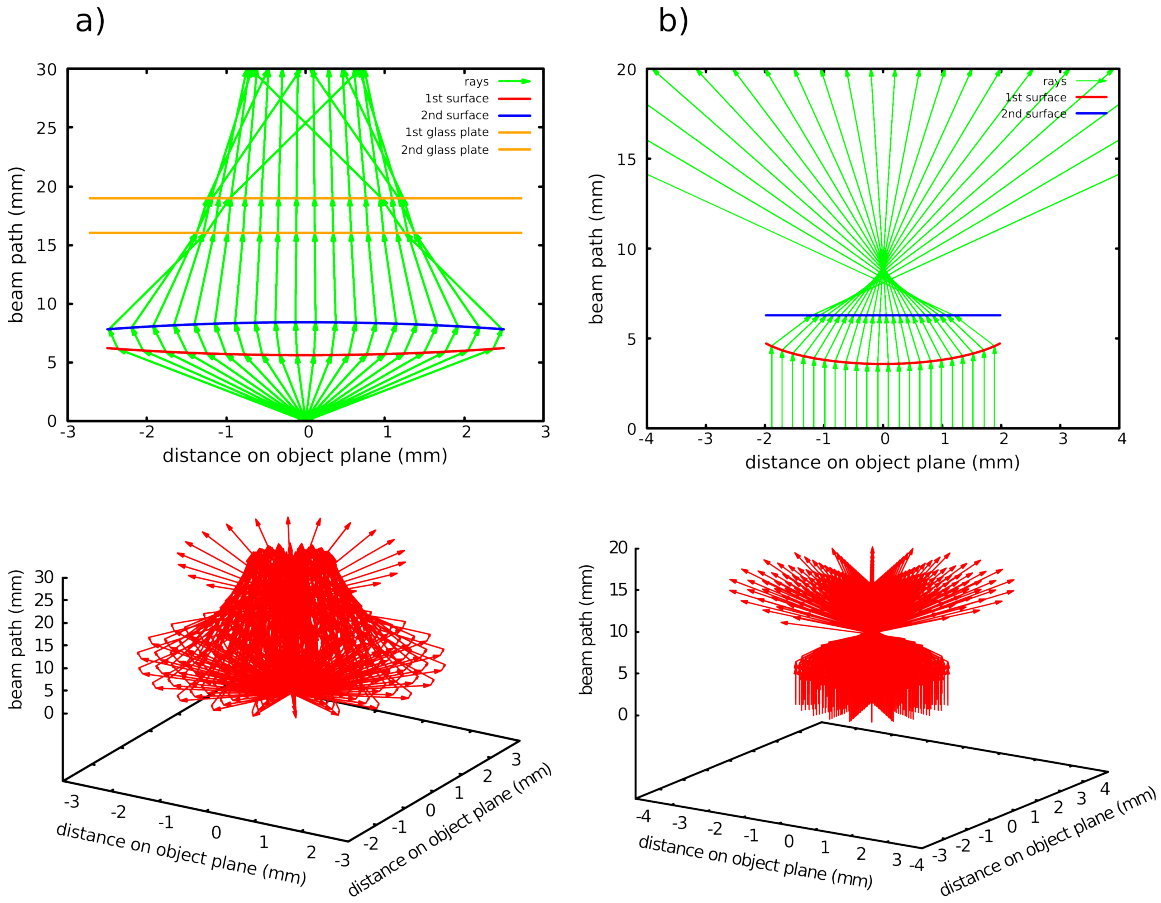

Figure 6.10: **a)** Refraction of a light bundle emanating from a point source. A biconvex lens with a radius of curvature $R_c = 5.52$ mm and a diameter $d_{\text{lens}} = 5.0$ mm is placed one focal length ($f = 6.21$ mm) from the light source. The lens has a center thickness of 2.8 mm and spherical aberrations are visible for rays hitting the outer region of the lens. A glass plate with a thickness of 3.0 mm is placed 16 mm from the light source. A selection of two- and three-dimensional ray patterns is depicted in the top and bottom panel, respectively. **b)** Ray tracing through a planoconvex lens with a focal length of $f = 4.7$ mm at 313 nm. The ray bundle is parallel to the optical axis and the refracted rays run through a focal point before diverging again.

6.4.2 Solid angle calculation

With a reliable optical ray tracer routine at hand, the code was modified such that the solid angle under which the imaging takes place can be calculated. Instead of considering a single point source or a parallel ray bundle, fluorescing OH molecules within the excitation volume defined by the laser beam were considered. Each OH molecule was treated as a point source from which rays are emitted towards the lens. The excitation volume of the laser V_{cyl} was discretised into a 3-dimensional grid and the solid angle was calculated at every grid position $(x_{\mathrm{g}}, y_{\mathrm{g}}, z_{\mathrm{g}})$. The cylindrical section V_{cyl} of the laser beam under consideration is given by

$$V_{\mathrm{cyl}} = \{(x, y, z) = (\rho\cos(\phi), \rho\sin(\phi), z) | \rho \in [0, 0.7], \phi \in [0, 2\pi], z \in [-1, 1]\}\,, \tag{6.6}$$

where ρ denotes the radius of the laser beam in mm, ϕ is the angle of revolution and $z \in [-1, 1]$ mm runs along the laser propagation direction. The Cartesian (x, y, z) directions coincide with the ones indicated in Fig. 6.6.

The solid angle calculations took into account the refraction of the lens and the geometry of the cryogenic shields, the windows and the active diameter of the PMT ($\varnothing$= 46 mm). At every grid position, an ensemble of $5{\cdot}10^7$ optical rays was generated. Their propagation directions were distributed isotropically such that the optical rays intersect the surface of a unit hemisphere facing the lens. Only rays propagating towards the lens were considered. It is of great importance that the rays are uniformly distributed on the unit sphere in order to prevent oversampling of a certain direction. The direction vectors were obtained from the following expression [311, 312]:

$$\vec{r_1} = \begin{bmatrix} s \\ \sqrt{1-s^2}\cos(\phi) \\ \sqrt{1-s^2}\sin(\phi) \end{bmatrix}\,, \tag{6.7}$$

where the polar coordinate system in Fig. 6.9 applies. $s \in [0, 1]$ denotes a uniformly distributed random number and ϕ is uniformly distributed over the interval $[0, 2\pi]$. The geometric paths of the rays were simulated taking into account the refraction of the lens and the fused silica window of the viewport. Upon hitting a solid obstacle such as the surface of the cryogenic shields or the imaging channel of the magnet holder, the ray was removed from the simulation and counted as lost. The effective solid angle was then obtained by the following expression:

$$\Omega(x_{\mathrm{g}}, y_{\mathrm{g}}, z_{\mathrm{g}}) = 2\pi \cdot \frac{\#\text{ rays reaching PMT}}{\#\text{ total rays simulated}}\,, \tag{6.8}$$

where the ratio between the rays reaching the active aperture of the PMT and the total number of generated rays has to be multiplied by 2π as only propagation directions towards the lens were considered for reasons of computational efficiency. This procedure was repeated for every point in the laser volume grid, which resulted in the solid angle maps depicted in Fig. 6.11 a) and b). In a subsequent step, a continuous solid angle function $\Omega_{\text{int}}(x, y, z)$ was obtained by interpolating between the grid points. This renders the solid angle function amenable to integration. Besides radiometric applications, the determination of solid angles by means of Monte Carlo simulations is a common problem encountered in the calibration of gamma-ray detectors in radiation dosimetry [311, 313].

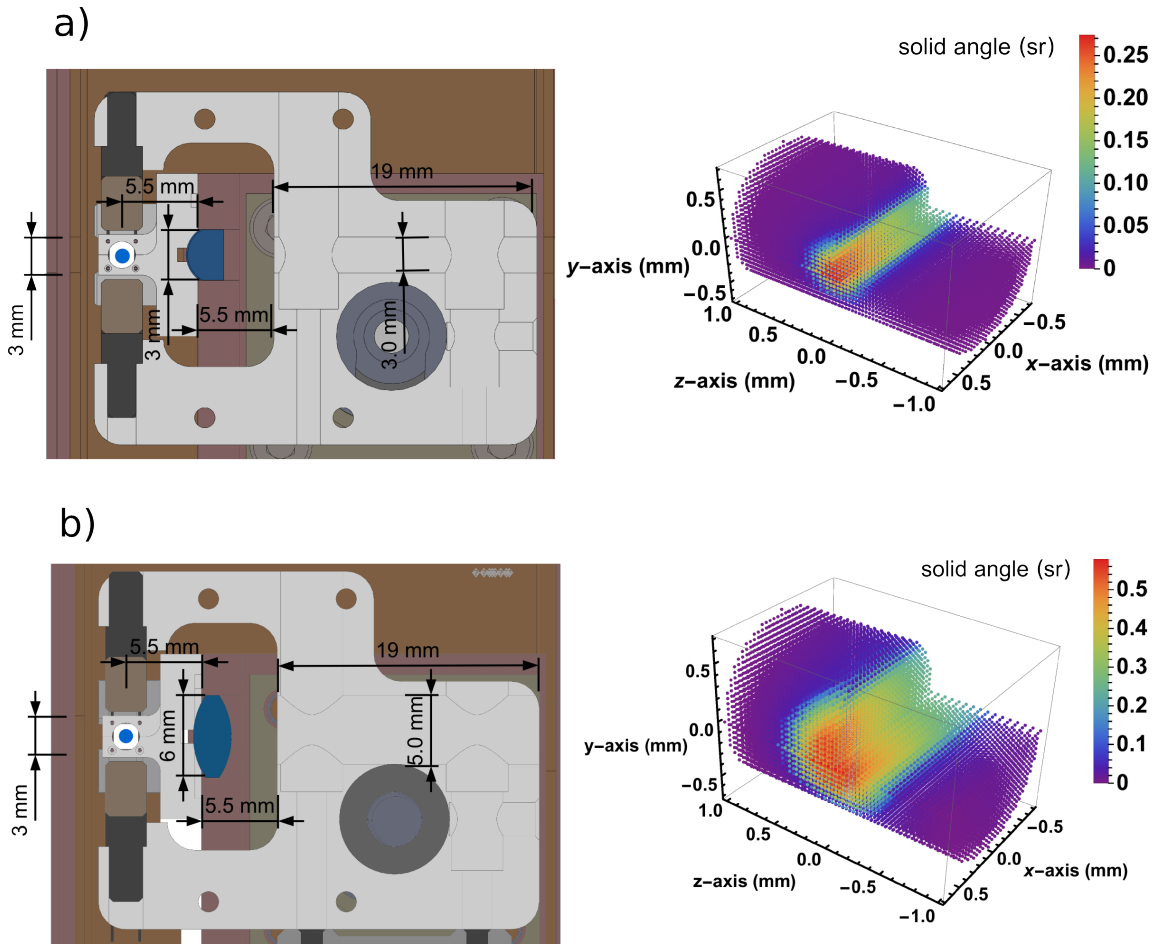

Figure 6.11: Cross sectional view of the hybrid trap illustrating the path of light propagation in the presence of two different collimation lenses. The blue dot depicts the 282 nm excitation laser. **a)** A planoconvex lens ($d = 4$ mm, $f = 5$ mm) was installed inside the chassis of the hybrid trap. LIF photons leave the setup via a $\varnothing = 3$ mm hole in the bar magnet holder. The solid angle under which photons are detected by the PMT is depicted on the right. **b)** A bi-convex lens ($d = 6$ mm, $f = 6$ mm) is used in combination with an enlarged photon duct ($\varnothing = 5$ mm). The improvement in photon collection efficiency is apparent from the corresponding solid angle function on the right.

6.4.3 Optimisation of the detection efficiency

In combination with the solid angle calculation module, the optical ray tracer was employed for optimising the detection efficiency of the OH cloud in the excitation volume spanned by the laser beam. Installing a collimation lens inside the chassis of the hybrid trap allows for an enhanced solid angle under which the PMT detects LIF photons. Two different optical setups were realised experimentally and are depicted in Fig. 6.11. The maximum extent of the laser beam is limited to a radius of 0.7 mm by the cylindrical endcap electrodes of the ion trap installed along the optical axis of the trap. The portion of the laser beam lying within the view-field of the lens was discretised and the solid angle for each point was calculated by propagating $5 \cdot 10^7$ rays from the source to the active zone of the PMT, while taking into account refraction at the lens surfaces. The resulting solid angle functions are depicted on the right panels of Fig. 6.11. The laser propagates along the z-direction and the optical axis coincides with the deceleration axis x. For emitters close to the lens surface (positive x-values), the solid angle increases as rays propagating at larger angles relative to the optical axis still intersect the lens and are collimated.

integrated solid angle (sr mm^3) $\phi = 0°, z \in [-0.5, 0.5]$ mm	integrated solid angle (sr mm^3) large $\phi, z \in [-1.0, 1.0]$ mm
Hybrid Trap, no lens	Hybrid Trap, no lens
$\varnothing =$ 3 mm $\quad 7.5 \cdot 10^{-3}$	$\varnothing =$ 3 mm $\quad 1.5 \cdot 10^{-2}$
$\varnothing =$ 5 mm $\quad 2.1 \cdot 10^{-2}$	$\varnothing =$ 5 mm $\quad 4.1 \cdot 10^{-2}$
a) $d = 4$ mm, $f = 5$ mm lens	a) $d = 4$ mm, $f = 5$ mm lens
$\varnothing =$ 3 mm $\quad 5.4 \cdot 10^{-2}$	$\varnothing =$ 3 mm $\quad 6.0 \cdot 10^{-2}$
$\varnothing =$ 5 mm $\quad 1.1 \cdot 10^{-1}$	$\varnothing =$ 5 mm $\quad 1.3 \cdot 10^{-1}$
b) $d = 6$ mm, $f = 6$ mm lens	b) $d = 6$ mm, $f = 6$ mm lens
$\varnothing =$ 3 mm $\quad 7.5 \cdot 10^{-2}$	$\varnothing =$ 3 mm $\quad 7.5 \cdot 10^{-2}$
$\varnothing =$ 5 mm $\quad 3.0 \cdot 10^{-1}$	$\varnothing =$ 5 mm $\quad 3.3 \cdot 10^{-1}$

Table 6.2: Integrated solid angle functions for the a) and b) cases depicted in Fig. 6.11. The solid angle function was also computed for the hybrid trap with no lens installed.

Interpolation and subsequent integration of the solid angle functions allows for an estimation of the signal gain between the two cases depicted in Fig. 6.11. The solid angle function in the absence of a lens was calculated as well. The integration was performed over the entire cross section of the cylindrical laser beam and two z-axis length intervals

of $z \in [-0.5, 0.5]$ mm and $z \in [-1.0, 1.0]$ mm to determine the signal gain for different OH package extensions. Integrated values of the solid angle functions are given in Tab. 6.2. Compared to operation of the hybrid trap without a lens, the detection efficiency improves by a factor of 7 for the small interval and by a factor of 4 for $z \in [-1.0, 1.0]$ mm upon installation of the lens configuration depicted in Fig. 6.11 a). Increasing the diameter of the photon duct to $\varnothing$= 5 mm and inserting a d = 6 mm, f = 6 mm lens into the hybrid trap chassis (case b) in Fig. 6.11) leads to a further enhancement of the detection efficiency by a factor 5 for both intervals compared to case a). The resulting signal gain comes at the cost of increased stray light levels as photons scattered from the hybrid trap have a greater chance of reaching the PMT in the presence of a larger lens and a wider photon duct. In conclusion, it can be said that the solid angle simulations have proven to be a valuable tool for designing the LIF detection setup of the hybrid trap.

6.5 Loading Results and discussion

6.5.1 Trap loading

Prior to trapping, the density of OH radicals after the decelerator was optimised as outlined in chapter 5. In brief, the process involved optimising the coupling of the molecular beam into the Stark decelerator and the discharge settings for achieving maximum OH densities in the source region. After the dissociation of H_2O into OH radicals, the mean velocity of the molecular beam was found to be $v = 425$ m/s with a velocity spread $\Delta v/v$ of 13% (FWHM) and a spatial spread of 13.5 mm (FWHM).

In a subsequent step, the molecular beam was coupled into the decelerator by adjusting the incoupling time, i.e. the time required for the molecules to reach the entrance of the Stark decelerator from their point of generation. The sequence of high voltage pulses applied to the deceleration electrodes was calculated to reach the desired final velocity. TOF profiles were acquired by monitoring the LIF signal intensity as a function of the time delay at the position of the trap centre 11.5 mm downstream from the exit of the Stark decelerator, 894.1 mm from the source. Finally, translationally cold packages of OH radicals in the $X^2\Pi_{3/2}(v = 0, J = 3/2, M_J = \pm 3/2, f)$ state exited the Stark decelerator. Here, v denotes the vibrational quantum number of the molecule, J is the quantum number of its total angular momentum, M_J is the corresponding space-fixed projection quantum number and f designates the parity label.

The OH molecules were probed by monitoring their laser-induced fluorescence (LIF) at the trap centre. However, the presence of the cryogenic shields imposed a significant reduction

in the solid angle under which fluorescence photons could be collected. To alleviate this effect, fluorescence from the molecules in the trap was acquired with a lens ($\varnothing$= 6 mm, f = 6 mm) mounted in the cryogenic chassis of the hybrid trap. All trapping data presented in this chapter was acquired with this detection configuration, which proved to be sufficient for an unambiguous characterisation of the trap loading dynamics in spite of the low LIF signal levels.

Before enabling the stopping fields, the performance of the decelerator was characterised in guiding mode and at a phase angle of $\phi = 55.468°$, which resulted in a package at 28.8 m/s. The time of flight (TOF) profiles for the guiding mode of operation and at the targeted loading velocity of 28.8 m/s are displayed in Fig. 6.12. Experimental time-of-flight (TOF) profiles of the molecules were validated against simulated TOF curves, as depicted in Fig. 6.12 a). The simulations take into account contributions from both low-field-seeking components $M_J\Omega = -9/4$ and $M_J\Omega = -3/4$ which were transported through the decelerator (Ω denotes the quantum number of the projection of $\vec{J}$ onto the molecular axis). As can be seen in Fig. 6.12 a), the simulations accurately reproduce the experimental arrival time of the OH packages as well as the relative LIF signal intensities. All TOF traces in Fig. 6.12 a) were normalised to the signal in guiding mode ($v_{\text{initial}} = v_{\text{final}} = 425$ m/s). By comparing the experiments with the simulations, a spatial spread of the initial OH packet of 13.5 mm (FWHM) was deduced. Due to the large spatial and velocity spreads of the molecular beam, three phase-stable regions were loaded and transported through the decelerator as indicated by the phase-space diagrams depicted in Fig. 6.12 c). This gives rise to a distinct triple-peak structure in the centre of the TOF profile of Fig. 6.12 a). Upon increasing the phase angle of the decelerator, more energy is removed from the OH package per decelerator stage and the number of molecules (and therefore the signal level) decreases due to a reduction of the phase-stable volume [35, 102]. At a phase angle of $\phi = 55.468°$, the target velocity for loading at $v_{\text{target}} = 28.8$ m/s was reached. The corresponding signal level was ≈ 70 times lower than the one observed in guiding mode (see inset of Fig. 6.12 a)). During the free flight over a distance of 11.5 mm between the decelerator exit and the detection point at the low final velocity of 28.8 m/s, the phase-space volume rotated significantly (see bottom panel of Fig. 6.12 c)) such that the signal in the TOF profile appears broadened.

To load the decelerated molecules into the magnetic trap, the stopping fields were switched at the points in time indicated by blue vertical lines in Fig. 6.12 b). The TOF curve depicting the onset of trapping is shown in Fig. 6.12 b). During the stopping process, the mean forward velocity of the molecule packet was reduced from 28.8 m/s to 0 m/s for loading the trap. The TOF profile of the molecules right after trap loading displays an

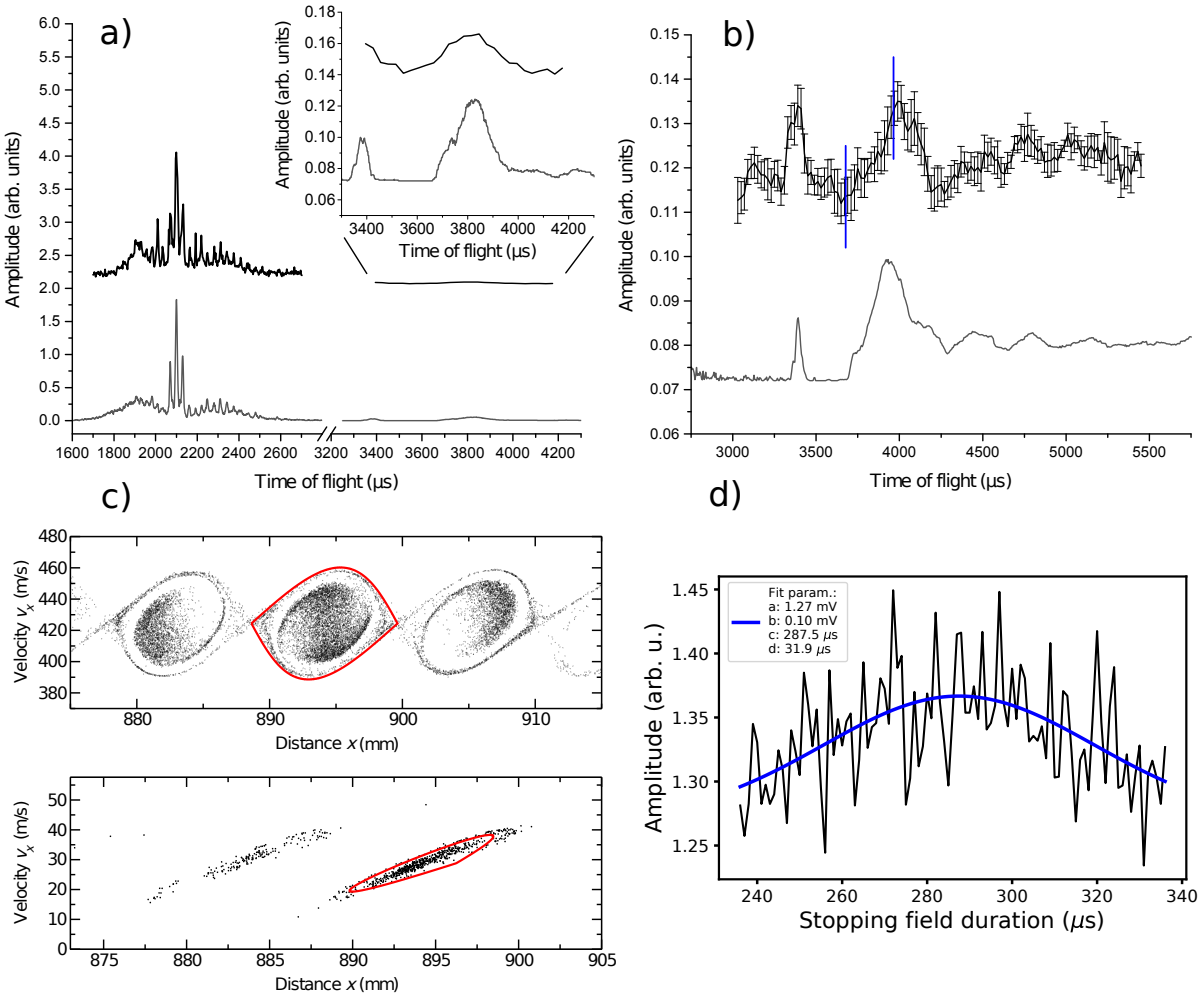

Figure 6.12: Time of flight (TOF) profiles of OH molecules at the trap centre and corresponding phase-space distributions. All TOF profiles were recorded by collecting laser-induced fluorescence (LIF) 11.5 mm downstream from the exit of the Stark decelerator. In a) and b), the dark solid lines (upper traces) represent experimental results and the light solid lines (lower traces) Monte-Carlo trajectory simulations. All traces are normalised with respect to the maximum signal observed in the trace in **a)** obtained in guiding mode (no deceleration, i.e., $v_{\text{initial}} = v_{\text{final}} = 425$ m/s). The inset in a) displays the TOF curve at the targeted loading velocity of $v_{\text{target}} = 28.8$ m/s and the signal intensity is reduced by a factor of 70 compared to guiding ($\phi_0 = 0°$). The reduction in signal is caused by the decrease of the phase stable volume at an elevated phase angle of $\phi_0 = 55.468°$. **b)** TOF trace illustrating the final deceleration and the onset of trapping at room temperature. The period of application of the electric stopping field, by which the mean forward velocity of the molecule packet is reduced from 28.8 m/s to 0 m/s, is indicated by two blue vertical lines. **c)** Top: Phase-space distribution of the OH package at the trap centre for the decelerator operating in guiding mode (see panel a)). Due to the large spatial and velocity spread of the molecular beam, a total of three phase-stable regions were loaded and transported through the decelerator. Bottom: Phase-space distribution at $v_{\text{target}} = 28.8$ m/s. The fastest phase-stable package is not shown. The phase-space volume is tilted due to the free flight from the decelerator to the trap. **d)** Optimisation of the trapping signal by varying the stopping field duration. The blue line is obtained by fitting the black data trace with a Gaussian model: $f(t) = a + b \cdot \exp((c-t)^2/(2 \cdot d^2))$.

oscillatory pattern which is due to the molecule packet oscillating inside the trap. This behaviour is reproduced by the simulations. The decelerator transports OH molecules in the $X^2\Pi(J = 3/2,\ M_J = \pm 3/2,\ \mathrm{f})$ states. However, in the presence of a magnetic field, only the $X^2\Pi(J = 3/2,\ M_J = +3/2,\ \mathrm{f})$ part of the population exiting the decelerator is magnetically low field seeking and amenable to trapping. As the $X^2\Pi(J = 3/2,\ M_J = +3/2,\ \mathrm{f})$ state comprises half of the molecules in the decelerated ensemble, a signal drop by a factor 2 is expected between the package entering the hybrid trap and the fraction that remains trapped. In part, the signal drop is also caused by molecules with sufficient kinetic energy to surmount the trapping potential. This signal loss is reproduced well by the TOF profile in Fig. 6.12, where the trapping signal level settles at half the value of the maximum peak at 3960 µs. In the simulation, this effect is captured by simulating the loading process twice, once with a confining magnetic trap and a second time with an anti-confining trap obtained by multiplying the acceleration arrays by -1.0, which mimics the behaviour of the $X^2\Pi(J = 3/2,\ M_J = +3/2,\ \mathrm{f})$. The average of the simulated TOF profiles is depicted in Fig. 6.12 b).

Extraction of the phase-space evolution from trajectory simulations (see Fig. 6.16) indicates that the trap loading is completed after 2.7 ms and after 0.1 s the molecule package has obtained an average velocity of 6.0 m/s (corresponding to a kinetic energy of $E_{\mathrm{kin.}} = 0.026$ cm^{-1} or a translational temperature $T = 37$ mK ($E_{\mathrm{kin.}} = k_{\mathrm{B}}T$)). The intensity of the trapped signal was optimised by scanning the discharge duration, as indicated in Fig. 6.12 d). The LIF laser was fired 1.3 ms after switching on the stopping field and the amount of OH remaining in the trap after varying the stopping duration was monitored. The data was fitted with a Gaussian model and the most intense trapping signal was obtained for a stopping duration of 287.5 µs. This value is in excellent agreement with the stopping duration of 287.9 µs obtained from Monte Carlo trajectory simulations.

6.5.2 Cryogenic Trapping and Lifetime measurements

In section 6.5.1 the successful loading of the magnetic trap with OH molecules in the magnetically low field seeking $X^2\Pi(J = 3/2,\ M_J = +3/2,\ \mathrm{f})$ state has been demonstrated for short trapping times. Naturally, one wonders how long the trapped OH package can be stored between the bar magnets. To this end, the LIF signal level of the trapped molecules was recorded as a function of the trapping time, i.e. the amount of time that has elapsed since switching off the stopping fields and probing the remaining population with a LIF laser. The resulting fractional population of trapped molecules as a function of the trapping time at room temperature and under cryogenic conditions is depicted in Fig. 6.13. The main processes which are detrimental to trapping OH for prolonged

periods of time are collisions with background gas molecules and the loss of trappable states due to black body radiation induced transitions into non-trappable states. Besides the aforementioned loss mechanisms, the ejection of hydroxyl radicals from the trap can result from Majorana transitions in proximity to the field-free trap centre and from non-adiabatic spin-flip transitions in crossed electric and magnetic fields [28, 62, 276, 314, 315]. In the trapping experiments described here, a significant loss of OH radicals during the loading procedure is not observed, as can be inferred from the signal levels in Fig. 6.12 a) and b). Furthermore, the electric stopping field is applied for a short duration of 287.9 µs only. This suggests that loss by spin-flip transitions in crossed electric and magnetic fields does not seem to cause a significant depletion of the trap density in this experiment.

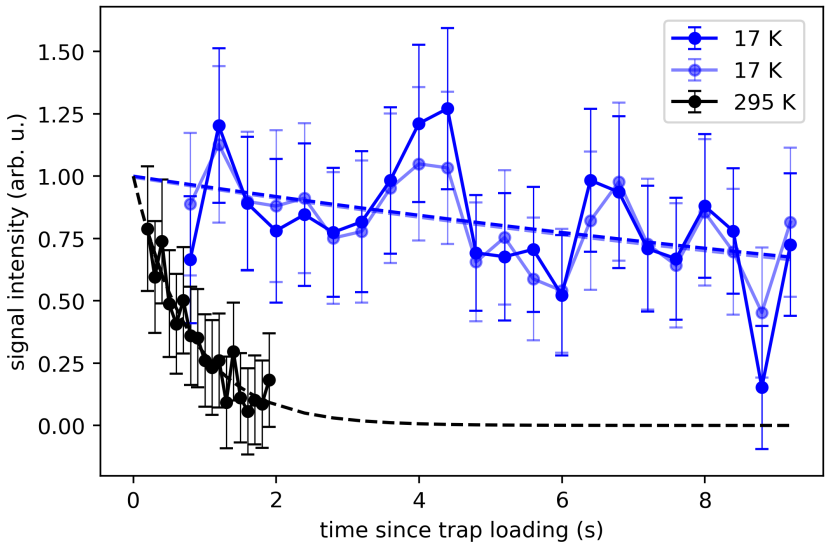

Figure 6.13: Fractional population of trapped OH radicals remaining inside the trap as a function of trapping time. The dashed lines correspond to fits of the data to an exponential decay model. A 1/e-lifetime of 0.8 ± 0.3 s was determined at a temperature of 295 K (black data). Point-by-point subtraction of the background resulted in a lifetime of 24 ± 13 s for the dark-blue data and subtraction of a mean background level yielded a lifetime of 23 ± 8 s for the light-blue trace. See section 6.5.2.2 for more information on the data analysis. The time origin coincides with switching off the stopping fields. The error bars of the black data trace represent standard errors obtained from 159 room temperature data sets, where each set was recorded as an average over 20 experimental cycles. The error analysis for the cryogenic (blue) data is described in section 6.5.2.2.

Under room temperature conditions (295 K) a 1/e-lifetime of 0.8 ± 0.3 s could be determined by fitting the black data points to an exponential decay model. Similar room temperature lifetimes have been reported in ref. [88], where a comparable magnetic trap geometry has been employed for retaining OH radicals. A more detailed description of the data analysis is given in sections 6.5.2.1 and 6.5.2.2. Under cryogenic conditions (17 K),

the 1/e-lifetime increased to 24±13 s, which represents an increase in the 1/e-storage time by a factor of 30 compared to the room temperature result. The 1/e-lifetimes achievable under cryogenic conditions are almost a factor 10 larger than previously reported trapping lifetimes in ref. [278].

Under room temperature conditions, a trap chamber pressure of $2 \cdot 10^{-8}$ mbar prevailed and under cryogenic conditions the pressure in the trap chamber was measured to be $(3-5) \cdot 10^{-9}$ mbar. As the pressure gauge was located outside of the trap, it is estimated that the actual pressure inside the cryogenic shields was lower by a factor 10. The background collision induced loss rate Z can be estimated by taking into account the local pressure inside the trap region p and requires knowledge of the elastic collision cross section σ between the OH radicals and Kr, which constitutes the main component of the background gas within the cryogenic shield. This is a reasonable assumption as Kr was employed as a seed gas and the loading hole in the cryogenic shield faces the decelerator opening. Furthermore, it is assumed that every elastic collision between an OH molecule and a Kr background atom leads to ejection of OH from the trap. The background collision rate Z is given by

$$Z = \sigma \cdot v_{\mathrm{Kr}} \cdot \frac{p}{k_B T} \quad \text{and} \quad v_{\mathrm{Kr}} = \sqrt{\frac{3\,k_{\mathrm{B}}\,T}{m_{\mathrm{Kr}}}}\,, \tag{6.9}$$

where v_{Kr} designates the velocity with which the Kr background atoms approach the almost stationary trapped OH molecules. Here, it is assumed that the krypton particles thermalise with the ambient temperature set by the cryogenic boundary represented by the shields. In order to assess whether the trap lifetimes are limited through collisions with the background gas or by the BBR pump rate out of trappable states, C. von Planta developed a trap lifetime model taking into account the BBR pumping rate as well as collisions with the background gas. Detailed accounts of the model can be found in the thesis of C. von Planta or in ref. [316]. The resulting loss rates are given in Tab. 6.3 and it can be perceived that the room temperature radiative lifetime is more than a factor 2 larger than the one determined experimentally. This suggests, that the lifetime is predominantly limited by background collisions. Assuming a background pressure of $3 \cdot 10^{-8}$ mbar, the background collision rate obtained from Eqn. 6.9 is more than a factor 2 larger than the BBR pumping rate.

At 17 K, the experimental 1/e-lifetime increases by a factor of 30 to 24 ± 13 s and the modelled BBR lifetime limit increases to 81 s. While the BBR pumping rate is significantly reduced under cryogenic conditions, the magnitude of the background collision loss rate is comparable to the BBR pumping rate, which suggests that collisional processes still

assembly temp. (K)	BG collision rate (s^{-1})	BBR pumping rate (s^{-1})	BBR lifetime (s)	expt. lifetime (s)
298	0.87	0.40	2.8	0.8 ± 0.3
17	0.020	0.030	81	24 ± 13

Table 6.3: Background collision and BBR pumping rates under room temperature and cryogenic conditions, as calculated by C. von Planta. The pumping takes place out of the initially trapped $|\nu = 0,\ J = 3/2, F = 3/2,\ M_J = 3/2,\ \mathrm{f}\rangle$ state. Experimental 1/e-lifetimes are stated in the last column and are to be compared with the 1/e-lifetime from the lifetime model in the fourth column. See section 6.5.2.2 for the experimental data analysis.

impose a limitation on the maximum lifetimes that can be achieved. A background pressure of $2 \cdot 10^{-10}$ mbar was assumed for the calculation of the cryogenic background collision rate. Under cryogenic conditions, heavier gases freeze out on the cryogenic shield and the collisions are presumed to originate from particles leaking in through the apertures of the shield and from lighter hydrogen molecules present on the surfaces of the vacuum chamber. The lifetime could be enhanced further by transporting the cloud to a position within the cryogenic shield with less BBR contribution, further away from the apertures. The storage time of the OH cloud between the two bar magnets critically depends on the experimental conditions. Nonetheless, the improvement in trapping lifetime under cryogenic conditions is sufficient to allow for transportation of the neutral OH cloud to the ion trap and superimpose the neutral cloud with ions stored inside the ion trap.

6.5.2.1 Data selection

The data depicted in Fig. 6.13 was recorded over several days. Each data point was obtained by integrating the LIF signal within a time window of 2.13 µs. The population remaining in the trap was probed at increasing delays relative to the end of the trap loading sequence. Because of the small number of LIF photons exiting the apertures of the cryogenic shield and the resulting low signal levels, special care had to be exercised in the analysis of the data and the handling of artificial variations in the photon counts caused by occasional glow-inducing electric discharges and variations in the stray light level.

The points pertaining to a single trap loss measurement at room temperature (295 K) were acquired as an average over 20 experimental cycles. In total, 164 such data sets were recorded. Likewise, the trap loss under cryogenic conditions (17 K) was recorded 165 times, where each acquisition comprised 5 repetition cycles of the experiment. Due to the prolonged measurement time, only data sets whose maximum value lay within

the confidence intervals depicted in Fig. 6.14 were accepted. The spikes represent strong fluctuations in the signal background due to occasional electrostatic discharges of the trap. Compared to the room temperature measurements, the signal maxima in the cryogenic measurement series are subjected to more, albeit smaller fluctuations. This is likely due to vibrations imposed onto the setup by the cryogenic cooler. In turn, the vibrations led to slight variations of the trap position relative to the laser, which has a negative effect on the stray light level recorded by the PMT. After selecting the data sets within the confidence intervals in Fig. 6.14, a total of 159 room temperature trap lifetime traces remained, which corresponds to an effective average over 3180 trap loading cycles for the data depicted in Fig. 6.13. The error bars for each point pertain to the standard error calculated from the 159 data sets. Similarly, 121 data sets were selected for the cryogenic conditions in accordance with Fig. 6.14 b), which corresponds to an effective average over 605 experimental repetitions and the standard error was obtained from these 121 data traces. The horizontal dashed line lies 0.7σ from the mean of the signal maxima (blue line), which represents a stringent selection criterion. Data sets with strong signal fluctuations are not considered. A large portion of the Python analysis script library for the Stark experiment was developed by C. von Planta, with occasional additions by myself. A more detailed description of the procedures can be found in the thesis of C. von Planta. The data analysis presented here was conducted by myself.

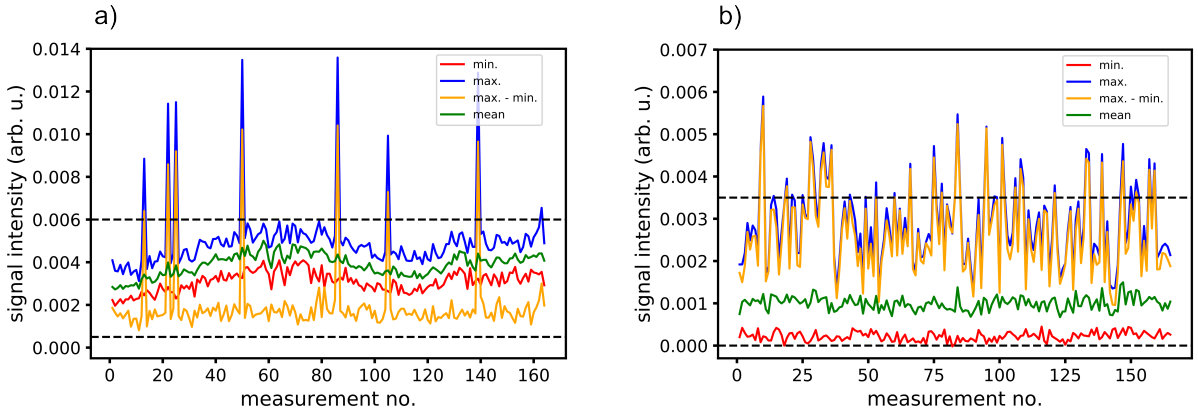

Figure 6.14: Scheme illustrating the data set selection process for the **a)** room temperature (295 K) data and for the data acquired under **b)** cryogenic (17 K) conditions. Only traces with maximum values lying between the indicated confidence intervals (bounded by the dashed lines) were accounted for in the trap lifetime estimation. In b), the upper limit lies 0.7σ above the mean value of the signal maxima depicted by the blue trace.

6.5.2.2 Trap lifetime determination

To determine the lifetime of the magnetically trapped OH molecules under room temperature conditions, the data selected by the process described above was fitted to an

exponential model of the form $a + b\exp(-t/c)$, where a denotes the background signal level, b designates a scaling parameter associated with signal height and c represents the 1/e-lifetime. The entire data set satisfying the conditions in Fig. 6.14 a) was subjected to a Levenberg-Marquardt least squares fitting algorithm [317, 318] and a lifetime of 0.8 ± 0.3 s was obtained. Convergence of the algorithm was assured by supplying different initial starting points. The fit function and the corresponding data points are depicted by the black data set in Fig. 6.13.

The acquisition of the cryogenic trap lifetime data required operation of the experiment at a repetition rate of 0.1 Hz, which allowed to address points in a time window with a maximum extent of 10 s relative to the onset of trapping. The trapping signal depicted in Fig. 6.15 was recorded over the course of four days (605 trap loading cycles) in order to improve the signal statistics. As the 10 s time frame only captures the initial part of the lifetime decay, a separate background measurement was conducted to determine the signal level towards which the lifetime curve decays. The background data was subjected to the same selection criteria outlined above for the trapping signals. Each background measurement consisted of 5 experimental repetition cycles and a total of 128 data sets were recorded. The square data points in Fig. 6.15 represent the average over 640 individual measurements and the error bars indicate the standard errors obtained from the 128 measurement series. The background was acquired in the absence of stopping fields.

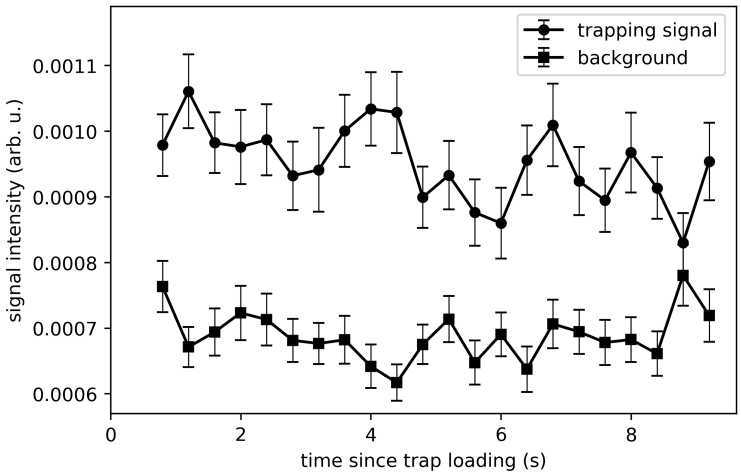

Figure 6.15: Comparison between the background and the trapping signal. The trapping signal represents an average over 605 trap loading cycles and is depicted by circles. The square symbols pertain to the background signal, which consists of 640 individual measurements recorded over the course of 128 trap lifetime scans. Subtraction of the background from the signal followed by normalisation results in the blue trapping data presented in Fig. 6.13. The error bars represent standard errors obtained from the 121 signal and 128 background data sets, respectively.

Consequently, the trap was not loaded and the signal contribution from OH 0.8 s after reaching the trap region is negligible. Compared to the trapping signal, the background level is lower and does not display a decaying behaviour, which indicates a consistent laser pointing stability and unchanged laser intensities throughout the measurement.

Two strategies can be envisaged for background correcting the trapping signal. As the trapping signal and the background level were probed at identical delays since trap loading, the background curve can be subtracted from the trapping signal in a point-by-point fashion, which is depicted by the dark blue data points in Fig. 6.13. For better comparability, the decay curves were scaled such that the exponential decay at the origin starts from 1.0. Subsequently, the background-corrected trapping signal was fitted with a 2-parameter exponential decay model of the form $b \cdot \exp(-t/c)$, where b denotes the signal height and c is the 1/e-lifetime. The fit function is depicted in Fig. 6.13 and a 1/e-trap lifetime of 24 ± 13 s was obtained from the dark-blue data. The standard errors s were propagated according to $s_{\text{subtracted}} = \sqrt{s^2_{\text{sig.}} + s^2_{\text{backg.}}}$. The large dip at long trapping times is due to an anti-correlation between the signal and the background. It could be that the pointing stability of the laser was inferior at this time point due to thermal instabilities resulting from the low repetition rate of the experiment.

Alternatively, the background can be averaged over the flat part between 2.4 s and 8.4 s, which results in a constant background level of $(6.8 \pm 0.3) \cdot 10^{-4}$. Subtraction of this value from the trapping signal followed by normalisation yields the light blue trace in Fig. 6.13. Compared to pointwise subtraction of the background, the subtraction of a constant characteristic background value reduces the modulation of the resulting signal as no further noise from the background is added. Employing the 2-parameter exponential decay model from above, a 1/e-trap lifetime of 23 ± 8 s was obtained. The lower degree of signal fluctuation is reflected in the reduced fit error and a lower least square sum.

6.5.3 Phase-space considerations and trap dynamics

6.5.3.1 Trap loading

Modelling the trap loading and trapping process by Monte Carlo trajectory simulations allows to extract phase-space distributions within the confining trap potential at arbitrary delays relative to switching off the stopping fields. The spatial as well as the velocity spread of the package exiting the decelerator is of great importance for loading the trap. As discussed in the PhD theses of J. J. Gilijamse [302] and B. Stuhl [301], the six-dimensional phase space of the package exiting the decelerator needs to be matched to the phase-space acceptance of the trap, both, spatially and in terms of velocity. All

phase-space distributions depicted in Fig. 6.16 b)-d) were extracted from the trapping TOF profile in Fig. 6.12 b).

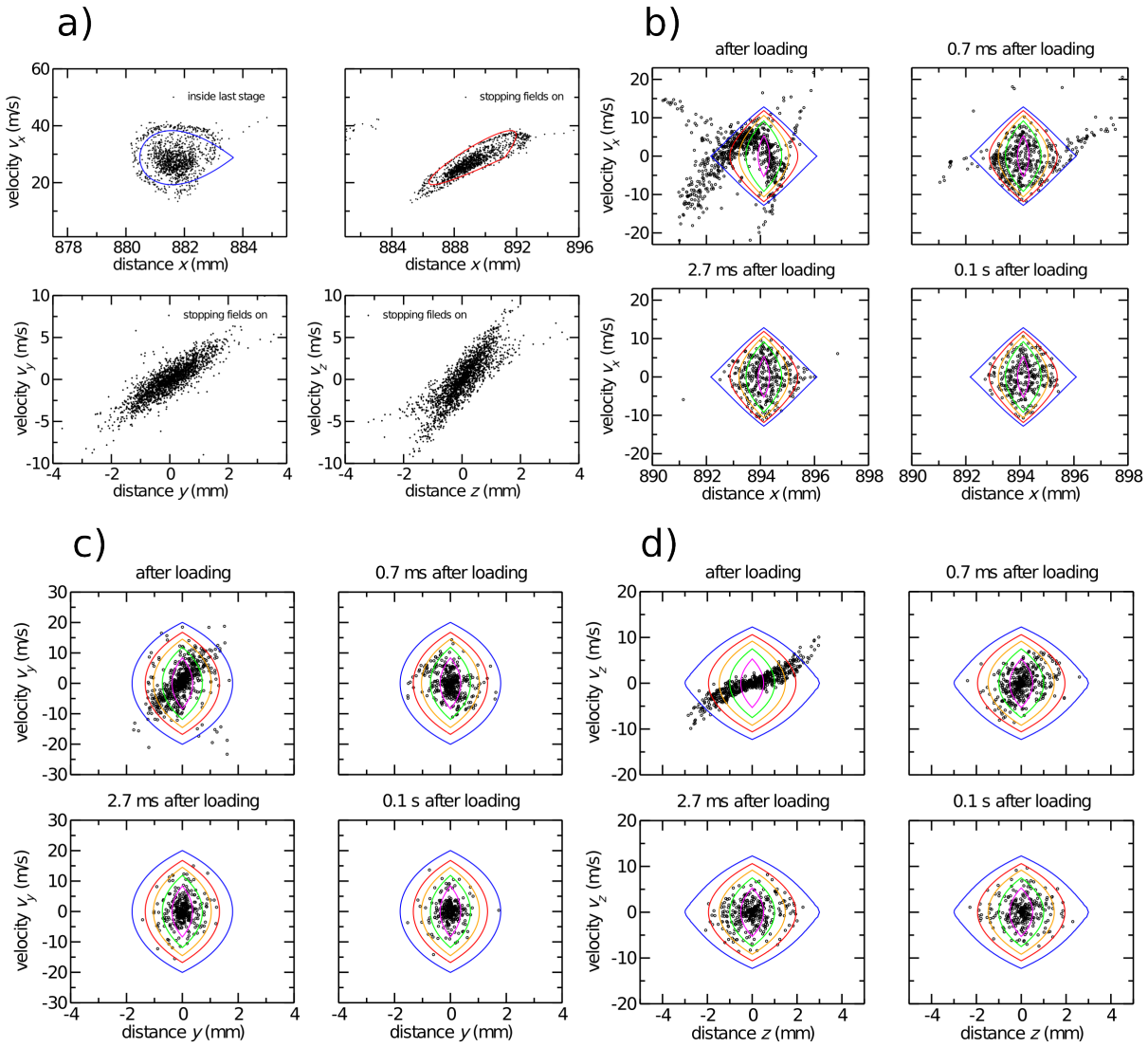

Figure 6.16: Phase-space evolution at different points in time after loading the trap, extracted from the simulations shown in Fig. 6.12 b). **a)** Top left: (x, v_x) phase-space distribution inside the decelerator. The blue separatrix was drawn according to Eqn. 3.27. The remaining three panels depict the phase-space distribution at the switch-on point of the stopping fields. **b)** Phase-space distribution (x, v_x) along the direction of loading and the contour lines indicate the phase-space acceptance of the trap in increasing order of energy: 0.02 (magenta), 0.06 (green), 0.08 (yellow), 0.10 (red) and 0.12 (blue) cm^{-1}. **c)** (y, v_y) phase-space distribution along a direction normal to the surfaces of the magnets and the trap depth is given by: 0.05 (magenta), 0.10 (green), 0.15 (yellow), 0.2 (red) and 0.29 (blue) cm^{-1}. **d)** (z, v_z) phase-space distribution along the largest extension of the trap and the corresponding trap depth contour lines are: 0.02 (magenta), 0.04 (green), 0.06 (yellow), 0.08 (red) and 0.11 (blue) cm^{-1}. See section 3.2.1 for a discussion of the trap phase-space dynamics in the context of Liouville's theorem.

The top left panel in Fig. 6.16 a) depicts the (x, v_x) phase space at the end of the last deceleration stage. The package displays a halo structure with a spatial extension of almost 3 mm along the deceleration axis and a dense core approx. 1.5 mm in length. The Halo ring is due to parametric amplification between longitudinal and transversal oscillations inside the deceleration bucket, which causes a non-phase stable region [61, 77]. After a free flight distance of 7.6 mm, the first cryogenic shield is reached and the stopping fields are switched on. At this position, the full six-dimensional phase-space distribution is depicted in the remaining panels of Fig. 6.16 a). The phase-space distributions are now tilted and the spatial extension of the package has increased to $(\Delta x, \Delta y, \Delta z) \approx (7\text{ mm}, 3\text{ mm}, 3\text{ mm})$, which is due to spreading of the package in accordance with its velocity distribution. The dense core of the package now extends over a distance of 3 mm in the longitudinal direction. The FWHM of the position distribution within the package was determined to be $(\Delta x_{\mathrm{FWHM}}, \Delta y_{\mathrm{FWHM}}, \Delta z_{\mathrm{FWHM}}) = (5.2\text{ mm}, 1.8\text{ mm}, 1.6\text{ mm})$ and the corresponding velocity distribution amounts to $(\Delta v_{x,\mathrm{FWHM}}, \Delta v_{y,\mathrm{FWHM}}, \Delta v_{z,\mathrm{FWHM}}) = (17.3\text{ m/s}, 4.6\text{ m/s}, 6.3\text{ m/s})$. For the magnetically low field seeking $\mathrm{X}^2\Pi(J = 3/2,\ M_J = +3/2,\ \mathrm{f})$ state of OH, the trap displays a depth of $(\Delta v_{x,\mathrm{trap}}, \Delta v_{y,\mathrm{trap}}, \Delta v_{z,\mathrm{trap}}) \approx (13.9\,\mathrm{m/s}, 21.7\,\mathrm{m/s}, 13.3\,\mathrm{m/s})$. Given that molecules can be trapped within the $(\Delta x_{\mathrm{trap}}, \Delta y_{\mathrm{trap}}, \Delta z_{\mathrm{trap}}) \approx (3.9\text{ mm}, 3.6\text{ mm}, 6.2\text{ mm})$ maximum extension of the trap, it is clear that the longitudinal extent of the OH package will be larger than the trap dimension by the time the trap centre is reached 11.5 mm downstream of the decelerator. Therefore, it would be advantageous to position the trap closer to the decelerator opening if larger loading efficiencies are desired. Alternatively, a significant reduction in the spreading of the OH package could be achieved by increasing the stopping potentials such that larger loading velocities are supported and the flight time to the trap centre is reduced.

Figs. 6.16 b)–d) depict phase-space distributions along all three spatial directions of the trap right after switching the stopping fields off. In addition, the evolution of phase space inside the trap is extracted after trapping times of 0.7, 2.7 and 100 ms. It can be perceived that a large portion of the OH cloud lies within the acceptance of the trap upon switching the stopping fields off. In the absence of collisions, which are not accounted for by the present model, the phase-space distribution after switching the stopping fields off determines the subsequent evolution under the influence of the confining Zeeman potential. Only molecules whose total energy, i.e. the sum of kinetic and potential energy, is lower than the shallowest trap potential remain trapped. As a guide to the eye, energy contour lines of the magnetic trap are indicated in Fig. 6.16. The contour lines were obtained

from the following expression:

$$v_{\text{cont.}} = \sqrt{\frac{2 \cdot (E_{\text{cont.}} - E_{\text{Zeeman}}(x, y, z))}{m_{\text{OH}}}}, \tag{6.10}$$

where $v_{\text{cont.}}$ denotes the velocity of a particle at a certain position within the trap potential $E_{\text{Zeeman}}(x, y, z)$ given its total energy amounts to the contour energy $E_{\text{cont.}}$.

Loading along the x-direction is most critical as the largest amount of kinetic energy is removed along the forward direction. With the present loading scheme, the reflection of the slow part of the OH distribution from the stopping slope is observed in the top left panel of Fig. 6.17 b). The slow part could partially be regained by loading at slightly higher velocities. The phase-space distribution would then be shifted towards the right as the package covers more distance during the time the stopping fields are on. While loading at faster velocities improves the loading efficiency, the average temperature of the trapped ensemble increases and a doughnut-shaped structure around the trap centre is obtained, i.e. no molecules are located close to the centre position with almost zero kinetic energy [302]. Increased loading efficiencies at higher loading velocities have also been reported in ref. [79], where the timings of the switching sequence were optimised using evolutionary strategies. In our case, the mesh adaptive direct search algorithm introduced in section 6.2.3 can be used for optimising the loading efficiency via the phase angle and the stopping fields are adjusted for a maximum loading efficiency.

From the v_x-velocity distribution in the right panel of Fig. 6.17 a), it can be perceived that a large portion of the molecules display residual velocities between 3-7 m/s after switching off the stopping fields. This represents a good compromise between maximising the loading efficiency and keeping the forward velocity of the ensemble reasonably low, such that a sufficient coverage of the inner region of phase space can be ensured. For the phase-space distributions depicted in Fig. 6.16, a loading efficiency of 10% was determined. In the end, a trade-off between increasing the loading velocity and loosing fewer molecules from the slow tail of the distribution via back reflection from the stopping slope and loading a cloud with a higher average kinetic energy has to be made. When loading a magnetic trap with the goal of superimposing the trapped neutral species onto a Coulomb crystal, it is considered advantageous to keep the velocity distribution reasonably small in order to obtain a compact cloud around the crystal, which increases the likelihood of collisions between the two species.

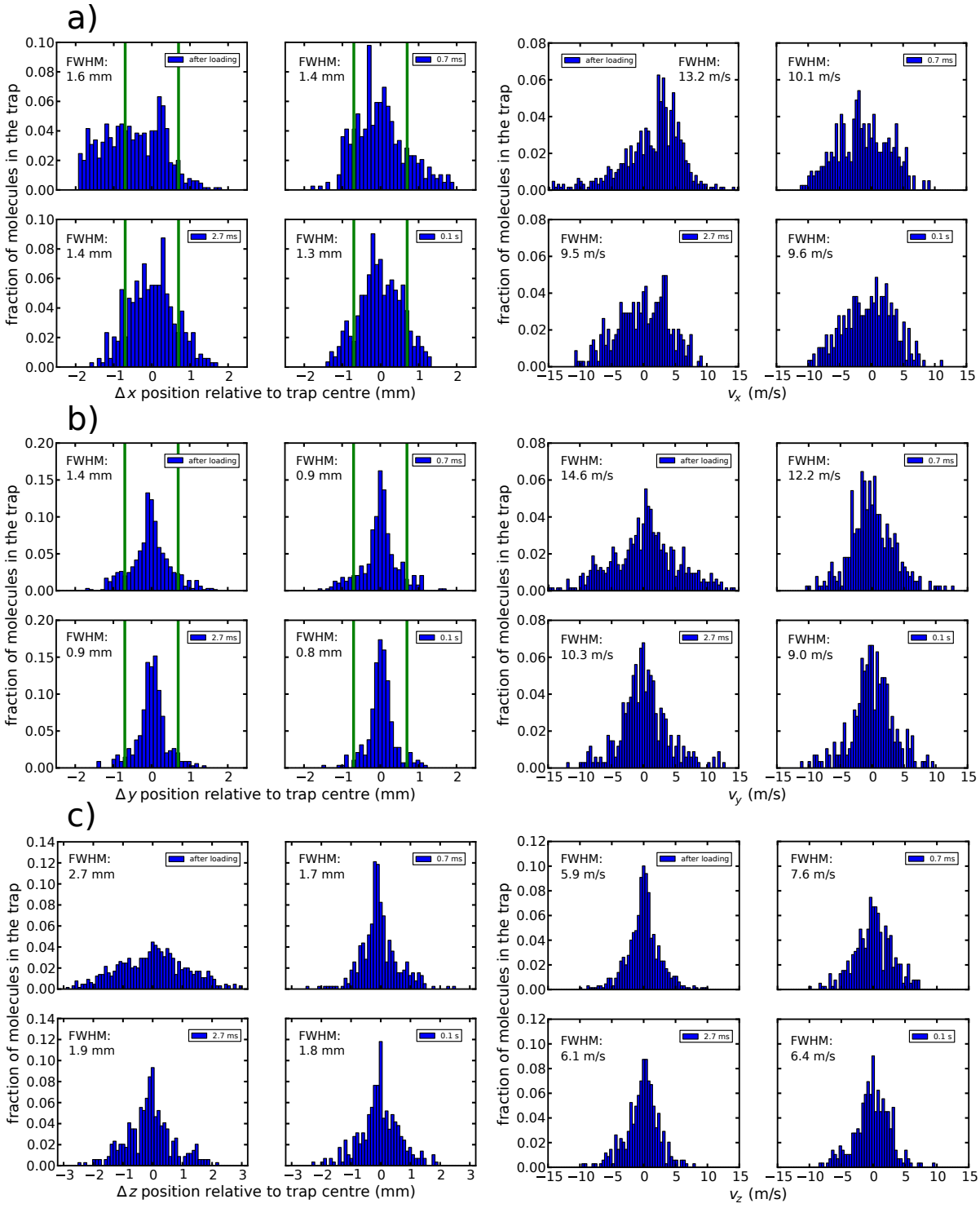

Figure 6.17: Fractional position and velocity distributions of the trapped OH cloud at various points in time after switching the loading fields off. Only OH particles lying within the trap are considered and positions are given relative to the trap centre. The coordinate system depicted in Fig. 6.7 applies. The sum over all bins amounts to unity and the FWHM position and velocity spreads are indicated. The green vertical bars denote the volume addressable with the LIF laser beam. **a)** Position and velocity distributions pertaining to the deceleration axis x. **b)** Position and velocity spreads normal to the bounding surface of the bar magnets y. **c)** Position and velocity distribution along the laser beam axis z.

Along the transversal y- and z- directions fewer molecules are lost during loading of the trap. Compared to the longitudinal direction, the transversal spatial and velocity spreads are smaller upon initiation of the stopping fields (see the lower panels Fig. 6.16 a)). Consequently, the package better fits the acceptance of the trap, as indicated in Fig. 6.16 c) and d). The trap is steepest along the y-direction and the molecules are confined close to the centre, which is in accordance with the narrow spatial distributions depicted in the left part of Fig. 6.17 b). Due to the large restoring forces along the y-direction, a larger velocity spread can be maintained than is the case for the remaining two directions. This is also mirrored in the relatively wide velocity spread depicted in the right section of Fig. 6.17 b) during the early stages of trapping. The largest extension of the trap lies along the z-axis, which results in a reduced restoring force towards the centre. Almost the entire z-distribution depicted in Fig. 6.16 a) fits into the trap, as can be seen from Fig. 6.16 d). The shallow and elongated trapping potential gives rise to a wide position spread and the trap does not support loading of OH molecules with a high velocity component along z. Again, it is insightful to consult the position and velocity distributions depicted in Fig. 6.17 c).

6.5.3.2 Trap Evolution and trap dynamics

After completion of the loading sequence, the trapped molecule cloud evolves in time under the influence of the confining Zeeman potential. The phase-space distribution rotates along the trap's isoenergetic contour lines in a clockwise fashion. This rotation is equivalent to oscillations from one side of the potential flank to the other. Over time, the particles spread out inside the trap and explore the regions of the trap which are energetically accessible. The trap potential couples the motion along all three spatial directions. It can therefore happen that the shape of the confining potential reallocates energy from one direction of motion to another, which results in particle energies that lie beyond the trap depth and particles are lost during the early stages of phase-space evolution. The distinct structure the stopping field imposes on the phase-space distribution (see Fig. 6.16 b) in particular) is gradually lost and the particles spread out within the phase space according to their energies. Furthermore, the oscillatory motion of the molecules decoheres, which manifests itself by the diffluence of the package along a given contour line. The loss of particles can be perceived by the thinning of the distribution in Figs. 6.16 and 6.17. 0.1 s after switching off the loading fields, the trap was found to be free from loss. Additionally, it is interesting to note how the spatial and velocity spreads change with increasing trapping time. As depicted in Fig. 6.17, the ejection of energetic particles from the trap leads to a narrowing of the spatial and velocity distribution as the trapping time advances. The TOF profile in Fig. 6.12 displays an oscillatory structure, which indicates

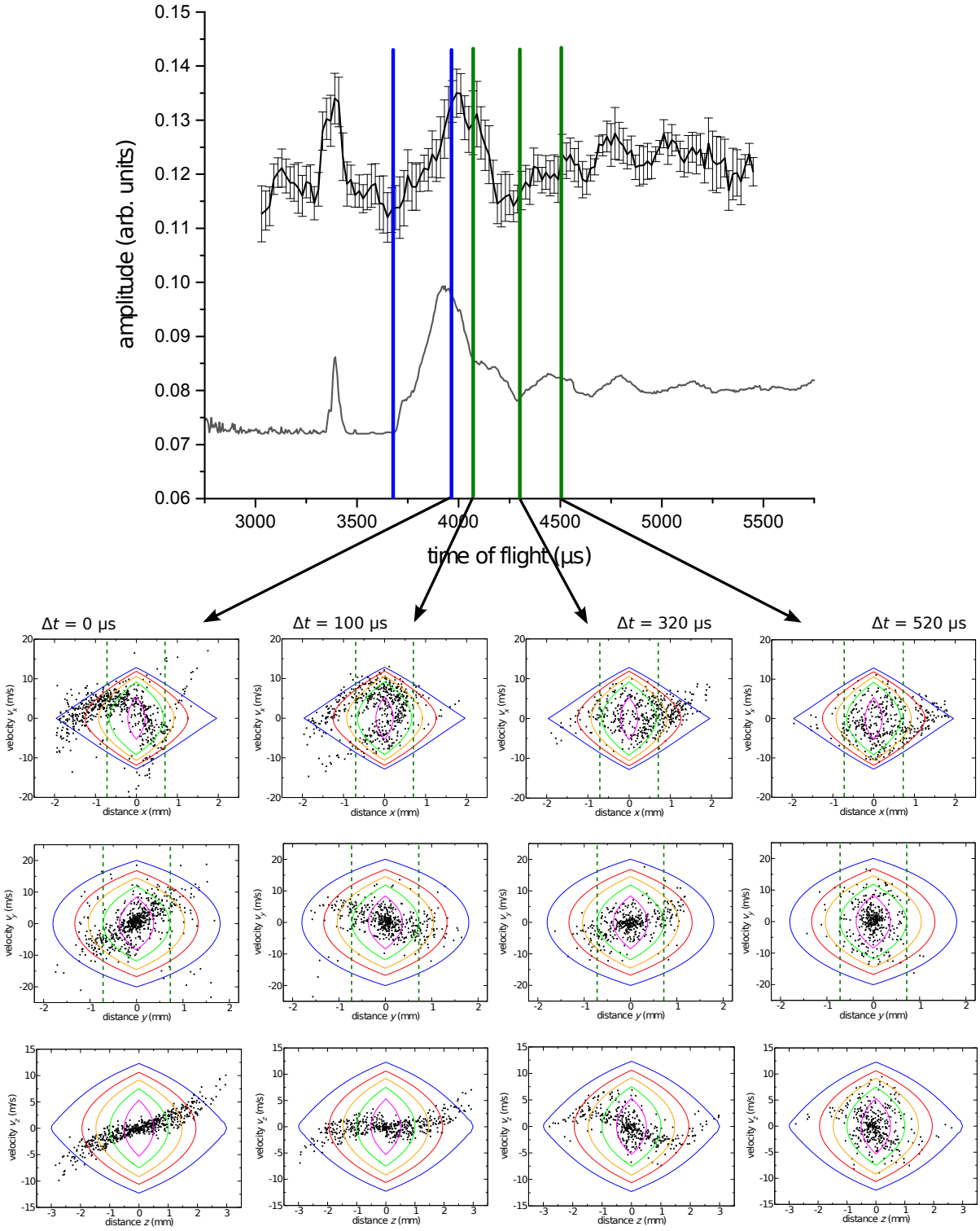

Figure 6.18: Evolution of the phase-space distribution $\Delta t = 0, 100, 320$ and 520 µs after loading. Oscillations of the package along the x-direction give rise to an oscillatory structure in the TOF profile. The first row depicts the (x, v_x) phase space, the second row displays the (y, v_y) coordinates and the panels in the third row pertain to the (z, v_z) phase space. The broken green vertical lines denote the extension of the laser beam along the x- and y-direction. The laser propagates along the z-direction. Similar investigations have been performed by J. J. Gilijamse [302].

that there are density fluctuations around the laser beam volume. In order to understand the source of these fluctuations, it is insightful to inspect the phase-space evolution at short times after loading the trap, as depicted in Fig. 6.18. Phase-space diagrams along all three spatial directions have been extracted from the simulations for trapping times of $\Delta t = 0, 100, 320$ and 520 µs. The corresponding times in the TOF profiles are indicated by arrows and vertical lines. The blue bars indicate the initiation and the end point of the stopping fields. A laser beam with a radius of 0.7 mm was considered and the width of the laser is indicated by the green vertical lines in Fig. 6.18. The laser beam propagates along the z-direction. Upon switching the stopping fields off, the dense part of the OH package lies on the left slope of the trap potential. During the next 100 µs, the package travels towards the trap centre and thereby moves through the centre of the laser beam, which leads to an increase in the number of detected photons. In the experiment as well as in the simulation, the signal increase at $\Delta t = 100$ µs is obscured by the loss of the magnetically high-field seeking component and the first green vertical bar is located on the falling slope of the TOF signal. During the subsequent 220 µs, the package moves partially out of the laser beam along the x-direction. At $\Delta t = 520$ µs the package moves back into the centre of the laser beam. Additionally, the (y, v_y) phase space is now also oriented in such a way that a maximum signal contribution is reached. Consequently, another maximum appears in the TOF profile. At longer delays, the position of the OH cloud in the trap is homogenised and oscillations are absent in the TOF profile. As pointed out by J. J. Gilijamse [302], the number of observable oscillation cycles depends on the laser beam. In this experiment, the observation of oscillations is fostered by the small 0.7 mm radius of the laser beam and the comparatively large final velocity of 3-7 m/s along the x-direction.

6.5.4 Density of trapped OH radicals

An important characteristic quantity in every experiment involving the manipulation of molecular beams is the density. The current experimental setup allows for the determination of the density in the source chamber as well as after the decelerator, which has been discussed in sections 4.5 and 5.6. The accurate determination of the density is a challenging task as the number of OH radicals has to be determined within the detection volume at the crossing point between the expanding gas cloud and the laser beam.

In the presence of the hybrid trap, the determination of the density is more challenging as the imaging setup in the trap chamber is no longer identical to the one installed in the source chamber. Furthermore, the cryogenic shields of the hybrid trap impair the optical access to the trap centre and the laser beam diameter is limited to 1.4 mm. This leads to a reduction in the excitation volume and the detection efficiency of LIF photons is decreased

due to the limited solid angle of the cryogenic shield aperture. In order to augment the photon count, a collimation lens ($\varnothing$= 6 mm, f = 6 mm) was incorporated into the trap mount and the imaging holes of the cryogenic shield were enlarged to a diameter of $\varnothing = 5$ mm, as described in section 6.4.3. When estimating the density of an acquired LIF signal, the solid angle under which photons are collected as well as the excitation volume have to be determined. As described in section 6.4, a Monte Carlo optical ray tracer was developed for the calculation of solid angles. The simulation took into account the refraction of the lens and the geometry of the cryogenic shields, the windows and the active diameter of the PMT. The position-dependent imaging solid angle function $\Omega(x, y, z)$ was calculated by discretising the cylindrical laser beam volume V_{cyl} and calculating the solid angle for every point in the laser volume grid, as depicted in Fig. 6.19 c). The cylindrical section V_{cyl} of the laser beam under consideration is given by Eqn. 6.11.

$$V_{\text{cyl}} = \{(x, y, z) = (\rho\cos(\phi), \rho\sin(\phi), z) | \rho \in [0, 0.7], \phi \in [0, 2\pi], z \in [-1, 1]\}\,, \qquad (6.11)$$

where ρ denotes the radius of the laser beam in mm, ϕ is the angle of revolution and $z \in [-1, 1]$ mm runs along the laser propagation direction. The Cartesian (x, y, z) directions coincide with the ones indicated in Fig. 6.6.

A further complication arises due to the overlap geometry of the laser beam and the OH cloud at the trap centre. The detection of photons is only possible if the laser beam overlaps with the molecular cloud at a position where the solid angle is appreciably large. The laser beam intensity was expressed as a 2-dimensional Gaussian intensity profile $I_{\text{laser}}(x, y)$ given by

$$I_{\text{laser}}(x, y) = I(x, y)/I_0 = \exp\left(-2\,\frac{x^2 + y^2}{w_0^2}\right)\,, \qquad (6.12)$$

where $I(x, y)/I_0$ denotes the position-dependent laser intensity ratio relative to the maximum intensity I_0 and w_0 is the $1/e^2$ radius of the laser beam at the intersection point with the OH beam. The $1/e^2$ radius inside the trap is estimated to lie between 0.6-0.7 mm, based on knife-edge skimming measurements before and after the skimmer (see section 6.3.5). For the density calculation, a $1/e^2$ radius of 0.7 mm will be adopted. However, it should be noticed that this value likely changed over time due to misalignment of the laser beam and due to deterioration of the 10 µm pinhole through photon damage. Also, the effective diameter of the beam depends on the laser intensity. Furthermore, it should be noticed, that the laser beam intensity does not influence the number of LIF photons emitted, as long as the intensity is sufficient to saturate the transitions.

In addition to the above considerations, the density distribution of the OH package leaving the decelerator is taken into account by $I_{\mathrm{beam}}(x, y, z)$. Instead of solely employing the solid angle Ω, a convolution of the solid angle with the laser beam intensity distribution and the OH density profile was used in the calculation of an optical throughput factor χ, which took into account the geometric overlap of the laser beam and the OH package. In equation 6.13, the convolution is performed by integrating over the whole cylinder volume defined by Eqn. 6.11 and the denominator is used for normalising the optical throughput factor χ, such that $\chi \in [0, 1]$.

$$\chi = \frac{\int_{V_{\mathrm{cyl}}} \Omega(x, y, z) \cdot I_{\mathrm{laser}}(x, y) \cdot I_{\mathrm{beam}}(x, y, z)\, \mathrm{d}x\, \mathrm{d}y\, \mathrm{d}z}{\int_{V_{\mathrm{cyl}}} 4\pi \cdot I_{\mathrm{laser}}(x, y) \cdot I_{\mathrm{beam}}(x, y, z)\, \mathrm{d}x\, \mathrm{d}y\, \mathrm{d}z} \,. \tag{6.13}$$

In guiding mode, Eqn. 6.13 evaluates to $\chi = 0.028$ and for a molecular package at 28 m/s, a value of $\chi = 0.027$ was determined. In order to obtain the number of OH radicals contributing to the measured signal, an altered form of equation 4.34 was employed. As the denominator in expression 6.13 normalises the convolution to the ideal case of a detector with a solid angle of 4π, the factor of 4π in Eqn. 4.34 was omitted and Ω was substituted by χ, which results in the following expression:

$$N_{\mathrm{OH}} = \frac{N_{\mathrm{photons}}}{\chi\, T\, Q\, \varepsilon} \,. \tag{6.14}$$

As discussed in section 5.6, N_{photons} is either determined by integrating the LIF signal or by photon counting in the case of low-level signals arising upon operating the decelerator at high phase angles. Typical LIF signals pertaining to the guiding mode and target velocity are depicted in Fig. 6.19 a) and b). For both data sets a stray light photon count rate of 1 photon/shot was employed. The background count rate was determined by T. Kierspel, who kindly made his peak finder algorithm available, which was used for photon counting in Fig. 5.14 b) and Fig. 6.19 b).

Once the number of OH molecules contributing to the signal is known, the only quantity left to be determined is the excitation volume $V_{\mathrm{exc.}}$ from which the photons are collected. While the solid angle can be calculated with satisfactory accuracy (see [311]), the determination of the excitation volume is more challenging. In spite of the Gaussian profile of the laser beam, a large portion of the beam allows for saturating the OH $\mathrm{X}^2\Pi(v = 0)$-$\mathrm{A}^2\Sigma(v = 1)$ transition, but towards the edge of the profile the laser intensity drops to such low values that hardly any contribution to the signal level results. One would like to exclude these regions from the excitation volume. Therefore, a numerical integration over the domain V_{cyl} was performed, where the integrand is either unity or zero,

depending on the size of the convolution integrand $C_{\text{conv.}}$. If the convolution integrand is larger or equal to $1/4 \cdot C_{\text{conv.}}^{\max}$, the contribution to the signal was considered significant and the volume element at the particular position was included in the calculation of the excitation volume. Consequently, the largest uncertainty concerning the density calculation in the trap chamber remains with the determination of the exact excitation volume.

$$V_{\text{exc.}} = \int_{V_{\text{cyl}}} \begin{cases} 1, \Omega_{\text{int}}(x,y,z) \cdot I_{\text{laser}}(x,y) \cdot I_{\text{beam}}(x,y,z) = C_{\text{conv.}} \geq 1/4 \cdot C_{\text{conv.}}^{\max} \\ 0, \Omega_{\text{int}}(x,y,z) \cdot I_{\text{laser}}(x,y) \cdot I_{\text{beam}}(x,y,z) = C_{\text{conv.}} < 1/4 \cdot C_{\text{conv.}}^{\max} \end{cases} \mathrm{d}x\,\mathrm{d}y\,\mathrm{d}z \tag{6.15}$$

In a final step, the density was obtained by dividing the number of OH molecules N_{OH} by the excitation volume $V_{\text{exc.}}$, i.e. $\rho_{\text{OH}} = N_{\text{OH}}/V_{\text{exc.}}$. Following the methodology outlined for the density calculation in the presence of the cryogenic trap, densities of approximately $8 \cdot 10^7$ OH molec./cm^3 were obtained for guiding (see Fig. 6.19 a)) and the densities at 28 m/s (see Fig. 6.19 b)) were determined to lie around $5 \cdot 10^6$ OH molec./cm^3. Due to the loss of the magnetically high-field seeking component, the signal level is diminished by a factor 2 (see Fig. 6.12 b)) and the density of trapped OH molecules in the $J = 3/2,\ M_J = \pm 3/2,\ f$ state is reduced accordingly. The density values obtained in this section agree with the experimentally determined densities in chapter 5 within a factor of three. The discrepancy is likely caused by the inability to determine the excitation volume more precisely. Similar densities of magnetically trapped molecules have been reported in ref. [88].

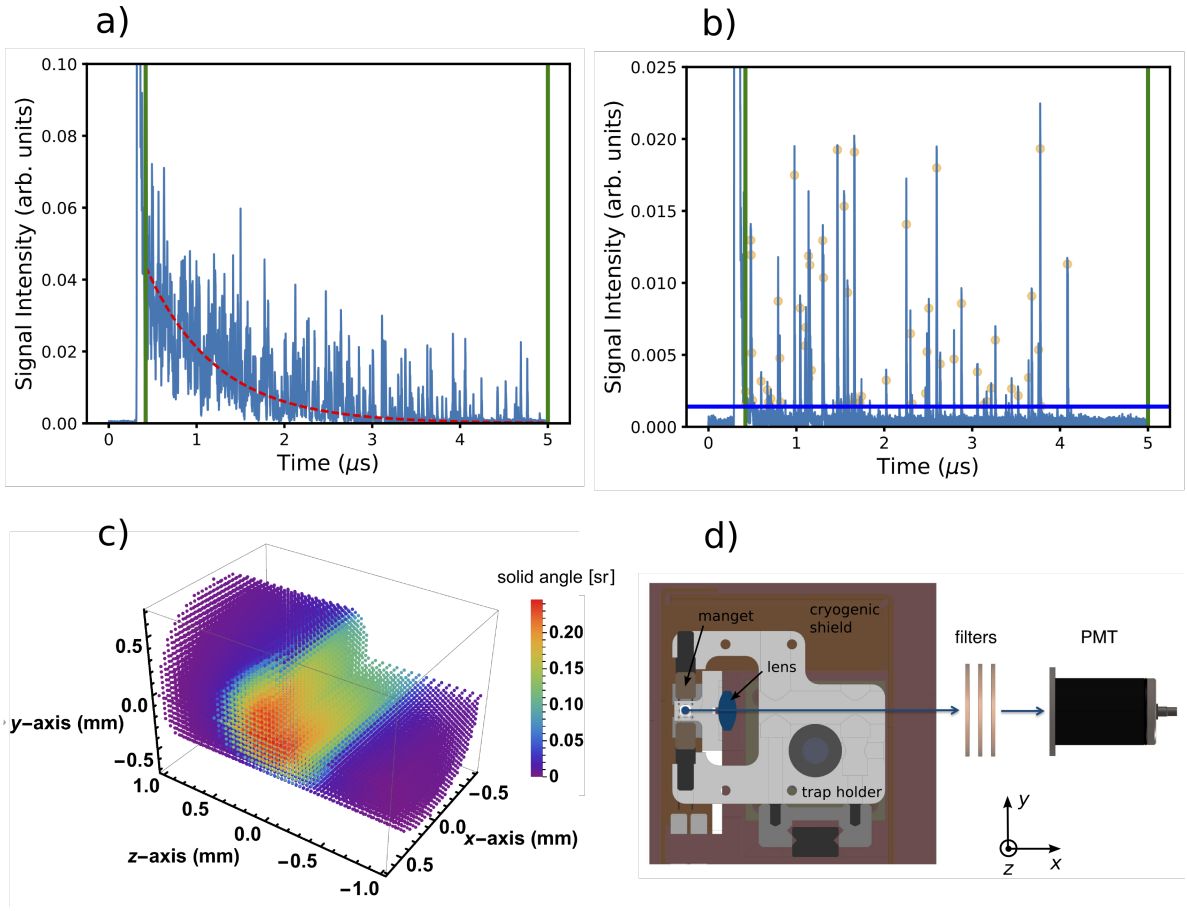

Figure 6.19: **a)** A typical LIF trace recorded in guiding mode at the time of flight time resulting in a signal maximum. The green vertical bars denote the integration range over which the red exponential fit is integrated. **b)** A typical LIF trace at the target velocity of 28.8 m/s. Due to the low signal levels the signal is no longer continuous and single photon peaks are recorded. Only peaks lying above the blue horizontal line are counted. Photon peaks contributing to the photon count are labelled with an orange circle. The signals also display a background photon count rate of 1 photon per laser shot. **c)** Imageable solid angle for the experimental geometry depicted in d). The solid angle is calculated for a cylindrical excitation volume with a diameter of 1.4 mm and a length of 2 mm, where the refraction of the lens is taken into account. All distances are given relative to the trap centre and the coordinate system from d) applies. **d)** Cross-sectional view of the OH trapping region and the LIF photon propagation pathway to the photomultiplier tube (PMT). The blue circle represents the laser beam propagating along the z-direction and passing through the trap centre. The photon collection efficiency is increased by a collimating lens ($d = 6$ mm, $f = 6$ mm).

6.6 Conclusion and outlook

Detailed accounts on the modelling and optimisation of the loading process of OH radicals into a magnetic trap have been given. The magnetic trap could successfully be loaded in spite of the large deviation of the current operation parameters from the optimum settings deduced with the help of a mesh adaptive search algorithm [113]. The current loading efficiency of approx. 10% could be improved to 25% by decreasing the distance towards the decelerator opening by 4 mm and by switching the stopping fields at ± 10 kV. However, due to electrostatic breakdown of the trap above 6 kV, operation at higher stopping potentials is currently not feasible.

A trapping lifetime of 0.8 ± 0.3 s was determined under room temperature conditions, where both, the BBR pumping out of trappable states and collisions with the background gas limit the achievable trapping time. Under cryogenic conditions, an increase of the lifetime by a factor 30 to 24 ± 13 s was established. The cryogenic environment reduces the background pressure significantly and the black body radiation pumping rate is reduced as well. A further improvement of the trap lifetime could be achieved by dislocating the OH cloud to a "darker" region of the trap, away from the apertures in the cryogenic shield. A density of OH molecules lying in the mid 10^6 OH molec./cm^3 range was estimated for the package at 28 m/s. Upon loss of the magnetic high-field seeking component, this value is reduced by a factor 2.

To counteract the severe reduction of the photon collection efficiency caused by installing the cryogenic shields, a LIF collection lens was inserted into the hybrid trap chassis and the diameter of the imaging channel was enlarged. To estimate the signal gain resulting from these measures, an optical ray tracer was developed and the solid angle under which photons are collected was deduced by means of Monte Carlo ray tracing. The solid angle obtained in this way also proved to be useful in the estimation of the density. Due to the low signal levels, the lifetime measurements were conducted over the course of several days to ascertain sufficient statistical certainty. It would be beneficial to change the detection scheme of OH radicals such that a better S/N ratio could be achieved. J. M. Gray et al. [290] have developed a 1+1‘ REMPI scheme for OH, which allows to detect the resulting ions with a TOF mass spectrometer. The experiments described in this chapter were conducted at low signal levels and would benefit significantly from a scheme detecting ions instead of photons, as the background level could be reduced by not having to discriminate against the laser stray light.

Chapter 7

Conclusion and Outlook

The work presented in this thesis describes the journey of hydroxyl radicals from the source to the end of a Stark decelerator and from there right into the depths of a quadrupolar cryogenic magnetic trap.

A pinhole discharge unit as well as a dielectric barrier discharge (DBD) head were successfully developed for the Nijmegen pulsed valve (NPV) [50, 178] and the molecular beam properties accessible from each source were characterised and compared. It was found that the DBD source yields colder OH radicals, whereas the pinhole discharge source provides a threefold larger radical density compared to the DBD discharge head. Consequently, the experiment was fitted with the pinhole discharge source for the deceleration and trapping experiments.

As Stark decelerators do not allow for the compression of phase space, the deceleration to low final velocities and the subsequent trapping of OH radicals would benefit from denser molecular beams with narrower spatial and velocity spreads. While the Nijmegen pulsed valve in combination with the pinhole discharge unit has proven to be a reliable basis for deceleration and trapping experiments, there is still room for improvements. To a certain degree, control over the molecular beam properties can be exercised by adjusting the geometry of the expansion cone. It would be interesting to experimentally investigate the dependence of the molecular beam parameters such as the density, rotational temperature, position and velocity spread on the shape of the expansion channel. Work along these lines is currently under way and I refer to the master thesis of D. Ostermayer[238], who tested a variety of expansion geometries. Alternatively, the density of OH radicals could be enhanced by altering the discharge chemistry via the addition of hydrogen peroxide radical precursors to the water vapour entrained carrier gas. Due to the corrosive nature of H_2O_2, such a procedure cannot be recommended without reproach, however. Furthermore, following ref. [214], expertise in the electrochemical manufacturing of copper skimmers

withstanding cryogenic conditions has been recuperated in collaboration with C. Mangeng. After having completed the first trapping experiments, the source chamber was equipped with a cryostat and a low-temperature skimmer mount to profit from reduced skimmer clogging upon placing the valve closer to the skimmer orifice, in accordance with references [211, 212]. It will be interesting to determine the maximum density with which the decelerator can be loaded after the successful implementation of the above mentioned improvements.

A 124-stage Stark decelerator was successfully set up and conditioned in the Basel labs. The decelerator was characterised and optimised for operation at low final velocities ($v < 40$ m/s). OH densities of $(3.7 \pm 2.7) \cdot 10^6$ part./cm^3 were determined at a velocity of 28 m/s. While molecular beams of OH were routinely slowed down below 30 m/s, the Stark deceleration technique is very versatile and a wide variety of species possessing a sufficiently large first order Stark shift to mass ratio have been decelerated [35]. As the discharge variant of the NPV was successfully employed for the formation of NH from NH_3 [319] and NH displays a magnetic moment, this radical is considered a suitable candidate for widening the chemical scope of the deceleration and trapping experiment.

With the demonstration of cryogenic magnetic trapping of hydroxyl radicals for an extended period of 24 s, a first hurdle towards hybrid trapping of cold molecules and ions has successfully been taken. The investigation of collisions between neutral molecules in a magnetic trap and atomic or molecular ions inside an ion trap has come into reach. In a next step, one would like to start the cryogenic stepper motor with the purpose of dislocating the neutral OH cloud away from the apertures of the cryogenic shield to a darker region of the trap where the BBR radiation intensity is suppressed even further. A significant increase of the trap lifetime is expected by adopting such an OH storing scheme. C. von Planta is pursuing the ongoing research towards characterising and exploiting the full potential offered by the novel hybrid trapping scheme.

While successful trapping was demonstrated, the current hybrid trap design is not without shortcomings. Due to electrostatic breakdown of the trap at stopping potentials above ± 6 kV, the loading efficiency is currently limited to approx. 10 %. Originally, a stopping potential of ± 10 kV was envisaged, which would have yielded loading efficiencies of up to 17 %. Additionally, positioning the hybrid trap centre closer to the decelerator opening by 4 mm would allow for loading efficiencies of around 25 %, given loading is performed at ± 10 kV. To complicate matters even more, the presence of the cryogenic shield imposed a severe impediment on the detection efficiency. The operation of the hybrid trap so far from its original design space in combination with the low LIF detection efficiency resulted

in a constant struggle for signal. In order to determine lifetimes with sufficient statistical certainty, long measurement times of several days were required. A new version of the hybrid trap offering better optical access to the trap centre is currently under development. The new design no longer requires electric fields for stopping and the loading process is based on magnetic compensation of the Zeeman entrance shoulder, similar to the trap design in ref. [283].

The complex electrode structure within the hybrid trap leads to a considerable amount of stray light upon clipping the laser beam. As the stray light photons aggravate the S/N ratio, it is projected to ionise the trapped molecules via a REMPI scheme, mass select the resulting ions within the trap and expel the ion cloud into a short MS TOF tube ending in front of a MCP. The advantage of such a detection scheme is twofold. First, it allows for a virtually background free detection of the trapped OH radicals. Secondly, ionic reaction products within the trap can be identified. A suitable $1 + 1'$ REMPI scheme for OH has been developed by J. M. Gray and co-workers [290] in the context of trap dynamics investigations within an electrostatic trap.

The hybrid trapping scheme for neutral molecules and ionic species described in this thesis represents a versatile environment for investigating ion-neutral reactions in the cold regime, while offering full control over the contributing quantum states. The present setup widens the chemical scope of the hybrid trapping technique [51] and OH + Ca^+, OH + N_2^+ and OH + H_2O^+ are promising reaction systems. The study of ion-molecule reactions is of great interest, as it allows for refining astrochemical models [298–300] and is the key to attaining a better understanding of chemical processes within interstellar clouds [297, 300]. From a mechanistic point of view, reactions between cold molecules and ions are governed by few partial waves. Therefore, these systems are interesting subjects of study for the observation of quantum phenomena such as scattering resonances and the tunnelling through centrifugal barriers [3, 18, 300]. Furthermore, the ion-molecule reactions addressable with the current experimental setup have the potential to serve as benchmark systems for theoretical models.

Bibliography

[1] L. D. Carr, D. DeMille, R. V. Krems and J. Ye, *New J. Phys.*, 2009, **11**, 055049.

[2] B. Friedrich and J. M. Doyle, *Chem. Phys. Chem.*, 2009, **10**, 604–623.

[3] M. T. Bell and T. P. Softley, *Mol. Phys.*, 2009, **107**, 99–132.

[4] M. Schnell and G. Meijer, *Angew. Chem. Int. Ed.*, 2009, **48**, 6010–6031.

[5] T. E. Wall, *J. Phys. B*, 2016, **49**, 243001.

[6] S. Willitsch, M. T. Bell, A. D. Gingell and T. P. Softley, *Phys. Chem. Chem. Phys.*, 2008, **10**, 7200.

[7] A. Härter and J. Hecker Denschlag, *Contemp. Phys.*, 2014, **55**, 33–45.

[8] W. D. Phillips, *Rev. Mod. Phys.*, 1998, **70**, 21.

[9] C. J. Foot, *Atomic Physics*, Oxford University Press, New York, 2005.

[10] E. Herbst, *Chem. Soc. Rev.*, 2001, **30**, 168–176.

[11] S. Borri and G. Santambrogio, *Adv. Phys. X*, 2016, **1**, 368–386.

[12] H. L. Bethlem, M. Kajita, B. Sartakov, G. Meijer and W. Ubachs, *Eur. Phys. J. Spec. Top.*, 2008, **163**, 55–69.

[13] S. Chefdeville, Y. Kalugina, S. Y. T. van de Meerakker, C. Naulin, F. Lique and M. Costes, *Science*, 2013, **341**, 1094–1096.

[14] A. von Zastrow, J. Onvlee, S. N. Vogels, G. C. Groenenboom, A. van der Avoird and S. Y. T. van de Meerakker, *Nat. Chem.*, 2014, **6**, 216–221.

[15] S. N. Vogels, T. Karman, J. Kłos, M. Besemer, J. Onvlee, A. van der Avoird, G. C. Groenenboom and S. Y. T. van de Meerakker, *Nat. Chem.*, 2018, **10**, 435–440.

[16] D. DeMille, *Phys. Rev. Lett.*, 2002, **88**, 067901.

[17] S. F. Yelin, K. Kirby and R. Côté, *Phys. Rev. A*, 2006, **74**, 050301(R).

[18] *Tutorials in Molecular Reaction Dynamics*, ed. M. Brouard and C. Vallance, RSC Publishing, Cambridge, 2011.

[19] R. V. Krems, *Phys. Chem. Chem. Phys.*, 2008, **10**, 4079.

[20] Y.-P. Chang, K. Długołęcki, J. Küpper, D. Rösch, D. Wild and S. Willitsch, *Science*, 2013, **342**, 98–101.

[21] Y.-P. Chang, D. A. Horke, S. Trippel and J. Küpper, *Int. Rev. Phys. Chem.*, 2015, **34**, 557–590.

[22] T. Amano, *J. Mol. Spectrosc.*, 1984, **103**, 436–454.

[23] M. R. Tarbutt, *Contemp. Phys.*, 2018, **59**, 356–376.

[24] J. F. Barry, D. J. McCarron, E. B. Norrgard, M. H. Steinecker and D. DeMille, *Nature*, 2014, **512**, 286–289.

[25] S. Truppe, H. J. Williams, M. Hambach, L. Caldwell, N. J. Fitch, E. A. Hinds, B. E. Sauer and M. R. Tarbutt, *Nat. Phys.*, 2017, **13**, 1173.

[26] K.-K. Ni, S. Ospelkaus, M. H. G. de Miranda, A. Pe'er, B. Neyenhuis, J. J. Zirbel, S. Kotochigova, P. S. Julienne, D. S. Jin and J. Ye, *Science*, 2008, **322**, 231–235.

[27] M. Viteau, A. Chotia, M. Allegrini, N. Bouloufa, O. Dulieu, D. Comparat and P. Pillet, *Science*, 2008, **321**, 232–234.

[28] B. K. Stuhl, M. T. Hummon, M. Yeo, G. Quéméner, J. L. Bohn and J. Ye, *Nature*, 2012, **492**, 396–400.

[29] M. Zeppenfeld, B. G. U. Englert, R. Glöckner, A. Prehn, M. Mielenz, C. Sommer, L. D. van Buuren, M. Motsch and G. Rempe, *Nature*, 2012, **491**, 570–573.

[30] A. Prehn, M. Ibrügger, R. Glöckner, G. Rempe and M. Zeppenfeld, *Phys. Rev. Lett.*, 2016, **116**, 063005.

[31] J. D. Weinstein, T. Guillet, B. Friedrich and J. M. Doyle, *Nature*, 1998, **395**, 3.

[32] N. R. Hutzler, H.-I. Lu and J. M. Doyle, *Chem. Rev.*, 2012, **112**, 4803–4827.

[33] R. deCarvalho, J. M. Doyle, B. Friedrich, T. Guillet, J. Kim, D. Patterson and J. D. Weinstein, *Eur Phys J D*, 1999, **7**, 289.

[34] H. L. Bethlem, G. Berden and G. Meijer, *Phys. Rev. Lett.*, 1999, **83**, 1558.

[35] S. Y. T. van de Meerakker, H. L. Bethlem, N. Vanhaecke and G. Meijer, *Chem. Rev.*, 2012, **112**, 4828–4878.

[36] R. Fulton, A. I. Bishop and P. F. Barker, *Phys. Rev. Lett.*, 2004, **93**, 243004.

[37] G. Dong, W. Lu and P. F. Barker, *Phys. Rev. A*, 2004, **69**, 013409.

[38] N. Vanhaecke, U. Meier, M. Andrist, B. H. Meier and F. Merkt, *Phys. Rev. A*, 2007, **75**, 031402.

[39] E. Narevicius, C. G. Parthey, A. Libson, J. Narevicius, I. Chavez, U. Even and M. G. Raizen, *New J. Phys.*, 2007, **9**, 358–358.

[40] T. Cremers, S. Chefdeville, N. Janssen, E. Sweers, S. Koot, P. Claus and S. Y. T. van de Meerakker, *Phys. Rev. A*, 2017, **95**, 043415.

[41] M. Gupta and D. Herschbach, *J. Phys. Chem. A*, 2001, **105**, 1626–1637.

[42] M. Strebel, F. Stienkemeier and M. Mudrich, *Phys. Rev. A*, 2010, **81**, 033409.

[43] L. Sheffield, M. S. Hickey, V. Krasovitskiy, K. D. D. Rathnayaka, I. F. Lyuksyutov and D. R. Herschbach, *Rev. Sci. Instrum.*, 2012, **83**, 064102.

[44] S. Chervenkov, X. Wu, J. Bayerl, A. Rohlfes, T. Gantner, M. Zeppenfeld and G. Rempe, *Phys. Rev. Lett.*, 2014, **112**, 013001.

[45] X. Wu, T. Gantner, M. Koller, M. Zeppenfeld, S. Chervenkov and G. Rempe, *Science*, 2017, **358**, 645–648.

[46] E. Narevicius, A. Libson, M. F. Riedel, C. G. Parthey, I. Chavez, U. Even and M. G. Raizen, *Phys. Rev. Lett.*, 2007, **98**, 103201.

[47] S. A. Rangwala, T. Junglen, T. Rieger, P. W. H. Pinkse and G. Rempe, *Phys. Rev. A*, 2003, **67**, 043406.

[48] S. Y. T. van de Meerakker, R. T. Jongma, H. L. Bethlem and G. Meijer, *Phys. Rev. A*, 2001, **64**, 041401(R).

[49] J. Riedel, S. Hoekstra, W. Jäger, J. J. Gilijamse, S. Y. T. van de Meerakker and G. Meijer, *Eur. Phys. J. D*, 2011, **65**, 161–166.

[50] B. Yan, P. F. H. Claus, B. G. M. van Oorschot, L. Gerritsen, A. T. J. B. Eppink, S. Y. T. van de Meerakker and D. H. Parker, *Rev. Sci. Instrum.*, 2013, **84**, 023102.

[51] P. Eberle, A. D. Dörfler, C. von Planta, K. Ravi, D. Haas, D. Zhang, S. Y. T. van de Meerakker and S. Willitsch, *J. Phys. Conf. Ser.*, 2015, **635**, 012012.

[52] K. Maeda, M. L. Wall and L. D. Carr, *New J. Phys.*, 2015, **17**, 045014.

[53] P. F. Bernath, *Spectra of Atoms and Molecules*, Oxford University Press, Oxford, 2nd edn., 2005.

[54] B. C. Sawyer, B. L. Lev, E. R. Hudson, B. K. Stuhl, M. Lara, J. L. Bohn and J. Ye, *Phys. Rev. Lett.*, 2007, **98**, 253002.

[55] J. J. Gilijamse, S. Hoekstra, N. Vanhaecke, S. Y. T. van de Meerakker and G. Meijer, *Eur. Phys. J. D*, 2010, **57**, 33–41.

[56] J. Brown and A. Carrington, *Rotational Spectroscopy of Diatomic Molecules*, Cambridge University Press, Cambridge, 2003.

[57] S. Willitsch, *Physikalische Chemie IV*, 2016.

[58] K. P. Huber and G. Herzberg, in *NIST Chemistry WebBook, NIST Standard Reference Database Number 69*, ed. P. J. Linstrom and W. Mallard, National Institute of Standards and Technology, Gaithersburg, 2019.

[59] P. Atkins and R. Friedman, *Molecular Quantum Mechanics*, Oxford University Press, 3rd edn., 1997.

[60] R. N. Zare, *Angular Momentum*, Wiley, 1st edn., 1988.

[61] S. Y. T. van de Meerakker, *Ph.D. thesis*, Radboud Universiteit, Nijmegen, 2006.

[62] M. Lara, B. L. Lev and J. L. Bohn, *Phys. Rev. A*, 2008, **78**, 033433.

[63] M. Gärttner, J. J. Omiste, P. Schmelcher and R. González-Férez, *Mol. Phys.*, 2013, **111**, 1865–1878.

[64] T. D. Hain, M. A. Weibel, K. M. Backstrand and T. J. Curtiss, *J. Phys. Chem. A*, 1997, **101**, 7674.

[65] W. L. Meerts, *Chem. Phys. Lett.*, 1977, **46**, 24.

[66] H. Lefebvre-Brion and R. W. Field, *The Spectra and Dynamics of Diatomic Moleulces*, Elsevier, San Diego, 2004.

[67] B. H. Bransden and C. J. Joachain, *Physics of Atoms and Molecules*, Pearson Education Ltd., Harlow, 2nd edn., 2003.

[68] J. J. Ter Meulen, W. Majewski, W. L. Meerts and A. Dymanus, *Chem. Phys. Lett.*, 1983, **94**, 4.

[69] G. H. Dieke and H. M. Crosswhite, *J. Quant. Spectrosc. Radiat. Transfer*, 1962, **2**, 97–199.

[70] H. L. Bethlem and G. Meijer, *Int. Rev. Phys. Chem.*, 2003, **22**, 73–128.

[71] S. E. Choi and R. B. Bernstein, *J. Chem. Phys.*, 1986, **85**, 150–161.

[72] T. D. Hain, R. M. Moision and T. J. Curtiss, *J. Chem. Phys.*, 1999, **111**, 6797.

[73] H. L. Bethlem, G. Berden, F. M. H. Crompvoets, R. T. Jongma, A. J. A. van Roij and G. Meijer, *Nature*, 2000, **406**, 491–494.

[74] S. Y. T. van de Meerakker, P. H. M. Smeets, N. Vanhaecke, R. T. Jongma and G. Meijer, *Phys. Rev. Lett.*, 2005, **94**, 023004.

[75] H. L. Bethlem, F. M. H. Crompvoets, R. T. Jongma, S. Y. T. van de Meerakker and G. Meijer, *Phys. Rev. A*, 2002, **65**, 053416.

[76] S. Y. T. van de Meerakker, N. Vanhaecke, H. L. Bethlem and G. Meijer, *Phys. Rev. A*, 2005, **71**, 053409.

[77] S. Y. T. van de Meerakker, N. Vanhaecke, H. L. Bethlem and G. Meijer, *Phys. Rev. A*, 2006, **73**, 023401.

[78] E. R. Hudson, J. R. Bochinski, H. J. Lewandowski, B. C. Sawyer and J. Ye, *Eur. Phys. J. D*, 2004, **31**, 351–358.

[79] J. J. Gilijamse, J. Küpper, S. Hoekstra, N. Vanhaecke, S. Y. T. van de Meerakker and G. Meijer, *Phys. Rev. A*, 2006, **73**, 063410.

[80] B. C. Sawyer, B. K. Stuhl, B. L. Lev, J. Ye and E. R. Hudson, *Eur. Phys. J. D*, 2008, **48**, 197–209.

[81] S. N. Vogels, Z. Gao and S. Y. T. van de Meerakker, *EPJ Tech. Instrum.*, 2015, **2**, 12.

[82] D. Zhang, G. Meijer and N. Vanhaecke, *Phys. Rev. A*, 2016, **93**, 023408.

[83] B. Friedrich, *Eur. Phys. J. D*, 2004, **31**, 313–336.

[84] K. Gubbels, G. Meijer and B. Friedrich, *Phys. Rev. A*, 2006, **73**, 063406.

[85] L. Scharfenberg, H. Haak, G. Meijer and S. Y. T. van de Meerakker, *Phys. Rev. A*, 2009, **79**, 023410.

[86] S. Y. van de Meerakker, N. Vanhaecke and G. Meijer, *Annu. Rev. Phys. Chem.*, 2006, **57**, 159–190.

[87] S. D. Hogan, M. Motsch and F. Merkt, *Phys. Chem. Chem. Phys.*, 2011, **13**, 18705.

[88] B. C. Sawyer, B. K. Stuhl, D. Wang, M. Yeo and J. Ye, *Phys. Rev. Lett.*, 2008, **101**, 203203.

[89] D. P. Engelhart, F. Grätz, R. J. V. Wagner, H. Haak, G. Meijer, A. M. Wodtke and T. Schäfer, *Rev. Sci. Instrum.*, 2015, **86**, 043306.

[90] C. Cheng, A. P. P. van der Poel, P. Jansen, M. Quintero-Pérez, T. E. Wall, W. Ubachs and H. L. Bethlem, *Phys. Rev. Lett.*, 2016, **117**, 253201.

[91] L. Scharfenberg, K. B. Gubbels, M. Kirste, G. C. Groenenboom, A. van der Avoird, G. Meijer and S. Y. T. van de Meerakker, *Eur. Phys. J. D*, 2011, **65**, 189–198.

[92] M. Kirste, X. Wang, H. C. Schewe, G. Meijer, K. Liu, A. van der Avoird, L. M. C. Janssen, K. B. Gubbels, G. C. Groenenboom and S. Y. T. van de Meerakker, *Science*, 2012, **338**, 1060–1063.

[93] S. N. Vogels, J. Onvlee, S. Chefdeville, A. van der Avoird, G. C. Groenenboom and S. Y. T. van de Meerakker, *Science*, 2015, **350**, 787–790.

[94] A. Marian, H. Haak, P. Geng and G. Meijer, *Eur. Phys. J. D*, 2010, **59**, 179–181.

[95] S. A. Meek, H. Conrad and G. Meijer, *Science*, 2009, **324**, 1699–1702.

[96] G. Santambrogio, *EPJ Tech. Instrum.*, 2015, **2**, 14.

[97] K. Wohlfart, F. Filsinger, F. Grätz, J. Küpper and G. Meijer, *Phys. Rev. A*, 2008, **78**, 033421.

[98] A. Osterwalder, S. A. Meek, G. Hammer, H. Haak and G. Meijer, *Phys. Rev. A*, 2010, **81**, 051401.

[99] P. Jansen, M. Quintero-Pérez, T. E. Wall, J. E. van den Berg, S. Hoekstra and H. L. Bethlem, *Phys. Rev. A*, 2013, **88**, 043424.

[100] M. Quintero-Pérez, P. Jansen, T. E. Wall, J. E. van den Berg, S. Hoekstra and H. L. Bethlem, *Phys. Rev. Lett.*, 2013, **110**, 133003.

[101] M. Quintero-Pérez, T. E. Wall, S. Hoekstra and H. L. Bethlem, *J. Mol. Spectrosc.*, 2014, **300**, 112–115.

[102] D. Haas, S. Scherb, D. Zhang and S. Willitsch, *EPJ Tech. Instrum.*, 2017, **4**, 6.

[103] T. C. Briles, *Ph.D. thesis*, University of Colorado, Colorado, 2015.

[104] W. Greiner, *Classical Mechanics: Systems of Particles and Hamiltonian Dynamics*, Springer, Heidelberg, 2nd edn., 2010.

[105] H. J. Metcalf and P. van der Straten, *Laser Cooling and Trapping*, Springer, New York, 1999.

[106] M. Cross, *Collective Effects in Equilibrium and Nonequilibrium Physics*, http://www.cmp.caltech.edu/~mcc/BNU/#SR2, 2008.

[107] A. Feldmeier, *Theoretische Mechanik*, Springer Spektrum, Berlin, 2013.

[108] W. Ketterle and D. E. Pritchard, *Phys. Rev. A*, 1992, **46**, 4051–4054.

[109] G. Sanna and G. Tomassetti, *Introduction to Molecular Beams Gas Dynamics*, Imperial College Press, London, 2005.

[110] S. Humphries, *Principles of Charged Particle Acceleration*, J. Wiley, New York, 1986.

[111] L. Scharfenberg, *Ph.D. thesis*, Technische Universität Berlin, Berlin, 2012.

[112] H. L. Bethlem, *Ph.D. thesis*, Katholieke Universiteit Nijmegen, Nijmegen, 2002.

[113] M. Abramson, C. Audet, G. Couture, J. Dennis, Jr., S. Le Digabel and C. Tribes, *The NOMAD Project*, Software available at https://www.gerad.ca/nomad/.

[114] D. A. Dahl, *SIMION 3D*, Idaho National Engineering Laboratory, Idaho Falls, rev. 4 edn. edn., 1995.

[115] C. E. Heiner, H. L. Bethlem and G. Meijer, *Phys. Chem. Chem. Phys.*, 2006, **8**, 2666.

[116] L. Dunoyer, *C. r.*, 1911, **152**, 92.

[117] O. Stern, *Z. Phys.*, 1920, **2**, 49–56.

[118] O. Stern, *Z. Phys.*, 1920, **3**, 417.

[119] W. Gerlach and O. Stern, *Z. Phys.*, 1922, **9**, 349.

[120] I. I. Rabi, J. R. Zacharias, S. Millman and P. Kusch, *Phys. Rev.*, 1938, **53**, 318–318.

[121] J. P. Gordon, H. J. Zeiger and C. H. Townes, *Phys. Rev.*, 1954, **95**, 282–284.

[122] A. Kantrowitz and J. Grey, *Rev. Sci. Instrum.*, 1951, **22**, 328.

[123] H. Pauly, *Atom, Molecule, and Cluster Beams I*, Springer, Berlin, 2000.

[124] R. Campargue, *Atomic and Molecular Beams*, Springer, Berlin, 2001.

[125] D. H. Levy, *Annu. Rev. Phys. Chem.*, 1980, **31**, 197–225.

[126] P. Casavecchia, *Rep. Prog. Phys.*, 2000, **63**, 355–414.

[127] K. Liu, *Annu. Rev. Phys. Chem.*, 2001, **52**, 139–164.

[128] A. Osterwalder, *EPJ Tech. Instrum.*, 2015, **2**, 10.

[129] R. Campargue, *J. Phys. Chem.*, 1984, **88**, 4466–4474.

[130] B. R. Rowe, G. Dupeyrat, J. B. Marquette and P. Gaucherel, *J. Chem. Phys.*, 1984, **80**, 4915–4921.

[131] M. D. Morse, *Exp. Methods Phys. Sci.*, 1996, **29 B**, 21.

[132] W. R. Gentry and C. F. Giese, *Rev. Sci. Instrum.*, 1978, **49**, 7.

[133] R. M. Jordan, *Jordan Valve*, http://www.rmjordan.com/c211-451.html, 2018.

[134] D. Irimia, D. Dobrikov, R. Kortekaas, H. Voet, D. A. van den Ende, W. A. Groen and M. H. M. Janssen, *Rev. Sci. Instrum.*, 2009, **80**, 113303.

[135] M. Janssen, *Amsterdam Piezo Valve*, http://www.amsterdampiezovalve.com/, 2018.

[136] D. Gerlich, G. Jerke, U. Person and U. Mück, *Fast Pulsed Piezo Valve*, https://www.tu-chemnitz.de/physik/ION/Technology/Piezo_Valve/index.html, 2018.

[137] U. Even, J. Jortner, D. Noy, N. Lavie and C. Cossart-Magos, *J. Chem. Phys.*, 2000, **112**, 8068.

[138] U. Even, *Adv. Chem.*, 2014, **2014**, 1–11.

[139] Parker, *General Valve Series 9*, http://ph.parker.com/us/12051/en/pulse-valves-miniature-high-speed-high-vacuum-dispense-valve, 2018.

[140] D. Pentlehner, R. Riechers, B. Dick, A. Slenczka, U. Even, N. Lavie, R. Brown and K. Luria, *Rev. Sci. Instrum.*, 2009, **80**, 043302.

[141] R. L. Byer and M. D. Duncan, *J. Chem. Phys.*, 1981, **74**, 2174–2179.

[142] T. Müller and P. H. Vaccaro, *Rev. Sci. Instrum.*, 1998, **69**, 406–411.

[143] M. D. Barry, N. P. Johnsong and P. A. Gorry, *J. Phys. E Sci. Instrum.*, 1986, **19**, 815.

[144] J. B. Cross and J. J. Valentini, *Rev. Sci. Instrum.*, 1982, **53**, 6.

[145] P. Andresen, M. Faubel, D. Haeusler, G. Kraft, H.-W. Luelf and J. G. Skofronick, *Rev. Sci. Instrum.*, 1985, **56**, 2038–2042.

[146] D. Proch and T. Trickl, *Rev. Sci. Instrum.*, 1989, **60**, 713–716.

[147] C. Abeysekera, B. Joalland, Y. Shi, A. Kamasah, J. M. Oldham and A. G. Suits, *Rev. Sci. Instrum.*, 2014, **85**, 116107.

[148] M. R. Adriaenst, W. Allison and B. Feuerbachert, *J. Phys. E Sci. Instrum.*, 1981, **14**, 1375.

[149] T. E. Adams, B. H. Rockney, R. J. S. Morrison and E. R. Grant, *Rev. Sci. Instrum.*, 1981, **52**, 5.

[150] C. Köster, J. Grotemeyer and E. W. Schlag, *Z. Naturforsch. A*, 1990, **45**, 1285.

[151] Y. Huang and M. Sulkes, *Rev. Sci. Instrum.*, 1994, **65**, 3868–3869.

[152] L. Abad, D. Bermejo, V. J. Herrero, J. Santos and I. Tanarro, *Rev. Sci. Instrum.*, 1995, **66**, 3826–3832.

[153] M. N. Slipchenko, S. Kuma, T. Momose and A. F. Vilesov, *Rev. Sci. Instrum.*, 2002, **73**, 3600–3605.

[154] W. Christen, *J. Chem. Phys.*, 2013, **139**, 154202.

[155] J. M. Hayes, *Chem. Rev.*, 1987, **87**, 745–760.

[156] K. L. Saenger, *J. Chem. Phys.*, 1981, **75**, 2467–2469.

[157] K. L. Saenger and J. B. Fenn, *J. Chem. Phys.*, 1983, **79**, 6043–6045.

[158] R. W. Gentry, in *Atomic and Molecular Beam Methods*, ed. G. Scoles, D. Bassi, U. Buck and D. Lainé, Oxford University Press, Oxford, 1988, vol. 1, pp. 54–82.

[159] H. R. Murphy and D. R. Miller, *J. Phys. Chem.*, 1984, **88**, 4474–4478.

[160] J. C. Whitehead, *Rep. Prog. Phys.*, 1996, **59**, 993.

[161] I.-C. Lu, W.-J. Huang, C. Chaudhuri, W.-K. Chen and S.-H. Lee, *Rev. Sci. Instrum.*, 2007, **78**, 083103.

[162] K. Luria, N. Lavie and U. Even, *Rev. Sci. Instrum.*, 2009, **80**, 104102.

[163] K. Liu, G. Macdonald and A. F. Wagner, *Int. Rev. Phys. Chem.*, 1990, **9**, 187.

[164] P. C. Engelking, *Chem. Rev.*, 1991, **91**, 399–414.

[165] P. Andresen, N. Aristov, V. Beushausen, D. Häusler and H. W. Lülf, *J. Chem. Phys.*, 1991, **95**, 5763–5774.

[166] J. W. Farthing, I. W. Fletcher and J. C. Whitehead, *J. Phys. Chem.*, 1983, **87**, 1663–1665.

[167] J. J. ter Meulen, W. L. Meerts, G. W. M. van Mierlo and A. Dymanus, *Phys. Rev. Lett.*, 1976, **36**, 1031.

[168] J. J. ter Meulen and M. C. van Beek, *Chem. Phys. Lett.*, 2001, **337**, 237.

[169] K. Ikejiri, H. Ohoyama, Y. Nagamachi, T. Teramoto and T. Kasai, *Chem. Phys. Lett.*, 2003, **379**, 255–260.

[170] H. Lewandowski, E. R. Hudson, J. Bochinski and J. Ye, *Chem. Phys. Lett.*, 2004, **395**, 53–57.

[171] E. A. Rohlfing, *J. Chem. Phys.*, 1988, **89**, 6103–6112.

[172] P. Chen, S. D. Colson, W. A. Chupka and J. A. Berson, *J. Phys. Chem.*, 1986, **90**, 2319–2321.

[173] J. R. Dunlop, J. Karolczak and D. J. Clouthier, *Chem. Phys. Lett.*, 1988, **151**, 362–368.

[174] S. K. Bramble and P. A. Hamilton, *Chem. Phys. Lett.*, 1990, **170**, 107.

[175] D. T. Anderson, S. Davis, T. S. Zwier and D. J. Nesbitt, *Chem. Phys. Lett.*, 1996, **258**, 207.

[176] S. Davis, D. T. Anderson, G. Duxbury and D. J. Nesbitt, *J. Chem. Phys.*, 1997, **107**, 5661.

[177] Z. Ren, M. Qiu, L. Che, D. Dai, X. Wang and X. Yang, *Rev. Sci. Instrum.*, 2006, **77**, 016102.

[178] L. Ploenes, D. Haas, D. Zhang, S. Y. T. van de Meerakker and S. Willitsch, *Rev. Sci. Instrum.*, 2016, **87**, 053305.

[179] J. Grzesiak, M. Vashishta, P. Djuricanin, F. Stienkemeier, M. Mudrich, K. Dulitz and T. Momose, *Rev. Sci. Instrum.*, 2018, 7.

[180] A. T. Droege and P. C. Engelking, *Chem. Phys. Lett.*, 1983, **96**, 316–318.

[181] P. C. Engelking, *Rev. Sci. Instrum.*, 1986, **57**, 2274–2277.

[182] T. D. Hain, M. A. Weibel, K. M. Backstrand, P. E. Pope and T. J. Curtiss, *Chem. Phys. Lett.*, 1996, **262**, 723–728.

[183] M. J. Verheijen, H. C. W. Beijerinck, L. H. A. M. van Moll, J. Driessen and N. F. Verster, *J. Phys. E Sci. Instrum.*, 1984, **17**, 904–910.

[184] S. J. Sibener, R. J. Buss, C. Y. Ng and Y. T. Lee, *Rev. Sci. Instrum.*, 1980, **51**, 167–182.

[185] M. Alagia, N. Balucani, P. Casavecchia, D. Stranges and G. G. Volpi, *J. Chem. Phys.*, 1993, **98**, 2459–2462.

[186] A. Bogaerts, E. Neyts, R. Gijbels and J. van der Mullen, *Spectrochim. Acta B*, 2002, **57**, 609–658.

[187] U. Kogelschatz, B. Eliasson and W. Egli, *J. Phys. IV*, 1997, **7 (C4)**, 47–66.

[188] U. Kogelschatz, *Plasma Chem. Plasma P.*, 2003, **23**, 1.

[189] J. B. Anderson, R. P. Andres and J. B. Fenn, in *Molecular Beams*, ed. I. Prigogine and J. Ross, J. Wiley, New York, 1966, vol. 10 of Advances in Chemical Physics, p. 275.

[190] S. Y. T. van de Meerakker, H. L. Bethlem and G. Meijer, *Nat. Phys.*, 2008, **4**, 595–602.

[191] C. Vallance, *Molecular Reaction Dynamics, Lecutre 1-4*, http://vallance.chem.ox.ac.uk/CVteaching.html, 2018.

[192] D. R. Miller, in *Atomic and Molecular Beam Methods*, ed. G. Scoles, D. Bassi, U. Buck and D. Lainé, Oxford University Press, Oxford, 1988, vol. 1, pp. 18–53.

[193] W. Demtröder, *Laser Spectroscopy Vol. 2 Experimental Techniques*, Springer, Berlin, Heidelberg, 4th edn., 2008.

[194] W. Christen and K. Rademann, *Phys. Rev. A*, 2008, **77**, 012702.

[195] H. Murphy and D. Miller, in *Proc. 14th Intl. Symp. on Rarefied Gas Dynamics (RGD)*, ed. H. Oguchi, Tokyo University Press, 1984, vol. 2, p. 743.

[196] H. Z. Ashkenas and F. S. Sherman, in *Proc. 4th Intl. Symp. on Rarefied Gas Dynamics (RGD)*, ed. J. H. De Leeuw, Academic press, 1966, vol. 2, p. 84.

[197] O. F. Hagena and W. Obert, *J. Chem. Phys.*, 1972, **56**, 1793–1802.

[198] J. T. McDaniels, R. E. Continetti and D. R. Miller, AIP Conference Proceedings, Whistler, British Columia (Canada), 2003, pp. 670–677.

[199] F. Dorchies, F. Blasco, T. Caillaud, J. Stevefelt, C. Stenz, A. S. Boldarev and V. A. Gasilov, *Phys. Rev. A*, 2003, **68**, 023201.

[200] S. Semushin and V. Malka, *Rev. Sci. Instrum.*, 2001, **72**, 2961–2965.

[201] C. T. Dewberry, R. B. Mackenzie, S. Green and K. R. Leopold, *Rev. Sci. Instrum.*, 2015, **86**, 065107.

[202] K. Luria, W. Christen and U. Even, *J. Phys. Chem. A*, 2011, **115**, 7362–7367.

[203] U. Even, *EPJ Tech. Instrum.*, 2015, **2**, 17.

[204] G. A. Bird, *The DSMC Method*, CreateSpace Independent Publishing Platform, 1st edn., 2013.

[205] G. A. Bird, *DSMC Resources from Graeme Bird*, http://gab.com.au/, 2013.

[206] R. T. Jongma, T. Rasing and G. Meijer, *J. Chem. Phys.*, 1995, **102**, 1925–1933.

[207] H. Pauly, *Atom, Molecule, and Cluster Beams II*, Springer, Berlin, 2000.

[208] R. J. Gallagher and J. B. Fenn, *J. Chem. Phys.*, 1974, **60**, 3487–3491.

[209] M. R. Tarbutt, J. J. Hudson, B. E. Sauer, E. A. Hinds, V. A. Ryzhov, V. L. Ryabov and V. F. Ezhov, *J. Phys. B At. Mol. Opt. Phys.*, 2002, **35**, 5013.

[210] D. Yuan, S. Yu, W. Chen, J. Sang, C. Luo, T. Wang, X. Xu, P. Casavecchia, X. Wang, Z. Sun, D. H. Zhang and X. Yang, *Nat. Chem.*, 2018, **10**, 653–658.

[211] H. Wu, D. Reens, T. Langen, Y. Shagam, D. Fontecha and J. Ye, *Phys. Chem. Chem. Phys.*, 2018, **20**, 11615–11621.

[212] Y. Segev, N. Bibelnik, N. Akerman, Y. Shagam, A. Luski, M. Karpov, J. Narevicius and E. Narevicius, *Sci. Adv.*, 2017, **3**, e1602258.

[213] G. A. Bird, *Phys. Fluids*, 1976, **19**, 1486.

[214] W. R. Gentry and C. F. Giese, *Rev. Sci. Instrum.*, 1975, **46**, 104–104.

[215] *Beam Dynamics Inc.*, http://www.beamdynamicsinc.com/, 2018.

[216] G. A. Bird, *Molecular Gas Dynamics and the Direct Simulation of Gas Flows*, Oxford University Press, Oxford, 2nd edn., 1994.

[217] J. Braun, P. K. Day, J. P. Toennies, G. Witte and E. Neher, *Rev. Sci. Instrum.*, 1997, **68**, 3001–3009.

[218] K. Teshima and Y. Yasunaga, *Jpn. J. Appl. Phys.*, 1983, **22**, 1.

[219] C. W. Bauschlicher and S. R. Langhoff, *J. Chem. Phys.*, 1987, **87**, 4665.

[220] D. R. Yarkony, *J. Chem. Phys.*, 1992, **97**, 1838.

[221] M. Kirste, *Ph.D. thesis*, Freie Universität Berlin, 2012.

[222] A. Mizouri, L. Z. Deng, J. S. Eardley, N. H. Nahler, E. Wrede and D. Carty, *Phys. Chem. Chem. Phys.*, 2013, **15**, 19575.

[223] R. Altkorn and R. N. Zare, *Annu. Rev. Phys. Chem.*, 1984, **35**, 265–289.

[224] S. E. Sanders, O. R. Willis, N. H. Nahler and E. Wrede, *arXiv:1308.1989 [physics]*, 2013.

[225] J. M. Hossenlopp, D. T. Anderson, M. W. Todd and M. I. Lester, *J. Chem. Phys.*, 1998, **109**, 10707–10718.

[226] D. R. Guyer, L. Hüwel and S. R. Leone, *J. Chem. Phys.*, 1983, **79**, 1259–1271.

[227] N. S. J. Braithwaite, *Plasma Sources Sci. Technol.*, 2000, **9**, 517–527.

[228] A. A. Fridman, *Plasma Chemistry*, Cambridge University Press, Cambridge, 1st edn., 2012.

[229] C. Tendero, C. Tixier, P. Tristant, J. Desmaison and P. Leprince, *Spectrochim. Acta B*, 2006, **61**, 2–30.

[230] M. J. Druyvesteyn and F. M. Penning, *Rev. Mod. Phys.*, 1940, **12**, 87–174.

[231] C. F. Gallo, *IEEE Trans. Ind. Appl.*, 1975, **IA-11**, 739–748.

[232] Y. P. Raizer, *Gas Discharge Physics*, Springer, Berlin, 1991.

[233] Y. Itikawa and N. Mason, *J. Phys. Chem. Ref. Data*, 2005, **34**, 1–22.

[234] J. McConkey, C. Malone, P. Johnson, C. Winstead, V. McKoy and I. Kanik, *Phys. Rep.*, 2008, **466**, 1–103.

[235] T. Harb, W. Kedzierski and J. W. McConkey, *J. Chem. Phys.*, 2001, **115**, 5507–5512.

[236] P. Bruggeman and D. C. Schram, *Plasma Sources Sci. Technol.*, 2010, **19**, 045025.

[237] *COMSOL Multiphysics Version 3.5a and 4.3a*, www.comsol.com.

[238] D. Ostermayer, *Sources of Cold Hydroxyl Radicals*, University of Basel, Basel, 2018.

[239] R. T. Jongma, *Ph.D. thesis*, Katholieke Universiteit Nijmegen, Nijmegen, 1997.

[240] S. Y. T. van de Meerakker, N. Vanhaecke, M. van der Loo, G. Groenenboom and G. Meijer, *Phys. Rev. Lett.*, 2005, **95**, 013003.

[241] K. Dulitz, A. Tauschinsky and T. P. Softley, *New J. Phys.*, 2015, **17**, 035005.

[242] J. Luque and D. R. Crosley, *LIFBASE*, SRI Technical Report 99, 1999.

[243] M. Brouard, D. H. Parker and S. Y. T. van de Meerakker, *Chem. Soc. Rev.*, 2014, **43**, 7279–7294.

[244] W. Siemens, *Ann. Phys. Chem.*, 1857, **178**, 66–122.

[245] H.-E. Wagner, R. Brandenburg, K. Kozlov, A. Sonnenfeld, P. Michel and J. Behnke, *Vacuum*, 2003, **71**, 417–436.

[246] R. Brandenburg, *Plasma Sources Sci. Technol.*, 2017, **26**, 053001.

[247] I. Radu, R. Bartnikas, G. Czeremuszkin and M. Wertheimer, *IEEE Trans. Plasma Sci.*, 2003, **31**, 411–421.

[248] Z. Falkenstein, *J. Appl. Phys.*, 1997, **81**, 7158–7162.

[249] R. Sankaranarayanan, B. Pashaie and S. K. Dhali, *Appl. Phys. Lett.*, 2000, **77**, 2970.

[250] K. McKay, D. X. Liu, M. Z. Rong, F. Iza and M. G. Kong, *J. Phys. Appl. Phys.*, 2012, **45**, 172001.

[251] B. Eliasson and U. Kogelschatz, *J. Phys. B*, 1986, **19**, 1241–1247.

[252] E. Flaxer, 2012 IEEE 27th Convention of Electrical and Electronics Engineers in Israel, Eilat, Israel, 2012, p. 1.

[253] J. Jankunas and A. Osterwalder, *Annu. Rev. Phys. Chem.*, 2015, **66**, 241–262.

[254] J. van Veldhoven, J. Küpper, H. L. Bethlem, B. Sartakov, A. J. A. van Roij and G. Meijer, *Eur. Phys. J. D*, 2004, **31**, 337–349.

[255] E. R. Hudson, H. J. Lewandowski, B. C. Sawyer and J. Ye, *Phys. Rev. Lett.*, 2006, **96**, 143004.

[256] B. L. Lev, E. R. Meyer, E. R. Hudson, B. C. Sawyer, J. L. Bohn and J. Ye, *Phys. Rev. A*, 2006, **74**, 061402.

[257] J. J. Gilijamse, S. Hoekstra, S. Y. T. van de Meerakker, G. Groenenboom and G. Meijer, *Science*, 2006, **313**, 1617.

[258] L. Scharfenberg, J. Kłos, P. J. Dagdigian, M. H. Alexander, G. Meijer and S. Y. T. van de Meerakker, *Phys. Chem. Chem. Phys.*, 2010, **12**, 10660.

[259] M. Kirste, L. Scharfenberg, J. Kłos, F. Lique, M. H. Alexander, G. Meijer and S. Y. T. van de Meerakker, *Phys. Rev. A*, 2010, **82**, 042717.

[260] S. N. Vogels, J. Onvlee, A. von Zastrow, G. C. Groenenboom, A. van der Avoird and S. Y. T. van de Meerakker, *Phys. Rev. Lett.*, 2014, **113**, 263202.

[261] B. K. Stuhl, M. T. Hummon and J. Ye, *Annu. Rev. Phys. Chem.*, 2014, **65**, 501–518.

[262] J. Onvlee, S. N. Vogels, A. van der Avoird, G. C. Groenenboom and S. Y. T. van de Meerakker, *New J. Phys.*, 2015, **17**, 055019.

[263] A. von Zastrow, J. Onvlee, D. H. Parker and S. Y. T. van de Meerakker, *EPJ Tech. Instrum.*, 2015, **2**, 11.

[264] J. Onvlee, S. D. S. Gordon, S. N. Vogels, T. Auth, T. Karman, B. Nichols, A. van der Avoird, G. C. Groenenboom, M. Brouard and S. Y. T. van de Meerakker, *Nat. Chem.*, 2016, **9**, 226–233.

[265] S. Hoekstra, M. Metsälä, P. C. Zieger, L. Scharfenberg, J. J. Gilijamse, G. Meijer and S. Y. T. van de Meerakker, *Phys. Rev. A*, 2007, **76**, 063408.

[266] J. J. Gilijamse, S. Hoekstra, S. A. Meek, M. Metsälä, S. Y. T. van de Meerakker, G. Meijer and G. C. Groenenboom, *J. Chem. Phys.*, 2007, **127**, 221102.

[267] S. Willitsch, M. T. Bell, A. D. Gingell, S. R. Procter and T. P. Softley, *Phys. Rev. Lett.*, 2008, **100**, 043203.

[268] B. R. Heazlewood and T. P. Softley, *Annu. Rev. Phys. Chem.*, 2015, **66**, 475–495.

[269] *Chemiker-Kalender*, ed. C. Synowietz and K. Schäfer, Springer-Verlag, Berlin, 3rd edn., 1984.

[270] A. West, Z. Lasner, D. DeMille, E. West, C. Panda, J. Doyle, G. Gabrielse, A. Kryskow and C. Mitchell, *arXiv:1607.01389v1 [physics.med-ph]*, 2016.

[271] H. C. Miller, *IEEE Trans. Electr. Insul.*, 1989, **24**, 765–786.

[272] H. C. Miller, *IEEE Trans. Dielectr. Electr. Insul.*, 2015, **22**, 3641–3657.

[273] *301-03-GSM HFB Data Sheet*, Behlke Power Electronics GmbH technical report, 2019.

[274] S. Y. T. van de Meerakker, I. Labazan, S. Hoekstra, J. Küpper and G. Meijer, *J. Phys. B*, 2006, **39**, S1077.

[275] B. C. Sawyer, B. K. Stuhl, M. Yeo, T. V. Tscherbul, M. T. Hummon, Y. Xia, J. Kłos, D. Patterson, J. M. Doyle and J. Ye, *Phys. Chem. Chem. Phys.*, 2011, **13**, 19059.

[276] B. K. Stuhl, M. Yeo, M. T. Hummon and J. Ye, *Mol. Phys.*, 2013, **111**, 1798–1804.

[277] W. C. Campbell, G. C. Groenenboom, H.-I. Lu, E. Tsikata and J. M. Doyle, *Phys. Rev. Lett.*, 2008, **100**, 083003.

[278] S. Hoekstra, J. J. Gilijamse, B. Sartakov, N. Vanhaecke, L. Scharfenberg, S. Y. T. van de Meerakker and G. Meijer, *Phys. Rev. Lett.*, 2007, **98**, 133001.

[279] M. Lemeshko, R. V. Krems, J. M. Doyle and S. Kais, *Mol. Phys.*, 2013, **111**, 1648–1682.

[280] W. H. Wing, *Phys. Rev. Lett.*, 1980, **45**, 631–634.

[281] M. Schnell, P. Lützow, J. van Veldhoven, H. L. Bethlem, J. Küpper, B. Friedrich, M. Schleier-Smith, H. Haak and G. Meijer, *J. Phys. Chem. A*, 2007, **111**, 7411–7419.

[282] H.-I. Lu, I. Kozyryev, B. Hemmerling, J. Piskorski and J. M. Doyle, *Phys. Rev. Lett.*, 2014, **112**, 113006.

[283] N. Akerman, M. Karpov, Y. Segev, N. Bibelnik, J. Narevicius and E. Narevicius, *Phys. Rev. Lett.*, 2017, **119**, 073204.

[284] J. S. Eardley, N. Warner, L. Z. Deng, D. Carty and E. Wrede, *Phys. Chem. Chem. Phys.*, 2017, **19**, 8423–8427.

[285] Y. Liu, M. Vashishta, P. Djuricanin, S. Zhou, W. Zhong, T. Mittertreiner, D. Carty and T. Momose, *Phys. Rev. Lett.*, 2017, **118**, 093201.

[286] E. Tsikata, W. C. Campbell, M. T. Hummon, H.-I. Lu and J. M. Doyle, *New J. Phys.*, 2010, **12**, 065028.

[287] Y. Liu, S. Zhou, W. Zhong, P. Djuricanin and T. Momose, *Phys. Rev. A*, 2015, **91**, 021403(R).

[288] J. G. E. Harris, R. A. Michniak, S. V. Nguyen, W. C. Campbell, D. Egorov, S. E. Maxwell, L. D. van Buuren and J. M. Doyle, *Rev. Sci. Instrum.*, 2004, **75**, 17.

[289] Y. Segev, M. Pitzer, M. Karpov, N. Akerman, J. Narevicius and E. Narevicius, *arXiv:1902.04549 [physics.atom-ph]*, 2019, 1.

[290] J. M. Gray, J. A. Bossert, Y. Shyur and H. J. Lewandowski, *Phys. Rev. A*, 2017, **96**, 023416.

[291] J. Kleinert, C. Haimberger, P. J. Zabawa and N. P. Bigelow, *Phys. Rev. Lett.*, 2007, **99**, 143002.

[292] B. G. U. Englert, M. Mielenz, C. Sommer, J. Bayerl, M. Motsch, P. W. H. Pinkse, G. Rempe and M. Zeppenfeld, *Phys. Rev. Lett.*, 2011, **107**, 263003.

[293] S. Willitsch, *Proc. Int. Sch. Phys. Enrico Fermi*, 2015, **189**, 255.

[294] S. Willitsch, *Adv. Chem. Phys.*, 2017, 307.

[295] T. Ray, S. Jyothi, N. B. Ram and S. A. Rangwala, *Appl. Phys. B*, 2014, **114**, 267–273.

[296] S. Willitsch, *Int. Rev. Phys. Chem.*, 2012, **31**, 175–199.

[297] J. M. Farrar, in *Springer Handbook of Atomic, Molecular and Optical Physics*, ed. G. W. F. Drake, Springer, New York, 2005, p. 983.

[298] I. W. M. Smith, *Angew. Chem. Int. Ed.*, 2006, **45**, 2842–2861.

[299] T. P. Snow and V. M. Bierbaum, *Annu. Rev. Anal. Chem.*, 2008, **1**, 229–259.

[300] D. Zhang and S. Willitsch, *arXiv:1703.07133v1 [physics.chem-ph]*, 2017.

[301] B. K. Stuhl, *Ph.D. thesis*, University of Colorado, Boulder, 2012.

[302] J. J. Gilijamse, *Ph.D. thesis*, University of Nijmegen, Nijmegen, 2009.

[303] R. Engel-Herbert and T. Hesjedal, *J. Appl. Phys.*, 2005, **97**, 074504.

[304] S. Le Digabel, *ACM Trans. Math. Softw.*, 2011, **37**, 1–15.

[305] F.-J. Börgermann, C. Brombacher, K. Üstüner and V. G. . C. KG, Proceedings of the 5th International Particle Accelerator Conference IPAC14, Dresden, 2014, p. 1238.

[306] L. M. García, F. Bartolomé and J. B. Goedkoop, *Phys. Rev. Lett.*, 2000, **85**, 429.

[307] Vacuumschmelze, *Vacuumschmelze Product Catalogue: Rare Earth Permanent Magnets*, Vacuumschmelze technical report, 2014.

[308] Phytron, *VSS Stepper Motors*, Phytron, GmbH technical report, 2014.

[309] F. L. Pedrotti, L. M. Pedrotti and L. S. Pedrotti, *Introduction to Optics*, Cambridge University Press, Cambridge, 3rd edn., 2018.

[310] M. Breinig, *Physics 421: Modern Optics*, http://electron9.phys.utk.edu/optics421, 2017.

[311] R. Whitcher, *Radiat. Prot. Dosim.*, 2002, **102**, 365–369.

[312] M.-Z. Shao and N. Badler, *Spherical Sampling by Archimedes' Theorem*, University of Pennsylvania Technical Report MS-CIS-96-02, 1996.

[313] R. Whitcher, *Radiat. Prot. Dosim.*, 2006, **118**, 459–474.

[314] D. Reens, H. Wu, T. Langen and J. Ye, *Phys. Rev. A*, 2017, **96**, 063420.

[315] G. Quéméner and J. L. Bohn, *Phys. Rev. A*, 2013, **88**, 012706.

[316] D. Haas, C. von Planta, T. Kierspel, D. Zhang and S. Willitsch, *Comms. Phys.*, 2019, **2**, 101.

[317] J. M. Moré, in *Lecture Notes in Mathematics*, ed. A. Dold and B. Eckmann, Springer Verlag, 1978, p. 105.

[318] E. Jones, T. Oliphant and others, *SciPy: Open Source Scientific Tools for Python*, 2001.

[319] T. deJongh, *Molecular Discharges as a Source for Zeeman Deceleration of NH Radicals*, Radboud Universiteit Nijmegen, Nijmegen, 2016.